Nanophotonics with Subwavelength Apertures: Theories and Applications

by

Yuanjie Pang
B.Eng., University of Victoria, 2008

A Dissertation Submitted in Partial Fulfillment of the
Requirements for the Degree of

DOCTOR OF PHILOSOPHY

in the Department of Electrical and Computer Engineering

Nanophotonics with Subwavelength Apertures: Theories and Applications

by

Yuanjie Pang
B.Eng., University of Victoria, 2008

Supervisory Committee

Dr. Reuven Gordon, Supervisor
(Department of Electrical and Computer Engineering)

Dr. Tao Lu, Departmental Member
(Department of Electrical and Computer Engineering)

Dr. Rogério de Sousa, Outside Member
(Department of Physics and Astronomy)

Supervisory Committee

Dr. Reuven Gordon, Supervisor
(Department of Electrical and Computer Engineering)

Dr. Tao Lu, Departmental Member
(Department of Electrical and Computer Engineering)

Dr. Rogério de Sousa, Outside Member
(Department of Physics and Astronomy)

ABSTRACT

This dissertation presents subwavelength optics with focus on the theory and applications of subwavelength apertures in a metal film. Two main issues regarding the optics with subwavelength apertures are investigated. As the first issue, the extraordinary optical transmission (EOT) through a single hole in a metallic waveguide is presented. A total transmission through a single subwavelength aperture is theoretically predicted for a perfect electric conductor regardless of the aperture size, without relying on aperture arrays and surface corrugations as presented in previous works. The waveguide EOT is then applied to boost the optical throughput of an apertured near-field scanning optical microscope (NSOM) probe. Using a new structure for the apertured NSOM probe which allows for waveguide EOT, the optical throughput and the damage threshold are boosted by 100× and 40× as compared to a conventional structure, and the experimental findings are backed-up by comprehensive finite-difference time-domain (FDTD) simulations. Single fluorescent molecules are scanned using the EOT apertured NSOM probe, and a spatial resolution of 62 nm is achieved.

As the second issue, subwavelength apertures are found useful for optical trapping. A small dielectric particle can significantly change the optical transmission through an aperture by dielectric loading, and subsequently, a large optical force is induced

which favors trapping. A self-induced back-action (SIBA) optical trap is designed using a circular nanohole in a gold film. Trapping of 50 nm polystyrene particle is experimentally achieved, which is not possible using a conventional single beam optical tweezers. The circular nanohole SIBA trap works beyond the perturbative regime, as proven by FDTD simulations and a Maxwell stress tensor analysis. We further improve the nanohole trapping using a double-nanohole, which is more sensitive for small dielectric changes due to the intense local field enhancement between its two sharp tips. A single 12 nm silica sphere is experimentally trapped using the double-nanohole, as the smallest trapped dielectric particle reported. We also achieve the trapping of a single protein – a bovine serum albumin (BSA) protein with a hydrodynamic radius of 3.4 nm in the folded form. The trapped BSA is also unfolded by the large optical force, as confirmed by experiments with changing optical power and changing pH. The high signal-to-noise ratio of 33 in monitoring single protein trapping and unfolding shows a tremendous potential for using the double-nanohole as a sensor for protein binding events at a single molecule level.

Contents

List of Tables

List of Figures

ACKNOWLEDGEMENTS

I would like to express a great gratitude to my dissertation supervisor, Dr. Reuven Gordon. He has been helping me ever since my undergraduate studies. In my graduate studies, Dr. Gordon set a high standard for me and kept providing guidance with insightful and intelligent innovations. In addition, he supported me by many other means including improving my language skills and supporting me for funding opportunities and job searching.

I would like to thank the other dissertation committee members, Dr. Tao Lu and Dr. Rogério de Sousa, as well as the outside examiner Dr. Michelle Xu, for providing valuable suggestions for improving my dissertation. I thank Dr. Alexandre G. Brolo, Dr. David Sinton, Dr. Ir. Frank C. J. M. van Veggel and Dr. Rustom Bhiladvala and their group members for giving me access to their lab equipments, and for providing helps in the areas I am less familiar with. I am grateful to Dr. Niek van Hulst, Dr. Romain Quidant and Dr. P. James Schuck and their group members that I have collaborated with in the collaborated works. In addition, I would like to thank Dr. Rodney Herring, Dr. Elaine Humphrey and Adam Schuetze for helping me in nanofabrication and in nanoimaging, and A. Nick Hone for helping me in numerical simulations using CST Microwave Studio.

I feel lucky to work in a very friendly environment. All my colleges have been very kind to me, and they keep providing insightful discussion in the academic work, as well as providing assistances in personal life. I would like to thank them all.

I also acknowledge The University of Victoria Fellowship, The Jarmila Vlasta Von Drak Thouvenelle Graduate Scholarship, The Chinese Government Award for Outstanding Self-Financed Students Abroad, and The Albert Hung Chao Hong Scholarship for financial supports.

DEDICATION

To my parents

and

Su Pu

Table 1: Common Abbreviations

Abbreviation	Meaning
APD	avalanche photodiode
AFM	atomic force microscope
BSA	bovine serum albumin
DERS	directivity-enhanced Raman scattering
DNA	deoxyribonucleic acid
EOT	extraordinary optical transmission
FDTD	finite-difference time-domain
FIB	focused-ion beam
IR	infrared
LSP	localized surface plasmon
MNP	Metal nanoparticle
mPEG	methoxypoly (ethylene glycol)
MST	Maxwell stress tensor
NSOM	near-field scanning optical microscope
PDMS	poly(dimethylsiloxane)
PEC	perfect electric conductor
PML	perfectly-matched layer
PMMA	poly(methyl methacrylate)
RNA	ribonucleic acid
SEM	scanning electron microscopy
SERS	surface-enhanced Raman scattering
SIBA	self-induced back-action
SNR	signal-to-noise ratio
SP	surface plasmon
SPP	surface plasmon polariton
TE	transverse-electric
TFSF	total-field scattered-field
TDI	Toluene diisocyanate
TM	transverse-magnetic
WGM	whispering-gallery-mode

Table 2: List of Symbols

Symbol	Meaning
α	polarizability
ϵ	permittivity
μ	permeability
ρ	charge density
λ	wavelength
ω	angular frequency
c	speed of light
B	magnetic flux density
D	electric flux density
E	electric field
H	magnetic field
J	current density
n	refractive index
p	dipole moment
r	radius
Z_0	free space impedance

Chapter 1

Introduction

1.1 Subwavelength Apertures

The general topic in this dissertation is subwavelength optics. Subwavelength optics focuses on the interaction between electromagnetic wave and objects with a feature size smaller than half of the light wavelength. For example, for visible light which has a wavelength roughly from 380 nm to 750 nm, the objects of interest are those having feature sizes significantly below 375 nm. This is why the research field is sometimes called "nanophotonics".

Many different subjects exist within the field of subwavelength optics, studying different subwavelength objects, for example, optical nanoantennas [11–15], metal nanoparticles [9], and metal nanowire gratings [8].

Of the diverse topics within subwavelength optics, the one that interests me the most is the study of subwavelength apertures in a metal film. This dissertation will be focused on the theory and the application of light interacting with different types of subwavelength apertures in different environments.

Subwavelength apertures have been studied intensively since the publication of Bethe's aperture theory in 1944 [16]. In that work, Bethe studied the optical transmission through an aperture with size much smaller than the wavelength on an infinitely extending metal sheet. Bethe found that the diffraction of light upon transmitting through such a subwavelength aperture can be approximated by the radiation of a magnetic dipole, and the transmitted power is proportional to the fourth power of the aperture size. Ultimately, the optical transmission through a small subwavelength aperture is very low.

1.1.1 Extraordinary Optical Transmission

Bethe's aperture theory has been challenged by the discovery of extraordinary optical transmission (EOT). Basically, EOT is the phenomenon where the optical transmission through subwavelength apertures is greatly increased when the apertures are arranged in specific ways. For example, when the subewavelength apertures are arranged in an array, resonantly increased optical transmissions [17] and even total transmissions [2, 18] have been predicted and observed. In addition, EOT has also been found for a single hole surrounded by corrugations on the surface of the metal film [19]. This is because the corrugations act as matching gratings which couple free-space light into surface plasmons (SP) bound to the metal surface, and focus the SP to the aperture.

However, it is somewhat unfair to compare Bethe's aperture theory with EOT relying on aperture arrays and surface corrugations, because Bethe's theory was based on only a single aperture on a flat metal film. In addition, it is worthy to notice that Bethe's original intention was to use the theory to study a subwavelength aperture in a transverse screen in a metallic waveguide. It remains a question whether EOT can be achieved through such an aperture in a waveguide screen.

1.1.2 Near-Field Optical Probes

Waveguide EOT is not only interesting in theoretical considerations, but it also has significant application in near-field optics. As a fundamental rule in optics, light that carries information with a spatial resolution smaller than half the wavelength cannot propagate to the far-field, and this leads to Abbe's resolution limit of a lens-based optical microscope [20]. To access the subwavelength features, a probe is needed to approach the light in the near-field before it evanescently decays. As a commonly used near-field probe, an apertured near-field probe is basically a metallic waveguide structure with a tapered glass fiber core, a metal coating and a subwavelength aperture at the tip. The apertured near-field probe benefits from a background-free working scheme, but suffers from a low optical transmission through the aperture [21]. It is desired to use the waveguide EOT to boost the optical transmission for an apertured near-field probe. It is always exciting to extend microwave regime concepts to visible-infrared (IR) regime for assisting in the light manipulation and the optical component design. For example, microwave antenna concepts [22] have been used in the visible-IR regime for achieving a highly directional light emission [13–

15]. However, extending a microwave design into the visible-IR regime, changes and limitations due to material properties and fabrication imperfections need to be well considered. In the dissertation, the issue of extending a microwave waveguide design into visible-IR regime will be discussed.

1.1.3 Optical Trapping and Apertures

Subwavelength apertures also find applications in optical trapping. Optical trapping is a technique of immobilizing and manipulating small objects using light. Since the first introduction of a single beam optical tweezers [23], optical trapping have been applied to trap dielectric particles [23, 24], carbon nanotubes [25], semiconductor nanowires [26], and metal nanoparticles [27–29]. Since it gives a gentle control to the trapped object, optical trapping is considered as a promising candidate for manipulating biological materials, which, from an optics perspective, are essentially dielectric particles. Optical trapping of small biological particles has included living cells [30–32], bacteria [33], tobacco mosaic virus particles [33]. Extremely elongated biological materials have been trapped and manipulated by tethering their ends to bigger particles [34–37].

However, a restriction to a single beam optical tweezers is that the required power dramatically increases as the trapped particle size decreases [5, 23]. This is because the optical force in a single beam optical tweezers obeys the perturbative gradient force formulation, in which the force scales with the third power of the particle size. The smallest dielectric particle can be trapped by a single beam tweezers has a diameter of 100 nm. For the smallest biological particle such as a single virus, a single bacteriophage or a single protein, we need to be able to trap dielectric particles smaller than 20 nm. In order to achieve trapping of smaller dielectric particles, many approaches have been proposed, including using silicon waveguides [38, 39], using whispering-gallery-mode optical resonators [40, 41] and using photonic crystal cavities [42–44].

As our approach for trapping small dielectric particles, we try to work beyond the perturbative regime. That is, we try to find a situation where even a small particle can induce a significant change to the electromagnetic field, and therefore induce a large optical force. We find that this is the case in a subwavelength aperture. Since the optical transmission through a subwavelength aperture is very sensitive to the aperture size (scales with the fourth power of the size), any change, including a

dielectric loading by a particle, inside the aperture gives a significant change to the optical transmission. We theoretically and experimentally study the possibility and implementation of an optical trap that works beyond the perturbative regime using a subwavelength aperture.

As it will be shown later, using a subwavelength aperture, the record of trapped particle size have been broken for a few times. The optical trapping experiment, including the design of the nanoaperture and the optical setup, has been improving along the way of aiming on trapping smaller and smaller particles. Finally, trapping of a smallest biological particle, a single protein, is achieved. The possibility of using the same trapping setup as a sensor will be also discussed. In addition to its tremendous trapping ability and sensing potential, a single subwavelength aperture is extremely small in size and is suitable for a dense optical integration.

1.2 Organization of Dissertation

This dissertation focuses on the theories and applications of subwavelength aperture on a metal film. Chapter 2 is a thorough review on single subwavelength aperture optics, with a significant part being my own contributions. This chapter gives the logical linking amongst my peer-reviewed journal publications in my Ph.D. study (fully reproduced in the Appendix). Chapter 3 gives a detailed summary of all the theoretical and experimental tools used in the investigations. Chapter 4 introduces my other contributions in my Ph.D. study. These additional studies do not particularly relate to apertures, but still fall into the category of nanophotonics. Chapter 5 concludes the dissertation as well as making the suggestion for some possible future research directions. All the peer-reviewed journal publications in my Ph.D. study are reprinted with permission and listed as appendices.

Chapter 2

Subwavelength Apertures and Applications

This chapter introduces and summarizes the main theme of this dissertation: optics with subwavelength apertures on a metal film. Bethe's aperture theory of the optical transmission through a subwavelength aperture is first reviewed. Then, using Bethe's theory, a total transmission through a subwavelength aperture in a metallic waveguide screen is theoretically derived. As an application to this phenomenon, a high-throughput apertured near-field probe is designed and experimentally tested. Subwavelength apertures are also applied in the optical trapping. After a review of the theoretical formulations of the optical force, a self-induced back-action optical trap using a circular nanohole is introduced. As an evolution to the circular nanohole trap, a double-nanohole is used for trapping even smaller dielectric particles and single proteins.

2.1 Bethe's Aperture Theory

2.1.1 Motivation

When light is incident onto an aperture (a hole) on a metal sheet, if the aperture has a much smaller dimension than the wavelength, the light will be cutoff in the aperture and cannot propagate. As a "hand-waving" explanation of light cutoff, light with a large wavelength cannot "fit" itself into a hole that is much smaller. As a stricter explanation, cutoff can be derived from the boundary condition of the electromagnetic field within the aperture: there is no way for the propagating wave to satisfy the

boundary condition that the tangential electric field on the metal boundary has to be zero. Under such a condition, light is diffracted at the edge of the subwavelength aperture.

Hans Bethe first studied the diffraction of light transmitted through a subwavelength hole in a metal screen [16]. Bethe set up the problem to solve for "the diffraction of electromagnetic waves by a small hole in an infinite plane conducting screen", but it should be noted that Bethe's original intention was to solve more practical problems such as "the effect of a small gap in a wave guide upon the propagation of waves along that guide." This intention is illustrated in Figure 2.1.

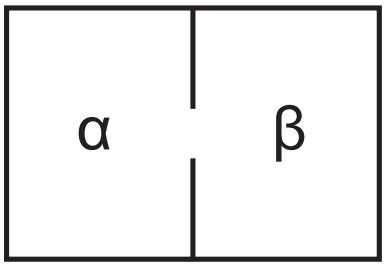

Figure 2.1: Bethe's original intention as an application of his aperture theory: to investigate transmission through a hole in a waveguide screen separating two cavities α and β.

2.1.2 Derivation to Bethe's Aperture Theory

The easiest way to reproduce Bethe's result is by the quasi-static approximation. When considering an object that is much smaller than the wavelength of light, the spatial variation of the field will be much more rapid than the temporal variation. In this case, we can neglect the time dependence and solve the field around the object using only boundary matching conditions in electrostatics.

In the case of a circular hole with a diameter much smaller than the wavelength on an infinite perfect electric conductor (PEC) plane, with plane wave incident normally to the PEC plane and the electric and magnetic field parallel to the PEC plane, the light diffracted by the hole can be approximated by the emission of a magnetic dipole. By solving the boundary condition of the magnetic potential at both sides of the PEC plane [45], the effective magnetic dipole moment of the hole in response of the incident plane wave can be obtained. The transmitted power through the hole can be subsequently formulated as the power emitted by this dipole. In free-space, the optical transmission is expressed as:

$$T = \frac{1}{2}\frac{4Z_0\pi^3}{3\lambda_0^4}\left(\frac{8r^3}{3}H_0\right)^2 \propto \frac{r^6}{\lambda^4}, \tag{2.1}$$

where Z_0 is the free-space impedance, λ_0 is the wavelength in free-space, r is the hole radius, and H_0 is the magnetic field of the incident wave. After normalizing to the area of the hole πr^2, we will obtain the most important conclusion in Bethe's theory of the optical transmission through a subwavelength hole: the optical transmission through a subwavelength aperture is inversely proportional to the fourth power of the light wavelength, that is $T \propto (\frac{r}{\lambda})^4$. This is summarized in Figure 2.2. In other words, a hole in a metal sheet with a dimension much smaller than the light wavelength permits little transmission through it.

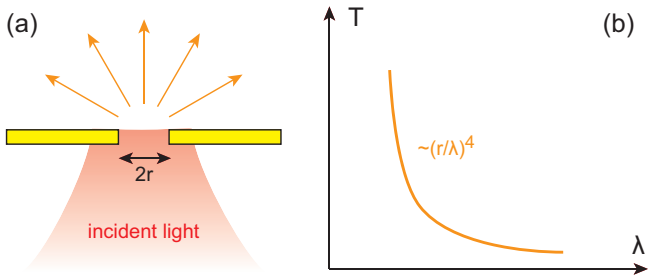

Figure 2.2: A schematic illustrating the transmission of light through a subwavelength hole. The spectrum is the most important summary of Bethe's aperture theory: the optical transmission is proportional to the inverse fourth power of wavelength.

If the aperture is surrounded by a dielectric medium with a refractive index n, the wavelength in the medium is scaled as $\lambda = \lambda_0/n$. Therefore, a larger optical transmission is expected for the same aperture size:

$$T = \frac{1}{2}\frac{4Z_0\pi^3 n^4}{3\lambda_0^4}\left(\frac{8r^3}{3}H_0\right)^2. \tag{2.2}$$

2.2 Aperture with Different Shapes

Bethe's aperture theory mainly focuses on a simple aperture shape, such as a circular aperture, on an infinitely thin PEC screen, as an idealized physical situation. In a more realistic situation, we need to consider the finite thickness and the material properties of the metal screen. In addition, it is possible to obtain a higher transmission through an aperture by changing aperture shape. For an aperture with a certain

shape, it can have a larger cutoff wavelength than other apertures. Therefore, more light can transmit through it even if its total area remains unchanged.

2.2.1 Aperture in a Real Metal Film

When considering the optical transmission through an aperture in a real metal in the visible-IR regime, the situation is more complicated because of the presence of surface plasmon polaritons (SPP). SPP is the electromagnetic wave confined near and propagating along the interface of metal and dielectric (including vacuum) material. In other words, it is a waveguiding mode that is bounded to a metal surface. It can be derived by solving Maxwell's equations near the metal-dielectric boundary, taking proper considerations to the real metal dielectric properties [46]. The relative permittivity of a real metal is commonly modeled by the Drude model and is given by the following formula:

$$\epsilon_r \simeq 1 - \frac{Ne^2}{\epsilon_0 m\omega(\omega + \frac{i}{\tau})} = 1 - \frac{\omega_p^2}{\omega(\omega + \frac{i}{\tau})}, \tag{2.3}$$

where i is the imaginary unity, N is the charge carrier density, τ is the mean free time of a free electron between collisions, e and m are the charge and the mass of an electron, ϵ_0 is the permittivity of vacuum, ω is the angular frequency, and $\omega_p = \sqrt{\frac{Ne^2}{\epsilon_0 m}}$ is called the plasma frequency. Therefore, it can be seen that the relative permittivity of a metal has a negative real part at a frequency smaller than the plasma frequency [47, 48]. When solving Maxwell's equation at a boundary of two materials, one with a positive permittivity, one with a negative permittivity with a large magnitude in the real part, the SPP solution is found as light wave travels along the boundary with a larger wave vector (or a smaller wavelength) than in free space, and it is evanescent in the direction perpendicular to the boundary. At visible-IR regime, using silver or gold as the metal, the decay length of this evanescent wave is typically a few hundreds of nanometers into the dielectric and a few to tens of nanometers into the metal [49]. For more sophisticated metal structures, different forms of SPP exist. For example, for a metal-dielectric-metal sandwich structure, the SPP at both metal surfaces couple to each other, leading to a solution called the gap plasmon. A novel reflective wave plate which utilizes the gap plasmon is discussed in Appendix G.

SP modes have been considered for the transmission through rectangular aper-

tures in past theoretical works [50, 51]. The transmission through rectangular and circular nanoapertures has been measured, showing a LSP resonance [52]. As Figure 2.3(a,b) shows, a broad transmission peak was found for a circular nanoaperture in a stand-alone silver sheet. For a rectangular aperture (Figure 2.3(c)), two LSP modes exist with the electric field polarized along the short and the long axes of the aperture, and the different mode geometries result in different resonant wavelengths. As Figure 2.3(d) shows, the two transmission peaks associated with these two LSP modes could be excited with orthogonal polarizations.

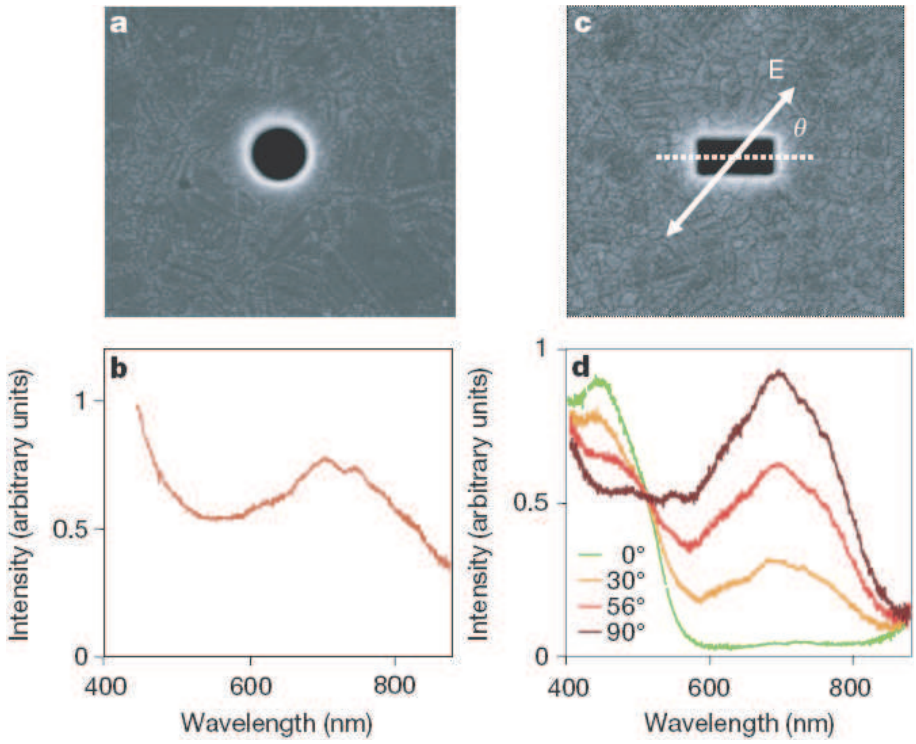

Figure 2.3: Transmission peaks associated with LSP modes for nanoapertures with different shapes in a stand-alone silver film. (a) A circular aperture with a 270 nm diameter in a 200 nm thick film and (b) its transmission spectrum. (c) A rectangular aperture with a 210 nm × 310 nm dimension in a 700 nm thick film and (d) its transmission spectrum for different polarizations. Figure reprinted with permission from Ref. [1].

For an aperture in a real metal film, the transmitting light couples into SPP and can penetrate into the wall of the aperture. Thus, the aperture is effectively larger. Early theoretical [50, 51] and experimental [52] works have been done on the light transmission through single circular and rectangular nanoholes on silver, taking the SPP into accounts. In addition, for a hole with a thin rectangular shape, the SPP in

the closely separated metallic walls couple as gap plasmon. A theoretical work has been done by solving the SPP mode in a rectangular hole in real metal using the effective index method [53]. In a narrower hole, the SPP modes on the two opposite sides of the hole have a stronger coupling giving a higher effective index, leading to an increased (or red-shifted) cutoff wavelength and therefore an increased transmission.

The coupled SPP in the hole in a real metal film also results in a shift in the Fabry-Perot resonance between the two metal-dielectric boundaries of the finite thickness metal film. For a hole in a film with a finite thickness, a resonant peak is found in the transmission. This is explained as a Fabry-Perot resonance of the light traveling in the longitudinal direction of the hole, experiencing multiple reflections at the two metal-dielectric boundaries, as theoretically studied using a PEC model [54]. For real metals, the Fabry-Perot resonance shifts for holes with different width on a metal sheet with the same thickness, because the SPP modes of the light transmitted through the hole have different effective propagation indexes for holes with different width [51].

2.2.2 Apertures with More Sophisticated Geometries

Subwavelength holes with more sophisticated geometries have also been studied. For example, C-shaped holes allow for much larger optical transmission than a square hole that gives a same near-field spot size [55], and this is confirmed by experiments using C-shaped nanoholes on gold film [56]. Another type of holes that attracts intensive interest has two closely facing sharp tips, such as a bowtie-shaped hole or a double-circular hole. In addition to an increase in transmission, it is also shown that a bowtie hole can lead to an intense local field at a tight spot between the tips [57, 58], and it is applied in near-field imaging [59] and photolithography [60]. Similar to a bowtie hole, a double-hole also uses the sharp tips for a high locally enhanced field and energy flux [61]. Increased optical transmission due to the sharp tips in a double-hole has also been presented [62]. Double-holes has been applied in second harmonic generation [63–65] and Raman spectroscopy [66]. The advantage of double-holes is that it may be easier to fabricate. A double-nanohole can be fabricated using a focused-ion beam (FIB) by milling two adjacent circular holes, and the separation between the tips in a double-hole can be controlled by the distance between and the radius of the two circular holes. Besides using the standard focused ion beam milling, double-holes can be fabricated by polystyrene nanosphere lithography using dimers [65].

2.3 Extraordinary Optical Transmission

2.3.1 Extraordinary Optical Transmission through Apertures in a PEC Film

The discovery of EOT presents a direct challenge to Bethe's aperture theory. The most important and surprising finding in EOT was the unusually high transmission, or even total transmission through subwavelength holes in certain conditions. EOT was first discovered in a condition similar to Bethe's investigation, but having an array of holes instead of a single hole on an infinite metal screen. Many later works have individually shown EOT using a PEC or a good electric conductor screen [2, 18, 67]. For example, a 100% transmission was found through a square array of subwavelength holes on an infinite PEC sheet [2], as summarized in Figure 2.4.

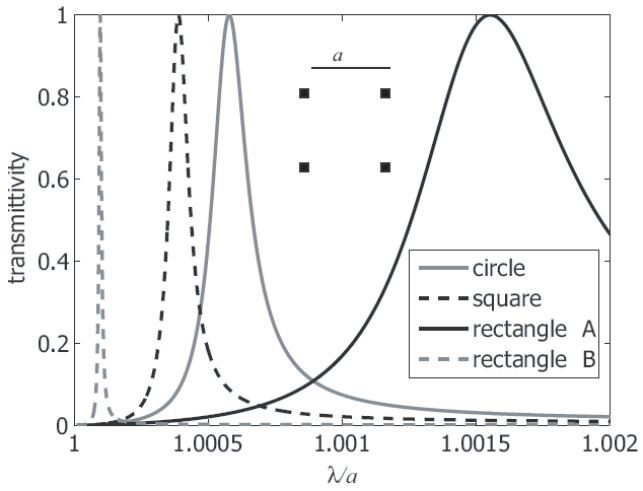

Figure 2.4: The optical transmission through a square array of subwavelength holes on an infinite PEC sheet, without any normalization, showing a total transmission at a certain wavelength. The inset represents the schematics of a hole array on a PEC screen. Reprinted with permission from [2].

From Figure 2.4, it can be seen that the total transmission through the hole array is resonant: the peaks for total transmission only happens at specific frequencies. The resonant nature is common to all known EOT phenomenon. This EOT phenomenon is due to a resonant condition of the mutual coupling between the apertures. It should also be noted that, although the aperture shape has been manipulated in this work, each individual hole is still well below cutoff. In this EOT phenomenon, changing the aperture shape does not have an effect on the transmission intensity - the

transmission remains 100% at each peak. However, the position and the quality of the peak is greatly modified by the aperture shape. To explain this, when the aperture polarizability is changed due to the shape, the mutual coupling condition between apertures is shifted. Moreover, for apertures with smaller polarizability, it takes a longer time to build up the optical energy for the total transmission, equivalent to a higher resonant quality.

2.3.2 Extraordinary Optical Transmission through Apertures in a Real Metal Film

EOT in the visible-IR regime through a hole array has been experimentally demonstrated by Ebbesen's pioneering work [17]. That work has found transmission peaks through a subwavelength nanohole array on silver and gold films. The peak transmission intensity was much higher than predicted by Bethe's theory, although lower than unity due to dissipation in real metal. In addition to the mutual coupling between apertures, Ebbesen found that the excitation of SPP on the metal surface plays a role in visible-IR regime EOT. The hole array acts as a light momentum matching grating, and it couples the free-space incident light into SPP and re-emits it at the transmission side. Only at certain wavelengths can the light and SPP momentum be matched by a hole array with a specific periodicity, making the EOT a resonant phenomenon. Subsequent theoretical and experimental studies have provided support to the plasmonic EOT phenomenon [68–71]. To confirm the role of SPP played in visible-IR regime EOT, an experiment was carried out using hole arrays on a free-standing nickel (a metal does not support SPP) film [68]. Transmission spectrums were compared using a bare nickel film and using a nickel film covered by 30 nm thick silver – a thickness comparable to the SPP decay length in silver. It was found that EOT peaks only existed for the silver-covered nickel film. Interestingly, a spoof surface plasmon can be derived by hole arrays in non-plasmonic metals (or even PEC) and can also support EOT [72], because the cutoff mode in the subwavelength holes has a surface wave profile (field decays in the direction perpendicular to the metal surface) that is equivalent to SPP in plasmonic metals.

Plasmonic EOT has a great potential in surface plasmon resonance (SPR) optical sensing for its high sensitivity and simplicity [73, 73–75]. Hole array SPR sensors has been used to sense small changes in the refractive index [76–78] and the surface binding of biological materials [79–84].

Using SPP coupling, it is also possible to achieve EOT through a single hole on a real metal film. A beaming of light with a large optical transmission was found through a subwavelength hole surrounded by corrugations, including an array of dimples [85] and concentric rings [19, 85]. The corrugations again serve as momentum matching gratings which couples the free-space light into SPP. The concentric rings also serve as focusing rings that constructively focus the SPP to the hole at the center. As a result, the optical transmission through the hole is greatly enhanced as compared with a hole without corrugation.

In all the previously discussed EOT, array effects and mutual coupling between the array elements have been a key factor, including in the metal structures for coupling free-space light into the SPP. Mutual coupling is a very interesting topic in electromagnetics, especially in considering arrays of apertures or slits. For example, to explain the well known Wood's anomaly diffraction effect which predicts a zero in the transmission spectrum through a metal spectrum (the opposite case of EOT) [86], Lord Rayleigh used an elegant argument by realizing the summed contributions through all the mutually excited slits to be divergent [87]. However, we are interested to know if EOT can happen without any array structures.

2.4 Single Hole Waveguide EOT

2.4.1 Revisiting Bethe's Original Motivation

Let us now revisit one of Bethe's intentional application of his aperture theory: to investigate the coupling of two waveguide sections through a hole in a transverse waveguide screen, as mentioned in Figure 2.1 in the beginning of this chapter. This is a standard microwave engineering problem and has been considered extensively, for example, in a widely used microwave engineering textbook written by Pozar [88].

Pozar used Bethe's formulation and approximated the hole as a magnetic dipole with a polarizability proportional to the magnetic field. Pozar's result is only an approximation, and it is self-inconsistent: it leads to a nonphysical result with the normalized reflection amplitude greater than unity [88]. This solution is valid when the hole has a small magnetic dipole moment, which is usually the case for a small hole. However, we find that at some resonant condition, taking higher order modes into account, even a small hole can be excited with a large dipole moment. This permits an EOT through a single subwavelength hole in a waveguide - the exact same

setup as Bethe's original intention and as considered in a standard textbook.

2.4.2 Resonant Total Transmission through a Waveguide Aperture

Figure 2.5 (a) shows a total transmission of optical power through a single hole in a transverse waveguide screen. We have analytically re-investigated the optical transmission through a single subwavelength hole at the center of a transverse metal screen in a rectangular waveguide, by using Bethe's magnetic dipole approximation of the small hole, and by using self-consistency relations with resonances and specific higher order modes. This transmission peak always exists and is always 100% as long as without material loss (PEC case), no matter how small the hole is. The hole size and shape only slightly shift the total transmission peak in the spectrum.

To obtain the total transmission, we considered a higher order TM_{12} mode (TM stands for transverse-magnetic) in addition to the lowest order propagating TE_{10} mode (TE stands for transverse-electric). The interesting feature of the TM_{12} waveguide mode is that, at its cutoff frequency, it gives a divergent magnetic field at the center of the waveguide for a finite electric field. By Bethe's theory, the hole's effective magnetic dipole moment is proportional to the magnetic field, so the hole is excited by an infinite magnetic field at the TM_{12} cutoff. All the energy is built up at the hole and is re-emitted at the other side of the metal screen, as illustrated in Figure 2.5 (b). Since the TM_{12} mode is cutoff, it is bounded to the metal screen and does not propagate; the TE_{10} mode is still the only propagating mode. We related the TE_{10} and TM_{12} mode amplitudes by a Fourier decomposition and solved the self-consistency equation, and we found that the total transmission actually occurs at a wavelength slightly longer than the TM_{12} cutoff. An equivalent explanation is from the impedance matching perspective. The TM_{12} cutoff mode has an infinite admittance, and so does an infinitesimal hole. Therefore, the impedances of the waveguide mode and the hole are perfectly matched, allowing a total transmission.

2.4.3 Relations to Previous Works

It is easy to miss the novelty of our waveguide EOT by confusing its working principle with other EOT phenomenon based on cutoff modes in the holes, for example [69, 72]. It should be noted that those works considered a cutoff mode in each individual aper-

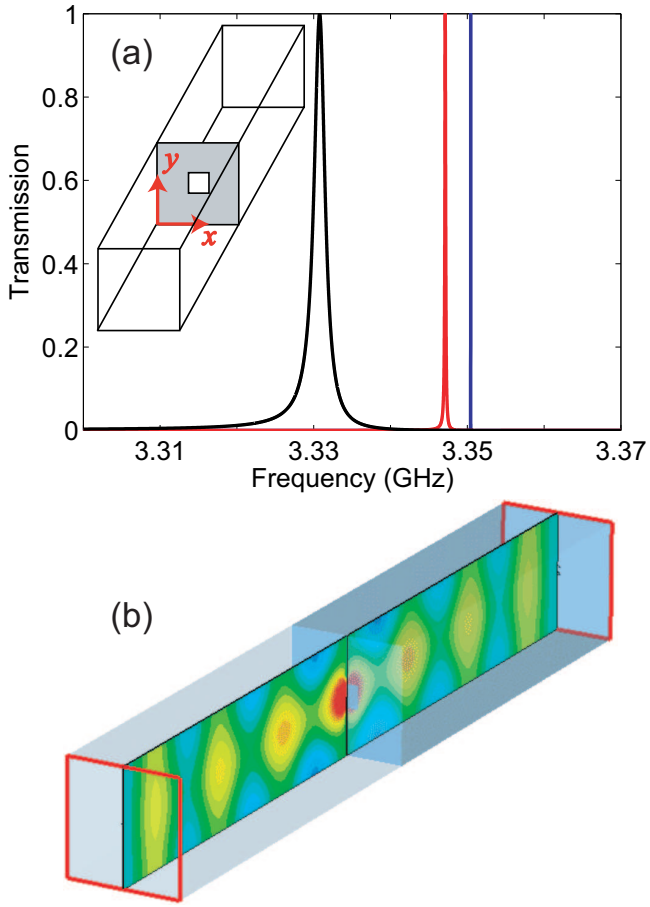

Figure 2.5: (a) Resonant total transmission of optical power through a single hole in a transverse waveguide screen. Three results are shown in this graph with aperture width equal to 0.1, 0.15 and 0.2 times of the waveguide width, in blue, red and black. (b) Finite integral simulation (CST Microwave Studio) showing the total transmission through the waveguide hole at the resonant condition. Reprinted with permission from [3].

ture, not a waveguide mode. Again, the aperture considered in our work can be arbitrarily small – giving an arbitrarily large cutoff frequency – and still permits a total transmission. The working principle of the waveguide EOT is in fact distinct from any previously found EOT phenomenon, it does not rely on SPP [17, 53], spoof-SPPs of thick films [72], array effects [2, 18], specific hole geometry [55, 56, 65], or Fabry-Perot resonances [54, 71], which can play a role in the EOT of arrays and single holes in a screen. The waveguide EOT is confirmed by finite-integral and finite-difference time-domain simulations with a high consistency, even when material loss is considered in the simulations. We did not have the resource to perform the experiment, but microwave measurements by other groups has confirmed our results [89–92]. An equivalent circuit model was also given for explaining the EOT, where the waveguide was represented by a transmission line model, and the screen and the hole were modeled by L-C circuits. At the resonant condition, the equivalent impedances of the hole and the waveguide are perfectly matched, allowing for a total transmission without reflection.

The reader is referred to Appendix A for the details of the study described in Section 2.4.

2.5 Abbe's Resolution Limit and Near-Field Optics

The waveguide EOT phenomenon can be potentially useful in many applications, such as sensing, waveguide filtering and local heating. Especially, it can be applied to boost the throughput of an apertured near-field scanning optical microscope (NSOM) probe. In order to understand the EOT brightened NSOM probe, we shall first review some theories in the diffraction limit and near-field optics.

2.5.1 Abbe's Resolution Limit

A conventional lens-based optical microscope which probes light in the far-field of the object has a fundamental limit to its resolution, as initially discovered by Ernst Abbe [93] (as translated in Ref. [94]) and subsequently quantified by Herman Helmholtz [95]. Two points on the object plane cannot be resolved by a lens-based optical microscope if they are spaced closer than

$$d \simeq \frac{\lambda}{2n \sin \alpha}, \tag{2.4}$$

where λ is the wavelength, n is the refraction index of the medium, and α is the half focusing angle. Abbe's resolution limit arises because light that varies spatially with a length scale smaller than half wavelength is evanescent in space: it is bound to the near-field and does not propagate away from the object.

Mathematical expressions that differentiate the near-field and the far-field are usually given for antennas in the microwave regime [22]. However, in near-field optics, the near-field and the far-field are not defined in such a rigorous way. Usually, the near-field region is considered to be within the order of a wavelength away from the object.

2.5.2 Near-Field Optics

The NSOM can probe light with spatial resolution well below the diffraction limit. As the main working principle of an NSOM, a probe is placed very close to the structure under study, typically within 10 nm. Such a distance is within the near-field of the light scattered by or emitted from the structure where the spatially fast-varying light component does not have enough distance to decay away, and the subwavelength spatial resolution can be probed.

NSOM relies heavily on the interaction between the near-field light and the probe, and the design of the near-field probe is therefore a hot topic. Two main categories of near-field probes exist: the apertureless probe and the apertured probe.

2.5.3 Apertureless Near-Field Probes

Apertureless probes are usually made of sharp metallic tips. These sharp metallic tips can utilize plasmon effects to generate a local field enhancement for a large optical throughput [96, 97]. Apertureless NSOM's have been applied in probing two-photon luminescence [98], imaging carbon nano-tubes [99] and fluorescent molecules [100, 101], imaging and mapping localized surface plasmon (LSP) modes [102].

As a novel apertureless NSOM design, nanoantennas are used at the tip of the probe for a strong local field enhancement with a tight light spot. Various nanoantennas are fabricated at the tip of a dielectric pyramid on an atomic force microscope (AFM) cantilever. For example, a bowtie antenna was fabricated on a silicon nitride

AFM tip for Raman spectroscopy mapping [103]. A nano-cone, fabricated on an AFM tip by ion milling with an etching mask, had a very sharp front with about 10 nm radius and has a potential toward for high resolution topographical imaging.

Despite their advantages of brightness, the main drawback of apertureless NSOM probes is the background light leakage. As the illumination of an apertureless NSOM probe comes from the far-field (usually a focused laser spot in free-space), it is difficult to distinguish the desired signal from the background illumination, and modulation schemes are usually required for an apertureless NSOM probe [100].

2.5.4 Apertured Near-Field Probes

For apertured near-field probes, on the other hand, signal is only coupled through a subwavelength aperture at the tip, and the background signal is blocked by metal coatings. A background-free scanning can be achieved in this way.

The simplest structure of an apertured near-field probe is formed by coating an optically thick metal layer at the periphery of a tapered optical fiber, leaving a waveguide structure with a silica core and a transmissive hole at the tip. The hole formed at the tip can be typically 100 nm in diameter or less [21]. Light is delivered through the metal coated taper and transmitted through the hole creating a very tight local illumination spot, and is detected in the far-field, as the opposite of an apertureless near-field probe. In this way, there is no "background" illumination.

The main drawback of an apertured near-field probe is the small light throughput at the hole. The overall light transmitted through a tapered fiber apertured near-field probe is of orders of magnitude less than an apertureless near-field probe. To practically improve the brightness of an apertured near-field probe, we cannot indefinitely increase the optical input to the fiber taper, because the thin fiber tip can be damaged by a high optical power.

Two reasons are responsible for the low light transmission through an apertured near-field probe. First, light transmission through a subwavelength hole is low, by Bethe's aperture theory. However, a smaller hole is desired for a small light spot, and therefore it is a trade-off between light throughput and resolution. Second, at the end of a conventional tapered fiber structure, the fiber waveguide diameter becomes too small and goes below cutoff for the light, making the light decay in the last section of the fiber. A larger fiber cone angle is desired for a smaller decay in the waveguide, but the cone angle is limited by fabrication issues. The conventional heat-and-pull

technique only allows for small cone angles [21]. Chemical etching technique is more suitable to create fiber tapers with larger cone angles [104], and high transmissions are achieved through near-field probes made by the chemical etched fibers [105]. However, the resulting surface quality of chemical etching is usually lower than the heat-and-pull technique.

Different approaches have been used to improve the optical throughput of an apertured near-field probe. A high throughput apertured near-field probe was achieved by changing the cavity shape [106, 107]. However, this method only deals with the waveguide loss; the other half of the problem, the low transmission through the subwavelength hole, is not solved. Several approaches have been used to improve the light transmission through the subwavelength hole. Concentric ring gratings have been created around the apertures using FIB milling, and they boost the light transmission by coupling light into SPP and focusing it at the aperture [108]. However, this method requires a relatively large end face to fit the rings. A 1/4 wavelength monopole antenna was created near the hole to improve the radiation efficiency [109]. A bowtie shaped aperture was used for a high transmission while keeping a tight focusing spot [110].

Coaxial apertures have also been used for apertured near-field probes. A coaxial aperture is fabricated on a gold coated SiN AFM cantilever and is used for Raman scattering signal scanning [111]. A coaxial aperture benefits from its local field enhancement through gap plasmon mode between the outer and inner metal parts, as well as a relatively wide transmission band [112, 113]. In addition, a coaxial aperture on the tip of a pyramid shaped AFM cantilever has a protuberant inner metal part, giving a tight scanning spot. A Raman imaging of single carbon nanotubes is obtained by the coaxial apertured near-field probe, and a whole Raman spectrum with highly enhanced Raman signal is obtained at each scanning point using a short exposure time.

2.6 EOT Brightened Near-Field Probe

We realized that the waveguide EOT phenomenon is a potential candidate for overcoming both issues that limits the apertured near-field probe light throughput - the waveguide decay and the low aperture transmission. Using this probe, we have achieved a 100-fold and a 40-fold increase in the light throughput and in the damage threshold, as compared to a conventional tapered fiber apertured near-field probe.

Using this high-throughput near-field probe, we scanned single fluorescent molecules with a 50 nm resolution.

2.6.1 Structure of the EOT Near-Field Probe

Figure 2.6 (a) shows a schematic of the proposed apertured near-field probe. We created an apertured near-field probe with a flat-end fiber taper coated by aluminum at the periphery and by gold on the end face, and with a subwavelength hole at the center of the end face. The structure of this probe is directly analogous to the waveguide with a transverse screen, which permits a resonant total transmission through a small hole in microwave regime. For the near-field probe, considering fabrication limitations and excitation wavelengths, we typically choose the tip diameter of the fiber core d_t to be about 500 nm, and the hole diameter d_a to be 50-100 nm. An scanning electron microscopy (SEM) image of the probe is given in Figure 2.6 (b). The fabrication steps will be mentioned below.

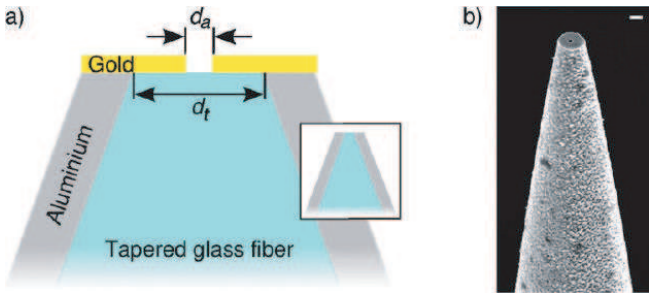

Figure 2.6: (a) Schematic of the waveguide EOT brightened near-field probe structure. For comparison, the conventional apertured near-field probe is drawn in the inset. (b) An SEM image of the near-field probe. Reprinted with permission from [4].

2.6.2 Measured Spectrums and Theoretical Supports

The proposed high-throughput near-field probe employs the same waveguide EOT as introduced in Section 2.4. In this circular waveguide, we consider two modes: the TE_{11} mode and the cutoff TM_{11} mode. The TE_{11} mode is the lowest order propagating mode in a circular waveguide. The TM_{11} mode in a circular waveguide plays the same role as the TM_{12} mode in the rectangular waveguide EOT. At the cutoff of the TM_{11} circular waveguide mode, the magnetic field is divergent at the

waveguide center, giving a huge excitation to the subwavelength hole, leading to a large transmission through the hole.

We have done experimental measurements and finite-difference time-domain (FDTD) simulations to this structure. Figure 2.7 (a) shows The transmission spectrum for two apertured near-field probes with taper diameters d_t equals 420 nm and 475 nm, obtained from FDTD simulations and experiments. As expected, an EOT peak was found for each probe at a wavelength slightly red-shifted than the TM_{11} cutoff. Because of the material loss of real metal in the visible-IR regime, a 100% transmission no longer be achieved; however, the EOT still permits a significantly larger transmission through the hole. The critical role of the TM_{11} mode is more clearly shown by investigating the EOT peak wavelengths of a number of probes with different diameters, shown in Figure 2.7 (b). Theoretically, the TM_{11} cutoff wavelength is linearly dependent on the waveguide diameter d_t, as shown by the red line. Notice that the TM_{11} cutoff wavelength in the figure is plotted by assuming PEC for the coating metal. We found the EOT peak wavelength follow the same linear dependence on the waveguide diameter, but red shifted from the TM_{11} cutoff. Two reasons are responsible for the red-shift of the EOT peaks from the TM_{11} cutoff. First, this is a result of the waveguide EOT theory obtained from the self-consistency [3]. Secondly, the finite penetration of the light into real metal in the form of the SPP mode increases the cutoff wavelength inside the fiber.

Figure 2.8 further confirms the critical role of the TM_{11} mode. Using FDTD simulations, we plotted the electric field and Poynting vector distributions at a transverse section inside the waveguide, near the end face. At the EOT resonant wavelengths, the longitudinal component of the electric field E_z shows a clear TM_{11} mode distribution, but at 100 nm longer and shorter wavelength, E_z is much weaker. We confirm that TE_{11} mode is the only propagating mode by plotting the real part of the longitudinal Poynting vector S_z. There is some asymmetry in the mode plots, this is because the apertures are offset from the probe center in the simulations to accurately account for the fabrication imperfection.

2.6.3 Improvements to Throughput and Damage Threshold

We used the same probes for investigating the enhancements on the throughput and the damage threshold of the proposed structure. We start with a conventional apertured near-field probe with a fiber taper core made by heat-and-pull method, and

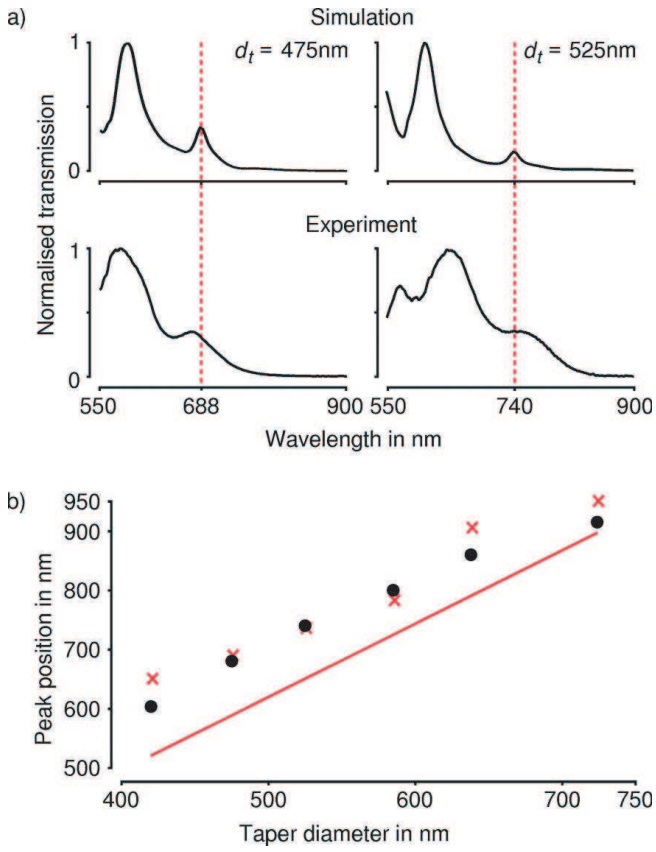

Figure 2.7: (a) The transmission spectrum from two apertured near-field probes with different taper diameters, obtained from FDTD simulations and experiments. Both methods show EOT peaks at the same wavelength for each individual probes. (b) The spectral positions of the EOT peaks attributed to mode cutoff. The numerical simulations (crosses) are in good agreement with the experimental data (circles). Indicated by the red line is the cutoff wavelength corresponding to the TM_{11} circular waveguide mode. Reprinted with permission from [4].

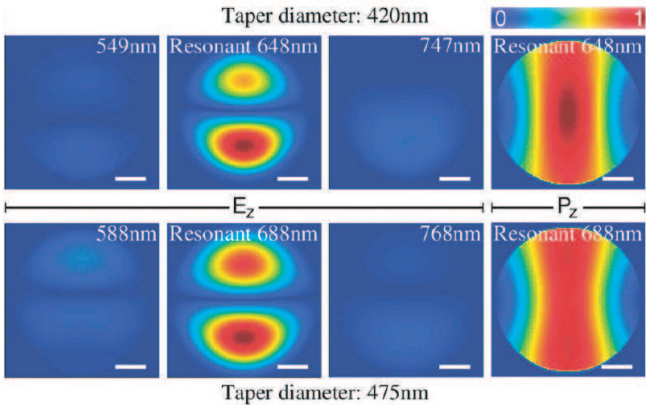

Figure 2.8: FDTD simulations showing the field and Poynting vector distributions at a transverse section inside the waveguide, near the end face. The longitudinal component of the electric field E_z shows a clear TM_{11} mode distribution on resonance, and a much weaker field off resonance; the longitudinal Poynting vector confirms that TE_{11} mode is the only propagating mode. Reprinted with permission from [4].

with an aluminum coating. After measuring the light transmission throughput of this probe, we pumped a large optical power into this fiber until its tip is damaged by the heat from the intense optical power, in which way we obtained the damage threshold of this conventionally structured probe. We then cleaved off the damaged tip at a position with a desired fiber diameter using FIB, coat the resulting flat end-face with gold, and drill a hole on the gold surface using FIB. After, we measured the throughput and damage threshold of this same tapered probe with a modified tip structure.

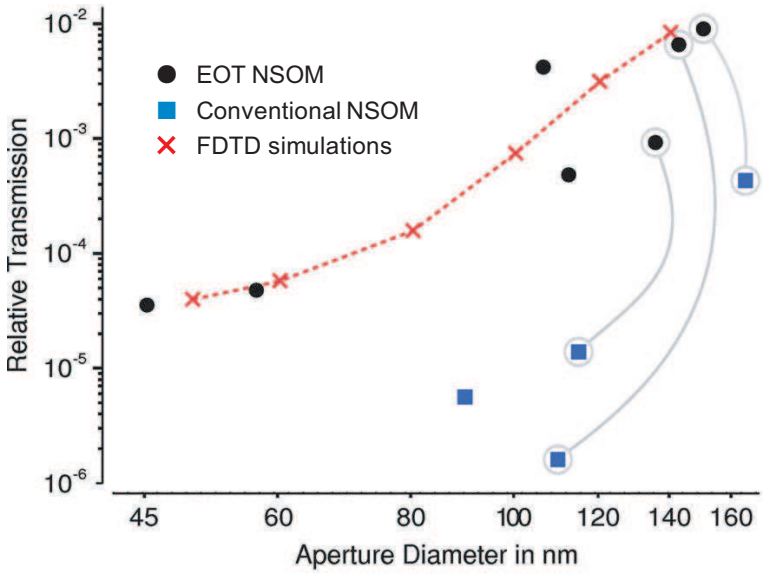

Figure 2.9: The optical throughput measured for conventional probe structures and EOT probe structures, backed up by FDTD simulations. The data points linked with a line were taken from the same taper. Reprinted with permission from [4].

As shown in Figure 2.9, the EOT probe typically permitted a 100× enhanced optical transmission (throughput) at the resonant wavelength as compared to a conventional near-field probe structure with the same aperture size, and this was confirmed by FDTD simulations.

2.6.4 Single Fluorescent Particle Scanning

To test the EOT brightened near-field probe in a real application, we scanned single fluorescent molecules using the probe. Toluene diisocyanate (TDI) molecules were mixed in a toluene solution of poly(methyl methacrylate) (PMMA) and spin-coated onto a glass slide. An excitation light with 647 nm wavelength was injected into a

near-field probe with an aperture diameter of 45 nm. The probe was scanned over the sample with a nanometric accuracy. Figure 2.10 shows the scanning map of single fluorescent molecules. The fluorescence spot shows full-width half-maximum widths of 61±3 nm and 62±3 nm on the two dimensions on the sample plane.

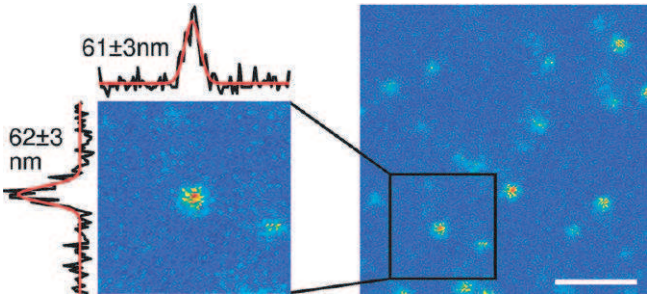

Figure 2.10: A scan across single TDI molecules with an EOT brightened near-field probe with an aperture diameter of 45 nm. The molecules were embedded in a PMMA matrix and were excited at a wavelength of 647 nm from the near-field probe. The scale bar is 500 nm. Reprinted with permission from [4].

The single fluorescent molecule scanning experiment also confirmed that the throughput enhancement at the resonance was solely due to the waveguide EOT through the nanoaperture, and the bulk plasmon leakage through the gold film was negligible. The tight scanning spot showed that the excitation light only came from the transmission through the nanoaperture, and the background was perfectly blocked by the gold film.

The reader is referred to Appendix B for the details of the study described in Section 2.6.

2.7 Optical Forces

In addition to an apertured near-field probe, subwavelength nanoholes in visible-IR regime can also be applied in the field of optical trapping. Optical trapping is a technique to immobilize and manipulate small objects using light. Compared to other techniques, optical trapping provides a very gentle capture to the trapped object, it therefore has a great potential in trapping biological objects without inducing damages. However, the challenge to trap a biological particle, which is modeled as a non-resonant dielectric particle in optics, dramatically increases as the particle size becomes smaller. For trapping the smallest biological particles such as single viruses

and protein molecules, we propose the use of subwavelength apertures, and it enables trapping of small dielectric particles that would be difficult, if not impossible, to be trapped by conventional methods. Before introducing nanohole optical trapping, we will first review some theoretical formulations of optical forces: the force exerted on small objects or particles by the light shining on them.

2.7.1 The Perturbative Formulations

When considering the optical force on a particle in a perturbative approximation, it is assumed that the presence of the particle does not significantly change the ambient electromagnetic field. To formulate the optical force in this case, we can approximately work out the ambient electromagnetic field distribution as if the particle was not in the field, and then compute the optical force on the particle based separately on the field distribution and on the particle property. The particle is approximated by an electric dipole in the ambient field.

To calculate the polarizability of the particle, we will use the quasi-static approximation again since the particles considered in this work have sizes well below the wavelength. Again, we assume a constant and static field over the subwavelength particle. We consider a plane wave with wavelength λ and an electric field amplitude $\vec{E_0}$ shining onto a spherical particle with a radius r and a refractive index n_p in a background medium with a refractive index n_m. We consider the boundary conditions at the particle surface: the electric potential is continuous in the direction orthogonal to the surface, and the electric field component in the direction parallel to the particle surface is also continuous. By solving these boundary conditions, the electric dipole moment $\vec{p_e}$ of the particle can be obtained as:

$$\vec{p_e} = \left(\frac{n_p^2 - n_m^2}{n_p^2 + 2n_m^2} \right) n_m^2 r^3 \vec{E_0} = \alpha \vec{E_0}, \tag{2.5}$$

where $\alpha = \left(\frac{n_p^2 - n_m^2}{n_p^2 + 2n_m^2} \right) n_m^2 r^3$ is the polarizability of the particle. The optical power P_{scat} scattered by the particle, known as the Rayleigh scattering for a dielectric particle, can be therefore approximated by the radiation of an electric dipole as [45]:

$$P_{scat} = \frac{c^2 Z_0 k^4}{12\pi} |\vec{p_e}|^2, \tag{2.6}$$

where $Z_0 = \sqrt{\mu_0/\epsilon_0}$ is the free space characteristic impedance, $k = 2\pi/\lambda$ is the wavenumber, c is the speed of light in free-space, ϵ_0 and μ_0 are the free space permit-

tivity and permeability. It is easy to see that:

$$P_{scat} \propto \frac{r^6}{\lambda^4}. \tag{2.7}$$

Therefore, Rayleigh scattering is the reason why the sky looks blue and the sun looks red from the earth: the blue side of the solar spectrum with a shorter wavelength gets scattered stronger by the subwavelength particles suspended in the atmosphere.

In the perturbative regime, two types of optical forces can be considered. As the first type, the scattering force is the force exerted in the direction of the incident beam, it is directly related the power scattered by the particle and can be expressed as [23]:

$$F_{scat} = \frac{I_0}{c}\frac{128\pi^5 r^6}{3\lambda^4}\left(\frac{n_p^2 - n_m^2}{n_p^2 + 2n_m^2}\right)^2 n_b, \tag{2.8}$$

where I_0 is the light intensity at the particle. The scattering force is a repelling force, and it originates from the momentum transferred from the photons to the particle in the forward direction.

As the second type of optical force, the gradient force F_{grad} is in the direction of the field intensity gradient. It can be derived from the differential force acted on an electric dipole in an electric field gradient as [114]:

$$F_{grad} = (n_m \alpha \vec{E} \cdot \nabla)\overrightarrow{E} = \frac{1}{2} n_m \alpha \nabla |E|^2 = \frac{n_b^3 r^3}{2}\left(\frac{n_p^2 - n_b^2}{n_p^2 + 2n_b^2}\right)\nabla |E|^2. \tag{2.9}$$

The gradient optical force is proportional to the particle polarizability and the gradient of the field intensity.

As the particle becomes smaller, the scattering optical force, proportional to the sixth power of the particle radius, decays much quicker than the gradient optical force which is proportional to the third power of the particle radius. Therefore, for a very small particle, the scattering optical force can be neglected, and this is the case for the particle size interested in this work.

The attractive nature of the gradient optical force leads to the idea of an optical trap - a particle can be attracted to and immobilized at a local maxima of the optical intensity. The most simply achieved local intensity maxima is at the Abbe's diffraction limited focal spot of a propagating wave in a uniform medium, leading to a traditional single beam optical tweezers [23].

2.7.2 Maxwell Stress Tensor

Compared to the inexact perturbative optical force formulations, the Maxwell stress tensor (MST) analysis is a rigorous way of computing the optical force acting on an object. MST analysis is based on the Lorentzian force. It starts with a force density formulation with the Lorentzian force term and an electromagnetic field energy term [115]:

$$f = \rho\vec{E} + \vec{J} \times \vec{B} - \frac{1}{2}|E|^2\nabla\epsilon - \frac{1}{2}|H|^2\nabla\mu. \tag{2.10}$$

where $\vec{E}$ and $\vec{H}$ are the electric and magnetic fields, $\vec{B}$ is the magnetic flux density, $\vec{J}$ is the current density, ϵ and μ are the permittivity and the permeability. The force acting on free charge ρ and free current flow $\vec{J}$ in space can be derived by integrating the first two terms in Equation 2.10 over the volume:

$$F = \int_V \left(\rho\vec{E} + \vec{J} \times \vec{B}\right) dV. \tag{2.11}$$

Then, using Guass's Law and Ampere's Law, we can rewrite the charge density ρ and the current density $\vec{J}$ as

$$\rho = \epsilon_0\epsilon_b\nabla \cdot \vec{E}, \tag{2.12}$$

$$\vec{J} = \frac{1}{\mu_0}\nabla \times \vec{B} - \epsilon_0\epsilon_b\frac{\partial\vec{E}}{\partial t}, \tag{2.13}$$

where ϵ_0 and μ_0 are the permittivity and the permeability of free-space. After applying matrix algebra, the Faraday's law and the divergence theorem, we can come to the optical force formula in terms of the MST:

$$F = \oint \left(\bar{\bar{T}} \cdot \vec{n}\right) da - \frac{\partial}{\partial t}\int \frac{\vec{S}}{c^2} dV, \tag{2.14}$$

where da is the particle surface area element, $\vec{n}$ is the normal vector of the particle surface, $\vec{S}$ is the Poynting vector which is the cross-product of the electric field $\vec{E}$ and the magnetic field $\vec{H}$, and c is the speed of light in free-space. $\bar{\bar{T}}$ is a 3 by 3 matrix (tensor) defined as the MST, with the element on the i^{th} row and the j^{th} column as:

$$T_{ij} = \epsilon_0\epsilon_b(E_iE_j - \frac{1}{2}\delta_{ij}|\vec{E}|^2) + \frac{1}{\mu_0}(B_iB_j - \frac{1}{2}\delta_{ij}|\vec{B}|^2), \tag{2.15}$$

where δ_{ij} is the Dirac delta notation, which is 1 for $i = j$ and 0 otherwise. The

second integral (the volume integral over $\frac{\vec{S}}{c^2}$) in Equation 2.14 can be shown to be the electromagnetic momentum P_{em} over the whole particle, by using Minkowski's relation $P_{em} = \vec{D} \times \vec{B}$ with $\vec{D}$ and $\vec{B}$ being the electric and magnetic flux densities. That is, the MST $\bar{\bar{T}}$ accounts for the conservation of both the mechanical momentum and the electromagnetic momentum.

Typically, the contribution due to P_{em} can be ignored. Therefore, Equation 2.14 can be re-written as:

$$F = \oint \left(\bar{\bar{T}} \cdot \vec{n} \right) da. \tag{2.16}$$

Alternatively, for a medium without free charge and free current, there is force acting on the medium itself due to its inhomogeneity. For example, for a dielectric particle which brings inhomogeneity into the background, the induced optical force can be derived by integrating the last two terms of Equation 2.10 over the volume. Considering a $\frac{1}{2}$ factor from the time averaging of the electric field, and assuming that there is no change in the permeability, the force acting on a dielectric particle is given by [116]:

$$F = -\frac{1}{4}\epsilon_0 \left(\int_V E^* E \nabla \epsilon_r dV \right), \tag{2.17}$$

where the superscript $*$ denotes the complex conjugation, and ϵ_r is the relative permittivity. A Matlab script formulating a MST analysis to compute the optical force based on the electromagnetic field obtained from a FDTD simulation is given in the Appendix D.

Usually, the perturbative optical force formulations is a good approximation to the MST analysis, as past works have been shown [38, 117]. However, in some specially designed cases, the dielectric particle can work beyond the Rayleigh regime and give a strong change to the ambient field. The perturbative approximation thus is no longer a good approximation, and the rigorous MST analysis needs to be used in this case. As we will see later, this is the case in a subwavelength nanohole, in which the MST analysis predicts a much higher optical force than the perturbative approximation.

2.8 Past Trapping Works

2.8.1 Single Beam Optical Tweezers

The first optical trap was experimentally demonstrated as a single beam optical tweezers by Ashkin [23]. Since then, single beam optical tweezers has been and still is the most widely used optical trapping technique in different applications. Single beam optical tweezers has been applied to trap dielectric particles [23, 24], carbon nanotubes [25], semiconductor nanowires [26], and metal nanoparticles [27–29]. Complex trapping patterns can be generated by manipulating the trapping beam using holography [118], but holographic optical trapping has the same principle as a single beam optical tweezers since its focus spot size is still limited by Abbe's resolution limit.

Single beam optical tweezers can be very accurately described using the perturbative gradient force formulation when trapping small Rayleigh regime particles [23]. In such a regime, it can be shown that the optical power required for trapping a particle against the random Brownian motion scales with the inverse fourth power of the particle size over all. As it can be seen in Equation 2.9, the gradient force scales with the third power of the particle size; in addition, the Stoke's drag force in a homogeneous liquid environment scales linearly as particle diameter, giving an additional dependence on the size. For trapping smaller and smaller particles, the only strategy is to keep increasing the power. Stable trapping of 10 nm gold nanospheres has been achieved with high power (400 mW) using a single laser beam [29], because gold particles have a large permittivity contrast to the background, they can be resonant [27, 119], and they are harder to damage than dielectric particles. However, these conditions are not available for dielectric particles. We are more interested in trapping a non-resonant dielectric particle with a small permittivity contrast to the background, as the case for biological particles. In this case, single beam tweezers have limited capability. For example, for trapping latex spheres of a size below 100 nm, a single beam tweezers require such a large intensity that it will damage the particle quickly before a reliable measurement can be made [23].

For trapping biological materials, single beam optical tweezers has been used to directly trap relatively large biological particles, for example bacteria [33] and living cells [30–32]. Some particles such as the tobacco mosaic virus are thin but extremely elongated and thus have a large polarizability, and they can also be trapped by a single beam tweezers [33]. Another common use of single beam optical tweezers in

biology is by tethering the ends of long bio-materials (e.g. deoxyribonucleic acid (DNA) strands, actin) to a large dielectric particle that can be trapped and moved by single beam tweezers, and then indirectly manipulating and studying the tethered bio-material. For example, stretching DNA strands [34], monitoring ribonucleic acid (RNA) transcription [35], studying actin mechanics [36] and unwinding hairpin RNA [37] have been done using this technique.

2.8.2 Novel Optical Traps

To generate a larger gradient force without increasing the optical incident power, we can produce a steeper optical intensity gradient. Nanostructures can be used to beat Abbe's diffraction limit and generate a tighter focusing spot. A tighter focusing spot than a diffraction limited focus of propagating wave can be achieved using evanescent waves of surface plasmon structures [120]. It was found that an optical antenna gap can give a tighter focusing spot and therefore a larger gradient trapping force to create a much tighter particle confinement than a single beam tweezers [121]. A resonant optical dipole antenna was designed and successfully trapped 200 nm polystyrene and living Escherichia coli bacteria using a low optical intensity [122].

Other than plasmonic structures, a whispering-gallery-mode (WGM) optical resonator also has an evanescent field with a large intensity gradient due to the total internal reflection. In addition to be used as a sensitive sensors [123–125], a WGM resonator can also be used as an optical trap utilizing its large evanescent field build-up, and single 280 nm polystyrene particles have been successfully trapped by a WGM resonator using a low input power [40, 41].

Another way to overcome Abbe's diffraction limit is by using a subwavelength waveguide structure. A silicon slot waveguide with a 100 nm gap between the two silicon plates have shown a great focused light in the gap [38], and this waveguide was used to trap 75 nm polystyrene nanospheres and λ-DNA strands [39].

Although a steeper intensity gradient and a tighter focusing spot can assist in the trapping of Rayleigh dielectric particles, it does not solve the fundamental challenge in optical trapping in the perturbative regime: the inverse fourth power dependence of required optical power on the particle size. In addition, some of the above experiments require a cumbersome setup. For example, a prism coupling setup in the Kretschmann configuration was required to excite the dipole nanoantennas [122]. To achieve optical trapping of even smaller dielectric and biological particles, we look for a solution

beyond the perturbative regime.

2.9 Self-Induced Back-Action Trapping using a Nanohole

2.9.1 Nanohole Trapping Concept

To design an optical trap which works beyond the perturbative regime, we look for a situation where a small particle induces a large change to the ambient electromagnetic field - larger than that predicted by Rayleigh scattering. We propose using a subwavelength nanoaperture, and operate at a wavelength slightly longer than its cutoff. Figure 2.11 summarizes the working principle of this nanoaperture trap. As Figure 2.11(a) shows, below cutoff, the optical transmission through the aperture at a normal angle is mainly through diffraction, and the transmitted power is low. As Figure 2.11(b) shows, when a dielectric particle, with smaller size than the aperture and a larger refractive index than water, enters into the aperture, the aperture will suddenly become optically larger due to the dielectric loading from the particle. The optical transmission through the aperture is thus increased. As Figure 2.11(c) shows, if the particle tries to leave the aperture, the transmission through the hole decreases, giving a change in the light momentum towards the outside of the hole. As Newton's Third Law states, this momentum change has to have a reaction on the particle in the opposite direction, generating an optical force towards the inside of the hole. As Figure 2.11(d) shows, according to Bethe's aperture theory, the optical transmission has a steep inverse fourth power dependence on the wavelength. Therefore, a small red-shift to the transmission spectrum due to the dielectric particle results in a large change to the transmission power at a certain wavelength. In other words, we now have a case in which a small particle can induce a much larger change to the ambient electromagnetic field than in the perturbative regime, having a great back-action to the particle itself. This so-called self-induced back-action (SIBA) optical trapping is stronger than a perturbative gradient trap.

Another explanation to the aperture trapping working principle comes from the increased trapping potential well depth. The electric field intensity $|E|^2$ inside the aperture is increased due to the increased optical transmission with particle loading. From the particle potential energy $P \propto -\alpha|E|^2$, it can be seen that increased field in-

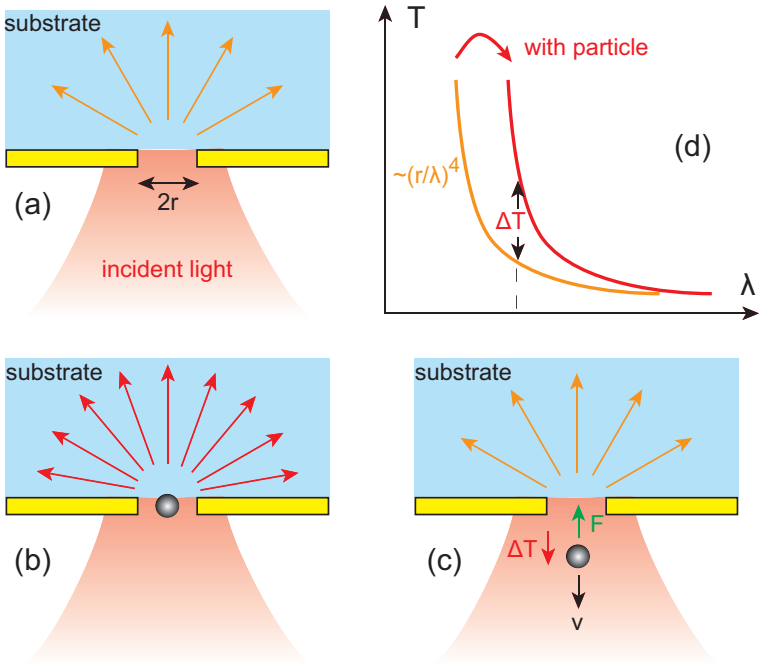

Figure 2.11: Optical transmission through a single subwavelength hole: (a) without particle; (b) transmission enhanced with a dielectric particle in the hole (dielectric loading); and (c) transmission decreased by ΔT when the particle tries to leave the hole. The change of the light momentum reacts onto the particle, inducing a force in the opposite direction, pulling the particle back to the hole. (d) The presence of the dielectric particle makes the hole optically larger through dielectric loading, red-shifting the transmission curve and giving the change ΔT in transmission.

tensity due to the particle gives a decreased particle potential energy or, equivalently, a deeper potential well for stronger trapping.

We notice that other promising self-induced optical trapping approaches exist, such as using a photonic crystal cavity. 48 nm polystyrene particles have been trapped using a one-dimensional silicon photonic crystal resonator [42]. Theoretical results have also been presented for optical trapping using one-dimensional [43] and two-dimensional [44] photonic crystal cavities. Subwavelength nanohole SIBA trapping does not rely on a sharp resonance and also has a simpler setup.

2.9.2 Nanohole Trapping Experiments

We used a single circular nanohole of 310 nm diameter on a 100 nm thick gold film for the first nanohole trapping project. The nanohole on the gold film was milled by using a FIB. The setup of the nanohole trapping experiment is simple, basically the same as shown in Figure 2.11. The colloidal solution of the nanoparticles to be trapped is sealed at the gold film using a 150 μm thick glass coverslip and a spacer well. The gold film is mounted facing downward so that gravity pulls the particles (with a slightly larger density than water) away from the gold film. As the trapping beam, 1064 nm wavelength continuous wave (CW) Nd:YAG laser beam is focused from the bottom onto the nanohole on the gold film, using a 40$\times$ microscope objective, giving a focus spot of about 2 μm diameter.The trapping beam has a linear polarization and is incident normally to the gold film. The detection of the trapping events is also easy for nanohole optical trapping. As suggested by the working principle, we can just monitor the optical transmission through the nanohole. When a particle comes into the nanohole and gets trapped, there will be a sudden increase in the optical transmission.

Figure 2.12 shows typical time traces in the trapping experiment. Using the circular hole optical trap, we tried to trap 100 nm and 50 nm polystyrene nanospheres, using different incident optical power. The time domain traces of the transmission clearly show abrupt jumps between a high and a low level, indicating the trapped and the vacant states. This type of abrupt jumps are typical indicators of trapping events in hole trapping [126]. As Figure 2.12 (a) shows, when increasing the optical incident power in the 100 nm nanosphere trapping, the length of the trapping time also increases, in agreement with the Arrhenius law, which basically states that the average trapping time is logarithmically dependent on the optical power. Using an optical

incident power of about 1 mW, stable trapping of 100 nm polystyrene nanosphere was obtained for over 5 minutes. As Figure 2.12 (b) shows, using a 1.9 mW of incident optical power, we were able to stably trap a single 50 nm polystyrene nanosphere for a period of 10 seconds. This is a great improvement over a conventional gradient force optical trap. If a single beam optical tweezers was used to trapped the 100 nm polystyrene nanosphere, an optical intensity of two orders of magnitude larger than our experiment would be needed [23]. Trapping a 50 nm polystyrene nanosphere would not even be possible using a single beam optical tweezers. Nanohole trapping has opened a new route in optical trapping.

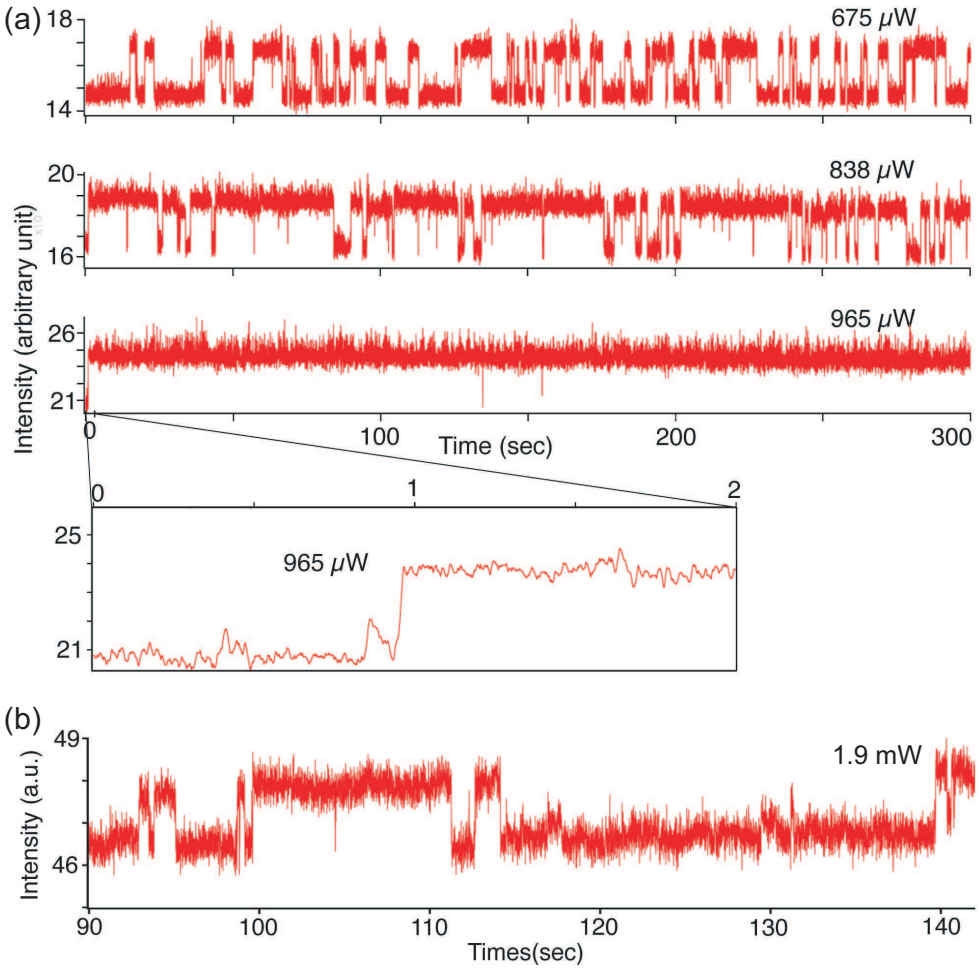

Figure 2.12: Time domain signal of the optical transmission in the circular nanohole optical trap. The sudden jumps in the signal indicates individual trapping events. (a) Trapping of 100 nm polystyrene spheres using 675, 838 and 965 μW of incident optical power. (b) Trapping of 50 nm polystyrene spheres using 1.9 mW of incident optical power. Figure reprinted from [5].

2.9.3 Optical Force Computations using MST

Figure 2.13 shows the FDTD simulations that we performed to study the optical force to gain a better understanding of the nanohole optical trap. Figure 2.13 (a-d) shows the force map at different points in and near the aperture. Based on the electromagnetic field distributions returned from the FDTD simulations, we compared two physical formulations for computing the optical force: the perturbative gradient force approximation based on Equation 2.9 and the comprehensive MST analysis based on Equation 2.17. For the perturbative gradient force approximation, only one simulation is needed: the field in a nanohole without a particle. The gradient force can then be computed using theoretical values of particle polarizability and field intensity gradient computed by numerical differentiation at different points. For the MST analysis, the simulation resource consumption is much larger. Since the change of the field by the particle must be accounted in the non-perturbative MST analysis, a separate simulation is needed for each point of interest, placing the particle there. It is found that the MST analysis predicts a much larger optical force than the gradient approximation does. Figure 2.13 (e and f) plot the force component along the electric field polarization direction versus the displacement from the hole center, with a 100 nm and a 50 nm trapped particle, using MST analysis and gradient force approximation. Again, the force-displacement curve obtained from MST analysis gives a much steeper slope and therefore a larger trapping stiffness. As discussed before, the optical transmission through a subwavelength nanohole is very sensitive to the refractive index change inside the hole, and even a small particle will induce a large change to the field inside the hole. This is the reason why a perturbative formulation is no longer a good approximation; the comprehensive MST analysis is needed in this case. Appendix D gives the Mablab code for computing the optical force using both the MST and the perturbative formulations based on FDTD simulation results.

The reader is referred to Appendix C for the details of the study described in Section 2.9.

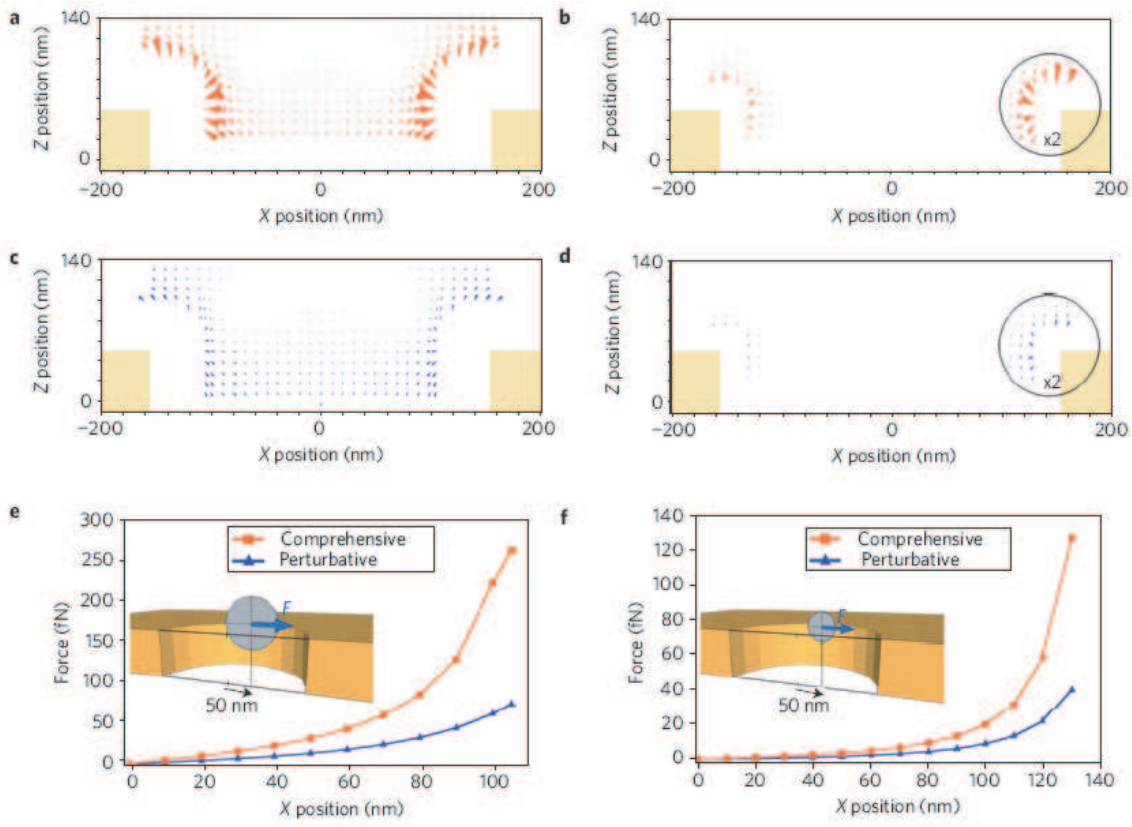

Figure 2.13: The numerically computed optical force in the nanohole trap based on FDTD simulations, in trapping 100 nm (a, c and e) and 50 nm (b, d and f) polystyrene spheres. Two physical formulations are compared: the comprehensive MST analysis (a and b) and the perturbative gradient force approximation (c and d). It is found that the perturbative gradient force approximation is no longer a good approximation in the nanohole optical trap, and the MST analysis predicts a much larger optical force than the gradient approximation does. Figure reprinted with permission from [5].

2.10 Double-Nanohole Trapping

2.10.1 Motivation for Double-Nanohole

The circular nanohole optical trap can generate a much larger optical force than perturbative optical traps can, and it can trap a polystyrene sphere as small as 50 nm using a low optical power. However, as discussed before, in many applications, better nanohole shapes than a circular hole can be designed for increased cutoff wavelength [53], increased transmission [57, 60] and local field enhancements [58]. Previously, double-nanoholes have been used for enhanced second harmonic generation [63, 64] and surface-enhanced Raman scattering (SERS) [66]. The field enhancements found at the apexes between the two holes lead to enhanced light-matter interaction [61]. Here we propose an optical trap using a single double-nanohole on a gold film, which has two sharp tips separated by a tiny gap. By using this double-nanohole, we extend the trapping to smaller dielectric particles. We also find a seemingly surprising behavior of this optical trap: a smaller particle might be even more easily trapped than a larger one for a certain double-nanohole.

2.10.2 Nanofabrication and Experimental Setup

Figure 2.14 shows an SEM image of a typical double-nanohole. The double-nanohole was milled by using a FIB (refer to the Methods chapter) on a 100 nm thick gold film. The tips in the hole are aligned in the x-direction with a separation of 15 nm in this particular double-nanohole. Compared to other nano-structures with sharp tips, the double-nanoholes are particularly simple to fabricate. Using FIB milling, a double-nanohole can be made by milling two closely spaced circular holes, and the tip geometries (especially the gap width between the tips) can be controlled by varying the hole diameters and separations. Other than using a FIB, a double-nanohole can be fabricated by a bottom-up process using metal evaporation over nanosphere dimers [65].

The double-nanohole trapping uses a similar experimental setup as the circular hole trapping. Colloidal solutions containing nanospheres are sealed at the gold film. Linearly polarized trapping beam was focused normally onto the sample, in a polarization with the electric field aligned to the x-direction (refer to Figure 2.14). The trapping events are monitored by abrupt jumps in the optical transmission through the double-nanohole. Comparing to the setup used for circular hole trapping, im-

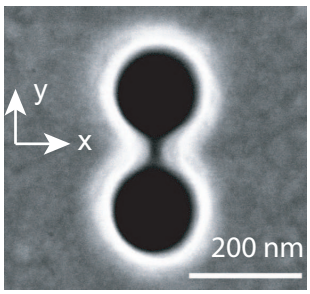

Figure 2.14: An SEM image of a typical double-nanohole an a 100 nm thick gold film. The tips in the hole are aligned in the x-direction with a separation of 15 nm in this particular double-nanohole. Figure reprinted with permission from [6].

provements to the light source, microscope objective and the detector, boosting the measurement signal-to-noise ratio (SNR).

2.10.3 Trapping of a 12 nm Silica Sphere

Figure 2.15 shows the trapping of 12 nm silica spheres using a double-nanohole with a 15 nm tip separation. This was done using an optical incident power of 7.2 mW, and trapping of 12 nm silica spheres was obtained for an average trapping time of 30 seconds. We believe this is the smallest dielectric particle trapped to-date. This is also a great improvement over the circular hole trapping, taking into account that the 12 nm silica sphere has a smaller size and smaller refractive index than the polystyrene spheres used in that experiment. If we were to trap a 12 nm silica sphere using a circular nanohole, about 270 mW of incident optical power would be needed, based on a hand-waving calculation using the previous circular hole trapping results and an inverse fourth power dependence of optical power on the particle size. Our 7.2 mW optical power is over an order of magnitude improvement on the required intensity.

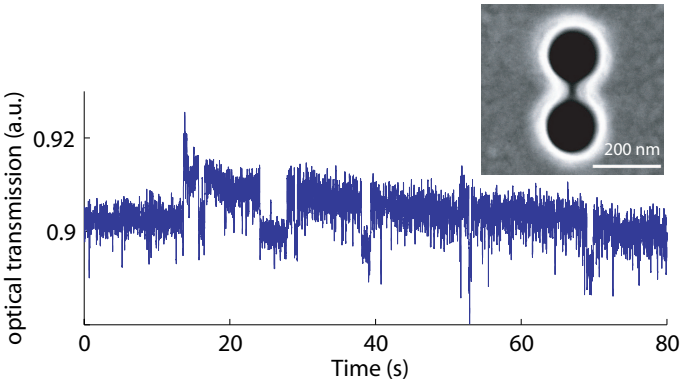

Figure 2.15: The time domain trace of the optical transmission through a double-nanohole with a 15 nm tip separation, exposed to a colloidal solution containing 12 nm silica spheres, clearly showing trapping of single 12 nm silica spheres. Figure reprinted with permission from [6].

The tremendous trapping ability comes from the large local field concentrated in the small area between the two tips. The optical transmission is much more sensitive to a local refractive index change in this small area, since this is where all the transmission power through the hole is concentrated. Therefore, only a small particle, with size comparable to the strong local field area, is needed to make enough change to the transmitted power and self-induce enough trapping force. By comparison,

a circular nanohole is isotropic and does not provide such local field enhancement. With a circular nanohole, only relatively large particles can change the transmitted power enough to self-induce enough trapping force. Therefore, a double-nanohole allows the trapping of much smaller particles than a circular nanohole. The double-nanohole structure is also advantageous over a rectangular nanohole. Although a rectangular nanohole can also give an enhanced local field through the coupling of surface plasmons between the two closely spaced sides [53], the enhanced local field is distributed along the sides of the hole, and the trapping force will be weaker along the long axis of a rectangular hole. In contrast, the double-nanohole gives a single trapping point where the field is strongest between the two tips.

2.10.4 Particle Size Selective Behavior

The double-nanohole optical trap has a counter-intuitive behavior: using the nanohole with a certain tip separation, a smaller nanoparticle might be easier to trap than a larger one. Figure 2.16 (a) shows a comparison between trapping 100 nm and 20 nm polystyrene spheres using a double-nanohole with a 30 nm tip separation. It can be seen that, using the same incident optical power, the trapping time of the 20 nm sphere is at least 10 times longer than that of the 100 nm sphere. This behavior is different from all the existing optical traps. The difficulty for trapping smaller particles for perturbative optical traps, in terms of required optical power, depends on the inverse fourth power of particle size. Even in the non-perturbative SIBA trap using a circular hole, a smaller particle still gives a smaller perturbation inside the hole and is therefore harder to be trapped. The double-nanohole trap, in contrast, have a very tight trapping area between the tips. A strongest trapping will happen if the particle fits the whole trapping area. A larger particle such as a 100 nm particle, will be blocked outside of the trapping area in between the 30 nm double-nanohole tip spacing due to steric hindrance, and therefore cannot be strongly trapped.

To prove the role of the tip separation in trapping, we tried to trap a 20 nm polystyrene sphere using double-nanoholes with different tip separations, and compared the transmission signal jumps at the trapping events. The change in optical transmission through the double-nanohole in the trapped and the vacant states relates to the optical force through Newton's Third Law. The largest transmission change happens when a nanoparticle is trapped using a hole with a tip separation (25 nm) barely larger than the particle size (20 nm), in which case the particle best occupies

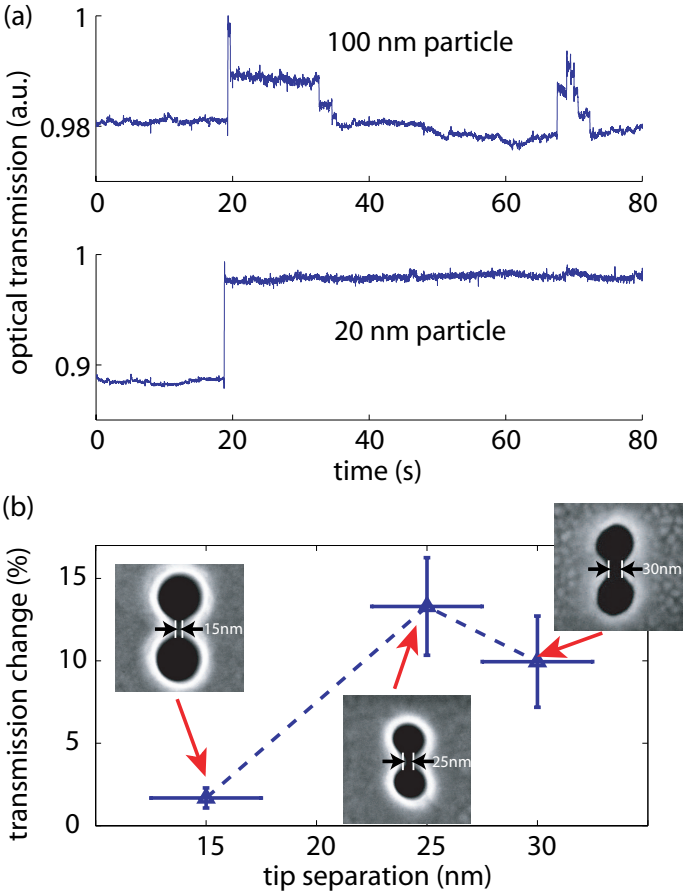

Figure 2.16: (a) Trapping results of 100 nm and 20 nm polystyrene spheres using a double-nanohole with a 30 nm tip separation. (b) Different transmission jumps when trapping 20 nm polystyrene spheres using double-nanoholes with different tip separations. Figure reprinted with permission from [6].

the trapping area. If a larger tip gap than the optimum is used, it does not generate a local field as strong as the smaller gap does. If a smaller tip gap than the optimum is used, it blocks the particle outside. In addition to be physically interesting, this behavior is potentially useful in a size sorting of particles.

The reader is referred to Appendix E for the details of the study described in Section 2.10.

2.11 Trapping and Unfolding a Single Protein

The trapped 12 nm silica sphere has a size and refractive index comparable to the smallest biological material, such as a single virus particle (a virion) and a protein molecule. Our technology is ready to be applied in biology.

2.11.1 Trapping of the Protein

We extend the double-nanohole trapping to a single protein: the bovine serum albumin (BSA). BSA is a "heart-shaped" molecule with a 9 nm length at its longest dimension and a 3.4 nm hydrodynamic radius. In this experiment, we have further optimized the trapping setup by replacing the trapping light source with a shorter wavelength 820 nm laser. With the silicon-based detector, the 820 nm wavelength has a 4× better detection responsivity than the 975 nm laser, this further increases the SNR in the experiment. Further, a shorter wavelength also has a lower water absorption and a larger structure-to-wavelength scaling, suitable for trapping smaller particles. To block the BSA from directly adsorbing onto the gold surface, which is a commonly known tendency of BSA, we formed a monolayer of methoxypoly (ethylene glycol) (mPEG) thiol on the Au surface before the BSA trapping experiment [127].

Figure 2.17 shows the BSA trapping results. Using a 8.5 mW optical incident power, the BSA can be trapped for at least 100 seconds. To confirm that the BSA is optically trapped as opposed to adsorbed to the gold surface, we have also performed an experiment showing the release of the BSA when the laser is turned off.

2.11.2 Unfolding of the Protein

In the transmission signal in BSA trapping, we have noticed the interesting "double-trapping states", corresponding to the lower (T1) and higher (T2) transmission levels

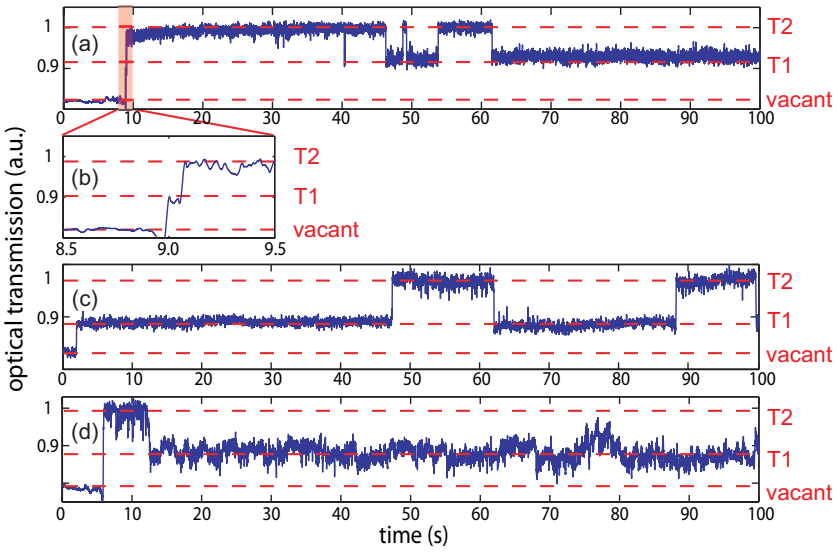

Figure 2.17: Time traces of the optical power transmitted through the double-nanohole, using a BSA solution in phosphate buffered saline (PBS) buffer with pH = 7.4, using an incident optical power of (a) 13.4 mW [(b) zoom-in of (a)], (c) 10.6 mW, and (d) 8.5 mW. The vacant state and two trapping states (T1 and T2) are clearly shown. Figure reprinted with permission from [7].

above the vacant level in Figure 2.17. The double trapping states reappears at the initial trapping point as well as in trapped state. As the explanation for the double-state, a single BSA molecule is trapped and unfolded by the strong optical force between the tips of the double-nanohole. BSA molecule is known to exist in different forms with different degrees of folding, and the transitions between the N form (folded heart-shaped) and the F form (unfolded elongated-shaped) has been achieved by changing the solution pH [128]. If the BSA, in the folded N form as initially trapped, is unfolded into the elongated F form by the optical force in the trap, it will have a stronger polarizability and suddenly permits a larger optical transmission through the double-nanohole, making the second jump in the transmission from T1 state to T2 state. As Figure 2.17 shows, we repeated the BSA trapping experiment using different optical incident powers. As expected, using a higher optical power, the BSA spends a longer time in the unfolded state, because there is a stronger optical force to unfold the BSA. In addition, when the BSA is unfolded and elongated, the transmission signal jumps to a higher level as equivalent to a larger optical force. This is expected since an elongated particle has a larger polarizability than a short one with a same volume. An extremely elongated particle such as the 300 nm long tobacco mosaic virus can also be trapped by a single beam tweezers [33], even it has a very thin cross-section.

To further support the unfolding BSA hypothesis, we performed trapping experiments with different solution pH. We used BSA colloidal solutions with a pH of 3.57, in which the BSA naturally exists in the unfolded F form, to compare with a solution with pH of 7.40, in which the BSA is naturally folded [128]. Figure 2.18 shows the trapping signal under different pH, using a same 8.4 mW incident optical power. As expected, the double-trapping-state only appears in the higher-pH environment; it does not appear in the lower-pH but otherwise identical environment, neither at the transition when the trapping initially starts nor in the trapped state, because the BSA in the low-pH is already unfolded. Again, we have shown that the optical force in the double-nanohole is strong enough for not only trapping a single BSA, but also enough for actually unfolding it.

2.11.3 Potential as a Biosensor

The double-nanohole configuration has a very high SNR of 33 in monitoring the trapping events of only a single BSA molecule. Notice that, the system noise here (e.g.

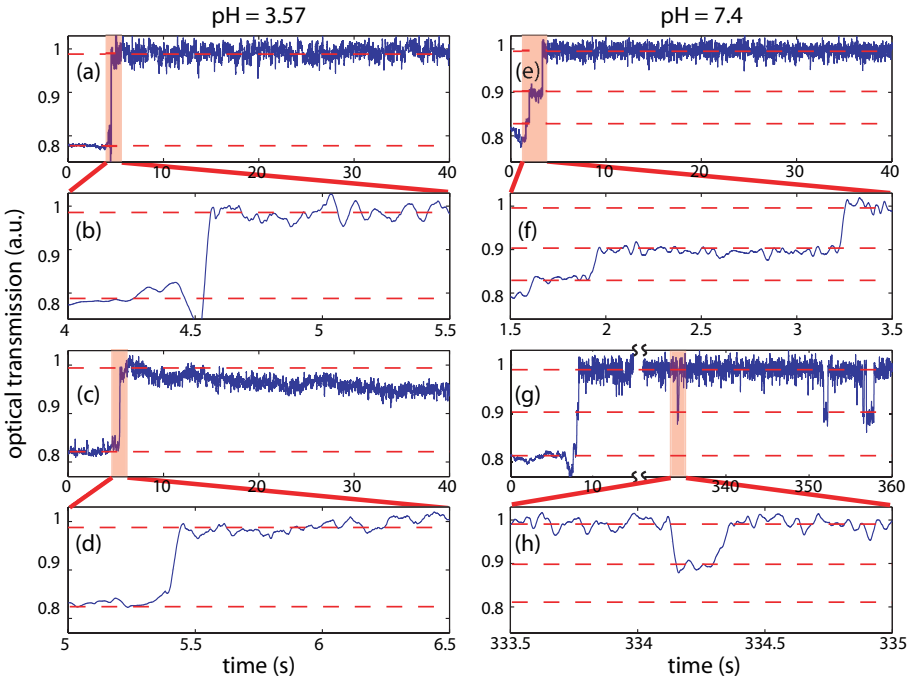

Figure 2.18: The time traces of the optical power transmitted through the double-nanohole, using an incident optical power of 8.4 mW in a BSA solution in PBS buffer with (a-d) pH = 3.57, and (e-h) pH = 7.4. Figure reprinted with permission from [7].

the laser power fluctuation, the detector shot noise, the mechanical vibration of the optical setup) means the noise seen in the vacant state. The larger transmission power fluctuation in the trapped states are due to the Brownian motions of the trapped BSA molecule. Therefore, the double-nanohole is also an extremely sensitive sensor at a single molecule level. Sensing and trapping are often the "dual-functionality" of one optical system - both based on the interaction between light and subwavelength-scale matters. For example, whispering gallery mode optical microresonators are common setups for both sensing [123–125] and trapping [40, 41].

We plan to extend the double-nanohole to sense protein binding at a single molecule level. A single protein sensor will have potential applications in drug discovery [129] and disease and infection detection [130]. To transfer the trapping setup into a sensing setup, a specific molecule monitoring scheme needs to be added to the system, and there are a number of ways for doing this. An antigen-antibody binding can be used for specific biomolecule detection [82, 84]. Raman spectroscopy can also be used as a highly specific label-free detection method [14, 111]. The strong local field at the tips of the double-nanohole is suitable for tip-enhanced Raman spectroscopy, as previously investigated [131]. Fluorescence is also a promising candidate for particle tracking. A single layer of fluorescent particle has been detected using an array of subwavelength slits and apertures [132–134]. Compared to periodic structures, the single double-nanohole is more compact and is suitable for sensing smaller amount of material and for compact optical integration.

The reader is referred to Appendix F for the details of the study described in Section 2.11.

2.12 Summary

In summary, this chapter has investigated theories and applications for subwavelength apertures in a metal film. A total transmission was found for a subwavelength aperture in a waveguide screen. This surprising result is obtained using Bethe's intentional setup and Bethe's theory. Using the waveguide EOT, we have designed and experimentally tested a novel apertured near-field probe with a 100× optical throughput and a 40× damage threshold as compared to conventional probes, and a 62 nm spatial scanning resolution. We have also found that an optical trap which generates a much larger optical force than perturbative traps can be constructed using subwavelength apertures, because the optical transmission is very sensitive to dielectric loadings in

the aperture. We have achieved trapping of 50 nm polystyrene spheres using a circular nanohole, and trapping of a 12 nm silica sphere and a single protein using a double-nanohole. The double-nanohole has a high SNR in monitoring single protein trapping events, showing potentials of sensing protein binding at a single molecule level.

Chapter 3

Methods

In this chapter, the experimental and numerical methods used for this dissertation are introduced. The optical setup for the optical trapping experiment is first introduced. For making the samples used for the different experiments, various micro- / nano-fabrication techniques are used, including focused-ion beam milling, thin-film depositions and spin-coating. Finite-difference time-domain simulations are used for supporting a theoretical analysis and for understanding experimental results.

3.1 Optical Trapping Experiments

3.1.1 Experimental Setup

Figure 3.1 (a) shows the schematic of the double-nanohole optical trap. The trapping setup is based on the Thorlabs optical tweezer kit OTKB with modifications. As the trapping beam, a fiber-coupled 975 nm semiconductor laser was collimated, expanded, and focused onto the sample using a 100× oil immersion microscope objective (1.25 numerical aperture), forming a laser spot of 1.1 μm diameter. An optical density filter was used to limit the optical power to below 10 mW at the output of the objective. A half-wave plate was used rotate the polarization of the laser beam. The transmission light through the double-hole was collected using a 10× condenser microscope objective (0.25 numerical aperture) and measured by a silicon-based avalanche photodiode (APD) (Thorlabs APD110A). The sample was mounted between the oil-immersion microscope objective and the condenser microscope objective and aligned using a piezoelectric controlled xyz sample stage to give a 20 nm positioning precision. The polarization of the trapping beam was chosen such that the electric field was aligned

with the two tips in the double-hole structure (x-direction in Figure 3.1(c)). With this polarization, there is a large local field enhancement in between the two tips creating a strong trapping point. For the data collection, the analog optical transmission signal measured by the APD is converted to digital signal using a data acquisition board (Omega USB-4711A Portable Data Acquisition Module). For the double-nanohole optical trapping experiments, we used a 101-point-window third-order Savitzky-Golay algorithm for noise reduction of the collected data for the time domain.

We have further modified the trapping setup for trapping setup for trapping BSA. This setup is improved by using a shorter wavelength 820 nm laser (Sacher Lasertechnik Group, Model TEC 120) that has approximately 4 $\times$ better detection efficiency for the APD and helps with trapping smaller objects (due to the favorable wavelength-dependent scaling). The 820 nm wavelength also has a lower absorption in water.

Figure 3.1 (b) shows an enlargement of the sample region. For trapping polystyrene or silica nanospheres, polystyrene nanospheres (Fisher Scientific) or silica nanospheres (Corpuscular Inc.) were suspended in water (0.05% w/v) with a trace amount of surfactant to prevent aggregation. The nanospheres suspension was ultrasonicated to further ensure against aggregation. For trapping BSA, BSA (Sigma-Aldrich) was mixed in PBS (1% w/w). Before the BSA trapping experiment, we formed a monolayer of mPEG thiol on the Au surface to block the BSA from adsorbing to the Au surface [135]. This was done by immersing the Au film sample in an 5 mM aqueous solution of mPEG thiol (with a molecular mass of 5000 g/mol) at room temperature overnight, and rinsing thoroughly with deionized water to remove any nonchemisorbed mPEG thiol molecules. The colloidal solution, containing either nanospheres or BSA, is then sealed at the Au film surface using a microfluidic chamber consisting of an 80 μm thick poly(dimethylsiloxane) (PDMS) spacer well and a 150 μm thick glass microscope coverslip. The sample was mounted with the Au film facing down so that the small contribution from gravity pulls the nanospheres away from the Au film, and the optical force works against gravity. Immersion oil with refractive index of 1.51 was used in between the oil immersion objective and the coverslip.

Figure 3.1 (c) shows an SEM images of the double-nanohole. The double-hole was milled into a commercially available 100 nm thick Au film on a glass substrate with a 2 nm Ti adhesion layer (EMF Corp.) using FIB. For the example shown in 3.1 (c), the diameter of each circular hole is 180 nm, and the tips are separated by 15 nm.

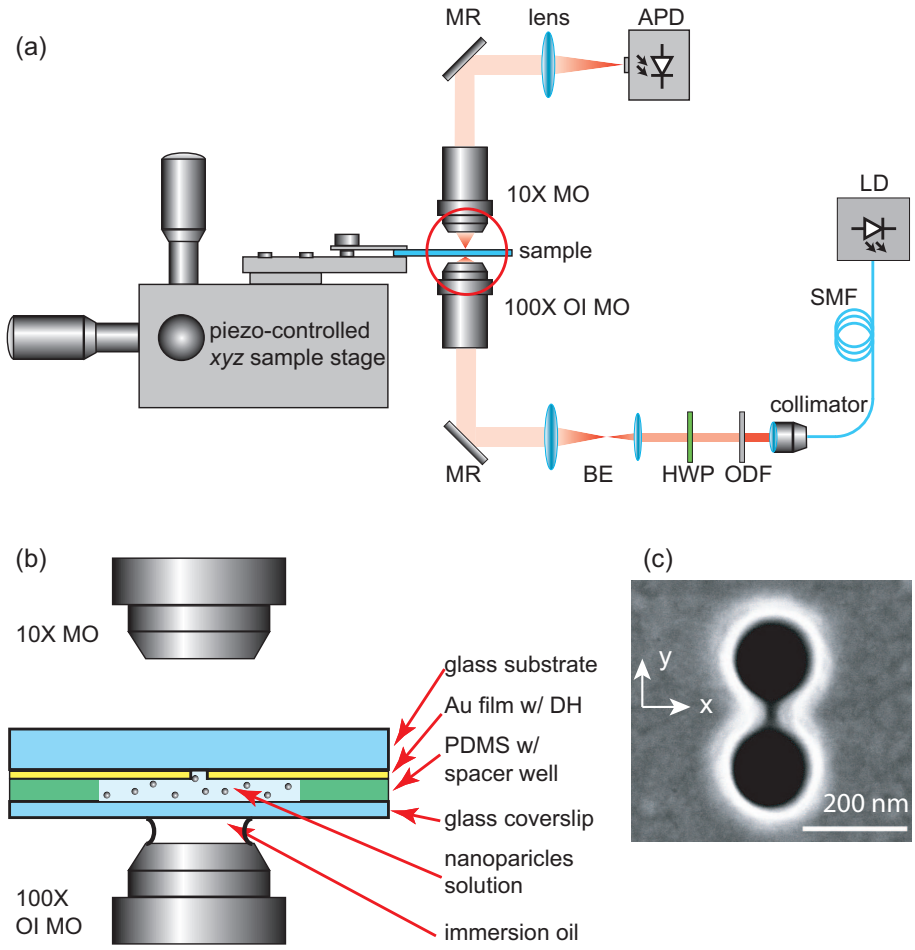

Figure 3.1: (a) Schematic drawing of the double-nanohole optical trap setup. (b) An enlargement of the red circle part in (a), showing details of the composition of the sample in the microfluidic chamber, the setup of the oil immersion microscope objective, and the condenser microscope objective. Abbreviations used: LD = laser diode; SMF = single-mode fiber; ODF = optical density filter; HWP = half-wave plate; BE = beam expander; MR = mirror; MO = microscope objective; OI MO = oil immersion microscope objective; DH = double hole; APD = avalanche photodiode. (c) An SEM image of the double-nanohole on a gold film. Figure reproduced with permission from [6].

3.1.2 Spectral Analysis of Particle Random Motion

We measured the random motion spectrum of the trapped particle which is predominantly due to a random Gaussian noise process accounting for all the Brownian forces on the trapped particle. If a parabolic trapping potential was assumed, for example, in the case of a single beam optical tweezers, the 3-dB cutoff frequency of the random motion spectrum can give information about the trapping stiffness [24, 136]. by performing a fast Fourier transform to a time signal taken with 5 kHz sampling frequency. A nonlinear least square method was used to fit the spectrum. Figure 3.2 shows two sample random motion spectra of the trapped BSA, when the BSA is in the folded (Part (a)) and unfolded (Part (b)) states.

However, in an aperture trapping environment, the trapping minimum is at the surface, this is clearly not a harmonic potential. Furthermore, there are hydrodynamic interactions with the surfaces of the aperture. Therefore, we are reluctant to perform spectral analysis to extract stiffness parameters, as has been done in the past.

3.2 Nanofabrication Techniques

3.2.1 Focused-Ion Beam Milling

The double-nanoholes on a gold film and the parabolic trench on a silicon substrate were fabricated using a FIB milling technique. This was done by using a Hitachi FB-2100 Focused-Ion Beam system. The milling pattern is input into the FIB controlling computer in the format of a bitmap figure. The Hitachi FB-2100 FIB system can process a bitmap figure with a maximum of 2000×2000 pixels. The bitmap figure can be designed in Matlab by creating a 2-dimensional matrix containing 0's (for black pixels which get exposed) 1's (for white pixels which do not get exposed), then outputting to a bitmap figure using the

```
imwrite()
```

command.

Figure 3.3(a) shows a sample bitmap (within the red dotted line box) used to fabricate the double-nanohole using FIB. The bitmap has a resolution of 2000×2000 pixels, corresponding to a real area of 400×400 μm^2. The bitmap consists of two solid circles. The diameters of the circles and the separation between them are varied to control the size and the tip separation of the double-nanohole. For having a

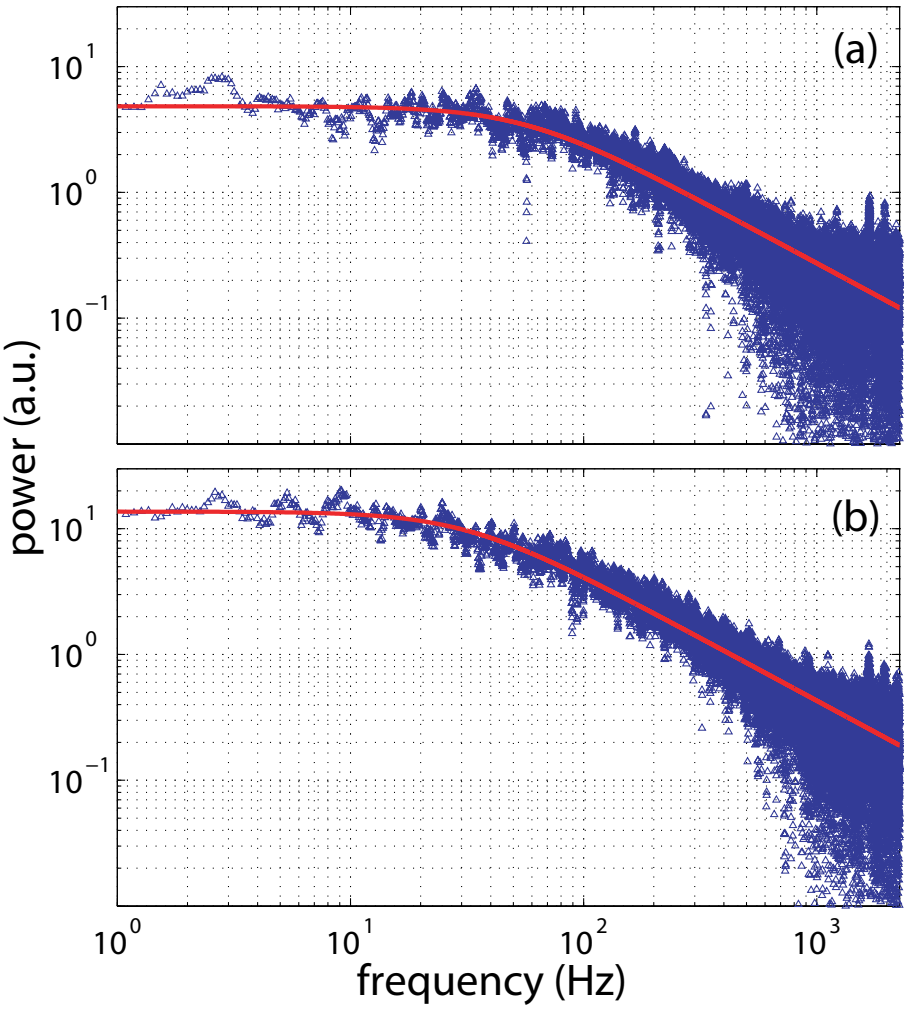

Figure 3.2: Sample random fluctuation spectra of the trapped particle. The particle used here is BSA. The blue triangles and the red curves represent experimental data and a fit to the fluctuation spectra of (a) folded BSA and (b) unfolded BSA.

double-nanohole with the smallest tip separation (desired for the largest local field enhancement), the two circles should be made just touch each other. Practically, due to the finite beam width of the FIB, the center-to-center separation between the two circles should be about 30 to 40 nm larger than the circle diameter in the bitmap for the resultant two circles to just touch each other. In the case of Figure 3.3(a), the circle diameters are 160 nm, and the center-to-center separation is 190 nm. A thin line connecting the two circles can be added to make sure there is no residue metal in the gap between the tips, but this is not mandatory.

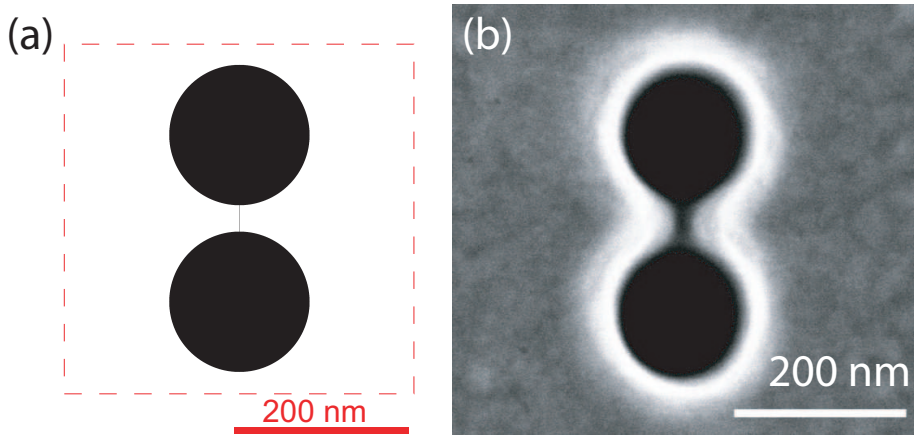

Figure 3.3: (a) Sample bitmap figure (within the red dotted line box) used to fabricate the double-nanohole using FIB. (b) An SEM image of the resultant double-nanohole fabricated using the bitmap in (a).

Figure 3.3(b) shows an SEM image of the resultant double-nanohole fabricated using the bitmap in (a). The double-nanohole was milled using an ion accelerating voltage of 40 kV and a beam limiting aperture with a 15 μm diameter, under a 60k$\times$ magnification. 80 passes were used for milling each double-nanohole and a 5 ms dose time was used for each pass. The resultant tip separation is about 15 nm.

Figure 3.4(a) shows a schematic diagram showing the layer-by-layer FIB milling procedure of the parabolic trench on silicon. The parabolic trench on silicon was milled by stacking a series of concentric solid circles with a thickness t and large to small diameters. The diameter of each circular layer d_{layer} can be calculate as:

$$d_{layer} = \left(\frac{h}{H}\right)^2 D, \tag{3.1}$$

where h is the vertical distance from the bottom of the parabolic trench to the corresponding layer, H is the total depth of the trench, and D is the diameter of the

trench upper opening.

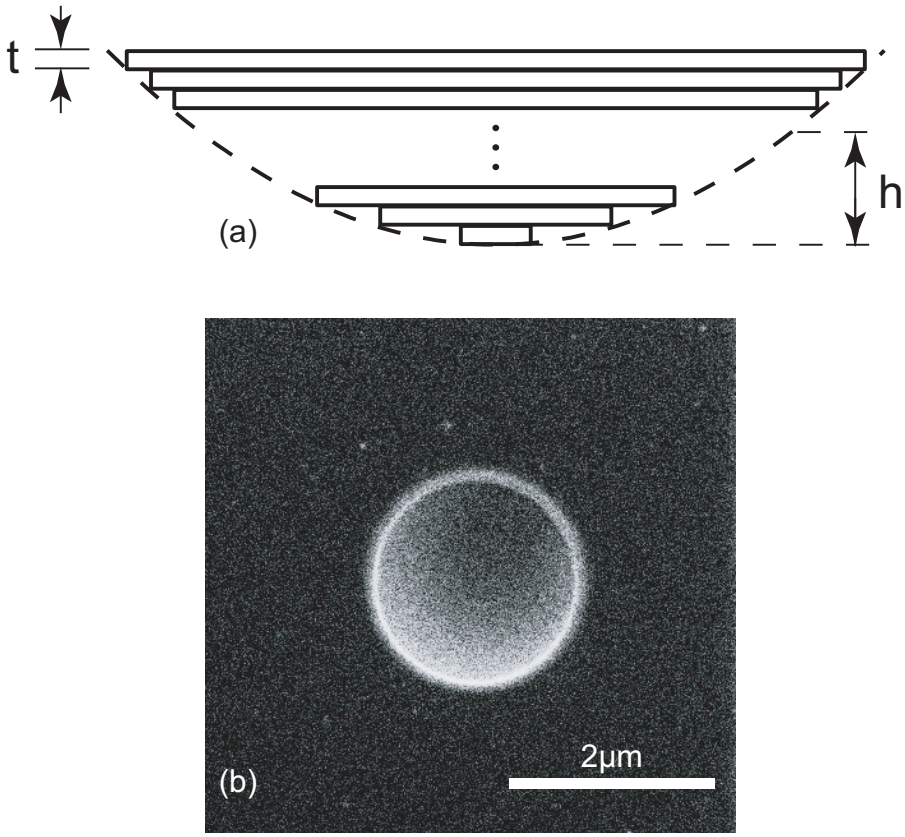

Figure 3.4: (a) A schematic diagram showing the layer-by-layer FIB milling procedure of the parabolic trench on silicon. (b) A scanning ion microscopic image of a parabolic trench on silicon.

Figure 3.4(b) shows a scanning ion microscopic image of a parabolic trench on silicon. This parabolic trench has an open diameter $D = 2000$ nm and a total depth of $H = 500$ nm. 19 layers (by inputting 19 bitmap images into the FIB system, each containing a solid circle with a different diameter) were used for milling. An ion accelerating voltage of 40 kV and a beam limiting aperture with a 30 μm diameter was used under a 35k$\times$ magnification. 42 passes were used for milling each layer and a 0.5 ms dose time was used for each pass. After all the layers were finished, the same beam was scanned over the whole trench for smoothing the staircase profile due to the finite layer thickness.

3.2.2 PMMA Thin Film Spin-Coating

PMMA from MicroChem Corp. is used in the research. The specification of the PMMA can be found online [137]. PMMA with a molecular weight of 495000 is dissolved in anisole. Spin-coating of PMMA is done using a Laurell Technologies WS-650SZ-6NPP / A1 / AR1 Spin-Coat System. PMMA is spread onto the sample at a spin speed of 500 rpm for 10 s, then spin at the designated speed for 60 s. Samples with pin-coated PMMA is baked on a hot plate at 180 °C for 5 min for crystallization. Table 3.1 lists some conditions for the spin-coating (including spin speed) and the final thickness of baked PMMA film.

Table 3.1: PMMA spin-coating conditions and final thicknesses

concentration (% solid w/w)	spin speed (rpm)	final thickness (nm)
3	4000	120
3	2000	140
4.5	4000	200
4.5	2000	240
6	4000	320
6	3000	350
6	2000	420
6	1500	480
6	1000	600

3.2.3 Electronic Evaporation Deposition

The metal and dielectric thin film coating deposition was done by electronic evaporation. The materials were evaporated by 7.5 kV electron beam source in an Angstrom Engineering physical vapor deposition system under a pressure of 2×10^{-6} Torr.

3.3 PDMS Microfluidic Channel Preparation

A microfluidic channel consists of a 150 μm thick glass coverslip and 80 μm thick PDMS spacer layer with a channel was used in the optical trapping experiment. Figure 3.5 illustrates the fabrication of the microfluidic channel. PDMS base (Sylgard 184 Silicone Elastomer Base, Dow Corning Canada) was mixed with Sylgard 184 Silicone Elastomer Curing Agent (Dow Corning Canada) at a ratio of 10:1. The

mixture was then degasified in a vacuum chamber for 30 minutes. As Figure 3.5(a, b) shows, the PDMS mixture was spin-coated onto the bottom of a Petri dish using a spin-coater (Specialty Coating System G3P-8 Spin-Coat System) at a spin rate of 500 rpm for 10 s for spreading, and then at a spin rate of 950 rpm for 60 s. The glass coverslip was then placed on top of the spin-coated PDMS mixture (Figure 3.5(c)). Due to the high viscosity of the PDMS mixture, the glass coverslip stays on top of the mixture. The coverslip-covered PDMS mixture was then degasified again in a vacuum chamber for 30 minutes to remove any air bubbles between the coverslip and the PDMS mixture, *i.e.* to make a seamless contact between the coverslip and the PDMS. The coverslip-covered PDMS mixture was then cured using a hot plate for 10 minutes to harden the PDMS (Figure 3.5(d)). After the curing, the coverslip could be peeled off from the bottom of the Petri dish with the PDMS layer on the coverslip (Figure 3.5(e)), since PDMS is more adhesive to glass than to the Petri dish (made of PMMA). A window of about 3 mm × 3 mm in size was then cut and removed from the PDMS as the microfluidic channel (Figure 3.5(f)).

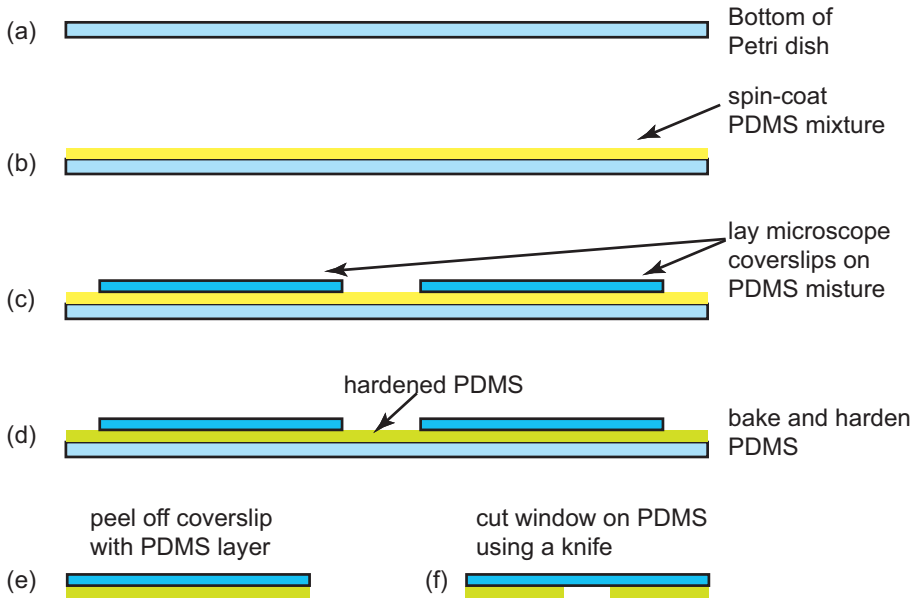

Figure 3.5: A process flow diagram illustrating the fabrication of the microfluidic channel consisting of a microscope coverslip and a PDMS spacer well.

The final thickness of the PDMS spacer layer can be measured by a micrometer gauge. It is found that an error of about 10 μm is usually associated with the thickness. This error is possibly due to the unevenness of the PDMS layer induced in the 30-minute vacuuming after the spin-coating. Any slight tilt of the Petri dish

will make the PDMS mixture uneven. Nevertheless, the 10 μm error in the PDMS spacer layer thickness is not a critical issue in the trapping experiment. As long as the PDMS spacer layer is thinner than 80 μm, the entire microfluidic chamber is within the working distance of the oil immersion microscope objective in the trapping setup. Thinner PDMS layer can be made by simply increasing the spin speed in the spin-coating step.

3.4 Finite-Difference Time-Domain Simulations

FDTD simulation is used as a modeling tool providing validations to the theories and supports to the experiments in my work. We use a commercially available comprehensive FDTD simulating package (Lumerical FDTD) for the FDTD simulations. This section describes some typical setups used in the FDTD simulations.

3.4.1 Simulation Boundaries

A number of different boundaries are used to enclose the simulation region. A perfectly-matched layer (PML) boundary is usually used to minimize the reflection at the simulation boundary. For periodically self-repeating structures such as an array or a periodic grid, periodic boundaries can be used over a unit cell of the repeating structure, so that only one unit cell needs to be simulated and computational resources can be saved. Sometimes, for computational speed considerations, periodic boundaries can be also used for non-periodic structures [9]. In this case, we set the periodicity to be much smaller than the half of the operating wavelength to minimize artifacts from coherent interference. Metallic boundaries can be used to emulate a metallic wall, such as a metallic waveguide boundary. In addition to these three commonly used boundaries, symmetry conditions can be used to further cut down the computational resource for symmetric structures with a symmetric excitation. Two symmetric boundaries, the even symmetry and the odd symmetry, need to be selected for appropriate situations. The electric field component normal to an even symmetric boundary is zero, and the component tangential to an odd symmetric boundary is zero.

3.4.2 Excitation Sources

A number of different types of sources are used for excitation in the simulations. A plane wave is the simplest source and can be used when the simulated structure is periodic. However, a plane wave cannot be used over a PML boundary. This is because a plane wave source is assumed to be unboundedly extending in space. If a plane wave source is spatially terminated at a PML, it is equivalently "apertured" in space and artifacts will be introduced in the frequency domain after a Fourier transformation. To remove the artifacts introduced by a plane wave source at a PML boundary, two other sources can be used. As a first one, a Gaussian source has a spatial intensity distribution given by a Gaussian function, and it can be used with PML boundaries. The intensity of the Gaussian source decays to nearly zero at the boundary due to its own distribution profile, and the artifact at the PML boundary is thus minimized. As a second one, a total-field scattered-field (TFSF) source contains the total field (sum of the fields from excitation source and from structure scattering) inside the source boundary, but only the scattered field is considered outside the source boundary. Therefore, the TFST source resolves the artifact due to PML boundaries by limiting the source region within the simulating region. As a last source used, a mode source is used to emulate waveguiding mode profiles such as an SPP mode, as will be discussed next.

3.4.3 Mesh Accuracy Considerations

FDTD simulations use rectangular meshes in space. A conformal mesh is used at metal boundaries to enforce an accurate boundary condition with a finite mesh grid. A mesh override region is sometimes introduced to increase the mesh density at some key structures in the simulation to make the simulation result more accurate. For example, a 2-nm mesh grid is usually needed to capture the SPP dispersion on the metal boundary. For the electromagnetic properties of metals used in the simulations, the permittivity values are taken from previous works [47, 48]. To ensure that we have used a sufficient mesh resolution, a convergence study is usually performed with different mesh densities and make sure the results from higher and higher mesh densities converge.

A sufficient mesh resolution can be ensured by computing the effective propagation index n_{eff} on a structure of interest using a mode source under different mesh resolutions. The mesh resolution is made finer and finer and the convergence of n_{eff}

is checked. As a simple example, we can investigate on the mesh resolution required for capturing the SPP mode at a metal-dielectric interface. The analytical effective propagation index of the SPP mode at a metal-dielectric interface is well-known as [1, 46]:

$$n_{eff} = \sqrt{\frac{\epsilon_m \epsilon_d}{\epsilon_m + \epsilon_d}}, \tag{3.2}$$

where ϵ_m and ϵ_d denotes the dielectric functions of the metal and the dielectric. Figure 3.6(a) shows the effective propagation index computed using a mode source perpendicular to a gold-air interface under different mesh accuracies, as compared to effective propagation index using the analytical expression in Equation 3.2. The wavelength is at 705 nm. It can be clearly seen that the effective index of the SPP mode converges for finer mesh resolutions, and the difference between the effective index computed by the FDTD mode source and the analytical expression falls under 0.01% for a mesh resolution of and below 2 nm. Figure 3.6(b) shows a plot of the mode shape of the SPP mode.

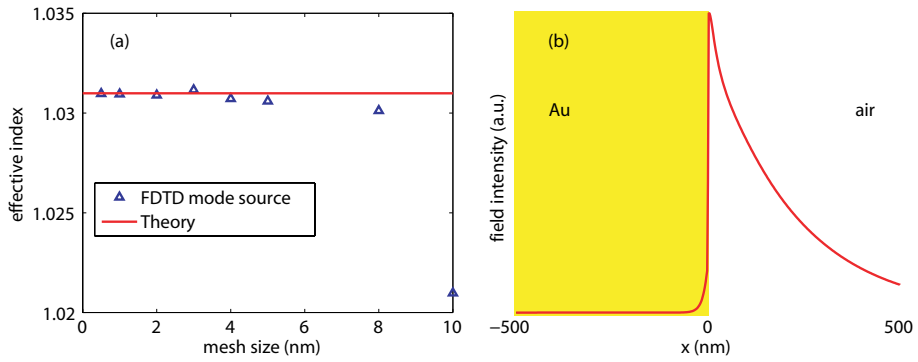

Figure 3.6: (a) The effective propagation index computed using a mode source perpendicular to a gold-air interface under different mesh accuracies, as compared to effective propagation index using the analytical expression in Equation 3.2. (b) A plot of the mode shape of the SPP mode.

3.5 Summary

In summary, the important computational and experimental techniques have been introduced in this chapter. These methods have served critical roles in the research. With the specifications introduced in this chapter, the results shown in the dissertations can be readily reproduced and tested.

Chapter 4

Other Contributions

In this chapter, some topics in nanophotonics using other metallic nanostructures than subwavelength apertures are introduced. First, using a metal nanowire grid, a novel reflective wave plate is designed. Second, a directivity-enhanced Raman spectroscopy (DERS) is achieved using nanoantennas with a ground reflector, including a planar reflector and a parabolic reflector. By applying standard antenna theory, the nanoantennas are able to direct the beam into the detector with a high efficiency.

4.1 Metal Nano-Grid Reflective Wave Plate

Wave plates give different retardation (or phase) to light with different polarizations. Conventional wave plates work in the transmission regime using birefringent crystals [138–142]. Two main disadvantages of conventional wave plates are their narrow operating bands due to long beam paths through the birefringence crystal, and their high material costs. We designed a reflective wave plate using a metal nanowire grid, as illustrated in Figure 4.1 (a). As the working principle, the TM polarization, with the electric field polarized in the x-direction, can propagate into the grid in the form of gap plasmons and it is reflected at the bottom of the grid; while the TE polarization, with the electric field polarized in the x-direction, is cut-off in the grid and it is reflected at the top surface. The different beam paths and therefore different retardation are shown in Figure 4.1 (b) using numerical simulations.

As the analytic theory, we modeled the TM mode in between the metal wires using a periodic version of the gap plasmon mode [143], and we found the propagation constant of the mode by solving for its dispersion relation. We used a single-mode-

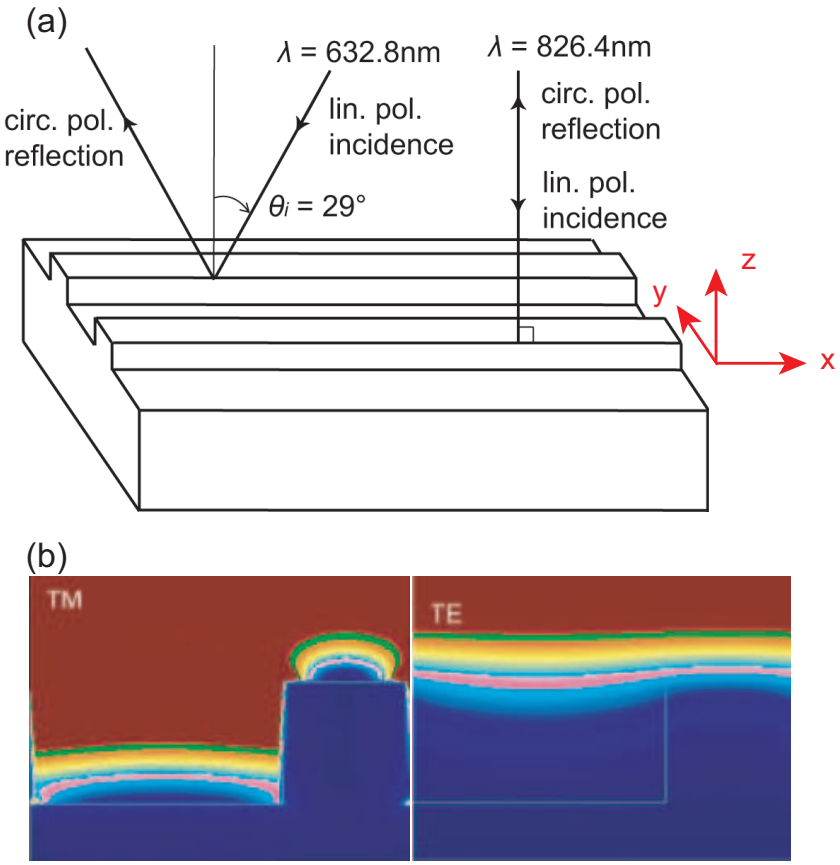

Figure 4.1: (a) Schematic illustration of the metal nanowire grid reflective wave plate. (b) Numerical simulations show that the TM and TE polarizations have different beam paths and different retardation upon reflecting from the metal nanowire grid. Figure reprinted with permission from [8].

matching technique to work out the complex reflectivities and transmittivities of the two polarizations at the top and the bottom of the metal wire grids. These computations allow angled beam incidence as well. With these parameters, the relative phase difference of the two polarizations upon reflecting from the wiregrid can be precisely analyzed and designed. We verify the analytic results using FDTD simulations.

Figure 4.2 shows the analytic theory and FDTD simulation results of the phase differences between the reflected TE and TM modes, for a quarter wave plate designed using the metal nanowire grid. The results show that the retardation between the two polarizations can be tuned by the incident angle. The angle tuning feature is also shown in the schematic in Figure 4.1 (a). For a quarter wave plate designed for operating at 826.4 nm wavelength upon normal incidence, the relative retardation between polarizations will be different for a 632.8 nm wavelength due to material dispersion and the different gap plasmon propagation constant. However, the same wave plate can be tuned to an incident angle of 29° and have the quarter wave difference between the two polarizations for 632.8 nm wavelength.

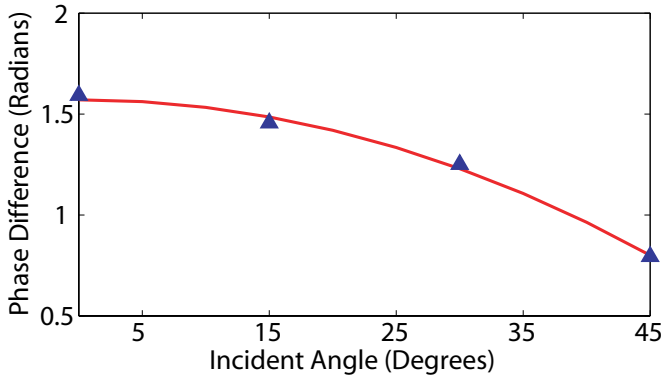

Figure 4.2: Analytic theory and comprehensive numerical simulation results showing the phase differences between the reflected TE and TM modes, under different incident angles, for a quarter wave plate designed using the metal nanowire grid. Figure reprinted with permission from [8].

Besides its angular tunability, this wave plate is broad-band due to its short beam path. The nanowire grid wave plate is not based on expensive birefringence crystals and therefore it has a lower cost. This has a great potential to be applied in reflective liquid crystal display (LCD) devices [144] and as a component to provide polarization rotated feedback in experiments on lasers [145].

The reader is referred to Appendix G for the details of the study described in Section 4.1.

4.2 Directivity-Enhanced Raman Spectroscopy

Raman spectroscopy is a highly specific label-free sensing tool; however, the Raman signal is usually extremely low. Metal nanoparticles (MNPs) can have localized surface plasmon resonances that stably enhance the local electric field leading to surface enhanced Raman spectroscopy (SERS) [146–153], but the enhanced signal has been still typically orders of magnitude less than randomly roughened substrates or aggregates. We further boosted MNP enhanced Raman signals by 50× by applying a nanoantenna concept. This was done by designing a metal ground plane underneath the MNPs spaced by a dielectric spacer layer, as illustrated in Figure 4.3(a). According to standard antenna theories, the directivity of an antenna can be modified using a ground plane. We were able to coherently direct the Raman signal out of the sample plane into the detector by modifying the dielectric spacer layer thickness, and achieve a higher near- and far-field coupling efficiency. This leads to a 50-fold enhancement to the Raman signal at the coherent conditions, as shown in Figure 4.3(b).

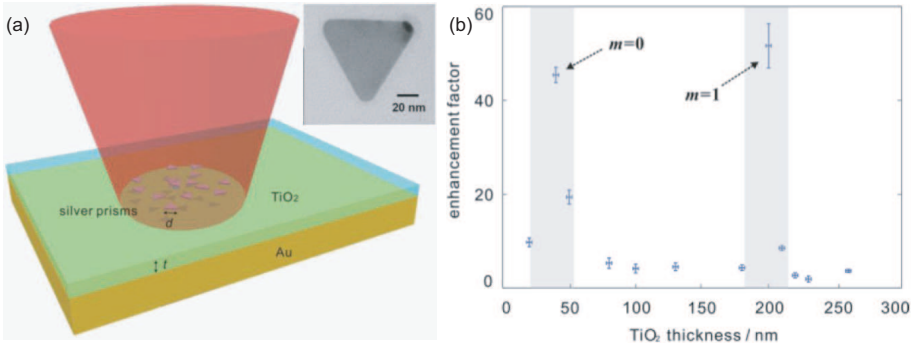

Figure 4.3: (a) Schematic of NMPs on TiO_2 spacer layer over a metallic ground plane. The inset shows a transmission electron microscope image of the NMP. (b) The coherently enhanced Raman signal as compared to using NMPs without a metallic ground plane, and m represents the order of the coherency. Figure reprinted with permission from [9].

To achieve a higher directivity enhancement to the Raman spectroscopy signal, we designed a parabolic reflector nanoantenna using a metal coated parabolic trench, a dielectric spacer layer, and a MNP as the feed element, as illustrated in Figure 4.4(a). Figure 4.4(b) shows that the parabolic nanoantenna has a high out-of-plane directivity as confirmed by FDTD simulations, similar to its macroscopic counterpart. We achieved a 1100-fold boost to the Raman signal compared to using only NMPs, as shown in Figure 4.4(c). The directivity enhancement scheme can be a general strat-

egy in enhancing weak optical signals in many other different experiments such as second harmonic generation and single photon emission.

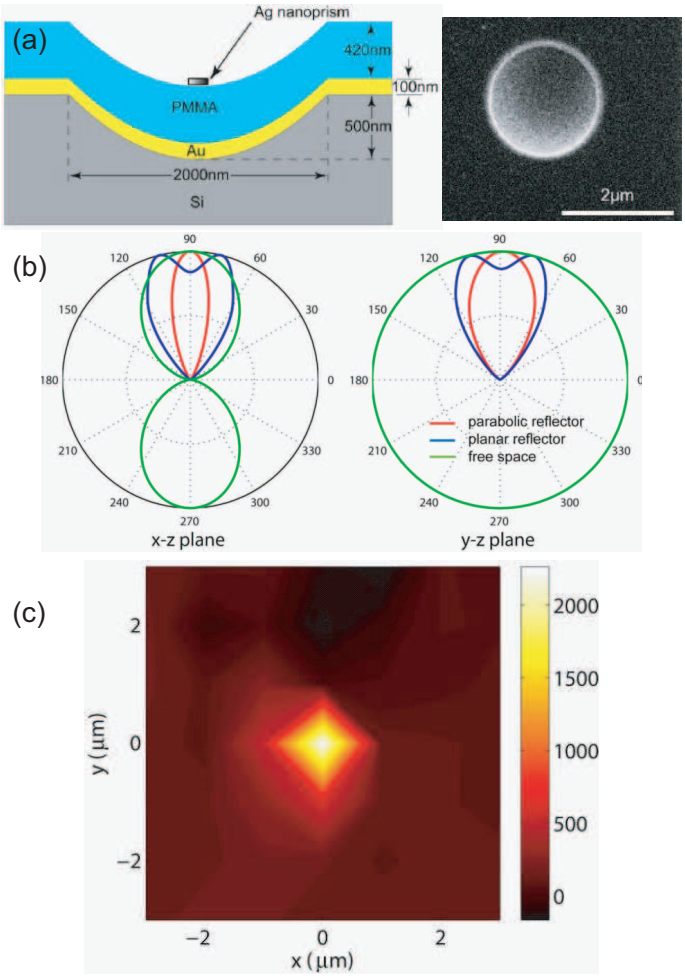

Figure 4.4: (a) Schematic illustration of the parabolic reflector nanoantenna and a scanning ion microscopic image of the parabolic trench. (b) Numerical simulations of the nanoantenna radiation pattern, showing the enhanced directivity of the Raman signal from the nanoantenna. (c) Raman spectroscopy experiment showing an enhanced Raman signal at the nanoantenna. Figure reprinted with permission from [10].

The reader is referred to Appendixes H and I for the details of the study described in Section 4.2.

4.3 Summary

In conclusion, some other metallic nanostructure were introduced in this chapter for light-matter interactions. A reflective wave plate was designed using a metal nanowire grid. This wave plate has a compact beam path, it is wide band, angular tunable and low-cost. Nanoantennas using metal reflectors were designed for DERS. Using a planar reflector, Raman signal was boosted by 50× by an enhanced directivity into the detector. An even higher 1100× Raman enhancement was experimentally observed using a parabolic reflector nanoantenna.

Chapter 5

Summary and Future Works

5.1 Summary of Contributions

In this dissertation, I have performed a comprehensive study on subwavelength apertures on a metal film, from theory to applications. I started with Bethe's aperture theory and found a surprising total transmission through a subwavelength hole that couples two metallic waveguide sections – the first EOT phenomenon found for the same setup as Bethe's original intention. A simple yet accurate analytical derivation was provided for this phenomenon by applying Bethe's theory and realizing a divergent magnetic field at the cutoff of a bounded TM waveguide mode. Then, I realized that the huge optical transmission through a small hole could lead to a method of beating Abbe's resolution limit for an optical microscope. A high optical throughput apertured NSOM probe was designed by utilizing the waveguide EOT. This EOT brightened NSOM probe structure has experimentally shown a 100× enhanced optical throughput and a 40× damage threshold as compared to an apertured NSOM probe with a comparable aperture size in a conventional structure. Using the EOT brightened NSOM probe, single fluorescent molecule scanning was shown experimentally with a spatial resolution of about 62 nm.

Optical trapping was another study based on subwavelength holes in this dissertation. We realized that a dielectric particle had a great influence to the electromagnetic field inside a subwavelength aperture than the perturbative Rayleigh scattering in a uniform background. A SIBA optical trap using a circular nanohole in a gold film was designed. When a dielectric particle entered the nanohole, it greatly increased the optical transmission by dielectric loading, and the change of light momentum

induced a large optical force reacted on the particle which favored trapping. We have experimentally achieved the trapping of 50 nm polystyrene spheres using a low optical power, which is impossible to trap by a conventional single beam tweezers. By FDTD simulations, I confirmed that the SIBA trap worked beyond the perturbative regime, because the rigorous MST analysis gives a larger optical force than a perturbative gradient force approximation. After that, we have realized that a better aperture shape can be designed for trapping smaller dielectric particles, and the smallest biological materials. A double-nanohole was designed for a huge local field enhancement between its two sharp tips. The optical transmission was made even more sensitive to small dielectric changes between the tips. Using the double-nanohole, we have achieved optical trapping of single 12 nm silica spheres, the smallest dielectric particle that have been trapped so far. We have also achieved trapping of a single protein. Interestingly, the trapped protein was unfolded by the large optical force in the trap, as confirmed by experiments with changing optical power and changing pH.

5.2 Future Works

The research contributions summarized in the dissertation have a broad spectrum in nanophotonics, especially with subwavelength apertures. They have significant potential applications and open the paths for many future research opportunities. The waveguide EOT is derived in the microwave regime and is proven for being able to extend into the visible-IR regime, and the designed high-throughput near-field probe is promising for high resolution near-field optical imaging. The nanohole optical trap for the first time shows the capability for trapping and sensing the smallest biological particle, promising for biomedical applications such as immunology study and drug discovery. In addition, the structures proposed in this dissertation are predominantly based on a single aperture without relying on periodic structures. This has a significant advantage in interacting with the smallest possible amount of material, and in extremely compact optical integration. All these topics have strong potentials to be further explored. Some research topics can combine into new, multidisciplinary fields: for example, it is possible to design a optical trap or a optical sensor using the EOT near-field probe. In the following section, I would like to outline some research ideas that may be developed from my past research contributions.

5.2.1 Long Term Goal for Optical Trapping

With the tremendous trapping ability shown by aperture trapping including the trapping of a single protein, it finds many potential applications. As a long term goal of the optical trapping project, a reliable and mature technique can be designed for the immobilization, characterization and manipulation of nanoparticles for biological applications and studies. Using the novel optical trap, a possible experiment that might be done is to trap and isolate a single virus, move it to the vicinity of a living cell or a bacteria, and study the infectious behavior at the single virus level (single species) [154]. In this way, the heterogeneity within a single virus species, which is usually a concern in immunology studies, can be removed.

In the short term, I propose the following directions.

5.2.2 Trapping Using a Near-Field Probe

As the most exciting future project, the nanohole trapping can be combined with the apertured near-field probe by putting the nanohole for trapping on the tip of a metal-coated optical fiber. To the best of my knowledge, an optical trap using a near-field probe without relying on additional structures (such as an optical nanoantenna on a separate substrate) has never been proposed. Using the optical trap based on a stand-alone near-field probe, or a "nano-pipette", a particle can be trapped at the tip of the near-field probe and transport it to a desired position simply by moving the probe. This allows a long-distance transportation of an object with an extremely small size.

5.2.3 Characterization of the Trapped Particle

As a second possible evolution to the trapping experiment, extra means of characterizing the trapped particle can be introduced. For example, incorporating a fluorescent detection scheme into the setup gives it an extra degree of freedom to chase the trapped fluorescent particles such as fluorescent-tagged viruses, semiconductor quantum dots or green fluorescent proteins. As a more interesting method, a Raman spectroscope can be integrated into the setup to specifically look at the Raman signal of the immobilized particle and subsequently monitor binding and reaction events at a single nanoparticle or even a single molecule level.

5.2.4 Optical Trapping in a Microfluidic Environment

Next, a lab-on-a-chip trapping device can be designed, and the most important step will be putting the trapping experiment in a microfluidic channel. A lab-on-a-chip device reduces the bulky instruments in the setup and makes it more robust. Another major advantage of using a microfluidic channel is its ability to control the environment during the trapping experiment. As a possible experiment, incorporating with the integrated Raman spectroscope, we can evacuate all extra particles/molecules in the fluid after the trapping, and study the Raman signal from the remaining single trapped particle/molecule. Another interesting project is to make a "flow-through" channel using a punch-through nanohole on an Au film on thin dielectric membrane. Comparing to a "flow-over" fluidics channel, a "flow-through" channel greatly reduces diffusion time and might enable a selective trapping of the particles going through the channel [82, 83].

5.2.5 Optical Biosensing

Many of my past projects have the potential for optical sensing applications, as they all relate to the enhanced light-matter interactions. In fact, I believe the structures I have studied in my previous contributions are highly advantageous as compared to existing technologies. For example, existing surface plasmon resonance sensors usually rely on periodic structures such as a hole array. In comparison, the technology in my research is based predominantly on a single hole, which is more compatible for sensing the smallest amount of analyte at the surface. Also, compared to the competing technology of an optical resonator cavity sensor, nanohole sensing is more robust because it does not rely on a complex and delicate optical coupling scheme. Ultimately, a single molecule sensing capability can be achieved based on the current setups, based on their recent successes.

5.2.6 Optical Biosensing Using Double-Nanohole

As noted before, in the double-nanohole optical trapping, the signal jump at a trapping event has a very high SNR of 33 for just a single protein. This means that the double-nanohole can be potentially used as a highly sensitive optical sensor with single molecule detecting capability. As a future project, a sensor can be built for sensing single protein binding events. This will include building a setup that will allow for spe-

cific identification of molecules, for which Raman spectroscopy and antigen-antibody binding can be used.

5.2.7 Optical Biosensing Using EOT Near-Field Probe

As another promising project for optical sensing, the waveguide EOT effect can be utilized, in which the peak wavelength is highly sensitive to the change to the aperture polarizability. This sensor relies on a high quality resonance. As compared to other sensing methods using a high quality resonance, for example, a whispering-gallery-mode (WGM) optical resonator or a photonic crystal optical cavity, the waveguide EOT sensor will have a much simpler and more robust experimental setup. This is because the EOT waveguide is essentially a metal-coated fiber taper; its excitation and detection are directly compatible to fiber optics, and it does not have a coupling efficiency that is delicate to the coupling distance like in WGM resonators. Moreover, the sensing region of the EOT waveguide is highly confined at the aperture, therefore, any binding events happened at other parts of the structure can be excluded in the analysis of the signal.

Bibliography

[1] C. Genet and T. W. Ebbesen. Light in tiny holes. *Nature*, 445(7123):39 – 46, 2007.

[2] R. Gordon. Bethe's aperture theory for arrays. *Physical Review A*, 76(5):053806, 2007.

[3] Y. Pang, A. N. Hone, P. P. M. So, and R. Gordon. Total optical transmission through a small hole in a metal waveguide screen. *Optics Express*, 17(6):4433–4441, 2009.

[4] L. Neumann, Y. Pang, A. Houyou, M. L. Juan, R. Gordon, and N. F. van Hulst. Extraordinary optical transmission brightens near-field fiber probe. *Nano Letters*, 11(2):355–360, 2011.

[5] M. L. Juan, R. Gordon, Y. Pang, F. Eftekhari, and R. Quidant. Self-induced back-action optical trapping of dielectric nanoparticles. *Nature Physics*, 5(12):915–919, 2009.

[6] Y. Pang and R. Gordon. Optical trapping of 12 nm dielectric spheres using double-nanoholes in a gold film. *Nano Letters*, 11(9):3763–3767, 2011.

[7] Y. Pang and R. Gordon. Optical trapping of a single protein. *Nano Letters*, 12(1):402–406, 2012.

[8] Y. Pang and R. Gordon. Metal nano-grid reflective wave plate. *Optics Express*, 17(4):2871–2879, 2009.

[9] Q. Min, Y. Pang, D.J. Collins, N. A. Kuklev, K. Gottselig, D. W. Steuerman, and R. Gordon. Substrate-based platform for boosting the surface-enhanced raman of plasmonic nanoparticles. *Optics Express*, 19(2):1648–1655, 2011.

[10] A. Ahmed, Y. Pang, G. Hajisalem, and R. Gordon. Antenna design for directivity-enhanced raman spectroscopy. *International Journal of Optics*, 2012:729138, 2012.

[11] P. J. Schuck, D. P. Fromm, A. Sundaramurthy, G. S. Kino, and W. E. Moerner. Improving the mismatch between light and nanoscale objects with gold bowtie nanoantennas. *Physical Review Letters*, 94:017402, 2005.

[12] P. Mühlschlegel, H. J. Eisler, O. J. F. Martin, B. Hecht, and D. W. Pohl. Resonant optical antennas. *Science*, 308(5728):1607, 2005.

[13] A. G. Curto, G. Volpe, T. H. Taminiau, M. P. Kreuzer, R. Quidant, and N. F. van Hulst. Unidirectional emission of a quantum dot coupled to a nanoantenna. *Science*, 329(5994):930, 2010.

[14] A. Ahmed and R. Gordon. Directivity enhanced raman spectroscopy using nanoantennas. *Nano Letters*, 11(4):1800–1803, 2011.

[15] D. Dregely, R. Taubert, J. Dorfmüller, R. Vogelgesang, K. Kern, and H. Giessen. 3d optical yagi-uda nanoantenna array. *Nature Communications*, 2:267, 2011.

[16] H. A. Bethe. Theory of diffraction by small holes. *Physical Review*, 66(7):163–182, 1944.

[17] T. W. Ebbesen, H. J. Lezec, H. F. Ghaemi, T. Thio, and P. A. Wolff. Extraordinary optical transmission through sub-wavelength hole arrays. *Nature*, 391(6668):667 – 669, 1998.

[18] F. J. García de Abajo, R. Gomez-Medina, and J. J. R. Saenz. Full transmission through perfect-conductor subwavelength hole arrays. *Physical Review E*, 2(1):016608, 2005.

[19] H. J. Lezec, A. Degiron, E. Devaux, R. A. Linke, L. Martín-Moreno, F. J. García-Vidal, and T. W. Ebbesen. Beaming light from a subwavelength aperture. *Science*, 297(5582):820–822, 2002.

[20] M. Born and E. Wolf. *Principle of Optics*. Cambridge University Press, Cambridge, UK, 2002.

[21] B. Hecht, B. Sick, U. P. Wild, V. Deckert, R. Zenobi, O. J. F. Martin, and D. W. Pohl. Scanning near-field optical microscopy with aperture probes: Fundamentals and applications. *Journal of Chemical Physics*, 112(18):7761–7774, 2000.

[22] C.A. Balanis. *Antenna Theory: Analysis and Design*. Harper & Row New York, 1982.

[23] A. Ashkin, J. M. Dziedzic, J. E. Bjorkholm, and S. Chu. Observation of a single-beam gradient force optical trap for dielectric particles. *Optics Letters*, 11(5):288–290, 1986.

[24] K. Dholakia, P. Reece, and M. Gu. Optical micromanipulation. *Chemical Society Reviews*, 37(1):42–55, 2008.

[25] O. M. Maragò, P. H. Jones, F. Bonaccorso, V. Scardaci, P. G. Gucciardi, A. G. Rozhin, and A. C. Ferrari. Femtonewton force sensing with optically trapped nanotubes. *Nano Letters*, 8(10):3211–3216, 2008.

[26] P. J. Reece, W. J. Toe, F. Wang, S. Paiman, Q. Gao, H. H. Tan, and C. Jagadish. Characterization of semiconductor nanowires using optical tweezers. *Nano Letters*, 11(6):2375–2381, 2011.

[27] M. Pelton, M. Liu, H. Y. Kim, G. Smith, P. Guyot-Sionnest, and N. F. Scherer. Optical trapping and alignment of single gold nanorods by using plasmon resonances. *Optics Letters*, 31(13):2075–2077, 2006.

[28] C. Selhuber-Unkel, I. Zins, O. Schubert, C. Sonnichsen, and L. B. Oddershede. Quantitative optical trapping of single gold nanorods. *Nano Letters*, 8(9):2998–3003, 2008.

[29] F. Hajizadeh and S. N. S Reihani. Optimized optical trapping of gold nanoparticles. *Optics Express*, 18(2):551–559, 2010.

[30] A. Ashkin, J. M. Dziedzic, and T. Yamane. Optical trapping and manipulation of single cells using infrared laser beams. *Nature*, 330(6150):769–771, 1987.

[31] Y. Liu, D. K. Cheng, G. J. Sonek, M. W. Berns, C. F. Chapman, and B. J. Tromberg. Evidence for localized cell heating induced by infrared optical tweezers. *Biophysical Journal*, 68(5):2137–2144, 1995.

[32] Y. Liu, G. J. Sonek, M. W. Berns, and B. J. Tromberg. Physiological monitoring of optically trapped cells: Assessing the effects of confinement by 1064-nm laser tweezers using microfluorometry. *Biophysical Journal*, 71(4):2158–2167, 1996.

[33] A. Ashkin and J. M. Dziedzic. Optical trapping and manipulation of viruses and bacteria. *Science*, 235(4795):1517–1520, 1987.

[34] M. D. Wang, H. Yin, R. Landick, J. Gelles, and S. M. Block. Stretching dna with optical tweezers. *Biophysical Journal*, 72(3):1335–1346, 1997.

[35] E. A. Abbondanzieri, W. J. Greenleaf, J. W. Shaevitz, R. Landick, and S. M. Block. Direct observation of base-pair stepping by rna polymerase. *Nature*, 438(7067):460–465, 2005.

[36] J. T. Finer, R. M. Simmons, and J. A. Spudich. Single myosin molecule mechanics: Piconewton forces and nanometre steps. *Nature*, 368(6467):113–119, 1994.

[37] W. Cheng, S. G. Arunajadai, J. R. Moffitt, I. Tinoco Jr, and C. Bustamante. Single–base pair unwinding and asynchronous rna release by the hepatitis C virus NS3 helicase. *Science*, 333(6050):1746–1749, 2011.

[38] A. H. J. Yang, T. Lerdsuchatawanich, and D. Erickson. Forces and transport velocities for a particle in a slot waveguide. *Nano Letters*, 9(3):1182–1188, 2009.

[39] A. H. J. Yang, S. D. Moore, B. S. Schmidt, M. Klug, M. Lipson, and D. Erickson. Optical manipulation of nanoparticles and biomolecules in sub-wavelength slot waveguides. *Nature*, 457(7225):71–75, 2009.

[40] S. Arnold, D. Keng, S. I. Shopova, S. Holler, W. Zurawsky, and F. Vollmer. Whispering gallery mode carousel - a photonic mechanism for enhanced nanoparticle detection in biosensing. *Optics Express*, 17(8):6230–6238, 2009.

[41] S. Lin, E. Schonbrun, and K. Crozier. Optical manipulation with planar silicon microring resonators. *Nano Letters*, 10(7):2408–2411, 2010.

[42] S. Mandal, X. Serey, and D. Erickson. Nanomanipulation using silicon photonic crystal resonators. *Nano Letters*, 10(1):99–104, 2009.

[43] J. Hu, S. Lin, L. C. Kimerling, and K. Crozier. Optical trapping of dielectric nanoparticles in resonant cavities. *Physical Review A*, 82(5):053819, 2010.

[44] M. Barth and O. Benson. Manipulation of dielectric particles using photonic crystal cavities. *Applied Physics Letters*, 89:253114, 2006.

[45] J. D. Jackson. *Classical Electrodynamics*. Wiley, New York, 1998.

[46] S. A. Maier. *Plasmonics: Fundamentals and Applications*. Springer, Bath, United Kingdom, 2007.

[47] P. B. Johnson and R. W. Christy. Optical constants of the noble metals. *Physical Review B*, 6(12):4370, 1972.

[48] E. D. Palik and G. Ghosh. *Handbook of Optical Constants of Solids*, volume 3. Academic press, 1998.

[49] J. Homola, S. S. Yee, and G. Gauglitz. Surface plasmon resonance sensors: Review. *Sensors and Actuators B*, 54(1-2):3–15, 1999.

[50] F. J. García de Abajo. Light transmission through a single cylindrical hole in a metallic film. *Optics Letters*, 10(25):1475–1484, 2002.

[51] F. J. García-Vidal, L. Martín-Moreno, E. Moreno, L. K. S. Kumar, and R. Gordon. Transmission of light through a single rectangular hole in a real metal. *Physical Review B*, 74(15):153411, 2006.

[52] A. Degiron, H. J. Lezec, N. Yamamoto, and T. W. Ebbesen. Optical transmission properties of a single subwavelength aperture in a real metal. *Optics Communications*, 239(1-3):61–66, 2004.

[53] R. Gordon and A. G. Brolo. Increased cut-off wavelength for a subwavelength hole in a real metal. *Optics Express*, 13(6):1933 – 1938, 2005.

[54] F. J. García-Vidal, E. Moreno, J. A. Porto, and L. Martín-Moreno. Transmission of light through a single rectangular hole. *Physical Review Letters*, 95(10):103901, 2005.

[55] X. L. Shi, L. Hesselink, and R. L. Thornton. Ultrahigh light transmission through a C-shaped nanoaperture. *Optics Letters*, 28(15):1320–1322, 2003.

[56] J. A. Matteo, D. P. Fromm, Y. Yuen, P. J. Schuck, W. E. Moerner, and L. Hesselink. Spectral analysis of strongly enhanced visible light transmission through single C-shaped nanoapertures. *Applied Physics Letters*, 85(4):648–650, 2004.

[57] E. X. Jin and X. Xu. Plasmonic effects in near-field optical transmission enhancement through a single bowtie-shaped aperture. *Applied Physics B*, 84(1-2):3–9, 2006.

[58] E. X. Jin and X. F. Xu. Enhanced optical near field from a bowtie aperture. *Applied Physics Letters*, 88(15), 2006.

[59] L. Wang and X. Xu. High transmission nanoscale bowtie-shaped aperture probe for near-field optical imaging. *Applied Physics Letters*, 90(26), 2007.

[60] L. Wang, S. M. Uppuluri, E. X. Jin, and X. F. Xu. Nanolithography using high transmission nanoscale bowtie apertures. *Nano Letters*, 6(3):361–364, 2006.

[61] L. K. S. Kumar and R. Gordon. Overlapping double-hole nanostructure in a metal film for localized field enhancement. *IEEE Journal of Selected Topics in Quantum Electronics*, 12(6):1228–1232, 2006.

[62] L. K. S. Kumar, A. Lesuffleur, M. C. Hughes, and R. Gordon. Double nanohole apex-enhanced transmission in metal films. *Applied Physics B*, 84(1):25–28, 2006.

[63] A. Lesuffleur, L. K. S. Kumar, and R. Gordon. Enhanced second harmonic generation from nanoscale double-hole arrays in a gold film. *Applied Physics Letters*, 88:261104, 2006.

[64] A. Lesuffleur, L. K. S. Kumar, and R. Gordon. Apex-enhanced second-harmonic generation by using double-hole arrays in a gold film. *Physical Review B*, 75(4):045423, 2007.

[65] T.-D. Onuta, M. Waegele, C. C. DuFort, W. L. Schaich, and B. Dragnea. Optical field enhancement at cusps between adjacent nanoapertures. *Nano Letters*, 7(3):557–564, 2007.

[66] A. Lesuffleur, L. K. S. Kumar, A. G. Brolo, K. L. Kavanagh, and R. Gordon. Apex-enhanced raman spectroscopy using double-hole arrays in a gold film. *Journal of Physical Chemistry C*, 111(6):2347–2350, 2007.

[67] F. Medina, F. Mesa, and R. Marques. Extraordinary transmission through arrays of electrically small holes from a circuit theory perspective. *IEEE Transactions on Microwave Theory and Techniques*, 56(12):3108–3120, 2008.

[68] D. E. Grupp, H. J. Lezec, T. W. Ebbesen, K. M. Pellerin, and T. Thio. Crucial role of metal surface in enhanced transmission through subwavelength apertures. *Applied Physics Letters*, 77(11):1569–1571, 2000.

[69] L. Martín-Moreno, F. J. García-Vidal, H. J. Lezec, K. M. Pellerin, T. Thio, J. B. Pendry, and T.W. Ebbesen. Theory of extraordinary optical transmission through subwavelength hole arrays. *Physical Review Letters*, 86(6):1114 – 1117, 2001.

[70] J. Bravo-Abad, L. Martín-Moreno, F. J. García-Vidal, E. Hendry, and J. Gomez Rivas. Transmission of light through periodic arrays of square holes: From a metallic wire mesh to an array of tiny holes. *Physical Review B*, 76(24):241102, 2007.

[71] F. J. García de Abajo. Colloquium: Light scattering by particle and hole arrays. *Reviews of Modern Physics*, 79(4):1267 – 1290, 2007.

[72] J. B. Pendry, L. Martín-Moreno, and F. J. García-Vidal. Mimicking surface plasmons with structured surfaces. *Science*, 305(5685):847–848, 2004.

[73] R. Gordon, D. Sinton, K. L. Kavanagh, and A. G. Brolo. A new generation of sensors based on extraordinary optical transmission. *Accounts of Chemical Research*, 41(8):1049–1057, 2008.

[74] R. Gordon. Commentary: Extraordinary optical transmission for surface-plasmon-resonance-based sensing. *Journal of Nanophotonics*, 2:020305, 2008.

[75] R. Gordon, A. G. Brolo, D. Sinton, and K. L. Kavanagh. Resonant optical transmission through hole-arrays in metal films: Physics and applications. *Laser & Photonics Reviews*, 4(2):311–335, 2010.

[76] A. De Leebeeck, L. K. S. Kumar, V. de Lange, D. Sinton, R. Gordon, and A. G. Brolo. On-chip surface-based detection with nanohole arrays. *Analytical Chemistry*, 79(11):4094–4100, 2007.

[77] M. Das, D. Hohertz, R. Nirwan, A. G. Brolo, K. L. Kavanagh, and R. Gordon. Improved performance of nanohole surface plasmon resonance sensors by the integrated response method. *IEEE Photonics Journal*, 3(3):441–449, 2011.

[78] A. P. Blanchard-Dionne, L. Guyot, S. Patskovsky, R. Gordon, and M. Meunier. Intensity based surface plasmon resonance sensor using a nanohole rectangular array. *Optics Express*, 19(16):15041–15046, 2011.

[79] A. G. Brolo, R. Gordon, B. Leathem, and K. L. Kavanagh. Surface plasmon sensor based on the enhanced light transmission through arrays of nanoholes in gold films. *Langmuir*, 20(12):4813–4815, 2004.

[80] F. Eftekhari, R. Gordon, J. Ferreira, AG Brolo, and D. Sinton. Polarization-dependent sensing of a self-assembled monolayer using biaxial nanohole arrays. *Applied Physics Letters*, 92:253103, 2008.

[81] J. Ferreira, M. J. L. Santos, M. M. Rahman, A. G. Brolo, R. Gordon, D. Sinton, and E. M. Girotto. Attomolar protein detection using in-hole surface plasmon resonance. *Journal of the American Chemical Society*, 131(2):436–437, 2008.

[82] F. Eftekhari, C. Escobedo, J. Ferreira, X. Duan, E. M. Girotto, A. G. Brolo, R. Gordon, and D. Sinton. Nanoholes as nanochannels: Flow-through plasmonic sensing. *Analytical Chemistry*, 81(11):4308–4311, 2009.

[83] C. Escobedo, A. G. Brolo, R. Gordon, and D. Sinton. Flow-through vs flow-over: Analysis of transport and binding in nanohole array plasmonic biosensors. *Analytical Chemistry*, 82(24):10015–10020, 2010.

[84] S. F. Romanuik, S. M. Grist, B. L. Gray, D. Hohertz, K. L. Kavanagh, N. Gulzar, J. K. Scott, R. Nirwan, C. Hui, A. G. Brolo, and R. Gordon. Detecting antibodies secreted by trapped cells using extraordinary optical transmission. *IEEE Sensors Journal*, 11(11), 2011.

[85] T. Thio, K. M. Pellerin, R. A. Linke, H. J. Lezec, and T. W. Ebbesen. Enhanced light transmission through a single subwavelength aperture. *Optics Letters*, 26(24):1972–1974, 2001.

[86] R. W. Wood. On a remarkable case of uneven distribution of light in a diffraction grating spectrum. *The London, Edinburgh, and Dublin Philosophical Magazine and Journal of Science*, 4(21):396–402, 1902.

[87] L. Rayleigh. Note on the remarkable case of diffraction spectra described by prof. wood. *The London, Edinburgh, and Dublin Philosophical Magazine and Journal of Science*, 14(79):60–65, 1907.

[88] D. M. Pozar. *Microwave Engineering*. John Wiley & Sons, Inc., Amherst, Massachusetts, USA, 2005.

[89] F. Medina, F. Mesa, and R. Rodriguez-Berral. Some advances in the circuit modeling of extraordinary optical transmission. *Radioengineering*, 18(2):103–110, 2009.

[90] F. Medina, J. A. Ruiz-Cruz, F. Mesa, J. M. Rebollar, J. R. Montejo-Garai, and R. Marques. Experimental verification of extraordinary transmission without surface plasmons. *Applied Physics Letters*, 95(7), 2009.

[91] F. Medina, F. Mesa, J. A. Ruiz-Cruz, J. M. Rebollar, and J. R. Montejo-Garai. Study of extraordinary transmission in a circular waveguide system. *IEEE Transactions on Microwave Theories and Techniques*, 58(6):1532–1542, 2010.

[92] F. Medina, F. Mesa, J. A. Ruiz-Cruz, J. M. Rebollar, and J. R. Montejo-Garai. Study of extraordinary transmission in a circular waveguide system. *IEEE Transactions on Microwave Theory and Techniques*, 58(6):1532–1542, 2010.

[93] E. Abbe. Beiträge zur theorie des mikroskops und der mikroskopischen wahrnehmung. *Archiv für Mikroskopische Anatomie*, 9(1):413–418, 1873.

[94] E. Abbe. A contribution to the theory of the microscope and the nature of microscopic vision. *Proceedings of the Bristol Naturalists' Society*, 1:200–261, 1874.

[95] H. Helmholtz. On the limits of the optical capacity of the microscope. *The Monthly Microscopical Journal*, 16:15–39, 1876.

[96] H. Furukawa and S. Kawata. Local field enhancement with an apertureless near-field-microscope probe. *Optics Communications*, 148(4-6):221–224, 1998.

[97] J. T. Krug, E. J. Sanchez, and X. S. Xie. Design of near-field optical probes with optimal field enhancement by finite difference time domain electromagnetic simulation. *Journal of Chemical Physics*, 116(24):10895–10901, 2002.

[98] E. J. Sanchez, L. Novotny, and X. S. Xie. Near-field fluorescence microscopy based on two-photon excitation with metal tips. *Physical Review Letters*, 82(20):4014–4017, 1999.

[99] A. Hartschuh, E. J. Sanchez, X. S. Xie, and L. Novotny. High-resolution near-field Raman microscopy of single-walled carbon nanotubes. *Physical Review Letters*, 90(9), MAR 7 2003.

[100] J. M. Gerton, L. A. Wade, G. A. Lessard, Z. Ma, and S. R. Quake. Tip-enhanced fluorescence microscopy at 10 nanometer resolution. *Physical Review Letters*, 93(18):180801, 2004.

[101] V. V. Protasenko and A. C. Gallagher. Apertureless near-field scanning optical microscopy of single molecules. *Nano Letters*, 4(7):1329–1332, 2004.

[102] R. Esteban, R. Vogelgesang, J. Dorfmueller, A. Dmitriev, C. Rockstuhl, C. Etrich, and K. Kern. Direct near-field optical imaging of higher order plasmonic resonances. *Nano Letters*, 8(10):3155–3159, 2008.

[103] A. Weber-Bargioni, A. Schwartzberg, M. Schmidt, B. Harteneck, D. F. Ogletree, P. J. Schuck, and S. Cabrini. Functional plasmonic antenna scanning probes fabricated by induced-deposition mask lithography. *Nanotechnology*, 21(6), 2010.

[104] P. Hoffmann, B. Dutoit, and R. P. Salathé. Comparison of mechanically drawn and protection layer chemically etched optical fiber tips. *Ultramicroscopy*, 61(1):165–170, 1995.

[105] D. Zeisel, S. Nettesheim, B. Dutoit, and R. Zenobi. Pulsed laser-induced desorption and optical imaging on a nanometer scale with scanning near-field microscopy using chemically etched fiber tips. *Applied Physics Letters*, 68:2491, 1996.

[106] T. Yatsui, M. Kourogi, and M. Ohtsu. Increasing throughput of a near-field optical fiber probe over 1000 times by the use of a triple-tapered structure. *Applied Physics Letters*, 73:2090, 1998.

[107] T. Yatsui, K. Itsumi, M. Kourogi, and M. Ohtsu. Metallized pyramidal silicon probe with extremely high throughput and resolution capability for optical near-field technology. *Applied Physics Letters*, 80(13):2257–2259, 2002.

[108] Y. Wang, W. Srituravanich, C. Sun, and X. Zhang. Plasmonic nearfield scanning probe with high transmission. *Nano Letters*, 8(9):3041–3045, 2008.

[109] T. H. Taminiau, R. J. Moerland, F. B. Segerink, L. Kuipers, and N. F. van Hulst. $\lambda/4$ resonance of an optical monopole antenna probed by single molecule fluorescence. *Nano Letters*, 7(1):28–33, 2007.

[110] M. Mivelle, I. A. Ibrahim, F. Baida, G. W. Burr, D. Nedeljkovic, D. Charraut, J. Y. Rauch, R. Salut, and T. Grosjean. Bowtie nano-aperture as interface between near-fields and a single-mode fiber. *Optics Express*, 18(15):15964–15974, 2010.

[111] A. Weber-Bargioni, A. Schwartzberg, M. Cornaglia, A. Ismach, J. J. Urban, Y. Pang, R. Gordon, J. Bokor, M. B. Salmeron, D. F. Ogletree, P. Ashby, S. Cabrini, and P. J. Schuck. Hyperspectral nanoscale imaging on dielectric substrates with coaxial optical antenna scan probes. *Nano Letters*, 11(3):1201–1207, 2011.

[112] D. Li and R. Gordon. Electromagnetic transmission resonances for a single annular aperture in a metal plate. *Physical Review A*, 82(4):041801, 2010.

[113] B. Heshmat, D. Li, T. E. Darcie, and R. Gordon. Tuning plasmonic resonances of an annular aperture in metal plate. *Optics Express*, 19(7):5912–5923, 2011.

[114] P. W. Smith, A. Ashkin, and W. J. Tomlinson. Four-wave mixing in an artificial kerr medium. *Optics Letters*, 6(6):284–286, 1981.

[115] I. Brevik. Experiments in phenomenological electrodynamics and the electromagnetic energy-momentum tensor. *Physics Reports*, 52(3):133–201, 1979.

[116] R. F. Marchington, M. Mazilu, S. Kuriakose, V. Garces-Chavez, P. J. Reece, T. F. Krauss, M. Gu, and K. Dholakia. Optical deflection and sorting of microparticles in a near-field optical geometry. *Optics Express*, 16(6):3712–3726, 2008.

[117] A. Rohrbach and E. H. K. Stelzer. Optical trapping of dielectric particles in arbitrary fields. *Journal of the Optical Society of America A*, 18(4):839–853, 2001.

[118] D. G. Grier. A revolution in optical manipulation. *Nature*, 424(6950):810–816, 2003.

[119] M. Dienerowitz, M. Mazilu, P. J. Reece, T. F. Krauss, and K. Dholakia. Optical vortex trap for resonant confinement of metal nanoparticles. *Optics Express*, 16(7):4991–4999, 2008.

[120] M. I. Stockman. Nanofocusing of optical energy in tapered plasmonic waveguides. *Physical Review Letters*, 93(13):137404, 2004.

[121] A. N. Grigorenko, N. W. Roberts, M. R. Dickinson, and Y. Zhang. Nanometric optical tweezers based on nanostructured substrates. *Nature Photonics*, 2(6):365–370, 2008.

[122] M. Righini, P. Ghenuche, S. Cherukulappurath, V. Myroshnychenko, F. J. García de Abajo, and R. Quidant. Nano-optical trapping of rayleigh particles and escherichia coli bacteria with resonant optical antennas. *Nano Letters*, 9(10):3387–3391, 2009.

[123] F. Vollmer and S. Arnold. Whispering-gallery-mode biosensing: label-free detection down to single molecules. *Nature Methods*, 5(7):591–596, 2008.

[124] F. Vollmer, S. Arnold, and D. Keng. Single virus detection from the reactive shift of a whispering-gallery mode. *Proceedings of the National Academy of Sciences*, 105(52):20701–20704, 2008.

[125] T. Lu, H. Lee, T. Chen, S. Herchak, J. H. Kim, S. E. Fraser, R. C. Flagan, and K. Vahala. High sensitivity nanoparticle detection using optical microcavities. *Proceedings of the National Academy of Sciences*, 108(15):5976, 2011.

[126] E. S. Kwak, T. D. Onuta, D. Amarie, R. Potyrailo, B. Stein, S. C. Jacobson, W. L. Schaich, and B Dragnea. Optical trapping with integrated near-field apertures. *Journal of Physical Chemistry B*, 108(36):13607–13612, 2004.

[127] E. Ostuni, R. G. Chapman, M. N. Liang, G. Meluleni, G. Pier, D. E. Ingber, and G. M. Whitesides. Self-assembled monolayers that resist the adsorption of proteins and the adhesion of bacterial and mammalian cells. *Langmuir*, 17(20):6336–6343, 2001.

[128] D. C. Carter and J. X. Ho. Structure of serum albumin. *Advances in Protein Chemistry*, 45:153–204, 1994.

[129] D. Yu, B. Blankert, J.C. Viré, and J. M. Kauffmann. Biosensors in drug discovery and drug analysis. *Analytical Letters*, 38(11):1687–1701, 2005.

[130] P. B. Luppa, L. J. Sokoll, and D. W. Chan. Immunosensors–principles and applications to clinical chemistry. *Clinica Chimica Acta*, 314(1-2):1–26, 2001.

[131] Q. Min, M. J. L. Santos, E. M. Girotto, A. G. Brolo, and R. Gordon. Localized raman enhancement from a double-hole nanostructure in a metal film. *Journal of Physical Chemistry C*, 112(39):15098–15101, 2008.

[132] Y. Liu and S. Blair. Fluorescence enhancement from an array of subwavelength metal apertures. *Optics Letters*, 28(7):507–509, 2003.

[133] Y. Liu and S. Blair. Fluorescence transmission through 1-d and 2-d periodic metal films. *Optics Express*, 12:3686 – 3693, 2004.

[134] D. Gérard, J. Wenger, N. Bonod, E. Popov, H. Rigneault, F. Mahdavi, S. Blair, J. Dintinger, and T. W. Ebbesen. Nanoaperture-enhanced fluorescence: Towards higher detection rates with plasmonic metals. *Physical Review B*, 77(4):045413, 2008.

[135] E. Ostuni, R. G. Chapman, M. N. Liang, G. Meluleni, G. Pier, D. E. Ingber, and G. M. Whitesides. Self-assembled monolayers that resist the adsorption of proteins and the adhesion of bacterial and mammalian cells. *Langmuir*, 17(20):6336–6343, 2001.

[136] A. Van Der Horst and N. R. Forde. Power spectral analysis for optical trap stiffness calibration from high-speed camera position detection with limited bandwidth. *Optics Express*, 18(8):7670–7677, 2010.

[137] MicroChem. NANO^{TM} PMMA and Copolymer. http://www.microchem.com/pdf/PMMA_Data_Sheet.pdf.

[138] D. R. Solli, C. F. McCormick, R. Y. Chiao, and J. M. Hickmann. Birefringence in two-dimensional bulk photonic crystals applied to the construction of quarter waveplates. *Optics Express*, 11(2):125 – 133, 2003.

[139] D. R. Solli, C. F. McCormick, R. Y. Chiao, and J. M. Hickmann. Experimental demonstration of photonic crystal waveplates. *Applied Physics Letters*, 82(7):1036 – 1038, 2003.

[140] Y. Inoue, Y. Ohmori, M. Kawachi, S. Ando, T. Sawada, and H. Takahashi. Polarization mode converter with polyimide half waveplate in silica-based planar lightwave circuits. *IEEE Photonics Technology Letters*, 6:626–628, 1994.

[141] E. M. Korenic, S. D. Jacobs, J. K. Houghton, A. Schmid, and F. Kreuzer. Nematic polymer liquid-crystal wave plate for high power lasers at 1054-nm. *Applied Optics*, 33:1889–1899, 1994.

[142] A. M. Radojevic, R. M. Osgood, M. Levy, A. Kumar, and H. Bakhru. Zeroth-order half-wave plates of $LiNbO_3$ for integrated optics applications at 1.55 μm. *IEEE Photonics Technology Letters*, 12:1653–1655, 2000.

[143] E. N. Economou. Surface plasmons in thin films. *Physical Review*, 182:539–554, 1969.

[144] H. S. Cole and R. A. Kashnow. New reflective dichroic liquid-crystal display device. *Applied Physics Letters*, 30:619–621, 1977.

[145] S. J. Jiang, Z. Q. Pan, M. Dagenais, R. A. Morgan, and K. Kojima. High-frequency polarization self-modulation in vertical-cavity surface-emitting lasers. *Applied Physics Letters*, 63:3545–3547, 1993.

[146] S. Nie and S. R. Emory. Probing single molecules and single nanoparticles by surface-enhanced raman scattering. *Science*, 275(5303):1102, 1997.

[147] K. Kneipp, Y. Wang, H. Kneipp, L. T. Perelman, I. Itzkan, R. R. Dasari, and M. S. Feld. Single molecule detection using surface-enhanced raman scattering (SERS). *Physical Review Letters*, 78(9):1667–1670, 1997.

[148] C. E. Talley, J. B. Jackson, C. Oubre, N. K. Grady, C. W. Hollars, S. M. Lane, T. R. Huser, P. Nordlander, and N.J. Halas. Surface-enhanced raman scattering from individual au nanoparticles and nanoparticle dimer substrates. *Nano Letters*, 5(8):1569–1574, 2005.

[149] P. L. Stiles, J. A. Dieringer, N. C. Shah, and R. P. Van Duyne. Surface-enhanced raman spectroscopy. *Annual Review of Analytical Chemistry*, 1:601–626, 2008.

[150] A. E. Grow, L. L. Wood, J. L. Claycomb, and P. A. Thompson. New biochip technology for label-free detection of pathogens and their toxins. *Journal of Microbiological Methods*, 53(2):221–233, 2003.

[151] F. De Angelis, M. Patrini, G. Das, I. Maksymov, M. Galli, L. Businaro, L.C. Andreani, and E. Di Fabrizio. A hybrid plasmonic-photonic nanodevice for label-free detection of a few molecules. *Nano Letters*, 8(8):2321–2327, 2008.

[152] X. Zhang, M. A. Young, O. Lyandres, and R. P. Van Duyne. Rapid detection of an anthrax biomarker by surface-enhanced raman spectroscopy. *Journal of the American Chemical Society*, 127(12):4484–4489, 2005.

[153] J. Ni, R.J. Lipert, G.B. Dawson, and M.D. Porter. Immunoassay readout method using extrinsic raman labels adsorbed on immunogold colloids. *Analytical Chemistry*, 71(21):4903–4908, 1999.

[154] G. Seisenberger, M.U. Ried, T. Endreß, H. Büning, M. Hallek, and C. Bräuchle. Real-time single-molecule imaging of the infection pathway of an adeno-associated virus. *Science*, 294(5548):1929, 2001.

[155] A. Y. Shulman. Edge condition in diffraction theory and maximum enhancement of electromagnetic field in the near zone. *Physica Status Solidi A*, 175(1):279 – 287, 1999.

[156] H. Shin, P. B. Catrysse, and S. Fan. Effect of the plasmonic dispersion relation on the transmission properties of subwavelength cylindrical holes. *Physical Review B*, 72(8):085436, 2005.

[157] R. Ulrich. Far-infrared properties of metallic mesh and its complementary structure. *Infrared Physics*, 7(1):37–&, 1967.

[158] N. Marcuvitz. *Waveguide Handbook*. Peter Peregrinus Ltd., London, UK, 1984.

[159] I. Stevanovic, P. Crespo-Valero, and J. R. Mosig. An integral-equation technique for solving thick irises in rectangular waveguides. *IEEE Transaction on Microwave Theory and Technology*, 54(1):189 – 197, 2006.

[160] M. Golosovsky and D. Davidov. Novel millimeter-wave near-field resistivity microscope. *Applied Physics Letters*, 68(11):1579–1581, 1996.

[161] J. W. Lee, M. A. Seo, J. Y. Sohn, Y. H. Ahn, D. S. Kim, S. C. Jeoung, C. Lienau, and Q. H. Park. Invisible plasmonic meta-materials through impedance matching to vacuum. *Optics Express*, 13(26):10681–10687, 2005.

[162] C. J. Bouwkamp. Diffraction theory. *Reports on Progress in Physics*, 17:35, 1954.

[163] A. J. L. Adam, J. M. Brok, M. A. Seo, K. J. Ahn, D. S. Kim, J. H. Kang, Q. H. Park, M. Nagel, and P. C. M. Planken. Advanced terahertz electric near-field measurements at sub-wavelength diameter metallic apertures. *Optics Express*, 16(10):7407 – 7417, 2008.

[164] J. W. Lee, M. A. Seo, D. J. Park, and D. S. Kim. Shape resonance omnidirectional terahertz filters with near-unity transmittance. *Optics Express*, 14(3):1253 – 1259, 2006.

[165] E. X. Jin and X. Xu. Plasmonic effects in near-field optical transmission enhancement through a single bowtie-shaped aperture. *Applied Physics B*, 84(1):3 – 9, 2006.

[166] Y. Liu, J. Bishop, L. Williams, S. Blair, and J. Herron. Biosensing based upon molecular confinement in metallic nanocavity arrays. *Nanotechnology*, 15:1368, 2004.

[167] A. P. Hibbins and J. R. Sambles. Squeezing millimeter waves into microns. *Physical Review Letters*, 92(14):143904, 2004.

[168] M. Silveirinha and N. Engheta. Tunneling of electromagnetic energy through subwavelength channels and bends using epsilon-near-zero materials. *Physical Review Letters*, 97(15):157403, 2006.

[169] A. Rauschenbeutel, G. Nogues, S. Osnaghi, P. Bertet, M. Brune, J. M. Raimond, and S. Haroche. Coherent operation of a tunable quantum phase gate in cavity qed. *Physical Review Letters*, 83(24):5166 – 5169, 1999.

[170] D. W. Pohl, W. Denk, and M. Lanz. Optical stethoscopy: Image recording with resolution $\lambda/20$. *Applied Physics Letters*, 44(7):651–653, 1984.

[171] E. Betzig and R.J. Chichester. Single molecules observed by near-field scanning optical microscopy. *Science*, 262(5138):1422, 1993.

[172] P. Yang, H. Yan, S. Mao, R. Russo, J. Johnson, R. Saykally, N. Morris, J. Pham, R. He, and H.J. Choi. Controlled growth of zno nanowires and their optical properties. *Advanced Functional Materials*, 12(5):323, 2002.

[173] M. Abashin, P. Tortora, I. Märki, U. Levy, W. Nakagawa, L. Vaccaro, H. Herzig, and Y. Fainman. Near-field characterization of propagating optical modes in photonic crystal waveguides. *Optics Express*, 14(4):1643–1657, 2006.

[174] E. Descrovi, T. Sfez, M. Quaglio, D. Brunazzo, L. Dominici, F. Michelotti, H.P. Herzig, O.J.F. Martin, and F. Giorgis. Guided bloch surface waves on ultrathin polymeric ridges. *Nano Letters*, 10(6):2087–2091, 2010.

[175] C. A. Michaels, X. Gu, D. B. Chase, and S. J. Stranick. Near-field infrared imaging and spectroscopy of a thin film polystyrene/poly (ethyl acrylate) blend. *Applied Spectroscopy*, 58(3):257–263, 2004.

[176] E. Betzig, J. K. Trautman, R. Wolfe, E. M. Gyorgy, P. L. Finn, M. H. Kryder, and C. H. Chang. Near-field magneto-optics and high density data storage. *Applied Physics Letters*, 61(2):142–144, 1992.

[177] J. Jersch, F. Demming, L. J. Hildenhagen, and K. Dickmann. Field enhancement of optical radiation in the nearfield of scanning probe microscope tips. *Applied Physics A*, 66(1):29–34, 1998.

[178] S. Sun and G. J. Leggett. Matching the resolution of electron beam lithography by scanning near-field photolithography. *Nano Letters*, 4(8):1381–1384, 2004.

[179] G. A. Valaskovic, M. Holton, and G. H. Morrison. Parameter control, characterization, and optimization in the fabrication of optical fiber near-field probes. *Applied Optics*, 34(7):1215–1228, 1995.

[180] J. A. Veerman, A. M. Otter, L. Kuipers, and N. F. Van Hulst. High definition aperture probes for near-field optical microscopy fabricated by focused ion beam milling. *Applied Physics Letters*, 72:3115, 1998.

[181] A. Sundaramurthy, P. J. Schuck, N. R. Conley, D. P. Fromm, G. S. Kino, and W. E. Moerner. Toward nanometer-scale optical photolithography: Utilizing the near-field of bowtie optical nanoantennas. *Nano Letters*, 6(3):355–360, 2006.

[182] L. Novotny and S. J. Stranick. Near-field optical microscopy and spectroscopy with pointed probes. *Annual Review of Physical Chemistry*, 57:303–331, 2006.

[183] F. Renna, D. Cox, and G. Brambilla. Efficient sub-wavelength light confinement using surface plasmon polaritons in tapered fibers. *Optics Express*, 17(9):7658–7663, 2009.

[184] J. H. Kang, J. H. Choe, D. S. Kim, and Q. H. Park. Substrate effect on aperture resonances in a thin metal film. *Optics Express*, 17(18):15652–15658, 2009.

[185] D. Richards, R. G. Milner, F. Huang, and F. Festy. Tip-enhanced raman microscopy: Practicalities and limitations. *Journal of Raman Spectroscopy*, 34(9):663–667, 2003.

[186] J. Wenger, D. Gérard, H. Aouani, H. Rigneault, B. Lowder, S. Blair, E. Devaux, and T. W. Ebbesen. Nanoaperture-enhanced signal-to-noise ratio in fluorescence correlation spectroscopy. *Analytical Chemistry*, 81(2):834–839, 2009.

[187] J. C. Johnson, H. Yan, R. D. Schaller, P. B. Petersen, P. Yang, and R. J. Saykally. Near-field imaging of nonlinear optical mixing in single zinc oxide nanowires. *Nano Letters*, 2(4):279–283, 2002.

[188] K. Imura and H. Okamoto. Properties of photoluminescence from single gold nanorods induced by near-field two-photon excitation. *Journal of Physical Chemistry C*, 113(27):11756–11759, 2009.

[189] H. Yin, M. D. Wang, K. Svoboda, R. Landick, S. M. Block, and J. Gelles. Transcription against an applied force. *Science*, 270(5242), 1995.

[190] L. Huang and O. J. F. Martin. Reversal of the optical force in a plasmonic trap. *Optics Letters*, 33(24):3001–3003, 2008.

[191] M. Nieto-Vesperinas, P. C. Chaumet, and A. Rahmani. Near-field photonic forces. *Philosophical Transactions of the Royal Society of London Series A - Mathematical Physical and Enginnering Sciences*, 362(1825):2889–2890, 2004.

[192] K. Okamoto and S. Kawata. Radiation force exerted on subwavelength particles near a nanoaperture. *Physical Review Letters*, 83(22):4534–4537, 1999.

[193] R. Quidant, D. Petrov, and G. Badenes. Radiation forces on a Rayleigh dielectric sphere in a patterned optical near field. *Optics Letters*, 30(9):1009–1011, 2005.

[194] M. Righini, C. Girard, and R. Quidant. Light-induced manipulation with surface plasmons. *Journal of Optics A*, 10(9), 2008.

[195] R. Sainidou and F. J. García de Abajo. Optically tunable surfaces with trapped particles in microcavities. *Physical Review Letters*, 101(13):136802, 2008.

[196] E. S. Kwak, T. D. Onuta, D. Amarie, R. Potyrailo, B. Stein, S. C. Jacobson, W. L. Schaich, and B. Dragnea. Optical trapping with integrated near-field apertures. *Journal of Physical Chemistry B*, 108(36):13607–13612, 2004.

[197] S. Arnold, D. Keng, S. I. Shopova, S. Holler, W. Zurawsky, and F. Vollmer. Whispering gallery mode carousel–a photonic mechanism for enhanced nanoparticle detection in biosensing. *Optics Express*, 17(8):6230–6238, 2009.

[198] C. S. Adams and E. Riis. Laser cooling and trapping of neutral atoms. *Progress in Quantum Electronics*, 21(1), 1997.

[199] P. W. H. Pinkse, T. Fischer, P. Maunz, and G. Rempe. Trapping an atom with single photons. *Nature*, 404(6776):365–368, 2000.

[200] T. Iida and H. Ishihara. Theoretical study of the optical manipulation of semiconductor nanoparticles under an excitonic resonance condition. *Physical Review Letters*, 90(5), 2003.

[201] K. C. Neuman and S. M. Block. Optical trapping. *Review of Scientific Instruments*, 75(9):2787–2809, 2004.

[202] P. C. Chaumet, A. Rahmani, and M. Nieto-Vesperinas. Optical trapping and manipulation of nano-objects with an apertureless probe. *Physical Review Letters*, 88(12), 2002.

[203] F. V. Ignatovich, D. Topham, and L. Novotny. Optical detection of single nanoparticles and viruses. *IEEE Journal of Selected Topics in Quantum Electronics*, 12(6, Part 1):1292–1300, 2006.

[204] M. Krishnan, N. Mojarad, P. Kukura, and V. Sandoghdar. Geometry-induced electrostatic trapping of nanometric objects in a fluid. *Nature*, 467(7316):692–695, 2010.

[205] P.E. Batson, A. Reyes-Coronado, R.G. Barrera, A. Rivacoba, P.M. Echenique, and J. Aizpurua. Plasmonic nano-billiards: Controlling nanoparticle movement using forces induced by swift electrons. *Nano Letters*, 11(8):3388–3393, 2011.

[206] M. J. Guffey and N. F. Scherer. All-optical patterning of au nanoparticles on surfaces using optical traps. *Nano Letters*, 10(11):4302–4308, 2010.

[207] C. T. Lee Jr, K. A. Smith, and T. A. Hatton. Photocontrol of protein folding: The interaction of photosensitive surfactants with bovine serum albumin. *Biochemistry*, 44(2):524–536, 2005.

[208] Y. Moriyama, E. Watanabe, K. Kobayashi, H. Harano, E. Inui, and K. Takeda. Secondary structural change of bovine serum albumin in thermal denaturation up to 130 degrees C and protective effect of sodium dodecyl sulfate on the change. *Journal of Physical Chemistry B*, 112(51):16585–16589, 2008.

[209] J. N. Anker, W. P. Hall, O. Lyandres, N. C. Shah, J. Zhao, and R. P. Van Duyne. Biosensing with plasmonic nanosensors. *Nature Materials*, 7(6):442–453, 2008.

[210] D. Kim and E. J. Sim. Segmented coupled-wave analysis of a curved wire-grid polarizer. *Journal of the Optical Society of America A*, 25(3):558 – 565, 2008.

[211] P. C. Deguzman and G. P. Nordin. Stacked subwavelength gratings as circular polarization filters. *Applied Optics*, 40(31):5731 – 5737, 2001.

[212] J. B. Young, H. A. Graham, and E. W. Peterson. Wire grid infrared polarizer. *Applied Optics*, 4(8):1023–1026, 1965.

[213] P. K. Cheo and C. D. Bass. Efficient wire-grid duplexer polarizer for CO_2 lasers. *Applied Physics Letters*, 18(12):565–567, 1971.

[214] J. J. Wang, W. Zhang, X. Deng, J. D. Deng, F. Liu, P. Sciortino, and L. Chen. High-performance nanowire-grid polarizers. *Optics Letters*, 30(2):195 – 197, 2005.

[215] J. J. Wang, J. D. Deng, X. G. Deng, F. Liu, P. Sciortino, A. Nikolov L. Chen, and A. Graham. Innovative high-performance nanowire-grid polarizers and integrated isolators. *IEEE Journal of Selected Topics in Quantum Electronics*, 11(1):241 – 253, 2005.

[216] J. J. Wang, F. Liu, and X. G. Deng. Monolithically integrated circular polarizers with two-layer nano-gratings fabricated by imprint lithography. *Journal of Vacuum Science and Technology B*, 23(6):3164 – 3167, 2005.

[217] D. Kim. Polarization characteristics of a wire-grid polarizer in a rotating platform. *Applied Optics*, 44(8):1366 – 1371, 2005.

[218] Z. Y. Yang and Y. F. Lu. Broadband nanowire-grid polarizers in ultraviolet-visible near-infrared regions. *Optical Express*, 15(15):9510 – 9519, 2007.

[219] A. S. Vengurlekar. Polarization dependence of optical properties of metallodielectric gratings with subwavelength grooves in classical and conical mounts. *Journal of Applied Physics*, 104(023109):023109–1 – 023109–8, 2008.

[220] H. Tamada, T. Doumuki, T. Yamaguchi, and S. Matsumoto. Al wire-grid polarizer using the s-polarization resonance effect at the 0.8-mu m-wavelength band. *Optics Letters*, 22(6):419 – 421, 1997.

[221] Y. Ekinci, H. H. Solak, C. David, and H. Sigg. Bilayer al wire-grids as broadband and high-performance polarizers. *Optics Express*, 14(6):2323 – 2334, 2006.

[222] X. Liu, X. Deng, Jr. P. Sciortino, M. Buonanno, F. Walters, R. Varghese, J. Bacon, L. Chen, N. O'Brien, and J. J. Wang. Large area, 38 nm half-pitch grating fabrication by using atomic spacer lithography from aluminum wire grids. *Nano Letters*, 6(12):2723 – 2727, 2006.

[223] J. J. Wang, L. Chen, XM. Liu, P. Sciortino, F. Liu, F. Walters, and X. G. Deng. 30-nm-wide aluminum nanowire grid for ultrahigh contrast and transmittance polarizers made by uv-nanoimprint lithography. *Applied Physics Letters*, 89(141105):141105–1 – 141105–3, 2006.

[224] S. I. Bozhevolnyi, V. S. Volkov, E. Devaux, and T. W. Ebbesen. Channel plasmon-polariton guiding by subwavelength metal grooves. *Physical Review Letters*, 95(046802):046802–1 – 046802–4, 2005.

[225] L. Qin, S. Park, L. Huang, and C.A. Mirkin. On-wire lithography. *Science*, 309(5731):113, 2005.

[226] C. L. Haynes and R. P. Van Duyne. Nanosphere lithography: A versatile nanofabrication tool for studies of size-dependent nanoparticle optics. *Journal of Physical Chemistry B*, 105(24):5599–5611, 2001.

[227] R. Jin, Y. W. Cao, C. A. Mirkin, K. L. Kelly, G. C. Schatz, and J. G. Zheng. Photoinduced conversion of silver nanospheres to nanoprisms. *Science*, 294(5548):1901, 2001.

[228] M. Fleischmann, P. J. Hendra, and A. J. McQuillan. Raman spectra of pyridine adsorbed at a silver electrode. *Chemical Physics Letters*, 26(2):163–166, 1974.

[229] M. Moskovits. Surface-enhanced spectroscopy. *Reviews of Modern Physics*, 57(3):783, 1985.

[230] L. C. T. Shoute. Multilayer substrate-mediated tuning resonance of plasmon and SERS EF of nanostructured silver. *ChemPhysChem*, 11(12):2539–2545, 2010.

[231] L. C. T. Shoute, A. J. Bergren, A. M. Mahmoud, K. D. Harris, and R. L. McCreery. Optical interference effects in the design of substrates for surface-enhanced raman spectroscopy. *Applied spectroscopy*, 63(2):133–140, 2009.

[232] H. C. Kim and X. Cheng. SERS-active substrate based on gap surface plasmon polaritons. *Optics Express*, 17(20):17234–17241, 2009.

[233] L. Du, X. Zhang, T. Mei, and X. Yuan. Localized surface plasmons, surface plasmon polaritons, and their coupling in 2d metallic array for SERS. *Optics Express*, 18(3):1959–1965, 2010.

[234] J. M. Montgomery, A. Imre, U. Welp, V. Vlasko-Vlasov, and S. K. Gray. SERS enhancements via periodic arrays of gold nanoparticles on silver film structures. *Optics Express*, 17(10):8669–8675, 2009.

[235] K. H. Drexhage, M. Fleck, F. Shäfer, and W. Sperling. Beeinflussung der fluoreszenz eines europium-chelates durch einen spiegel. *Berichte der Bunsen-Gesellschaft Physical Chemistry Chemical Physics*, 20:1179, 1966.

[236] R. M. Amos and W. L. Barnes. Modification of the spontaneous emission rate of Eu^{3+} ions close to a thin metal mirror. *Physical Review B*, 55(11):7249–7254, 1997.

[237] K. H. Drexhage. Influence of a dielectric interface on fluorescence decay time. *Journal of Luminescence*, 1:693–701, 1970.

[238] R. R. Chance, A. Prock, and R. Silbey. Molecular fluorescence and energy transfer near interfaces. *Advances in Chemical Physics*, pages 1–65, 1978.

[239] J. A. Dieringer, B. Robert, I. I. Lettan, K. A. Scheidt, and R. P. Van Duyne. A frequency domain existence proof of single-molecule surface-enhanced raman spectroscopy. *Journal of the American Chemical Society*, 129(51):16249–16256, 2007.

[240] J. Zhao, J. A. Dieringer, X. Zhang, G. C. Schatz, and R. P. Van Duyne. Wavelength-scanned surface-enhanced resonance raman excitation spectroscopy. *Journal of Physical Chemistry C*, 112(49):19302–19310, 2008.

[241] A. D. McFarland, M. A. Young, J. A. Dieringer, and R. P. Van Duyne. Wavelength-scanned surface-enhanced raman excitation spectroscopy. *Journal of Physical Chemistry B*, 109(22):11279–11285, 2005.

[242] M. Born, E. Wolf, and A.B. Bhatia. *Principles of Optics: Electromagnetic Theory of Propagation, Interference and Diffraction of Light*. Cambridge University Press, 1999.

[243] B. Nikoobakht and M. A. El-Sayed. Preparation and growth mechanism of gold nanorods (nrs) using seed-mediated growth method. *Chemistry of Materials*, 15(10):1957–1962, 2003.

[244] M. Kerker, D. S. Wang, and H. Chew. Surface enhanced raman scattering (SERS) by molecules adsorbed at spherical particles: Errata. *Applied Optics*, 19(24):4159–4174, 1980.

[245] E. C. Le Ru, M. Meyer, and P. G. Etchegoin. Proof of single-molecule sensitivity in surface enhanced raman scattering (SERS) by means of a two-analyte technique. *Journal of Physical Chemistry B*, 110(4):1944–1948, 2006.

[246] T. H. Taminiau, F. D. Stefani, and N. F. van Hulst. Enhanced directional excitation and emission of single emitters by a nano-optical Yagi-Uda antenna. *Optics Express*, 16(14):10858–10866, 2008.

[247] T. Kosako, Y. Kadoya, and H. F. Hofmann. Directional control of light by a nano-optical Yagi-Uda antenna. *Nature Photonics*, 4(5):312–315, 2010.

[248] P. Bharadwaj, B. Deutsch, and L. Novotny. Optical antennas. *Advances in Optics and Photonics*, 1(3):438–483, 2009.

[249] H. Yagi. Beam transmission of ultra short waves. *Proceedings of the Institute of Radio Engineers*, 16(6):715–740, 1928.

[250] A. Hartschuh, H. Qian, C. Georgi, M. Böhmler, and L. Novotny. Tip-enhanced near-field optical microscopy of carbon nanotubes. *Analytical and Bioanalytical Chemistry*, 394(7):1787–1795, 2009.

[251] S. Kawata and Y. Inouye. Scanning probe optical microscopy using a metallic probe tip. *Ultramicroscopy*, 57(2-3):313–317, 1995.

[252] C. Fumeaux, M. A. Gritz, I. Codreanu, W. L. Schaich, F. J. González, and G. D. Boreman. Measurement of the resonant lengths of infrared dipole antennas. *Infrared Physics & Technology*, 41(5):271–281, 2000.

[253] F. Neubrech, T. Kolb, R. Lovrincic, G. Fahsold, A. Pucci, J. Aizpurua, TW Cornelius, ME Toimil-Molares, R. Neumann, and S. Karim. Resonances of individual metal nanowires in the infrared. *Applied Physics Letters*, 89:253104, 2006.

[254] L. Novotny. Effective wavelength scaling for optical antennas. *Physical Review Letters*, 98(26):266802, 2007.

[255] S. B. Hasan, R. Filter, A. Ahmed, R. Vogelgesang, R. Gordon, C. Rockstuhl, and F. Lederer. Relating localized nanoparticle resonances to an associated antenna problem. *Physical Review B*, 84(19):195405, 2011.

[256] J. N. Farahani, D. W. Pohl, H. J. Eisler, and B. Hecht. Single quantum dot coupled to a scanning optical antenna: A tunable superemitter. *Physical Review Letters*, 95(1), 2005.

[257] S. Kühn, U. Håkanson, L. Rogobete, and V. Sandoghdar. Enhancement of single-molecule fluorescence using a gold nanoparticle as an optical nanoantenna. *Physical Review Letters*, 97(1):17402, 2006.

[258] T. H. Taminiau, F. D. Stefani, F. B. Segerink, and N. F. Van Hulst. Optical antennas direct single-molecule emission. *Nature Photonics*, 2(4):234–237, 2008.

[259] A. Sundaramurthy, P. J. Schuck, N. R. Conley, D. P. Fromm, G. S. Kino, and W. E. Moerner. Toward nanometer-scale optical photolithography: utilizing the near-field of bowtie optical nanoantennas. *Nano Letters*, 6(3):355–360, 2006.

[260] H. Wang, D. W. Brandl, F. Le, P. Nordlander, and N. J. Halas. Nanorice: A hybrid plasmonic nanostructure. *Nano Letters*, 6(4):827–832, 2006.

[261] P. Anger, P. Bharadwaj, and L. Novotny. Enhancement and quenching of single-molecule fluorescence. *Physical Review Letters*, 96(11):113002, 2006.

[262] S. Graells, S. Aćimović, G. Volpe, and R. Quidant. Direct growth of optical antennas using e-beam-induced gold deposition. *Plasmonics*, 5(2):135–139, 2010.

[263] E. Ozbay. Plasmonics: merging photonics and electronics at nanoscale dimensions. *Science*, 311(5758):189, 2006.

[264] S. Wedge, J. A. E. Wasey, W. L. Barnes, and I. Sage. Coupled surface plasmon-polariton mediated photoluminescence from a top-emitting organic light-emitting structure. *Applied Physics Letters*, 85:182, 2004.

[265] R. Corkish, M. A. Green, and T. Puzzer. Solar energy collection by antennas. *Solar Energy*, 73(6):395–401, 2002.

[266] S. Pillai, K. R. Catchpole, T. Trupke, and M. A. Green. Surface plasmon enhanced silicon solar cells. *Journal of Applied Physics*, 101(9), 2007.

[267] H. R. Stuart and D. G. Hall. Absorption enhancement in silicon-on-insulator waveguides using metal island films. *Applied Physics Letters*, 69(16):2327–2329, 1996.

[268] L. Tang, S. E. Kocabas, S. Latif, A. K. Okyay, D. S. Ly-Gagnon, K. C. Saraswat, and D. A. B. Miller. Nanometre-scale germanium photodetector enhanced by a near-infrared dipole antenna. *Nature Photonics*, 2(4):226–229, 2008.

[269] A. M. Marks. Device for conversion of light power to electric power, April 24 1984. US Patent 4,445,050.

[270] C. C. Neacsu, J. Dreyer, N. Behr, and M. B. Raschke. Scanning-probe raman spectroscopy with single-molecule sensitivity. *Physical Review B*, 73(19):193406, 2006.

[271] N. Liu, M.L. Tang, M. Hentschel, H. Giessen, and A.P. Alivisatos. Nanoantenna-enhanced gas sensing in a single tailored nanofocus. *Nature Materials*, 10(8):631–636, 2011.

[272] S. A. Maier. Plasmonic field enhancement and SERS in the effective mode volume picture. *Optics Express*, 14(5):1957–1964, 2006.

[273] H. Xu, E. J. Bjerneld, M. Käll, and L. Börjesson. Spectroscopy of single hemoglobin molecules by surface enhanced raman scattering. *Physical Review Letters*, 83(21):4357–4360, 1999.

[274] J. Kim, O. Benson, H. Kan, and Y. Yamamoto. A single-photon turnstile device. *Nature*, 397(6719):500–503, 1999.

[275] B. Lounis and W. E. Moerner. Single photons on demand from a single molecule at room temperature. *Nature*, 407(6803):491–493, 2000.

[276] T. Kalkbrenner, U. Håkanson, A. Schädle, S. Burger, C. Henkel, and V. Sandoghdar. Optical microscopy via spectral modifications of a nanoantenna. *Physical Review Letters*, 95(20):200801, 2005.

[277] C. Höppener and L. Novotny. Antenna-based optical imaging of single ca2+ transmembrane proteins in liquids. *Nano Letters*, 8(2):642–646, 2008.

[278] T. Pakizeh and M. Kall. Unidirectional ultracompact optical nanoantennas. *Nano Letters*, 9(6):2343–2349, 2009.

[279] A. Alù and S. Maslovski. Power relations and a consistent analytical model for receiving wire antennas. *IEEE Transactions on Antennas and Propagation*, 58(5):1436–1448, 2010.

[280] A. Alù and N. Engheta. Tuning the scattering response of optical nanoantennas with nanocircuit loads. *Nature Photonics*, 2(5):307–310, 2008.

[281] T. J. Seok, A. Jamshidi, M. Kim, S. Dhuey, A. Lakhani, H. Choo, P. J. Schuck, S. Cabrini, A. M. Schwartzberg, and J. Bokor. Radiation engineering of optical antennas for maximum field enhancement. *Nano Letters*, 11(7):2606–2610, 2011.

Appendix A

Extraordinary Optical Transmission through a Small Hole in a Metal Waveguide Screen

Originally published:
Y. Pang, A. N. Hone, P. P. M. So, and R. Gordon. Total optical transmission through a small hole in a metal waveguide screen. Optics Express, 17(6):4433–4441, 2009.

ABSTRACT

We present the theory of total optical transmission through a small hole in metal waveguide screen. Unlike past works on extraordinary optical transmission using arrays, there is only a single hole; yet, the theory predicts total transmission for a perfect electric conductor (not normalized to the hole size) 100% transmission, regardless of how small the hole. This is very surprising considering the usual application of Bethe's theory to waveguide apertures. Comprehensive numerical simulations agree well with the theory and their modal-analysis supports the proposed evanescent-mode mechanism for total transmission. These simulations are extended to show the influence of realistic material response (including loss) at microwave and visible-infrared frequencies. Due to the strong resonant field localization and transmission from only a thin metal screen with a single hole, many promising applications arise for this phenomenon including filtering, sensing, plasma generation, nonlinear optics,

spectroscopy, heating, optical trapping, near-field microscopy and cavity quantum electrodynamics.

A.1 Introduction

In the past decade, Bethe's theory for the diffraction of light through a small hole in a metal film [16] has been challenged by the discovery of extraordinary optical transmission (EOT) through hole-arrays [1, 17]. Recently, Bethe's theory was extended to the array configuration and it showed 100% transmission at resonant wavelengths [2, 18]; therefore, total transmission for an array of holes is not a contradiction to Bethe's original work. It should be noted, however, that the original motivation of Bethe's work was not for arrays, but for "the effect of a small hole in a cavity" and "the effect of a small gap in a wave guide" [16].

Here we revisit the waveguide system and show that total electromagnetic transmission is possible from only a single aperture in a waveguide wall; this is very surprising considering the the usual application of Bethe's theory waveguides [88]. For the same configuration as considered here, the usual finding is that the transmission can be made arbitrarily small as the aperture size is reduced [88], with the limitation on effective hole-size coming from electromagnetic penetration into real materials [155, 156]. We demonstrate, both by theory and by comprehensive numerical calculations, that total transmission remains when the aperture size is reduced. In the past, we have suggested that the resonance can occur in the waveguide system (Sec. IIID of [2]), and here we extend the array theory of that work and present supporting calculations. A recent study of resonances in the array and waveguide systems provided an analysis of array and single aperture systems using numerical mode-matching calculations and a parametric circuit model [67]. The circuit description provides a nice interpretation of these results and can be traced back to early works of aperture arrays in screens [157]. Here we discuss the circuit interpretation of our model as well. The comprehensive numerical simulations are also extended to include the material response (including loss) at microwave and the visible-infrared frequencies.

In addition to its surprising relation to Bethe's original work, this phenomenon is interesting for applications across several disciplines. First, at the resonance frequency, all of the electromagnetic energy is squeezed into the aperture, allowing for enhanced interaction with matter at an extreme subwavelength scale. This has pos-

sible applications in many areas of physics, ranging from the generation of plasmas to cavity quantum electrodynamics. Second, the transmission resonance wavelength is sensitive to the polarizability of the aperture, so that small perturbations to the aperture will lead to large resonant frequency shifts that may be used for sensor applications. Third, the transmission resonance may be used as a compact waveguide filter. The results presented in this paper can be readily tested with existing methods, at least for the microwave regime where standard waveguide components exist.

A.2 Analysis

A.2.1 Analytic Theory

FigureA.1(a) shows the geometry of the structure under consideration: a waveguide with a transverse metal screen containing a hole at the center. For simplicity, the waveguide and the hole are considered to be square; however, this may be easily generalized to other configurations, for example, a rectangular waveguide with a circular aperture. The waveguide has side-length a and the aperture has side-length a_h. The lower-left corner of the screen is chosen to be the origin of the x-y-z coordinate system, with the z-axis pointing along the waveguide. A TE_{10} mode is incident from the negative z-direction.

The y-component of the electric field at the iris can be written as a Fourier decomposition of the waveguide modes:

$$E_y(x, y, z = 0^-) = 1 + \sum_{m,n} r_{mn} \sin \frac{m\pi x}{a} \cos \frac{n\pi y}{a} \tag{A.1}$$

on the incident side and

$$E_y(x, y, z = 0^+) = \sum_{m,n} t_{mn} \sin \frac{m\pi x}{a} \cos \frac{n\pi y}{a} \tag{A.2}$$

on the transmitting side. The time-harmonic convention we use here and throughout the paper is $e^{i\omega t}$ where i is the imaginary unit. Due to the boundary conditions, the fields on each side should be equal. For the excitation of modes with small m and n, the TM_{12} mode for example, the field of the mode have a slow variation in space. In the extremely small aperture limit, the field can be considered constant over the aperture region [2]. It is also noted that the y-polarized excitation will excite only

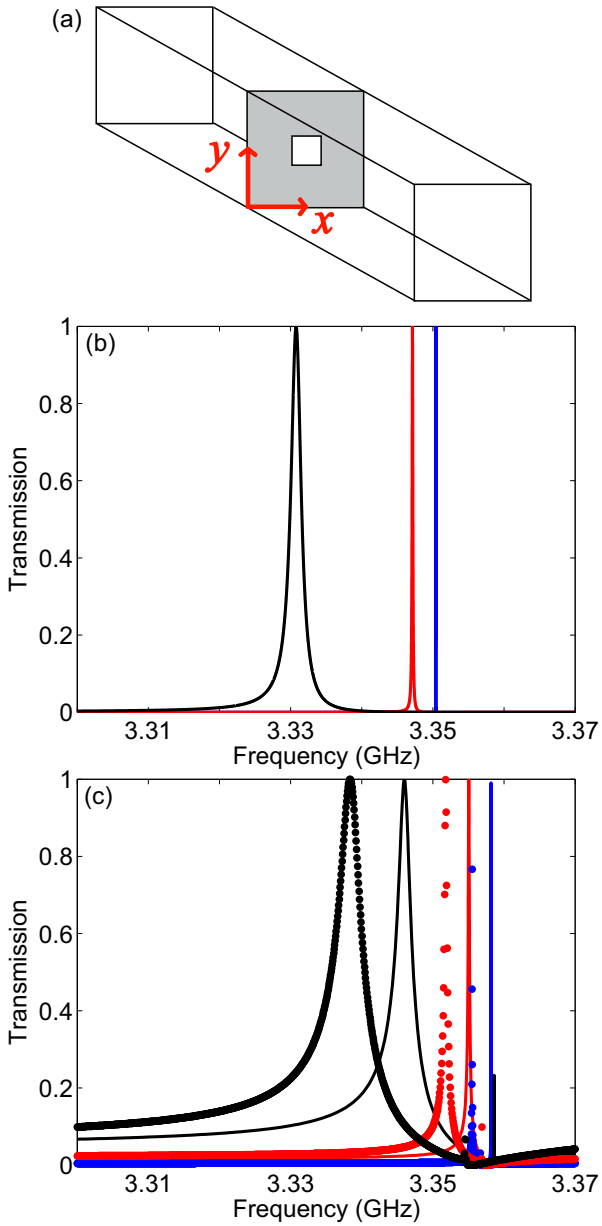

Figure A.1: (a) Schematic of square waveguide with a metal screen and a square aperture at the center of the screen. (b) Theoretical transmission spectrum of the TE_{10} mode through a perfect-electric conductor (PEC) screen with a square aperture at the center in a 10 cm wide square waveguide. Three results are shown in this graph with aperture width 1 cm, 1.5 cm and 2 cm, in blue, red and black. (c) Comprehensive numerical simulation showing transmission of the TE_{10} mode through equivalent structures as in (b), except for 1 mm metal screen-width. Simulations were done using a PEC metal (lines) and lossy aluminum (circles) as the material of the waveguide and the screen.

the TE_x waveguide modes, they do not have electric components in the x-direction and magnetic components in the y-direction. Moreover, the field should be zero at the surface of the PEC. By applying a Fourier decomposition to this field profile, the coefficients in Eq. I.2 can be found:

$$t_{mn} \simeq 2t_{10} \tag{A.3}$$

for $m, n \neq 0$ and

$$t_{m0} \simeq t_{10} \tag{A.4}$$

for $m \neq 0$.

The magnetic field is calculated at the aperture to apply Bethe's theory. Of critical importance to the proposed resonance phenomenon, the x-component of the magnetic field of the TM_{12} mode diverges as the frequency approaches the cutoff, for any finite electric field. The magnetic field is calculated from the electric field by using Faraday's law and evaluated at the center of the waveguide at the position of the aperture $(\frac{a}{2}, \frac{a}{2}, 0)$. This is done for frequency $f \to f_{c12}^-$, where the cutoff frequency is $f_{c12} = \frac{\sqrt{5}c}{2a}$, and c is the speed of light. Since $H_x(\frac{a}{2}, \frac{a}{2}, 0) \to \infty$ as $f \to f_{c12}^-$, we may approximate the modal expansion solely by the excitation TE_{10} mode and the divergent TM_{12} mode. This approximation requires that the infinite series contribution from remaining modes has negligible contribution. We have not found a supporting proof to that approximation; however, the dominant role of the TM_{12} mode is supported well by our numerical calculations, as will be described below. The x-component of the magnetic field is:

$$H_x\left(\frac{a}{2}, \frac{a}{2}, 0^+\right) \simeq \frac{t_{10}}{Z_0} + \frac{5}{2}\frac{i2t_{10}}{Z_0\sqrt{\frac{f_{c12}^2}{f^2} - 1}}, \tag{A.5}$$

where i is the imaginary unit and $t_{12} = 2t_{10}$, or Eqs. A.3 and A.4, has been used and Z_0 is the impedance of free-space. A similar expression is found for the side of reflection.

Bethe's aperture theory can now be applied directly using the magnetic fields on the aperture [45]. This requires using self-consistency so that the transmitted power is equal to the power that the magnetic dipole emits [2]. The transmittance of the of

TE_{10} mode is:

$$T = |t_{10}|^2 = \frac{1}{1 + \left(\frac{ca^2}{4\pi f \alpha_m} - \frac{5}{\sqrt{\frac{f_{c12}^2}{f^2} - 1}} \right)^2} \tag{A.6}$$

where the magnetic polarizability is given by $\alpha_m = \frac{\pi a_h^3}{16}$ for a square aperture with sides of a_h. There is a resonant peak with 100% transmission at the frequency where the term in brackets of Eq. A.6 goes to zero – all of the energy from the incident waveguide mode is transmitted through the hole. This total transmission occurs close to the cutoff frequency. Clearly, at the cutoff wavelength of the TM_{12} mode, that is $f = f_{c12}$, the transmittance T is zero.

Equation A.6 is the main analytic result of this work for applying Bethe's theory to the waveguide structure, allowing for a complete-transmission resonance. Figure A.1(b) shows the theoretical transmission through a hole in an infinitesimally thin metal in a square waveguide with solid lines. The following dimensions were used: waveguide side $a = 10$ cm and aperture side a_h of 1 cm, 1.5 cm and 2 cm. This result can be readily tested experimentally with well-established microwave techniques [158].

A.2.2 Comprehensive Numerical Simulations

To test the theoretical result predicting 100% transmission with comprehensive numerical solutions to Maxwell's equations, we used both the finite-integration method and the finite-difference time-domain method (both within CST Microwave Studio). Figure A.1(c) shows the result of finite-integration (FI), which is more efficient than finite-difference time-domain simulation (FDTD) due to the high-quality of the resonance. We simulated a structure with the same dimensions as in Fig. A.1(b), with a finite metal screen thickness $d = 1$ mm. A TE_{10} mode was generated at the input, 35 cm from the screen, towards the screen and the transmitted wave was measured at the output, 35 cm after the screen. Table A.1 shows that the transmission peaks obtained from the FI simulations are very close to the prediction by the theory. To show that the result can be extended to a waveguide with the same dimensions, but using a real metal including losses, we repeated the simulation by changing the material of the waveguide and the screen to aluminum (Al). This result is also shown in Fig. A.1(c), and as expected, the nearly total transmission peak remains since aluminum is a good conductor for microwaves. The resonance frequency of the PEC and the real-metal simulations also agree well.

Table A.1: Transmission peak frequencies (GHz)

Method	1cm Hole	1.5cm Hole	2cm Hole
Theory	3.3504	3.3472	3.3308
FI	3.3582	3.3551	3.3460
FDTD	3.3449	3.3437	3.3327

We repeated the simulations using a FDTD method. For this method, the transmission was less than unity due to the truncated integration time in the transient. However, the accuracy of the relative peak frequency increased (Table A.1). Nevertheless, as it is most concerned in this paper, the strong resonance near the cutoff frequency of the TM_{12} mode remains. Aside from computational error, some additional discrepancy is expected from the finite screen thickness and the fact that the theory considered only 2 modes, which requires further investigation. Nevertheless, the main result is retained: a resonance with total transmission is found near the cutoff frequency of the TM_{12} mode.

To investigate the limitations to directly extend these EOT results to visible and near-IR frequencies, additional simulations were performed using the usual Drude model for silver and an appropriately scaled-down structures (results not shown). In the shortest wavelength example attempted, considering practical fabrication limits, we chose the dimensions of the waveguide as follows: waveguide width $a = 550$ nm, hole-size $a_h = 125$ nm, metal screen thickness $d = 40$ nm, and length of 1500 nm. As expected, there was still a transmission peak at 513 nm with $> 65\%$ transmission and a quality of approximately 30. There is also the expected minimum transmission feature exactly at the cutoff wavelength (508.5 nm) of the TM_{12} mode for that structure. We have seen similar resonances for 1550 nm resonant structure. These are promising early results and further investigation of the visible-IR regime is required to find the optimal configurations for demonstrating this effect.

A.3 Discussion

A.3.1 Origin of Resonance Phenomenon and Comparison with Other Effects

This phenomenon is distinct from past works on EOT. Since the theory is formulated for a single hole in an infinitely thin PEC screen, it does not rely on surface plasmon polaritons (SPPs) [17, 51], spoof-SPPs of thick films [72], array effects [18], or Fabry-Perot resonances [54, 71], which can play a role in the EOT of arrays and single holes in a screen. The hole considered in this work is well below cutoff, and therefore this phenomenon is also distinct from resonant transmissions happening near the cutoff frequency for the hole [159]. Resonant total transmission of millimeter-wave through a slit in a waveguide is previously reported and employed [160], but the physical explanation is not given. The physics of total transmission in the waveguide screen aperture can be explained by considering the role of the TM mode below the cutoff frequency. Since this mode is bound to the screen, it stores the photons scattered by the aperture like a cavity, only to re-scatter them into the lowest-order propagating mode on the other side of the screen. The evanescent TM mode is required because its magnetic-to-electric field ratio diverges when approaching cutoff – it has a large mode admittance. This means that, for small apertures, the TM mode is coupled most-efficiently to the large admittance of the aperture. EOT phenomena originated from impedance matching are discussed previously by considering a perfect metal [67] and plasmonic metamaterials [161]. Specifically, the impedance matching of a near cutoff mode to a waveguide screen hole has been well documented [67], and we now show that this impedance matching technique is equivalent as Bethe's theory in the small hole limit. Mathematically, the root of the bracketed term in equation A.6 is a formulation of impedance matching. For the perfect metal case, the size of the hole can be infinitesimally small when compared to the wavelength, and there will still be 100% transmission at the resonant frequency.

As described in this theory, the TM_{12} mode dominates the transmission process for small apertures. To validate that the enhanced transmission is accompanied by the strong excitation of the TM_{12} mode, the simulated electric field distribution is analyzed away from the aperture. Figure A.2 shows the z-component of the electric field spatial distribution at $z = 30$ cm at the transmission side for the resonant frequency, which matches the distribution of a TM_{12} mode. This numerical result confirms the

role played by the TM_{12} mode as an energy reservoir in the resonant transmission process. There is no propagating power associated with this evanescent mode. Theoretically, the TM_{12} mode is not the only one that has a divergent magnetic-to-electric field ratio near cutoff. In fact, for the hole being at the center of the waveguide, all $TM_{2m+1,2n}$ bounded mode (where $m, n = 0, 1, 2...$) have this property near their cutoff frequencies, and unity transmissions will be observed also at these frequencies. We only consider the TM_{12} mode because it has the lowest order of all.

Movies of the numerical calculations are provided for dynamic visualization of the transmission resonance phenomenon. Media 1 and Media 2 show two-dimensional slices of the steady-state electric field (y-component) using on-resonance and off-resonance frequency values, as calculated using CST Microwave Studio. Media 1 shows that total transmission is obtained on-resonance, which is the result of the excitation of the TM_{12} at the aperture. Media 2 shows that off-resonance, there is negligible transmission. Media 3 shows the same results, but for a time-domain calculation using the FDTD method. (Note that the vertical z-direction is compressed by a scaling factor of 9). This shows long-lived ringing of the electric field from the resonance.

A.3.2 Field Enhancement

Figure A.2 also shows the y-component of the electric field spatial distribution at the aperture ($z = 0$ cm) at the resonant transmission frequency. The maximum field strength in this contour shows a 16-fold enhancement over the maximum of the incident field. By energy conservation, only a 5-fold average enhancement is expected. The additional field enhancement is the result of the near-field distribution in the aperture differing from the incident field distribution, both in shape and scale. A sharply-peaked near-field distribution was predicted by early aperture theory [162], and recently confirmed with near-field measurements [163]. This additional field enhancement will benefit the many applications involving electromagnetic-matter interactions. Most importantly, these numerical simulations confirm that the waveguide structure with an aperture has the ability to concentrate the electromagnetic energy effectively.

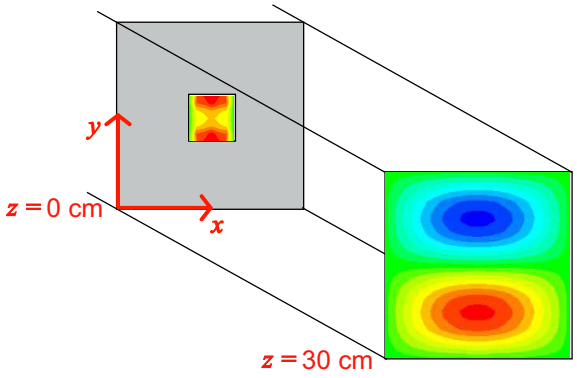

Figure A.2: Comprehensive numerical simulation showing the z-component of the electric field at $z = 30$ cm for the resonant frequency and the y-component of the electric field in the hole. The side of the aperture is 2 cm. The profile at 30 cm matches the TM_{12} mode. The color-scale of this field has red as the maximum (blue as the equal magnitude negative minimum) and the absolute maximum field strength is 6.2 times the incident field maximum. The y-component of the electric field at the screen has a color-scale where red is the maximum field strength with a 16-fold enhancement compared with the incident field maximum.

A.3.3 Potential Applications

Aside from the interesting physics of EOT in a waveguide, there are many potential applications such as filtering, enhanced electromagnetic-matter interactions, sensing and extremely localized heating and plasma generation. In addition, the structure may be used as a compact high-quality waveguide filter. Our device can be used as a resonant filter in the terahertz regime, which have shown near-unity transmission in arrays [164]; however, only a single aperture is needed here. Moreover, it is possible to tune the pass-band frequency and the bandwidth of this filter by changing the shape of the aperture, as described in past works [164, 165]. The dependence of the transmission peak on hole shape is expected to be more sensitive in our structure due to the very narrow bandwidth. The sensitive dependence of the transmission peak on the aperture polarization naturally lends this transmission mechanism to sensing applications. For example, a spectrum shift away from the transmission peak can be easily detected when there is a slight change in the polarizability at the aperture, due to the attachment of certain molecules or the introduction of a gas. A useful feature of the proposed structure is that it uses a guided TE_{10} mode as input, which can be excited and manipulated by standard methods. Overall, sensing technology is a rapidly developing area of research and much work has been done on apertures in metals: for example single apertures [134] and apertures arrays [166] have been investigated for sensing very small quantities of fluorescent molecules.

Due to the fact that a total transmission is achieved at the resonant frequency for this structure, there can be a huge field concentration in the hole. Previous works have proposed ways to squeeze electromagnetic waves well-below the optical wavelength. Some of those works exploited interesting modes for different material properties [167, 168]. Here, a perfect electric conductor is assumed, so the mechanism that squeezes the electromagnetic waves is geometric in nature.

It should be noted that there is a practical consideration when using the proposed configuration for extremely small apertures. The total transmission happens at a frequency very close to the cutoff frequency of the TM_{12} mode – the smaller the aperture is, the closer the resonant frequency to cutoff. Near cutoff, if the waveguide is too short, the bounded TM_{12} mode will be disrupted and the total transmission will be hindered. Therefore, for high-quality resonances, a longer waveguide is required.

A.4 Conclusion

A theory of total optical transmission through a small hole in a metal screen in a waveguide was presented, which was the physical result of resonant energy storage in the evanescent TM_{12} mode near cut-off. Theoretically, this 100% transmission remains for a PEC metal, no matter how small the hole. The theoretical result was confirmed by comprehensive electromagnetic simulations, and the near-total transmission was retained when including loss at microwave frequencies and strong transmission was observed using a Drude model at optical frequencies. The direct consequence of this total transmission was the extreme squeezing of the resonant field into the hole. Based on this effect, a number of potential device applications were possible, including sensors, filters, field concentrators for electromagnetic interaction with matter (including trapping, plasma generation, linear and nonlinear spectroscopy) and local heating. This high-quality resonance with strong local field could have profound impact on cavity QED as well [169] and the strong field concentration may be useful for near-field optical scanning.

Appendix B

Extraordinary Optical Transmission Brightens Near-Field Fiber Probe

Originally published:
L. Neumann, Y. Pang, A. Houyou, M. L. Juan, R. Gordon, and N. F. van Hulst. Extraordinary optical transmission brightens near-field fiber probe. Nano Letters, 11(2):355–360, 2011.

ABSTRACT

Near-field scanning optical microscopy (NSOM) offers high optical resolution beyond the diffraction limit for various applications in imaging, sensing, and lithography; however, for many applications the very low brightness of NSOM aperture probes is a major constraint. Here, we report a novel NSOM aperture probe that gives a 100× higher throughput and 40× increased damage threshold than conventional near-field aperture probes. These brighter probes facilitate near-field imaging of single molecules with apertures as small as 45 nm in diameter. We achieve this improvement by nanostructuring the probe and by employing a novel variant of extraordinary optical transmission, relying solely on a single aperture and a coupled waveguide. Comprehensive electromagnetic simulations show good agreement with the measured transmission spectra. Due to their significantly increased throughput

and damage threshold, these resonant configuration probes provide an important step forward for near-field applications.

Near-field scanning optical microscopy (NSOM) combines optical microscopy with scanning probe microscopy to achieve an optical resolution well beyond the diffraction limit. Its high resolution has found many applications in fields as optical imaging [170, 171], material science [172–175], and nanolithography [176–178]. Technically, a NSOM probe is usually realized by a single, subwavelength aperture that is formed by tapering an optical fiber and coating its side walls to prevent light leakage. However, the drawback of subwavelength apertures is their very limited throughput. Bethe's theory for optical transmission through a subwavelength aperture in a metal screen gives a steep fourth-power reduction in the transmission with the aperture diameter, necessitating a trade-off between resolution and brightness [16]. Apart from the transmission through the aperture, the absolute throughput is limited by the low damage threshold of conventional near-field probes. Here, the light delivery through the taper to the aperture depends greatly on the actual taper shape, its length, and the quality of the metal layer (aluminum) preventing light leakage. These limitations result in an optical throughput of near-field probes of typically only 10^{-5} to 10^{-7} [21, 179, 180].

Many approaches have been explored to improve the coupling through subwavelength apertures. The transmission through a single aperture was enhanced by reshaping the aperture [60, 65, 181]. Aperture arrays have shown extraordinary optical transmission (EOT) [17], and related to EOT is the beaming of light from single apertures flanked with a periodic structure [19]. Reshaping and grating structures have only been demonstrated in thin, extended films, which are also required for the aperture arrays in standard EOT. Essential for NSOM, however, is a tiny end face that, similar to atomic force microscopy, interacts with the sample and is directly responsible for resolution and sensitivity. Thus, the aforementioned approaches do not provide a practical solution. Alternatively, "apertureless" NSOM employs a sharp tip or nanoparticle to concentrate the electric field and thus provides this tiny end face [182]; however, as apertureless probes are excited from the farfield, modulation schemes are necessary to overcome the strong background illumination [100]. Few approaches have been made to enhance transmission and brightness while maintaining resolution and applicability as an aperture NSOM probe. Among those are the incorporation of antenna structures with the aperture [109, 110] or a photonic crystal [151]

and the excitation of plasmons along and inside the probe [108, 183].

In this report we demonstrate a NSOM probe that offers both improved absolute throughput and efficient coupling through the aperture and thus allows sufficient brightness to image single molecules with an aperture of 45 nm diameter. We have implemented an alternative realization of EOT that does not require an array of apertures or a grating structure [2, 3, 67]; instead, it uses resonant coupling to the adjacent waveguide. So far, this waveguide resonance EOT (WR-EOT) has only been demonstrated for coupling between two waveguides and the microwave regime [90]. Here, we demonstrate a nanoscale version WR-EOT providing enhanced transmission through a NSOM probe at visible to near-IR wavelengths. By varying the geometry of the fiber optic waveguide, we demonstrate tuning of the transmission resonance wavelength from 600 to 900 nm. Comprehensive electromagnetic simulations confirm that energy resonantly stored in the waveguide above a single mode's cutoff wavelength is responsible for the WR-EOT. We also show that the absolute throughput is enhanced by this nanostructuring of the tapered fiber. While these probes have a slightly wider base than conventional metal-coated tapered fiber probes, they show 40× improvement in the optical damage threshold and a 100× enhancement in throughput.

Figure B.1a shows a schematic and Figure B.1b a side view scanning electron microscopy (SEM) image of the metal-coated tapered fiber with an aperture in the end face. The taper was fabricated by heat-pulling an optical fiber [179]. A 220 nm thick aluminum coating was deposited around the fiber to prevent light leakage, which would otherwise add a strong background to the aperture signal. Aluminum was chosen here as it offers the smallest optical penetration depth and thus prevents leakage effectively. Next, the end face of the fiber was cut using focused ion beam (FIB) milling. In contrast to conventional NSOM fibers, the tapered fiber was not cut such that it directly forms a subwavelength aperture. Instead it was cut at a much larger diameter of the taper d_t corresponding to cutoff of the TM_{11} mode for a specific wavelength.

Panels a-c of Figure B.2 show the stages of the fabrication process. The fiber in Figure B.2a was cut at a final taper diameter dt of 370 nm and the end face coated with a 90 nm thick gold film [134], as shown in Figure B.2b. The choice of gold as the material for the end face was motivated by its favorable optical properties in the red and infrared where our optical measurements were carried out. In a final step a single subwavelength aperture with diameter da was milled into the gold layer, nominally at

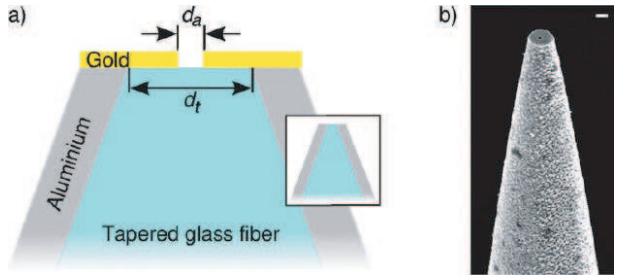

Figure B.1: Schematic and SEM image of the EOT near-field fiber probe. (a) The fiber is tapered and then coated with a 220 nm aluminum layer to prevent light leakage. We adjust the final taper diameter d_t, which determines the resonant TM mode cutoff-wavelength, by focused ion beam (FIB) milling. The aperture with diameter da is milled into a 90 nm gold layer that is evaporated onto the end face. Inset: Conventional NSOM fiber. (b) The SEM image shows the final configuration with an aperture of diameter $d_a = 110$ nm. The scale bar is 500 nm.

the center (with a variance of 30 nm in placement). Figure B.2c shows a SEM image of an aperture with a diameter of 110(10 nm in the gold-coated end face. Calibration of the milling process ensured that the aperture was milled through the gold layer only and not into the glass fiber core, avoiding spurious effects on the resonance [184]. Apertures with diameters as small as 45 nm were fabricated, which is well within the cutoff regime where Bethe's theory is typically applied. Several different diameter fiber probes were fabricated by this method, with the glass core diameter dt ranging from 400 to 730 nm (Figure B.2d-f).

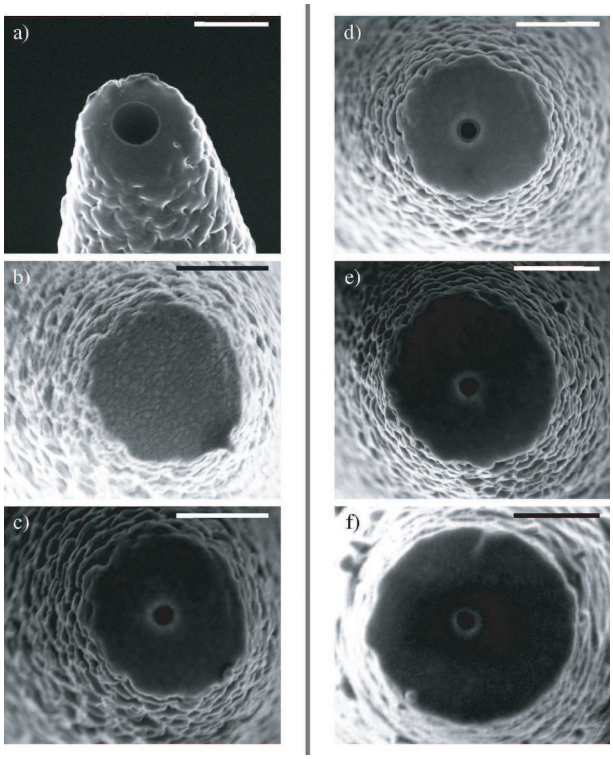

Figure B.2: The SEM images in the left column show the three fabrication steps of an EOT near-field fiber probe. (a) The aluminum-coated fiber is cut by focused ion beam (FIB) milling at the desired taper diameter d_t, here 370 nm, which determines the wavelength of the TM mode cutoff. (b) A gold layer of 90 nm is deposited on the end face. (c) Again by FIB, we mill the final aperture into the gold layer. The diameter of the aperture d_a is held constant at 110±10 nm in all fiber probes. The images in the right column show how the overall diameter of the probe as the sum of the taper diameter and coating increases while the taper diameter is varied to achieve different cutoffs of the resonant TM mode. The presented fiber probes have taper diameters of (d) 420 nm, (e) 525 nm, and (f) 724 nm. The scale bar is 500 nm.

The relative transmission of the fabricated enhanced NSOM probes and, for com-

parison, also of conventional NSOM probes is shown for various aperture diameters in Figure B.3. The throughput was determined by coupling light with known intensity at a wavelength of 647 nm into the fiber and recording the transmitted intensity with a large photodetector placed in very close proximity to the fiber end with the aperture. As variations in the taper shape of these probes can have spurious effects on the transmission data, we recorded the throughput of some of the tapered probes first in conventional NSOM configuration; afterward, we processed these probes into the enhanced configuration and recorded the throughput again.

Figure B.3 clearly shows the roughly 2 orders of magnitude improved transmission for enhanced probes compared to conventional fiber aperture probes. For a typical aperture size of around 100 nm, the throughput in the resonant configuration was determined to be 10^{-3}, while conventional NSOM probes showed a throughput of approximately 10^{-5} [179, 180]. The enhanced configuration allows a reduction in aperture diameter to as little as 45 nm, while still yielding a throughput of 10^{-5}.

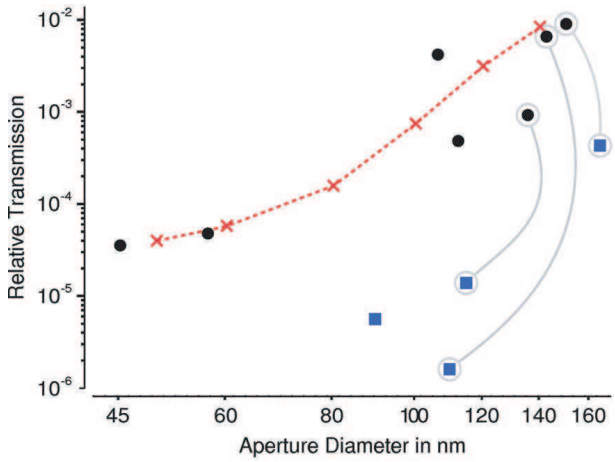

Figure B.3: The figure shows the relative transmission as a function of the aperture diameter at a wavelength of 647 nm. The transmission in the enhanced configuration (circles) is 2 orders of magnitude larger than for conventional NSOM probes (squares) for comparable aperture sizes and agrees well with our numerical simulations (crosses, line is guide for the eye). The simulated throughput is fitted to the experimental data in order to account for losses not included in the simulations. Some of the fiber probes were first fabricated as conventional NSOM probes and then processed into the enhanced configuration; data points belonging to the same probe are connected by gray lines.

To provide a more quantitative comparison with the experimental results, as well as further insight into the underlying physics of WR-EOT, comprehensive finite-

difference time domain (FDTD) simulations were performed. For these simulations, a mode source with TE_{11} mode profile was incident on the aperture from inside the fiber and the transmission through the gold film and aperture was measured. Perfectly matched layers were placed far enough from the fiber to ensure no spurious effects from coupling to evanescent waves, as confirmed by convergence studies. Convergence studies were also performed on the mesh size to ensure that the impact of plasmonic effects associated with penetration into the metals was accurately captured. We correct for any losses that were not included in the simulations by fitting the simulated relative throughput to the absolute values in the experimental data. As shown in Figure B.3, the simulated throughput values for smaller aperture sizes follow nicely the same trend as the experimental values. In particular, the optical transmission for a 50 nm aperture in our setup is still significantly larger than for a 100 nm aperture in a conventional NSOM probe with a 10° taper angle. Therefore, 2 orders of magnitude enhancement in the coupling throughput of the laser power or equivalently a reduction in aperture diameter by over a factor 2 while maintaining the excitation power is achieved with this configuration.

The brightness of conventional aperture probes is in practice limited by their damage threshold that restricts the high power needed to compensate for the low throughput. For our novel probe design, with a higher throughput, one would expect less heat to be absorbed by the coating and thus a higher damage threshold. To investigate the threshold, we coupled light into the fiber and recorded the transmitted power up to damage simultaneously with the power at the fiber launch. As the fiber is tapered, the coupling efficiency at the fiber launch into a propagating fiber mode and thus the absolute power coupled into the fiber cannot be determined with full accuracy. Therefore, once threshold was reached and the aperture is destroyed, we removed the tapered region of the fiber. The damage threshold was then defined as the recorded intensity inside the fiber and above the taper at which the aperture is destroyed [21]. For the fiber in Figure B.2e, with an aperture diameter of 105 nm, we measured the damage threshold to be 8 mW inside the fiber, or, assuming a typical coupling efficiency for NSOM setups of 5%, 160 mW at the launch. For comparison, the conventional aperture probes have a damage threshold of typically less than 0.2 mW inside the fiber or, equivalently, less than 4 mW at the launch. Therefore, the presented configuration improves the damage threshold by approximately 40×. We explain this improved damage threshold by a combination of reduced absorption due to an enhanced coupling efficiency and lower optical intensities due to the broader

probe design and the cutoff of the lowest order mode, effectively reducing the heat load on the metal coating.

We have measured the performance of the enhanced probe configuration in a home-built NSOM setup on single fluorescent molecules. TDI molecules dissolved in toluene/PMMA solution were spin coated on a glass slide and excited through the nearfield of the fiber probe at a wavelength of 647 nm. The fiber probe was scanned over the sample with nanometric accuracy and the fluorescence signal of single molecules recorded with an avalanche photodetector. Figure B.4 shows fluorescence measurements of single TDI molecules. The fluorescence spot shows a confinement to 61±3 nm (FWHM), which is close to the aperture diameter of 45±10 nm, as determined from SEM images of this specific fiber. The slightly larger size of the fluorescence spot is attributed to the penetration of the electric field into the gold film, which increases the effective aperture size, and to the finite aperture-molecule distance.

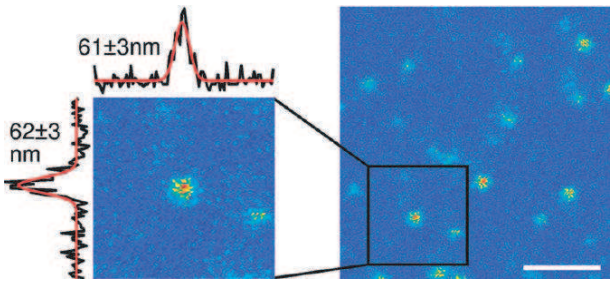

Figure B.4: A scan across single TDI molecules with an enhanced NSOM probe with an aperture diameter of 45 nm reveals the improved resolution. The molecules were embedded in a PMMA matrix and were excited at a wavelength of 647 nm. The spatial width of the fluorescence spot is 61±3 and 62±3 nm, respectively. The scale bar is 500 nm.

So far, we have assumed that the observed increase in throughput and damage threshold was a sole effect of the absence of a subwavelength taper in this probe design. However, what is the contribution of the WR-EOT? In an effort to determine its effect, we measured the out-coupling transmission and the incoupling collection spectrum of the probe with both a supercontinuum and a thermal source. These two different configurations yielded nearly identical transmission spectra, when normalized to the light source and detection efficiency. Due to the brightness of the supercontinuum source, the results for the out-coupling transmission spectrum are presented here. For comparison, the transmission spectra of the fibers before the gold coating were

alsomeasured. In addition, comparison was made with conventional tapered NSOM aperture probes with the same final aperture diameter.

Figure B.5a shows typical measured and simulated transmission spectra of two of the fabricated fiber probes. As the reported EOT phenomena is associated with mode cutoff in the fiber waveguide, we expect the longest-wavelength peak to result from EOT and thus to depend on the final taper diameter. This assumption is confirmed as an almost linear dependence between final taper diameter and peak position is clearly visible in Figure B.5b. Each fiber probe shows a distinct transmission peak that shifts to longer wavelengths with increasing diameter of the taper, and the calculations show good quantitative agreement with the measurements in the location of the resonances in Figure B.5a.

This peak in transmission is the result of WR-EOT. The WR-EOT occurs for wavelengths above the cutoff of one of the higher order TM modes in the waveguide. Approaching the cutoff, the admittance of that waveguide mode diverges, as does the admittance of the aperture as it is made infinitesimally small. Therefore, the transmission phenomenon may be considered as a problem of impedance matching, where the energy builds up resonantly in the TM mode above its cutoff. This phenomenon is similar to EOT in aperture arrays, where surface waves store the energy to allow for enhanced transmission at wavelengths longer than the Wood's anomaly [17]; except here, only a single aperture is present. A criterion for WR-EOT is that the mode inside the fiber has a divergent transverse magnetic field at its cutoff wavelength, which enhances the coupling to the aperture through Bethe's theory [16]. Various TM modes may be chosen to satisfy these criteria; however, the TM_{11} mode was selected in this case because it is the lowest order mode that allows for concentric apertures (i.e., it has a nonzero transverse magnetic field in the center of the waveguide) [67]. This cutoff mode inside the fiber is evanescent away from the metal film at the NSOM tip; therefore, it is equivalent to a surface wave, and its energy is stored near the surface with the aperture. This is analogous to the surface waves in EOT of hole arrays, except that here the geometry of the fiber replaces the periodicity of the array. The mode cutoff, which is analogous to the Wood's anomaly wavelength in the array case, is given by [88]

$$\lambda_c = \frac{\pi d_t n_f}{3.832} \tag{B.1}$$

where n_f is the refractive index of the fiber, d_t is the final taper diameter, and it

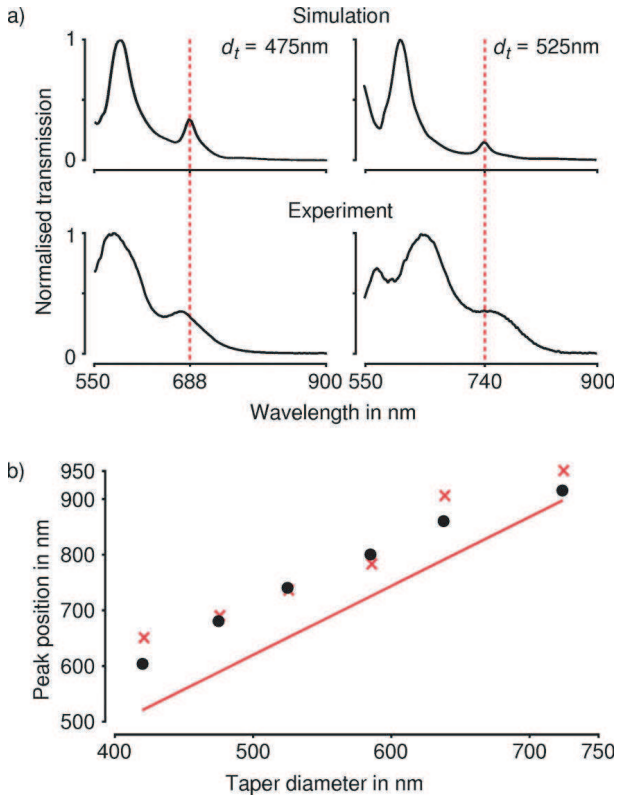

Figure B.5: (a) Simulations (top row) and experimentally recorded transmission spectra (bottom row), are shown exemplary for two fiber probes with final taper diameters d_t of 475 nm (left column) and 525 nm (right column). The dashed lines indicate the transmission peak where the TM_{11} mode at cutoff in the tapered fiber waveguide couples resonantly to the aperture and extraordinary transmission is observed. (b) The spectral positions of the transmission peaks attributed to mode cutoff. The numerical simulations (crosses) are in good agreement with the experimental data (circles) and confirm the existence of the waveguide resonant extraordinary optical transmission. Indicated by the red line is the cutoff wavelength corresponding to the TM_{11} mode as predicted by Eq. B.1 for a perfect electric conductor.

is assumed for simplicity that the aluminum coating is a perfect electric conductor. Figure B.5b shows the location of the cutoff predicted by this equation as a red line. Indeed eq. B.1 describes the trend, yet it is clear that the peak resonant transmission occurs for wavelengths slightly longer than the cutoff of the TM_{11} mode.

As emphasized above, the TM_{11} cutoff mode plays a critical role in the WR-EOT as it stores energy at the resonant peak, and it is crucial to verify that the resonant peak corresponds to a TM_{11} mode profile inside the fiber, within the decay length of the cutoff mode. Figure B.6a shows numerical simulations of the z-component of the electric field inside the two fiber probes adjacent to the gold-coated end face at the resonance wavelength of 648 and 688 nm for the fibers with taper diameter dt of 420 and 475 nm, respectively. The field distribution, shown 150 nm inside the fiber, matches that of the TM_{11}. In Figure B.6b we have also monitored the field at two interfaces and at the center of the aperture. These have very similar field intensity profiles, represented by the enhanced field confined to the aperture region, with a dominant resonant background from the TM_{11} mode. To distinguish our excitation mode from the TM_{11} cutoff mode, we also monitored the Poynting vector (obtained by the cross product of the transverse electric and magnetic fields) 150 nm inside the fiber in Figure 6a. As expected, the Poynting vector profile is predominantly the TE_{11} mode, which is the propagating mode by which we excite the fiber. Fabrication margins and a resulting small offset of the aperture on the end face were included in the simulations and cause the slight asymmetry of the field distribution. For wavelengths 100 nm below and above the resonance wavelength, the resonance is 10 $\times$ weaker. Experimentally, in Figure B.5a we observed a 2- to 3-fold increase in intensity at the resonance wavelengths compared to the nonresonant contribution in the spectra.

The 100 $\times$ total improvement in throughput over a conventional NSOM fiber probe is due to the effect of EOT and an increase in magnitude of the electric field arriving at the aperture, with both being a consequence of carefully nanostructuring the probe. The absence of a strongly attenuating subwavelength taper, present in conventional NSOM fiber probes, improves the coupling through the taper region to the aperture, effectively increasing the magnitude of the electric field at the aperture; the effect of EOT is to enhance the coupling through the subwavelength aperture itself. As the shape of the subwavelength taper and thus the strength of the attenuation depend strongly on the fabrication parameters, its absence in the enhanced configuration also improves the fabrication yield as compared to conventional probes. The challenge of

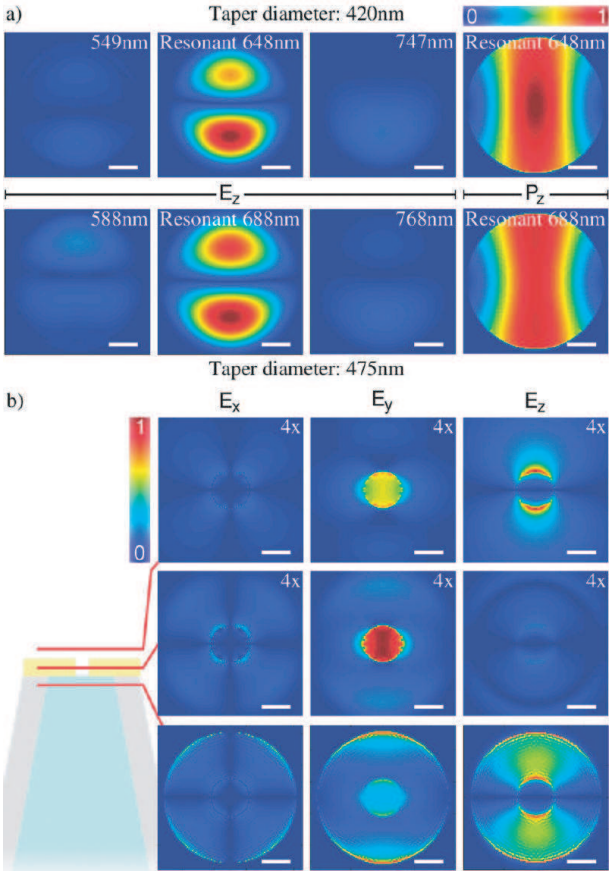

Figure B.6: (a) The z-component of the electric field (Ez) at 150 nm from the gold surface inside the fiber matches the field distribution expected of a TM_{11} mode for the fiber in Figure B.2d (diameter 420 nm, top) and Figure B.2e (diameter 525 nm, bottom), with some asymmetry from the offset of the aperture from the middle (included in the simulations). The field intensity is 10× greater at the resonant wavelength than at a nonresonant wavelength. The Poynting vector (P_z) at the same position matches the profile of the TE_{11} mode by which we excite the fiber. All electric fields are normalized to the respective resonant case, and the Poynting vector is normalized to 1. (b) The electric field components E_x, E_y, and E_z above, inside, and beneath the aperture are normalized to the same strongest field component for easy comparison. The scale bar is 100 nm.

matching the probe dimensions to a specific wavelength depends merely on the quality of the nanofabrication.

In conclusion, we have experimentally demonstrated a novel, efficient near-field probe that shows an improvement of a 40 × enhanced damage threshold and a 100 × enhanced throughput over conventional tapered fiber probes. We have realized aperture probes of only 45 nm in diameter and successfully imaged single molecules with this resolution, which confirms the subwavelength confinement of the transmitted light and the practicality of the probes for near-field scanning optical microscopy. Contributing to the high probe efficiency is a new type of EOT that relies solely on the coupling between the fiber waveguide at mode cutoff and the aperture, as confirmed with comprehensive electromagnetic simulations. We have shown that the spectral position of the resonance depends on the cutoff wavelength of the fiber waveguide, so that the peak wavelength could be tuned while maintaining the same aperture size. In the future, smaller diameter WR-EOT probes are envisioned by exploiting the cutoff resonances of lower order modes, as has already been demonstrated in the microwave regime [90].

Potential applications that benefit from the high efficiency of the demonstrated NSOM probe include imaging, sensing (Raman scattering [185]), nanolithography, and trapping and manipulation of nanoscale particles, such as viruses [5]. EOT on a single aperture has applications in high sensitivity sensing [186], as had been studied extensively in aperture arrays [79]. We also believe that this configuration may open up new applications for fiber probes where nonlinear interactions are required, such as with higher-harmonic generation [187] or two-photon luminescence [98, 188].

Appendix C

Self-Induced Back-Action Optical Trapping of Dielectric Nanoparticles

Originally published:
M. L. Juan, R. Gordon, Y. Pang, F. Eftekhari, and R. Quidant. Self-induced back-action optical trapping of dielectric nanoparticles. Nature Physics, 5(12):915–919, 2009.

ABSTRACT

Optical trapping has widely affected both the physical and life sciences. Past approaches to optical trapping of nanoscale objects required large optical intensities, often above their damage threshold. To achieve more than an order of magnitude reduction in the local intensity required for optical trapping, we present a self-induced back-action (SIBA) optical trap, where the trapped object has an active role in enhancing the restoring force. We demonstrate experimentally trapping of a single 50 nm polystyrene sphere using a SIBAoptical trap on the basis of the transmission resonance of a nanoaperture in a metal film. SIBA optical trapping shows a striking departure from previous approaches, which we quantify by comprehensive calculations. The SIBA optical trap enables new opportunities for non-invasive immobilization of a single nanoscale object, such as a virus or a quantum dot.

Optical trapping has found many applications in the physical and life sciences because it allows for precise control and positioning of micrometre-sized dielectric objects [23, 24]. For example, optical trapping has been applied to objects of biological interest, such as cells, bacteria and viruses, to indirectly manipulate DNA and to measure the forces involved in RNA transcription [33, 189]. There are two fundamental challenges in extending optical trapping to nanoscale objects, smaller than 100 nm, with a refractive index close to, but greater than, the surrounding medium. First, the gradient optical force becomes much weaker as the object gets smaller, scaling with the third power of its size. Second, the thermal motion of the object increases with decreasing object size owing to a reduction in the viscous drag, thereby favouring escape from the trap. So far, the only approach to trap smaller objects is to increase the trapping laser intensity; halving the particle size requires an order of magnitude increase in the local field intensity within the trap. Consequently, trapping very small objects involves intensities that can exceed their damage threshold. For example, a previous work reported that 109-nmdiameter polystyrene particles survived only 25 s in a focused beam optical trap, and 85-nm particles were damaged so quickly that they could not be measured reliably1. Optical damage becomes even more important for biological specimens [31, 33], where small thermal changes are critical.

An alternative to conventional lens-based optical tweezers uses nanostructures to focus light below the diffraction limit and enhance the local optical intensity within the trap [190–192]. As a result, the nanostructure can increase the potential energy and the confinement of the trap [193–195]. Nanoscale objects have been confined to subwavelength regions using nanostructured optical traps [39, 121, 122, 196]. For example, a recent work has shown one-dimensional trapping of 76-nm dielectric particles in the vicinity of a Si slot waveguide coupled to a 300 mW laser beam [39]. For those past approaches to trapping with nanostructures, the trapping followed the usual perturbative Rayleigh gradient force, so photo damage remains a concern. Evanescent whispering-gallery modes in microsphere resonators have also been used to trap and sense nanoparticles and viruses; however, in that configuration the particle moves around the circumference of the microsphere without being confined in three dimensions [124, 197].

Here, we consider the possibility of creating an optical trap in which the particle itself has a strong influence on the local electric field and thereby has an active role in the trapping mechanism. This so-called self-induced back-action (SIBA) optical

trapping is enhanced by the use of an optical resonance. Our approach differs in a fundamental way from trapping using resonances of atoms [198, 199] or quantum dots [200]: here, there is no resonance required from the trapped object; it is only a generic dielectric particle and the resonance is sustained by the trap itself. In this work, we demonstrate a SIBA optical trap using a nanoaperture in a metal film that is close to its cutoff resonance [1]. The SIBA mechanism provides superior trapping ability for Rayleigh particles, with improved performance as the particle size is reduced. It is important to emphasize that in this situation the aperture is only a model system; SIBA could be implemented in other systems where the presence of the trapping object enhances the local electric field. Our experiments show the trapping of 100-nm and 50-nm polystyrene spheres, with incident powers of only 0.7 mW and 1.9 mW, respectively. Beyond substantially decreasing the minimum incident laser intensity as compared with past approaches, SIBA enables reducing by one order of magnitude the local intensity within the trap.

The experiment used a 310-nm-diameter cylindrical aperture made by focused-ion-beam milling in a 100-nm-thick gold film on a glass substrate, as shown schematically in Fig. 1. (Further details are provided in the Supplementary Information.) This aperture-film sample was inserted into a liquid chamber containing 0:05%w=v spherical polystyrene particles (refractive index of 1.575) of either 100nm or 50nm diameter in water (refractive index of 1.33) with a 5% concentration of sodium dodecyl sulphate solution (5%w=v) to prevent aggregation. The sample was mounted upside-down so that gravity pulls the particles away from the gold film. The light from a 1,064nm wavelength continuous-wave Nd:YAG laser was focused onto the aperture using a 40× microscope objective (0.65 numerical aperture) to a 2-μm-diameter spot-size. The illumination was linearly polarized along the X-direction. Under this polarization, stable trapping occurs at the aperture side on the X-axis. The aperture was chosen to have a calculated transmission cutoff resonance in solution of 990 nm, just shorter than the laser wavelength of 1064 nm (refs [50, 51, 54]). A schematic diagram of the experimental geometry is shown in Fig. C.1a, where I, I_R and I_T are the incident, reflected and transmitted intensities, respectively. As the aperture's transmission resonance is sensitive to small changes of the local refraction index, the presence of a particle in the aperture can be tracked by changes in the transmitted and reflected intensities. Figure C.1b shows a schematic of a 100nm polystyrene bead particle trapped at the aperture.

Above the cutoff resonance of the aperture, the optical transmission is particu-

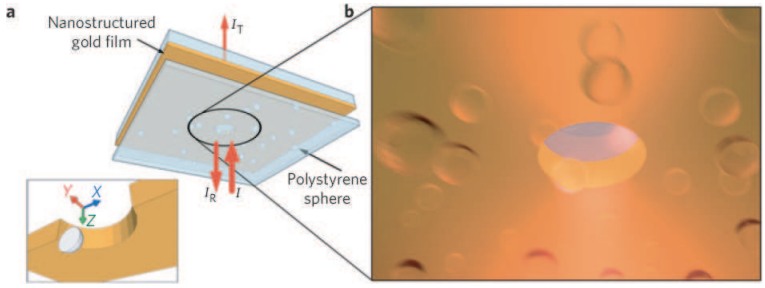

Figure C.1: SIBA optical trapping using a nanoaperture in a metallic film. a, Schematic representation of the trapping set-up for a 310 nm aperture in a 100-nm-thick gold film and 100-nm polystyrene spheres in water. The diagram in the left-bottom corner shows the coordinate system used, with the origin at the centre of the aperture. b, Schematic of the trapping of a single polystyrene sphere, while others experience thermal diffusion.

larly sensitive to the location of the particle owing to the associated change of its surrounding refractive index. Having a larger refractive index than water, a particle occupying the aperture makes the aperture "appear" larger, which allows for more transmission above the usual cutoff wavelength. To illustrate the SIBA effect, we consider the equilibrium point for the particle at the opening of the aperture on the side of optical incidence, the forces associated with the change in photon transmission rate, and Newton's third law. The transmission drops when the particle is moved away from the aperture, with a corresponding drop in the rate of photon momentum travelling through the aperture. By Newton's third law, it is expected that a force in the opposite direction will act on the particle to balance this momentum rate change; the balancing force will be directed towards the aperture, thereby pulling the particle back to the equilibrium position. On the other hand, if the particle moves further into the aperture the transmission will increase and the restoring force will push the particle out. There is also a lateral force that arises from the symmetry breaking of an offset particle in the aperture. As the particle moves towards the edge, it concentrates the field there to enhance the trapping. This is most evident from the calculations that show the redistribution of the local field from the particle (see Supplementary Information). In this way, the SIBA effect provides an extra physical mechanism, in addition to the conventional gradient force, which enhances the trapping efficiency.

The observed time evolution of the nanoaperture transmission resulting from trapping of 100-nm particles is shown in Fig.C.2a, for incident powers of 675, 838 and 965 μW. We applied a seven-point-window second-order Savitzky-Golay algorithm to smooth out the noise from 2.5 ms fast sampling. During laser exposure, the transmission showed abrupt jumps, revealing two discrete states. Moreover, the occurrence and duration of these states depended strongly on the incident power. No corresponding changes in the transmitted intensity were observed for a solution without particles. Owing to gravity, the particles were pulled away from the aperture when the laser was off. The recording of the transmitted intensity began immediately after the laser was turned on. Therefore, the initial lower intensity values of the transmission were thus obtained in the absence of particles in the aperture. By turning on the laser, the optical scattering force gently agitated the particles. It should be noted that the optical scattering force was five orders of magnitude smaller than the gradient force, so that it had no role in the observed trapping (see Supplementary Information).

The time evolution of the transmission, presented in Fig.C.2a, shows clearly the

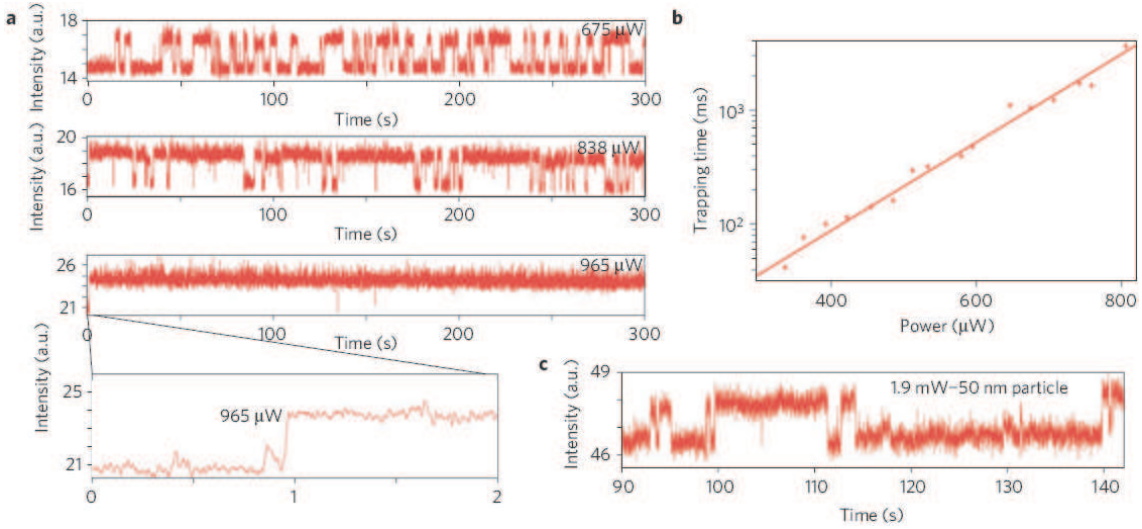

Figure C.2: Experimental trapping of 100- and 50-nm particles. a, Experimental time evolution of the intensity transmitted through a 310 nm aperture using different incident laser power when exposed to a solution of 100-nm polystyrene particles. Abrupt increases are from a particle trapped in the aperture. b, Evolution of the trapping time as a function of the incident power. The crosses are the experimental data; the line is the exponential fit corresponding to the Arrhenius law. c, Experimental time evolution of the transmitted intensity showing the trapping of a 50 nm particle at 1.9 mW.

trapping of a single 100 nm polystyrene particle, where the higher value of the transmission corresponds to the time when a particle occupied the aperture. Stable trapping over an acquisition time of 5 min was observed for a relatively small incident power of 1mW, corresponding to a maximum intensity in the focus centre of 1 mWμm^{-2}. This is an improvement over powers larger than 12 mW, as found for a conventional trap for 109-nm polystyrene spheres [23]. Accounting for the higher numerical aperture and the wavelength used in that work, the maximum intensity is estimated to have been 110 mWμm^{-2}, two orders of magnitude larger than in our experiment.

FigureC.2b shows the dependence of the trapping time τ on the incident power. It shows clearly the exponential behaviour expected from the Arrhenius law, where the incident power is linearly related to the trapping potential: $\tau = Aexp(U_trap/kT)$, with U_trap being the trapping potential, A a constant and kT the thermal energy, where k is the Boltzmann constant and T is the temperature. The variance in trapping time was found to be close to the mean value for all power levels. The trapping time distribution fits well to an exponential distribution, which is consistent with the Poisson statistics characteristic of independent events (see Supplementary Information).

To obtain further insight into the SIBA trapping mechanism, we carried out a numerical evaluation of the active role of the trapped specimen. Usually, the trapping force experienced by low-refractive-index nanoscale objects in the Rayleigh regime is calculated with a perturbative approach. In the perturbative approach, first the electromagnetic fields are computed without the object and then the gradient and scattering forces on the particle are calculated using the point-dipole approximation [201]. Several works have included the particle in the electromagnetic simulations *a priori*, and then used the Maxwell stress tensor (MST) method to calculate the trapping forces [202]. Usually, the comprehensive MST calculations and the perturbative dipole approximation agree well for particles in the Rayleigh regime [117]. Close agreement between the two approaches, to within approximately 10%, has even been shown for recent works on nanostructured optical traps [38]. For our calculations, however, there is a large discrepancy between the two approaches and the perturbative approach is no longer valid. This discrepancy arises precisely because the SIBA optical trap is not perturbative: the particle itself has an active and favourable role in the trapping.

The force field in the vertical plane was calculated using both the perturbative

approach and the comprehensive MST calculation, as shown in Fig. C.3. The potential well was found to be nearly isotropic in this plane. We found that the MST approach (Fig. C.3a,b) gives substantially greater force magnitudes over the perturbative approach (Fig. C.3c,d).

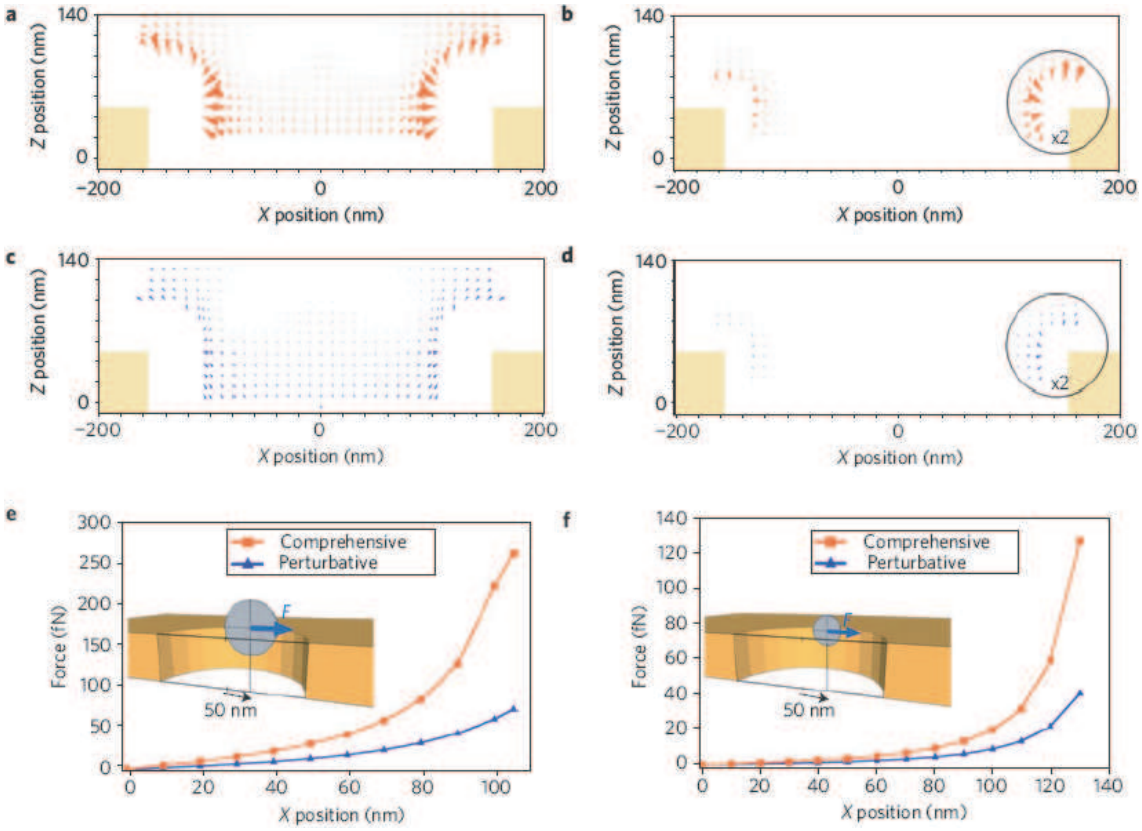

Figure C.3: Numerical evaluation of SIBA trapping. aCd, Numerical force field calculated for 100-nm particles (a,c) and for 50-nm particles (b,d) using a comprehensive MST analysis of FDTD calculations (a,b) and a perturbative method based on gradient forces (c,d). The insets in b and d show two times force magnifications. e,f, The lateral trapping force acting on 100-nm (e) and 50-nm particles (f) as a function of the distance to the aperture centre obtained with the comprehensive and the perturbative method. The calculations were made for an injected power in the aperture of 1 mW.

To quantify the active role of the particle in the trapping mechanism, we computed the incident light intensity required to obtain a trapping energy equal to the thermal energy ($kT = 4.0 \times 10^{-21}$ J). For the 100-nm particles, the required incident intensity is 250 $\mu W \mu m^{-2}$ for the MST as compared with 870 $\mu W \mu m^{-2}$ for the perturbative case. For a 50nm particle, the influence of the particle was found to be even greater,

with required intensities of 1.6 and 20 mWμm^{-2} for the MST and perturbative cases, respectively. In other words, the active role of the 50 nm particle in the trapping efficiency reduces the incident intensity requirement by an order of magnitude as compared with the perturbative approach.

In the SIBA trap, the trapping stiffness calculation is also strongly modified when using the full MST calculation as compared with the commonly used perturbative method (Fig. 3e,f). Using the MST approach, we obtained a theoretical stiffness for 1W of injected power of 9.3 pNnm^{-1} and 6.6 pNnm^{-1} for the 100- and 50-nm particles respectively at the minimum energy trapping point at the side of the hole and along the X direction. The stiffness on the Z direction is similar, with 8.2 pNnm^{-1} and 7.2 pNnm^{-1} (see Supplementary Information). For comparison, a previous work reported a 0.2 pNnm^{-1} for 100-nm particles [39].

To show the influence of the aperture resonance on the SIBA, we considered tuning the resonance properties by adjusting the aperture size. Figure C.4 shows both experiment and theory for various aperture sizes at a constant incident power of 1.6 mW. The trapping time is maximized for aperture sizes close to the cutoff, as shown in Fig. C.4a. Compared with the 500 nm aperture, which is the same size as used in a previous work [121], the trapping time of a 316 nm aperture is increased by over two orders of magnitude. The percentage change in the measured transmitted intensity is doubled for the 316 nm aperture, showing a stronger feedback effect from the photon momentum change in the aperture close to its cutoff. The trapping energy was also calculated for different aperture sizes, and it was found to double when increasing the aperture size from 310 to 500 nm. Therefore, both experimental and theoretical data show clearly a maximized SIBA effect close to the cutoff resonance of the aperture.

Past works relied on a strong enhancement of the local intensity provided by the nanostructure. Here, the local intensity is only moderately enhanced by the nanostructure, by a factor of seven. This is one of the main benefits of the SIBA trap: efficient trapping can be achieved with factor of 20 lower local intensities than found previously13 when accounting for the local enhancement of the trapping structure, thereby drastically reducing the likelihood of optical damage.

Exploiting SIBA optical trapping, we were also able to trap experimentally 50-nm polystyrene spheres. Figure C.2c shows the time evolution of the transmission through the 310 nm aperture with an incident laser power of only 1.9 mW.

We have demonstrated SIBA optical trapping capable of stabilizing 50-nm nanopar-

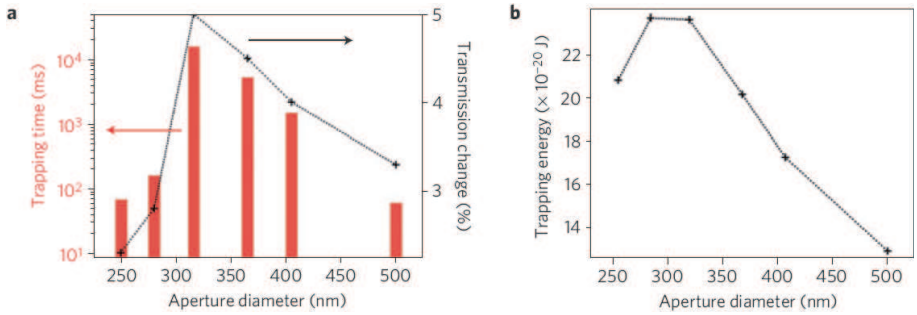

Figure C.4: Trapping time evolution with the aperture diameter for 100 nm particles at 1.6 mW. a, Experimental evolution of the average trapping time with the aperture diameter (red bars). In addition, the changes in the transmitted intensity related to the trapping of a particle are presented (black curve). b, Theoretical evolution of the trapping energy with the aperture diameter.

ticles, within a subwavelength volume, with less than 2 mW of total power. The active role of the particle in the optical trap allowed for an order-of-magnitude improved trapping efficiency over the usual perturbative approach, as confirmed by both experimental results and comprehensive numerical simulations. Such enhanced performance comes along with a large decrease, by at least an order of magnitude, of the local intensity experienced by the trapped particle. Low-intensity optical trapping of small dielectric particles (∼50 nm) enables new opportunities for isolating and studying biological nanoscopic entities, such as viruses. Another interesting feature of our experiment is the possibility to monitor a single trapped nanoscale object through transmission changes. This dual trapping-sensing capability may be useful in sorting applications. In the past, optical trapping configurations have been modified to be sensors for particles that are too small to be trapped, such as viruses [203]. Here, the proposed approach makes it possible to simultaneously immobilize and sense them in a single nanoscale aperture, providing optical integrated capabilities for biological analysis *in situ*.

Supplementary Information

Details of experimental setup

Fig. C.5a shows a scanning electron microscope image of a nanoaperture in a 100 nm thick gold film created by focused ion beam milling. Polystyrene nanoparticles (1% w/t) were diluted (5%) in deionized water with sodium dodecyl sulfate to prevent aggregation and added to the surface of the gold. A spacer and 150 μm thick glass cover slip where then added to create a liquid chamber containing the polystyrene nanoparticles, as shown schematically in Fig. C.5b.

The experimental set-up, schematically presented Fig. C.6, uses an inverted microscope. The beam from a Nd:YAG (wavelength 1064 nm) was focused onto the nanoaperture. Two silicon-based photo-detectors were used to measure the transmitted and reflected light from the aperture. In parallel, a spectrometer was placed after a 20 μm pinhole spatial filter to perform confocal spectral measurements from the aperture region. A CCD camera was used for visualization purposes and sample positioning. To achieve fine positioning and mechanical stability, the sample was mounted on a XYZ piezoelectric stage. The experiment was computer interfaced through a DAQmx card (National Instruments) allowing fast acquisition of the detec-

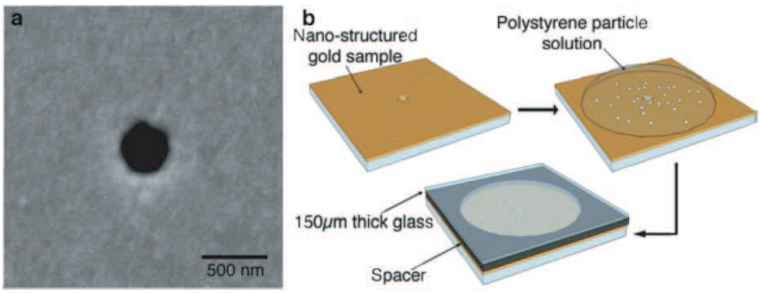

Figure C.5: Experimental sample. a, SEM image of a 310 nm aperture obtained by focused ion beam on a 100 nm thick gold layer. b, Schematic view of the liquid chamber preparation using a nano-structured sample. A drop of particle containing solution is deposited on the sample and then covered with a 150 μm thick cover slip glass with a spacer.

tors' signals (2.5 ms acquisition period) as well as the operation of the spectrometer, the CCD image, and the stage position.

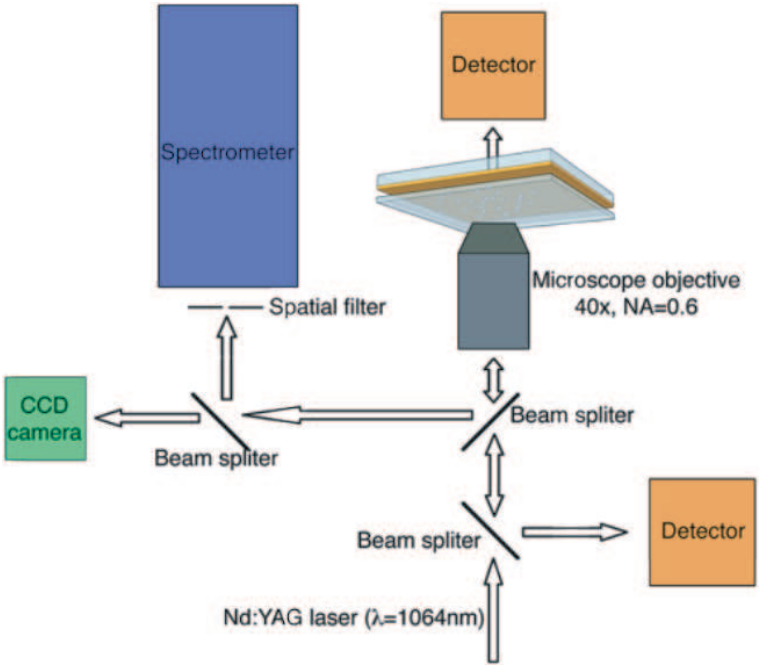

Figure C.6: Schematic of experimental configuration.

Calculation of scattering force

The scattering force, in the Rayleigh regime, is usually expressed using the point-dipole approximation [23]:

$$F_{scat} = \frac{I_0 \sigma_{scat} n_m}{c} \tag{C.1}$$

with

$$\sigma_{scat} = \frac{128\pi^5 R^6}{3\lambda^4} \left(\frac{n_p^2 - n_b^2}{n_p^2 + 2n_b^2} \right)^2 \tag{C.2}$$

where I_0 is the incident laser intensity, σ_{scat} is the scattering cross section of the particle, n_m the refractive index of the surrounding medium and c the speed of light in vacuum. The scattering cross section is a function of the particle radius R, the incident laser wavelength λ and m the ratio of the particle refractive index over the surrounding medium refractive index ($m = n_p/n_m$). For the largest particles used in

our experiment (100 nm), the calculated scattering force was 1.2×10^{-17} N for an intensity of 1 mWμm^{-2}. Since the scattering force is non-conservative, one can compare the necessary work to keep the particle in the aperture to the thermal energy. For a 100 nm thick aperture this work is 6×10^{-25} J, 4 orders of magnitude lower than the thermal energy (4×10^{-21} J).

Calculation of gradient force

The gradient optical force arises from the interaction of the induced dipole and the inhomogeneous field. In the Rayleigh regime, using the point-dipole approximation, this force is given by [23]:

$$F_{grad} = \frac{2\pi n_m R^3}{c} \left(\frac{n_p^2 - n_b^2}{n_p^2 + 2n_b^2} \right)^2 \nabla I, \tag{C.3}$$

where R is the particle radius, n_m the refractive index of the surrounding medium, c the speed of light in vacuum, m the ratio of the particle refractive index over the surrounding medium refractive index ($m = n_p/n_m$) and I the incident laser intensity. In the specific conditions of our experiment (100 nm particle and 1 mW/μm^2 maximum incident intensity), the numerical simulations gave a maximum for the gradient force of 2×10^{-14} N. The scattering forces were then 3 orders of magnitude weaker than the optical gradient forces.

Numerical calculations

Numerical calculations used a finite-difference time-domain (FDTD) Maxwell-equations solver. A 2 nm mesh was used to ensure that plasmonic effects associated with the aperture were accurately captured, as verified by convergence studies with 5 nm and 1.5 nm meshes. The simulation region was enclosed with perfectly-matched layer boundaries and a total-field scattered-field source was used to ensure that there were no aperturing effects from the boundaries. The relative permittivity of the metal was obtained from Drude model fit of experimental values [48]. The FDTD method is fully vectorial; however, due to the weak focusing of the microscope objective used, a transverse linearly polarized excitation source is assumed for simplicity.

Changes in the local electric field intensity associated with the presence

of a particle

Fig. C.7 shows that the horizontal component of the electric field intensity is modified by the presence of the particle.

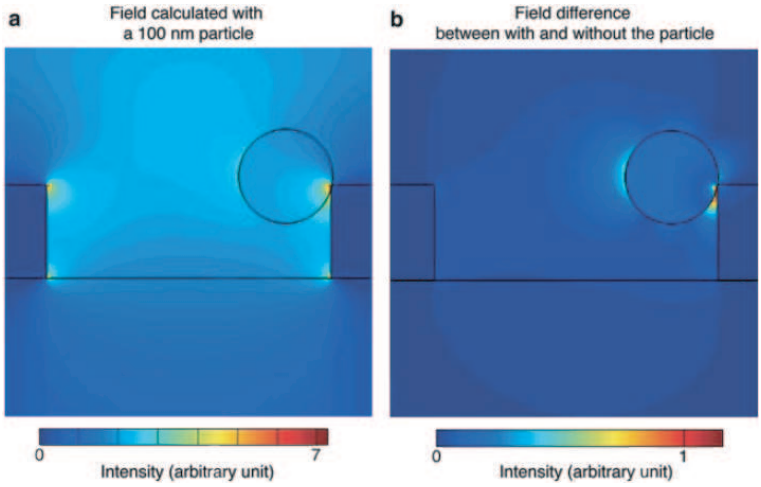

Figure C.7: Cross-section view of horizontal electric field intensity calculated using FDTD. The presence of the particle alters the local field intensity: with a 100 nm particle (a), and the field difference between the calculated field obtained with and without the 100 nm particle (b).

Calculated transmission changes

The change in transmitted intensity was calculated using FDTD and found to be 5% for 100 nm particle trapping. By comparison, the experimentally observed jump in intensity upon trapping was 13%. Considering differences in the excitation and collection geometries between the experiment and the calculations, as well as nanofabrication tolerances of approximately 10 nm, we believe that this represents reasonable agreement.

In the case of the 50 nm particle trapping, the calculated transmission change is of 0.8%, a factor of 5 lower than for the 100 nm particle. In the experimental measurement, this transmission change is of 3% a factor of 4 lower than for the experimental value obtained for the 100 nm particles.

Force-distance dependence along the Z-direction

The force along the Z-direction is presented in Fig. C.8. The impact of the particle is clear from the comparison between the perturbative and the comprehensive calculations. While the force dependence along the Z-direction is slightly stronger than the dependence along the X-direction for the 50 nm particle, the trend is reversed for 100 nm particles. The X and Y positions are defined by the stable trapping position given by the calculations.

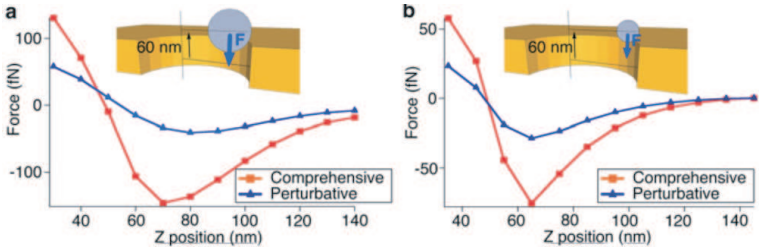

Figure C.8: Theoretical trapping force along the Z-direction. Longitudinal trapping force along the Z-direction obtained theoretically with both the comprehensive and perturbative method. The calculations have been made for an injected power of 1 mW.

Trapping time evolution with the aperture diameter

Fig. C.9 shows the evolution of the trapping for a given particle size (100 nm) and at a given incident power (1.6 mW) when the aperture diameter is changed. The most efficient trapping is obtained for the 316 nm aperture where the incident wavelength is close to the aperture cut-off.

Distribution of trapping times

The evolution of the transmitted intensity reveals the trapping events occurring during a measurement. Fig. C.10 present the trapping time distribution obtained with 0.49 mW for 100 nm particle using a 310 nm aperture. The average trapping time calculated from the raw data (Fig. C.10a) is 176 ms. Fig. C.10b presents the distribution of trapping time obtained during a 5 minute experiment. The best fit is obtained using an exponential, providing an average value of 160±26 ms.

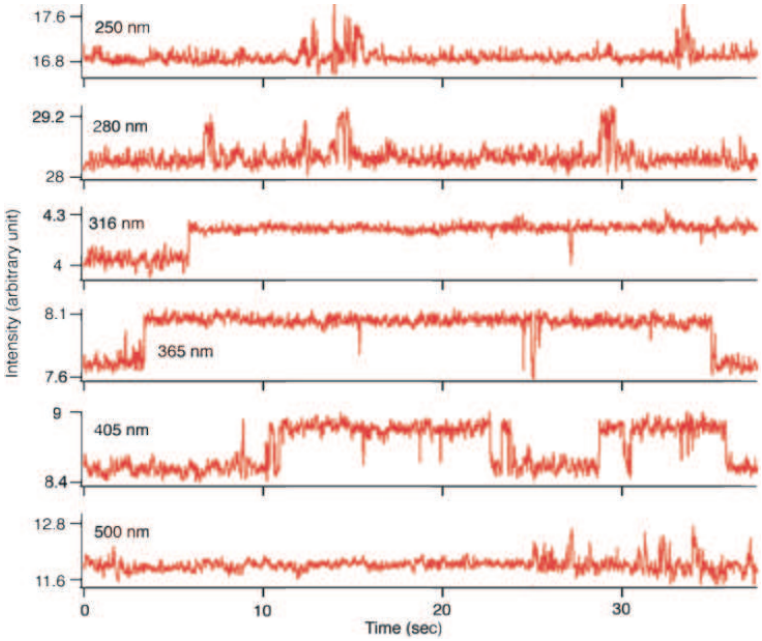

Figure C.9: Trapping time evolution with the aperture diameter for 100 nm particles. Transmission changes obtained at 1.6 mW of incident power with 100 nm particles for aperture diameters ranging from 250 nm to 500 nm.

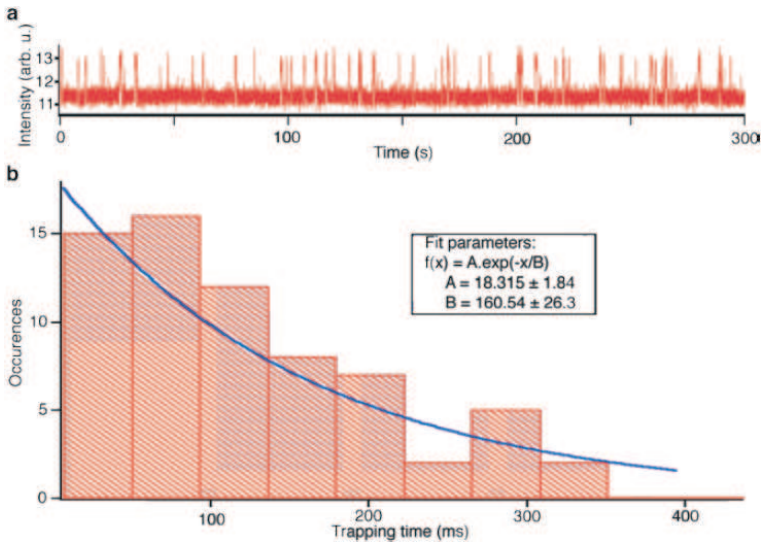

Figure C.10: Trapping distribution. a, Transmission changes obtained at 0.49 mW of incident power with 100 nm particles for a 310 nm aperture. The average trapping is time is 176 ms. b, trapping time distribution obtained from the data presented in (a). The exponential fit is in good agreement with the experimentally obtained average trapping time.

Appendix D

Matlab Scripts for Optical Force Computations Based on FDTD Simulation Results

D.1 Plotting a Force Field Using MST

```
%%%%%%%%%%%%%%%%%%%%%%%%%%%%%%%%%%%%%%%%%%%%%%%%%%%%%%%%%%%%%%%%%%%%%%%%%%%%%%%%
%
% force_field.m
%
% This function loads the data files from FDTD simulations of the
% non-perturbative nanohole optical trapping. Each of the data files
% contains the electric field information for computing the optical force
% at a single point only. The optical force is computed using Maxwell
% stress tensor (MST) by calling the function ot_singlewl.


clear;

% Define some constants
c = 3e8;
epsilon = 8.854e-12;
```

```
n_m = 1.333;
n_p = 1.55;

xrange = -180:10:180;
yrange = -10:10:10;
zrange = -35:10:145;

[cx cy cz] = meshgrid(xrange,yrange,zrange);

% Loop through each point in the map
for posi = 1:length(xrange)
    for posj = 1:length(yrange)
        for posk = 1:length(zrange)
            % Read in datafile from FDTD results
            datafile = strcat( 'D310_50Part_x', int2str(xrange(posi)), ...
                        'y', int2str(yrange(posj)), ...
                        'z', int2str(zrange(posk)), '_Mesh2.mat');

            if exist(datafile);
                load(datafile);

                for i = 1:length(x_n)
                    for j = 1:length(y_n)
                       for k = 1:length(z_n)
                            if (nx(i, j, k) ~= n_m) && (nx(i, j, k) ~= n_p)
                               nx(i, j, k) = n_m;
                            end
                            if (ny(i, j, k) ~= n_m) && (ny(i, j, k) ~= n_p)
                               ny(i, j, k) = n_m;
                            end
                            if (nz(i, j, k) ~= n_m) && (nz(i, j, k) ~= n_p)
                               nz(i, j, k) = n_m;
                            end
                       end
                    end
```

```
                end

                % Perform MST computation for the force
                ot_singlewl;

                % Store computed force values
                U(posj, posi, posk) = tempx;
                V(posj, posi, posk) = 0;
                W(posj, posi, posk) = tempz;

            else
                U(posj, posi, posk) = 0;
                V(posj, posi, posk) = 0;
                W(posj, posi, posk) = 0;
            end

            % Compute the magnitude of the force at each point
            Mag(posj, posi, posk) = sqrt(U(posj, posi, posk)^2 + ...
                V(posj, posi, posk)^2 + W(posj, posi, posk)^2);

        end
    end
end

% The following code is solely about plotting the force field, not about
% any computation
figure(4);

[cylx, cyly, cylz] = cylinder(155);
surf(cylx, cyly, cylz*50, 'FaceAlpha', 0.6, ...
    'EdgeAlpha', 0, 'FaceColor', 'yellow');
hold on;

% make an invisible cylinder to define boundary
[cylx, cyly, cylz] = cylinder(200);
```

```
surf(cylx, cyly, cylz*150, 'FaceAlpha', 0, 'EdgeAlpha', 0);

axis([-200 200 -200 200 0 150]);
axis equal;
hcone = coneplot(cx, cy, cz, U, V, W, cx, cy, cz, 1.5);
set(hcone,'FaceColor','red','EdgeColor','none', 'FaceAlpha', .5);
% The left side is symmetric
hcone_left = coneplot(-cx, cy, cz, -U, V, W, -cx, cy, cz, 1.5);
set(hcone_left,'FaceColor','red','EdgeColor','none', 'FaceAlpha', .5);

xlabel('x (nm)', 'fontsize', 16);
ylabel('y (nm)', 'fontsize', 16);
zlabel('z (nm)', 'fontsize', 16);
title('MST, 2 nm mesh', 'fontsize', 18);

view(0, 0)
```

D.2 Computing MST at a Single Point

```
%%%%%%%%%%%%%%%%%%%%%%%%%%%%%%%%%%%%%%%%%%%%%%%%%%%%%%%%%%%%%%%%%%%%%%%%%%%%
%
% ot_singlewl.m
%
% This function is called by the force_field function. It is responsible
% for taking the loaded values of the electric field and compute the
% optical force exerted on the particle using a Maxwell stress tensor (MST)
% analysis.

Nx = length(x);
Ny = length(y);
Nz = length(z);
Nf = 26;    % correspond to lambda = 1059nm
```

```
dx = abs(x(2) - x(1));
dy = abs(y(2) - y(1));
dz = abs(z(2) - z(1));

% ====================== z component ==================================
aix = (abs(Ex(:, : , 1:(Nz-1) , Nf)).^2 + abs(Ex(:, : , 2:Nz , Nf)).^2)/2;
aiy = (abs(Ey(:, : , 1:(Nz-1) , Nf)).^2 + abs(Ey(:, : , 2:Nz , Nf)).^2)/2;
aiz = (abs(Ez(:, : , 1:(Nz-1) , Nf)).^2 + abs(Ez(:, : , 2:Nz , Nf)).^2)/2;
dez = nz(:, :, 1:(Nz-1)).^2 - nx(:, :, 2:(Nz)).^2;

for iz = 1:(Nz-1)
    dez(:, :, iz) = dez(:, :, iz)/(z(iz) - z(iz + 1));
end

clear el;
el(:, :, :) = (aix(:, :, :) + aiy(:, :, :) + aiz(:, :, :)) .* dez * dx*dy*dz;
tempz = 0;

for ix = 1:Nx
    for iy = 1:Ny
        for iz = 1:(Nz-1)
                tempz = tempz + (-epsilon/4) * real(el(ix, iy, iz));
        end
    end
end

% ====================== x component ==================================
clear ai* dex el;
aix = (abs(Ex(1:(Nx-1), : , : , Nf)).^2 + abs(Ex(2:(Nx), : , : , Nf)).^2)/2;
aiy = (abs(Ey(1:(Nx-1), : , : , Nf)).^2 + abs(Ey(2:(Nx), : , : , Nf)).^2)/2;
aiz = (abs(Ez(1:(Nx-1), : , : , Nf)).^2 + abs(Ez(2:(Nx), : , : , Nf)).^2)/2;
dex = nx(1:(Nx-1), :, :).^2 - nx(2:(Nx), :, :).^2;

for ix = 1:(Nx-1)
```

```
    dex(ix, :, :) = dex(ix, :, :)/(x(ix) - x(ix + 1));
end

el(:, :, :) = (aix(:, :, :) + aiy(:, :, :) + aiz(:, :, :)) .* dex * dx*dy*dz;
tempx = 0;

for ix = 1:(Nx-1)
    for iy = 1:Ny
        for iz = 1:Nz
                tempx = tempx + (-epsilon/4) * real(el(ix, iy, iz));
        end
    end
end

% ====================== y component ===================================
aix = (abs(Ex(:, 1:(Ny-1) , : , Nf)).^2 + abs(Ex(:, 2:Ny , : , Nf)).^2)/2;
aiy = (abs(Ey(:, 1:(Ny-1) , : , Nf)).^2 + abs(Ey(:, 2:Ny , : , Nf)).^2)/2;
aiz = (abs(Ez(:, 1:(Ny-1) , : , Nf)).^2 + abs(Ez(:, 2:Ny , : , Nf)).^2)/2;
dey = ny(:, 1:(Ny-1), :).^2 - ny(:, 2:(Ny), :).^2;

for iy = 1:(Ny-1)
    dey(:, iy, :) = dey(:, iy, :)/(y(iy) - y(iy + 1));
end

clear el;
el(:, :, :) = (aix(:, :, :) + aiy(:, :, :) + aiz(:, :, :)) .* dey * dx*dy*dz;
tempy = 0;

for ix = 1:Nx
    for iy = 1:(Ny-1)
        for iz = 1:Nz
                tempy = tempy + (-epsilon/4) * real(el(ix, iy, iz));
        end
    end
end
```

D.3 Computing and Plotting Force Field Using the Perturbative Formulation

```
%%%%%%%%%%%%%%%%%%%%%%%%%%%%%%%%%%%%%%%%%%%%%%%%%%%%%%%%%%%%%%%%%%%%%%%%%%%%
%
% perturbative.m
%
% This function calculates the optical force using a perturbative
% formulation by computing the gradient force and the scattering force. It
% computes the optical force at all points of interest based on the
% electromagnetic field from a single FDTD simulation without any particle.

clear;

% Define some constants
c = 2.997e8;
epsilon = 8.854e-12;
mu = 4*pi * 1e-7;
eps_m = 1.333^2;  % medium is water
eps_s = 1.55^2;   % sphere
R = 25e-9;      % radius of the sphere in meters

datafile = 'D310_empty_Mesh2.mat';
load (datafile);

lambda = c./f_f;

E2 = abs(Ex_f).^2 + abs(Ey_f).^2 + abs(Ez_f).^2;

% polarizability of sphere
```

```
alpha = 4*pi * epsilon * R^3 * (eps_s - eps_m) / (eps_s + 2*eps_m);
sigma = 128/3 * pi^5 * R^6 ./ lambda.^4 * ((eps_s - eps_m) / (eps_s + 2*eps_m))

dx = x_f(2) -x_f(1);
dz = z_f(2) -z_f(1);

% ==================== z-dependance ==========================
f_ind = 1;    % correspond to lambda = 1059nm

xrange = -180:10:180;
yrange = -10:10:10;
zrange = -25:10:145;

[cx cy cz] = meshgrid(xrange,yrange,zrange);
fprintf('x \t y \t z \t Fx \t Fy \t Fz \n', y);

for posi = 2:length(xrange)
    for posj = 2:length(yrange)
        for posk = 2:length(zrange)

            % if  yrange(posj)~=0 || zrange(posk)<100
            if U(posj, posi, posk)==0 && V(posj, posi, posk)==0 && W(posj, posi

                Ugs(posj, posi, posk) = 0;
                Vgs(posj, posi, posk) = 0;
                Wgs(posj, posi, posk) = 0;

            else

                i = round((xrange(posi)*1e-9 - x_f(1))/dx + 1);
                j = 1;
                k = round((zrange(posk)*1e-9 - z_f(1))/dz + 1);
                gradE = [ (E2(i,j,k,f_ind) - E2(i-1,j,k,f_ind)) / (x_f(i) - x_f
                          0;
                          (E2(i,j,k,f_ind) - E2(i,j,k-1,f_ind)) / (z_f(k) - z_f
```

```
                % Gradient force computation
                F_grad = alpha/4 * gradE;   % Neuman's Review Paper

                clear gradE;

                % Light intensity obtained by the cross-produce of E and H
                I = abs(1/2 * cross([Ex_f(i,j,k,f_ind); Ey_f(i,j,k,f_ind); ...
                    Ez_f(i,j,k,f_ind)], [Hx_f(i,j,k,f_ind); Hy_f(i,j,k,f_ind);
                    Hz_f(i,j,k,f_ind)]));

                % scattering force computation
                F_scat = I * sigma(f_ind) * sqrt(eps_m) / c;

                Ugs(posj, posi, posk) = F_grad(1) + F_scat(1);
                Vgs(posj, posi, posk) = 0;
                Wgs(posj, posi, posk) = F_grad(3) + F_scat(3);

                % For printing the force values only
                fprintf(strcat(int2str(xrange(posi)), '\t'), y);
                fprintf(strcat(int2str(yrange(posj)), '\t'), y);
                fprintf(strcat(int2str(zrange(posk)), '\t'), y);
                fprintf(strcat(num2str(Ugs(posj, posi, posk)), '\t'), y);
                fprintf(strcat(num2str(Vgs(posj, posi, posk)), '\t'), y);
                fprintf(strcat(num2str(Wgs(posj, posi, posk)), '\n'), y);
            end
        end
    end
end
fprintf('\n \n', y);

% The following code is solely about plotting the force field, not about
% any computation
figure(4);
```

```
[cylx, cyly, cylz] = cylinder(155);
surf(cylx, cyly, cylz*50, 'FaceAlpha', 0.6, 'EdgeAlpha', 0, 'FaceColor', 'yello
hold on;
% make an invisible cylinder to define boundary
[cylx, cyly, cylz] = cylinder(200);
surf(cylx, cyly, cylz*150, 'FaceAlpha', 0, 'EdgeAlpha', 0);

axis([-200 200 -200 200 0 150]);
axis equal;

hcone_pert_R = coneplot(cx, cy, cz, Ugs, Vgs, Wgs, cx, cy, cz, 1.5);
set(hcone_pert_R,'FaceColor','green','EdgeColor','none', 'FaceAlpha', .5);
% % The left side is symmetric
hcone_pert_L = coneplot(-cx, cy, cz, -Ugs, Vgs, Wgs, -cx, cy, cz, 1.5);
set(hcone_pert_L,'FaceColor','green','EdgeColor','none', 'FaceAlpha', .5);

xlabel('x (nm)', 'fontsize', 16);
ylabel('y (nm)', 'fontsize', 16);
zlabel('z (nm)', 'fontsize', 16);

view(0, 0)
% view(4, 8)
```

Appendix E

Optical Trapping of 12 nm Dielectric Spheres Using Double-Nanoholes in a Gold Film

Originally published:
Y. Pang and R. Gordon. Optical trapping of 12 nm dielectric spheres using double-nanoholes in a gold film. Nano Letters, 11(9):3763–3767, 2011.

ABSTRACT

Optical tweezers have found many applications in biology, but for reasonable intensities, conventional traps are limited to particles >100 nm in size. We use a double-nanohole in a gold film to experimentally trap individual nanospheres, including 20 nm polystyrene spheres and 12 nm silica spheres, at a well-defined trapping point. We present statistical studies on the trapping time, showing an exponential dependence on the optical power. Trapping experiments are repeated for different particles and several nanoholes with different gap dimensions. Unusually, smaller particles can be more easily trapped than larger ones with the double-nanohole. The 12 nm silica sphere has a size and a refractive index comparable to the smallest virus particles and has a spherical shape which is the worst case scenario for trapping.

Optical trapping has attracted significant research attention for its capability to immobilize, move, and manipulate small objects in a gentle way [23, 24]. Optical trapping has been applied to trap dielectric nanospheres [23, 24, 196], carbon nanotubes [25], semiconductor nanowires [26], and metal nanorods [27, 28]. Stable trapping of 10 nm gold nanospheres has been achieved with high power (∼400 mW) focused laser beams [29]. For dielectric particles, trapping of 48 nm particles has been achieved [42]. Optical trapping of biological objects (i.e., typically nonresonant dielectric particles) has included living cells [32], bacteria [33], 300 nm long tobacco mosaic virus particles [33], and DNA strains [39]. The manipulation of biomolecules (e.g., DNA, actin) has been achieved by attaching micrometer-sized beads to the ends of the biomolecule [34–36]. However, direct manipulation of smaller biomatter, without tethering to a bead, presents a significant challenge because the trapping force on nonresonant dielectric particle decreases dramatically with size. In a conventional optical trap configuration, such as a single beam optical tweezer [23], the optical force obeys the perturbative formulation for small (Rayleigh) particles [23, 196]: the influence of the particle on the electromagnetic field is neglected. In such a regime, the optical power required for trapping a subwavelength dielectric particle scales with the inverse fourth power of the particle size over all [5]. When trapping single latex nanospheres, a perturbative optical trap can only trap spheres with diameter down to about 100 nm before the large required intensities damage the particle [23]. A self-induced backaction (SIBA) optical trap was designed to work in a nonperturbative regime, where the existence of a small dielectric particle in the trap significantly changed the surrounding field in a way in favor of the trapping action. The previously designed SIBA optical trap using single circular nanoholes in an Au film successfully pushed the limit of the trapped polystyrene nanosphere diameter to 50 nm [5]. However, the difficulty to trap smaller dielectric particles still increases, although not as abruptly as in a perturbative trap.

Many other promising approaches also exist for optical trapping. A silicon slot waveguide has been used to trap 75 nm polystyrene particles and relatively large (48 kbp) λ-DNA [39], and this slot waveguide can trap dielectric and Au particles as small as 10 nm in theory [38]. The whispering gallery mode (WGM) optical resonator is well-known for its high-quality resonance and huge field build-up in the near field of the cavity. It is used as a sensitive optical sensing tool [123, 124] to detect the binding of a single 47 nm influenza A virus. When a WGM resonator is used for optical trapping, the evanescent field at the resonator surface generates a

large gradient force, and single 280 nm polystyrene particles have been successfully trapped by a WGM resonator using a low input power [40]. Photonic crystal optical cavities are also considered as strong candidates for self-induced optical trapping, and 48 nm polystyrene particles have been trapped using a one-dimensional silicon photonic crystal resonator [42]. Theoretical results have also been presented for optical trapping using one-dimensional [43] and two-dimensional [44] photonic crystal cavities. Unlike the high-quality resonator configurations, the aperture-based SIBA trap is not as sensitive to wavelengthby monitoring the transmitted power through the aperture, the trapping event can be monitored. In this respect, the aperture trap can also be thought of as a sensor.

In this work, we demonstrate an optical trap using a double-nanohole structure in an Au film to trap 20 nm polystyrene nanospheres and 12 nm silica nanospheres. This small size limit will enable the trapping of even the smallest biomatter, such as virions and bacteriophages. Spherical objects, such as the nanospheres used in this work, have the smallest electric dipole moments of all shapes at the same size and are therefore the most challenging to trap. We attribute the facile trapping ability to the extreme local field at the trapping point provided by the 15-nm-apart sharp tips of the double-hole structures. Perhaps most surprisingly at first glance, we show that the double-nanohole is able to trap smaller particles even more easily than larger particles, which is the opposite of other optical traps. Statistical data are presented to show the exponential dependence of the trapping time on the incident optical power. Nanoholes with different dimensions are used to trap nanospheres with different size and different material, and the optimum trapping condition is found to be as predicted.

Figure I.1 shows two scanning electron microscope (SEM) images of the double-nanohole, normal to the surface and at 45 ∘. The double-hole was milled into a commercially available 100 nm thick Au film on a glass substrate with a 2 nm Ti adhesion layer (EMF Corp.) using a focused ion beam (FIB). For the example shown in Figure I.1, the diameter of each circular hole is 110 nm, and the tips are separated by 30 nm.

Previously, we have studied the use of double-hole arrays for enhanced second harmonic generation [63, 64] and surface-enhanced Raman scattering (SERS) [66]. The field enhancements found at the apexes between the two holes lead to enhanced light-matter interaction [61]. While our work has focused on the fabrication of double-hole structures by FIB milling (as is the case in this work), it is interesting to note that bot-

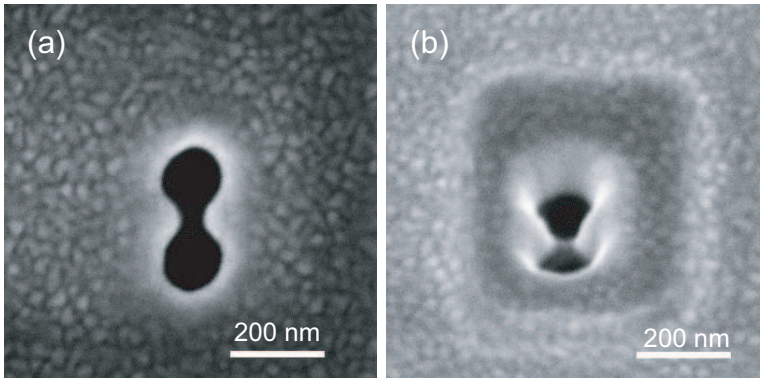

Figure E.1: SEM image of the double-hole on Au film, taken (a) normal to the surface and (b) at 45o.

tom up fabrication of double-hole structures by polystyrene nanosphere lithography using dimers is an effective way to achieve the same structure [65].

Figure I.2a shows the schematic of the double-nanohole optical trap. As the trapping beam, a fiber-coupled 975 nm semiconductor laser was collimated, expanded, and focused onto the sample using a 100× oil immersion microscope objective (1.25 numerical aperture), forming a laser spot of 1.1 μm diameter. An optical density filter was used to limit the optical power to below 10mW at the output of the objective. A half-wave plate was used rotate the polarization of the laser beam. The transmission light through the double-hole was collected using a 10× condenser microscope objective (0.25 numerical aperture) and measured by a silicon-based avalanche photodetector (Thorlabs APD110A). The sample was mounted between the oil-immersion microscope objective and the condenser microscope objective and aligned using a piezoelectric controlled xyz sample stage to give a 20 nm positioning precision. The polarization of the trapping beam was chosen such that the electric field was aligned with the two tips in the double-hole structure. With this polarization, there is a large local field enhancement in between the two tips creating a strong trapping point.

Figure I.2b shows an enlargement of the sample region. As the particles to be trapped, polystyrene nanospheres (Fisher Scientific) or silica nanospheres (Corpuscular Inc.) were suspended in water (0.05% w/v) with a trace amount of surfactant to prevent aggregation. The nanospheres suspension was ultrasonicated to further ensure against aggregation and then sealed at the Au film surface using a microfluidic chamber consisting of an 80 μm thick poly(dimethylsiloxane) (PDMS) spacer well and a 150 μm thick glass microscope coverslip. The sample was mounted with the Au film facing down so that the small contribution from gravity pulls the nanospheres away from the Au film, and the optical force works against gravity. Immersion oil with refractive index of 1.51 was used in between the oil immersion objective and the coverslip.

The double-nanohole optical trap has a working principle similar to the SIBA optical trap using a circular nanohole proposed in previous work [5]. The double-hole on the Au film is designed to have a cutoff wavelength slightly shorter than the wavelength of the main trapping laser beam in water using numerical simulations with the finite-difference time-domain method (see Supporting Information). When a polystyrene nanosphere with a larger refractive index than water enters the vicinity of the double-nanohole, the local increase of refractive index makes the hole optically "larger" (by dielectric loading), thereby increasing the cutoff wavelength and making

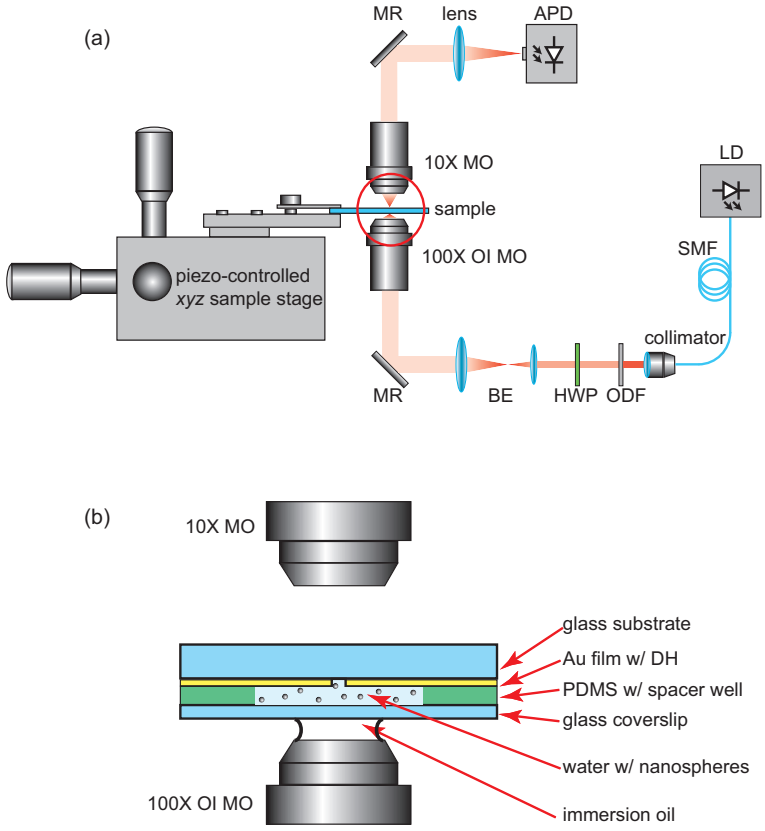

Figure E.2: (a) Schematic drawing of the nanoscale double-hole self-induced back-action optical trap. (b) An enlargement of the red circle part in (a), showing details of the composition of the sample in the microfluidic chamber, the setup of the oil immersion microscope objective, and the condenser microscope objective. Abbreviations used: LD = laser diode; SMF = single-mode fiber; ODF = optical density filter; HWP = half-wave plate; BE = beam expander; MR = mirror; MO = microscope objective; OI MO = oil immersion microscope objective; DH = double hole; APD = avalanche photodetector.

the double-nanohole transmit more light. From Newton's third law, the change rate of the light momentum due to the presence of the nanosphere generates a force acting back on the nanosphere, and this self-induced force always pulls the nanosphere back to equilibrium position.

Figure I.3 shows the time evolution of the transmitted optical power through a double-nanohole with 30 nm tip separation and through a 290 nm diameter circular hole, using 100 and 20 nm polystyrene spheres. Forty nanometer polystyrene spheres were also tested (not shown). We used a 1 kHz sampling rate with a Savitzky-Golay algorithm for noise reduction of the collected data. In the waveforms, the abrupt changes (jumps) of the optical transmission power showed clearly the transition between the vacant and trapped stages, corresponding to low and high transmission powers. Such abrupt transmission power level transitions are the characteristic signal of trapping events [5, 196]. The measurements were repeated on different days with freshly made nanosphere suspensions each time and the abrupt transitions and the relative signal difference was repeatable for all types of holes and all nanospheres used. Furthermore, this dependence was not observed when pure water without nanospheres.

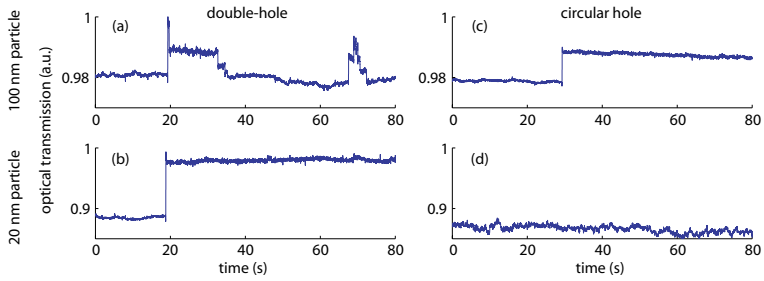

Figure E.3: Experimental optical transmission evolution in time using (a, b) a double-hole and (c, d) a circular nanohole, to trap (a, c) 100 nm and (b, d) 20 nm polystyrene nanospheres.

As Figure I.3 shows, a double-nanohole (Figure I.3a) and a circular nanohole (Figure I.3c) were both able to trap relatively large (100 nm) particles. In fact, the circular nanohole gave a more stable trapping to a 100 nm particle than the double-hole, with an approximately 10× longer trapping time. However, when attempting to trap very small (20 nm) spheres, the circular nanohole does not show any stable trapping (Figure I.3d), whereas a double-hole shows stable trapping of a 20 nm particle for a period of more than 5 min.

The double-nanohole also shows an unusual and potentially useful feature: it traps

smaller particles more easily than larger ones. We trapped polystyrene spheres of three different sizes (100, 40, and 20 nm) using the double-hole. While stable trapping periods for a 100 nm sphere were always less than 20 s, long trapping periods of over 5 min were observed for both the 40 and 20 nm spheres. The percentage change in optical transmission at the abrupt transition of each trapping relates to the trapping stability: a larger change in the light momentum indicates a larger force on the spheres according to Newton's third law. The changes in optical transmission were 0.78%, 6.05%, and 9.95% when 100, 40, and 20 nm polystyrene spheres were trapped at the double-nanohole. Therefore, the double-nanohole provides a larger optical force on smaller particles for the same trapping beam power.

Figure I.4 shows the dependence of the trapping time on the incident optical power. The data were taken using a double-nanohole with a 25 nm tip separation to trap 20 nm polystyrene spheres. The error bars are the standard deviations of the trapping times for multiple events (greater than six events for each power). The straight line is an exponential fit of all the data (noting the semilog plot). This dependence is similar to previous circular hole trapping results [5]; however, the nanoparticle here is 2.5 times smaller.

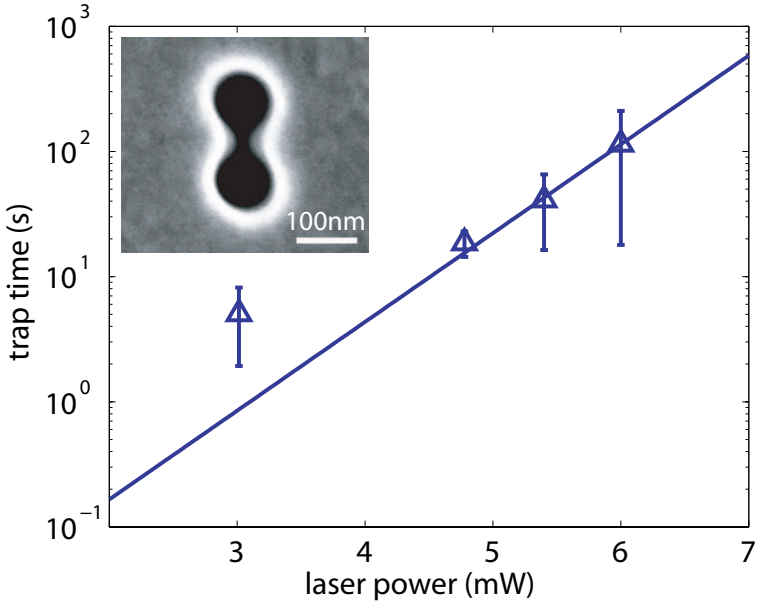

Figure E.4: Trapping time as a function of incident power, studied using 20 nm polystyrene spheres and a double-nanohole with 25 nm tip separation. The triangles are the mean values of experiment data taken, the error bars are the standard deviation of the data, and the straight line is the exponential fit to the data. The inset shows the SEM image of the double-nanohole.

The advantage of the proposed double-nanohole structure over a circular nanohole is that there is a large local field concentrated in the small area between the two tips. The optical transmission is much more sensitive to a local refractive index change in this small area, since this is where all the transmission power through the hole is concentrated. Therefore, only a small particle, with size comparable to the strong local field area, is needed to make enough change to the transmitted power and self-induce enough trapping force. By comparison, a circular nanohole is isotropic and does not provide such local field enhancement. With a circular nanohole, only relatively large particles can change the transmitted power enough to self-induce enough trapping force. Therefore, a double-nanohole allows the trapping of much smaller particles than a circular nanohole.

The small trapping area with strong local field between the tips (cusps) where the nanoholes overlap explains why a smaller particle can be trapped more strongly using a double-nanohole. Only particles with size smaller than the tip separation can fit between the tips, whereas larger particles are blocked outside the tip region and induce a much weaker trapping force. In other words, steric hindrance plays an important role in the double-nanohole trap. This surprising result is opposite of all existing optical traps, which gave a stronger trapping for larger particles, as will be considered in more detail below. The double-nanohole structure is also advantageous over a rectangular nanohole. Although a rectangular nanohole can also give an enhanced local field through the coupling of surface plasmons between the two closely spaced sides [53], the enhanced local field is distributed along the sides of the hole, and the trapping force will be weaker along the long axis of a rectangular hole. In contrast, the double-nanohole gives a single trapping point where the field is strongest between the two tips.

Figure I.5 shows the different jumps in optical transmission at trapping events using double-nanoholes with different tip separation for trapping. This shows the importance of the tip separation on double-nanohole trapping. If the gap size is comparable to the particle size (25 nm gap with 20 nm particle), there is a large jump in the optical transmission, corresponding to strong trapping. With a larger gap or smaller gap, the particle is not optimally fitted for the local field enhanced region. If the particle is larger than the gap, it does not fit; if the particle is smaller, then the gap could be smaller to create a stronger local field and enhanced transmission due to gap plasmons [61].

Figure I.6 shows the trapping of single 12 nm diameter silica spheres (refractive

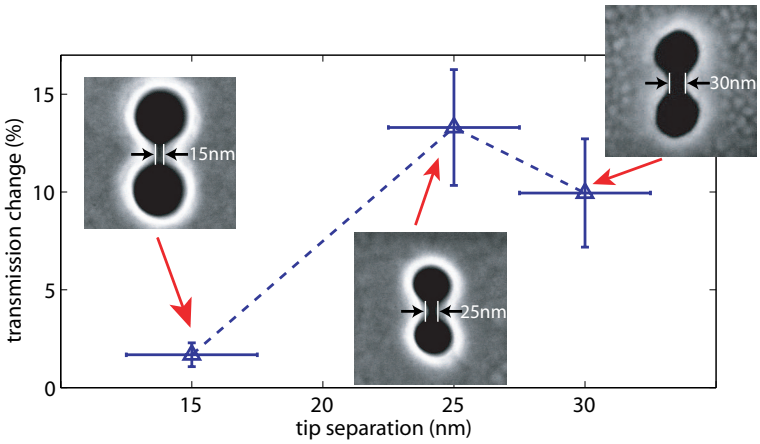

Figure E.5: The changes in optical transmission as a function of double-nanohole tip separation, when trapping 20 nm polystyrene nanospheres. Error bars are from the resolution of the SEM image (horizontal axis) and from the standard deviations in transmission jumps (vertical axis). The insets show SEM images of different double-nanoholes used.

index 1.45). By use of a double-nanohole with a 15 nm tip separation, barely larger than the particle size, and an incident optical power of 7.2 mW, trapping of 12 nm silica spheres was obtained for 30.0±12.4 s. A plot relating the trapping time with incident power shows an exponential dependence similar to Figure I.4 (please refer to Figure F.6 in the Supporting Information). We compare this result with the previous SIBA trapping of polystyrene nanospheres using a circular hole [5]. In that experiment, single 50 nm polystyrene spheres (refractive index 1.57) were trapped for 10 s using 1.9 mW of optical power in the optimized circular hole. Considering the usual perturbative approach [23, 196], going from a 50 nm polystyrene sphere to a 12 nm silica sphere would require 142 times of light intensity, considering both reductions in the size and in the refractive index. Taking into account the tighter focusing spot in this work, 81 mW of optical power would be needed to trap the 12 nm silica sphere. By using a double-nanohole, we used only 7.2 mW of optical power, over 10 times less than the perturbative scaling from the SIBA optical trap with a circular hole. This type of analysis is only for discussion since the perturbative theory is not valid for SIBA aperture trapping, and a more detailed theory of trapping for varying hole shapes needs to be developed.

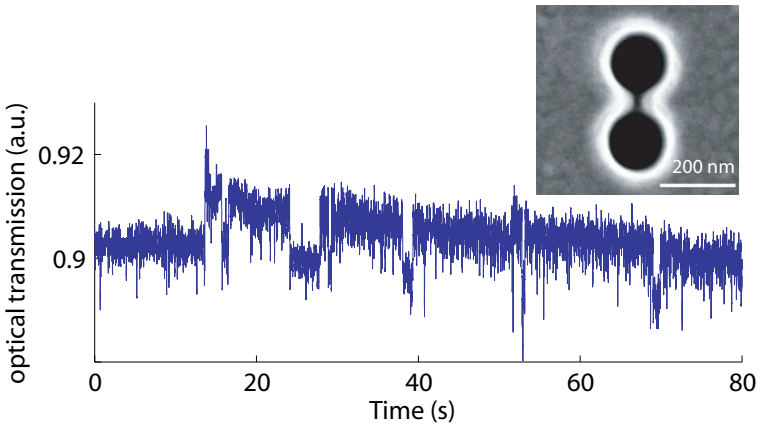

Figure E.6: Optical trapping of 12 nm silica spheres using a double-nanohole with a 15 nm tip separation.

As a future evolution to the double-nanohole trapping system, we suggest an optical "nanopipet" which can trap a single nanoscale particle and move it to a desired position. This can be realized by milling the proposed double-nanohole structure on a near-field probe [4, 111]. This nanopipet can have many other applications in addition to optical trapping. The signal shifting at the arrival of a small particle can be used for optical sensing [123, 124], and the large local field enhancement in the

double-nanohole is suitable for spectroscopy such as SERS mapping [111].

The double-nanohole optical trap has a significant potential for applications in biology. The capability to trap a single 12 nm dielectric sphere opens the door to trap the smallest virus particles, or virions. By allowing for the isolation and manipulation of individual virions, the optical nanopipet may be used to study population diversity as it relates to infection. Within a single species virus population there is great heterogeneity. Most virus studies sample that heterogeneous population, and this ensemble averaging is a major issue. Only very few works have managed to study virus infection in isolation [154].

In conclusion, we experimentally observed stable trapping of a 12 nm silica sphere, using a double-nanohole on Au film. Counterintuitively, the double-nanohole could trap small particles more easily than large ones at a single well-defined stable point. We attribute this behavior to the high transmission power concentration in an extremely small area between the two tips of the double-hole. The best case for double-nanohole optical trapping is to use a tip separation that is barely larger than the particle size, and this was confirmed by studies using double-nanoholes with different dimensions. For future works, we suggest that an optical nanopipet structure with a double-hole on a near-field probe will give even larger optical force and enable the manipulation of the trapped particle. Such an optical nanopipet will be of interest, for example, for the study of virus population diversity as it relates to infection.

Supporting Information

Design of the Double-Nanohole

To design a double-nanohole for the self-induced back-action optical trapping experiment, we used a commercially available comprehensive finite-difference time-domain (FDTD) simulation tool to compute the transmission spectrum through the double-nanohole. Figure F.5a shows the schematic setup of the simulation. The three dimensional simulation region is enclosed with perfectly-matched layer (PML) boundaries. A total-field scattered-field source is used to avoid truncation artifacts at the PML boundaries. The electric field of the source is aligned with the tips in the double-nanohole. The Au permittivity values were taken from a previous work [47]. A 2 nm mesh was also used around the silver nano-prism to ensure that plasmonic effects were accurately captured. Figure F.5b shows the transmission spectrum through a

double-hole with a 110 nm diameter for each hole and a 30 nm tip separation. The main transmission peak is at 955 nm, slightly shorter than the 975 nm trapping beam.

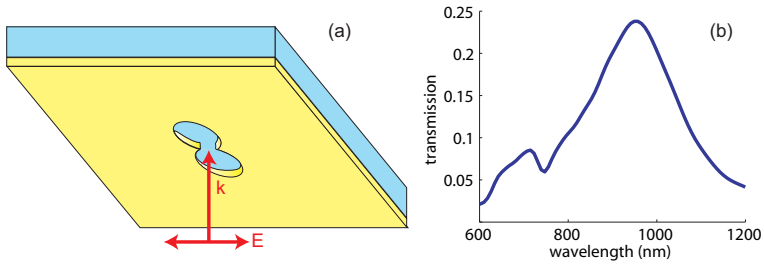

Figure E.7: (a) Schematic drawing of the finite-difference time-domain simulation setup. (b) Transmission spectrum through the designed double-nanohole.

Trapping of a 12 nm Silica Sphere

Figure F.6 shows the dependence of the trapping time on the incident optical power. The data was taken using a double-nanohole with a 15 nm tip separation to trap 12 nm silica spheres. The error bars are the standard deviations of the trapping times for multiple events (¿7 events for each power). The straight line is an exponential fit of all the data (noting the semi-log plot). An exponential dependence similar to the 20 nm polystyrene sphere experiments is shown.

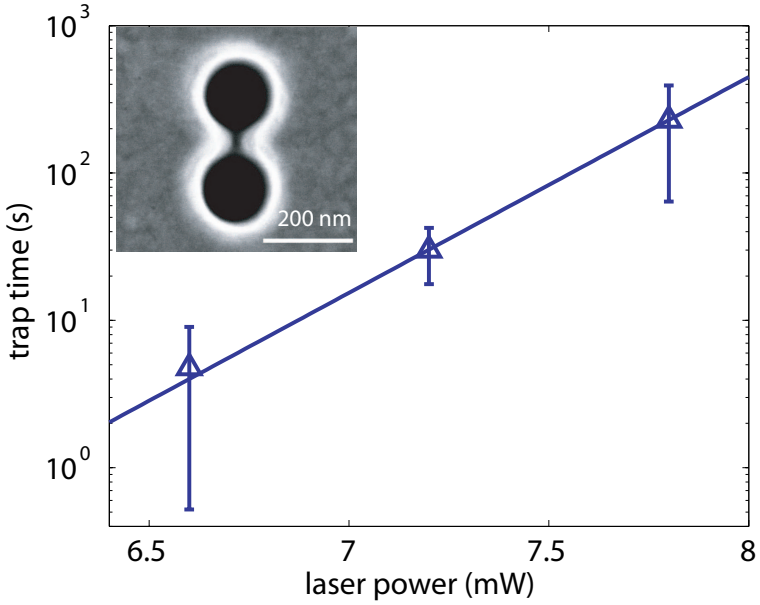

Figure E.8: Trapping time as a function of incident power, studied using 12 nm silica spheres and a double-nanohole with 15 nm tip separation. The triangles are the mean values of experiment data taken, the error bars are the standard deviation of the data, and the straight line is the exponential fit to the data. The inset shows the SEM image of the double-nanohole.

Appendix F

Optical Trapping of a Single Protein

Originally published:
Y. Pang and R. Gordon. Optical trapping of a single protein. Nano Letters, 12(1):402–406, 2012.

ABSTRACT

We experimentally demonstrate the optical trapping of a single bovine serum albumin (BSA) molecule that has a hydrodynamic radius of 3.4 nm, using a double-nanohole in an Au film. The strong optical force in the trap not only stably traps the protein molecule but also unfolds it. The unfolding of the BSA is confirmed by experiments with changing optical power and with changing solution pH. The detection of the trapping event has a signal-to-noise ratio of 33, which shows that the setup is extremely sensitive to detect the presence of a protein, even at the single molecule level.

Trapping techniques [23, 204, 205] can gently immobilize and manipulate small objects, which is useful in many applications. In particular, optical trapping, which uses the momentum change of light scattering to impart forces on small objects, has been applied to trap dielectric nanospheres [23, 24, 41, 196], carbon nanotubes [25], semiconductor nanowires [26], and metal nanoparticles [27–29, 206]. Optical trapping

has great potential in microbiology applications because of its ability to trap tiny bioparticles without inducing damage. Direct optical trapping of biological particles, however, has been limited to relatively large objects, for example, living cells [32], bacteria [33], 300 nm long tobacco mosaic virus particles [33] and DNA strains [39]. For trapping smaller particles, a common approach is to tether the end of the particle onto a large micrometer-sized bead [34–36]. This introduces steric challenges, hydrodynamic effects and experimental complexity (e.g., the need for binding). Therefore, it is desired to directly manipulate nanoparticles with optical forces without tethering. Direct trapping and manipulation of smaller biological particles remain challenging, primarily because the difficulty of trapping a nonresonant dielectric particle dramatically increases as the particle size decreases. For example, using a traditional perturbative trap, the laser power needed to trap a particle for a given average time scales with the inverse fourth power of the particle size [5].

In the recent years, optical trapping has been extended to nanometer scales. Trapping dielectric particles of 10-50 nm has been shown by both experimental techniques [5, 39, 42] and theoretical computations [38, 43, 44]. Improving on our past successes [5], recently we trapped a 12 nm silica sphere using a double-nanohole in an Au film and found that such small particles could be even more easily trapped than larger ones with specifically designed nanoholes [6]. These techniques provide promising paths toward trapping of the smallest biological particles, for example, a single virus particle (or a virion), or a single protein molecule.

In this work, we report the trapping of a single protein: the bovine serum albumin (BSA) molecule with a hydrodynamic radius of 3.4 nm in the N-state [207]. The trapping is achieved using an improved double-hole setup. We observe that the trap can actually unfold the protein. Furthermore, the trapping configuration is simultaneously a highly sensitive sensor of the individual BSA molecules.

Figure I.1a,b shows a schematic of the experimental setup (based on the Thorlabs optical tweezer kit OTKB). A doublenanohole was milled on a commercially available 100 nm thick Au film on a glass substrate with a 2 nm Ti adhesion layer (EMF Corp.) using a focused ion beam. Figure I.1c shows a scanning electron microscope (SEM) image of the doublenanohole with two sharp tips (cusps) separated by 15 nm. One percent BSA solution (w/w) in PBS buffer was sealed at the Au surface using a microwell consisting of an 80 μm thick poly(dimethylsiloxane) spacer and a 150 μm thick glass microscope coverslip. This setup is improved compared to our past work [6] by using a shorter wavelength 820 nm laser (Sacher Lasertechnik Group, Model TEC

120) that has approximately 4× better detection efficiency for the photodetector and helps with trapping smaller objects (due to the favorable wavelength-dependent scaling). The 820 nm wavelength also has a lower absorption in water. The laser was focused onto the sample using a 100× oil immersion microscope objective (1.25 numerical aperture) in a polarization with the electric field aligned with the tips of the doublehole (along the x-direction in Figure I.1c). The transmitted light through the double-nanohole was collected using a 10× condenser microscope objective (0.25 numerical aperture) and measured by a silicon-based avalanche photodiode (APD) (Thorlabs APD110A). A data acquisition board was used to record the voltage values generated by the APD at a sampling frequency of 2 kHz.

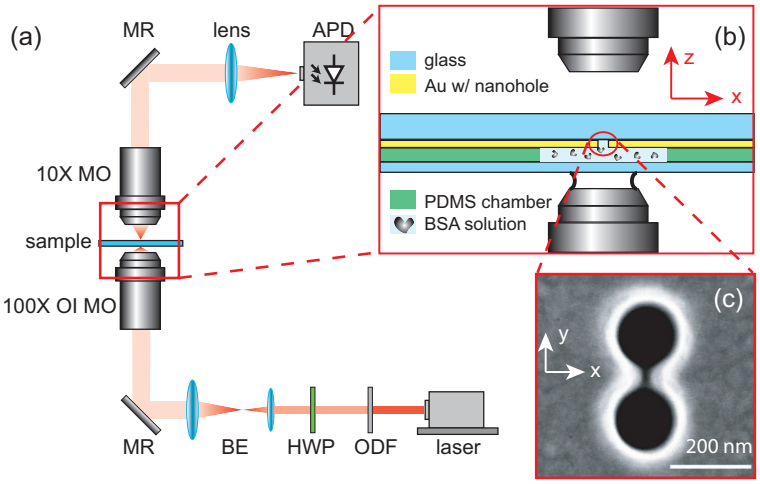

Figure F.1: (a) A schematic of the trapping experiment. Abbreviations used: ODF = optical density filter; HWP = half-wave plate; BE = beam expander; MR = mirror; MO = microscope objective; OI MO = oil immersion microscope objective; APD = avalanche photodiode. (b) An enlargement of the red rectangle part in (a), showing details of the composition of the sample in the microfluidic chamber, the setup of the oil immersion microscope objective, and the condenser microscope objective. (c) An SEM image of the double-nanohole.

Figure I.2 shows time traces of the transmission power through the double-nanohole. When a BSA molecule with a greater refractive index than that of water comes between the tips of the double-nanohole, it dielectrically loads the region with the most intense local field enhancement, thereby significantly increasing the light transmission. By Newton's third law, the change of light momentum reacts on the molecule, forming an optical force, which favors trapping [5]. The distinct jumps in the light transmission serve also as a convenient and highly sensitive sensor for the individual

molecules with a signal-to-noise ratio (SNR) of 33. The type of trapping seen in Figure I.2 was found consistently for all trapping events observed and for measurements on different days over a period of months.

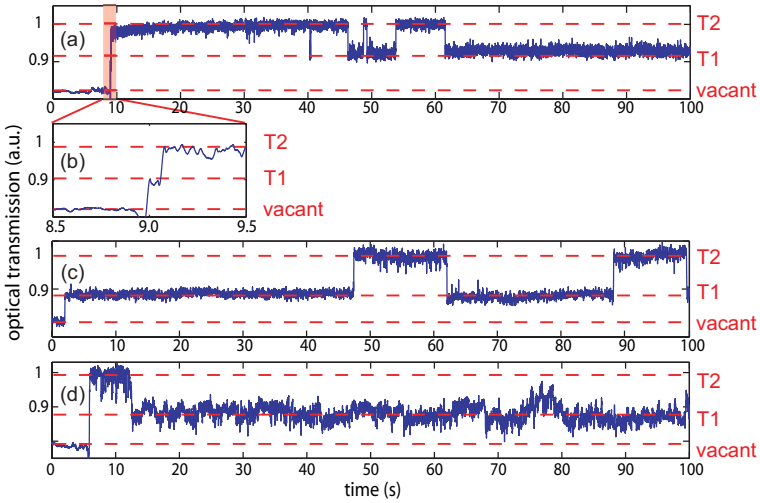

Figure F.2: Time traces of the optical power transmitted through the double-nanohole, using a BSA solution in PBS buffer with pH = 7.4, using an incident optical power of (a) 13.4 mW [(b) zoom-in of (a)], (c) 10.6 mW, and (d) 8.5 mW. The vacant state and two trapping states (T1 and T2) are clearly shown.

Figure I.3 shows the reversibility of trapping, which demonstrates that the optical force is the underlying mechanism in trapping. To block the BSA from adsorbing to the Au surface, we formed a monolayer of mPEG thiol on the Au surface before the BSA trapping experiment [135]. This was done by immersing the Au film sample in an 5 mM aqueous solution of mPEG thiol (with a molecular weight of 5000) at room temperature overnight, and rinsing thoroughly with deionized water to remove any nonchemisorbed mPEG thiol molecules. We then observed the release of the BSA after it has been trapped. To do this, we turned off the trapping laser beam after a trapping event, and then turned it back on after $\tilde{1}0$ s. As Figure I.3 shows, the transmission power falls back to the "vacant" state each time the trapping laser is reapplied after being turned off, and jumps back to the trapping states after a certain amount of time showing retrapping (refer to Supporting Information for more details). This result clearly shows that the BSA is released when the trapping laser beam is turned off.

To further demonstrate the role of the optical force on the trapping, we show that there is a minimum laser power needed for trapping. We tried the trapping

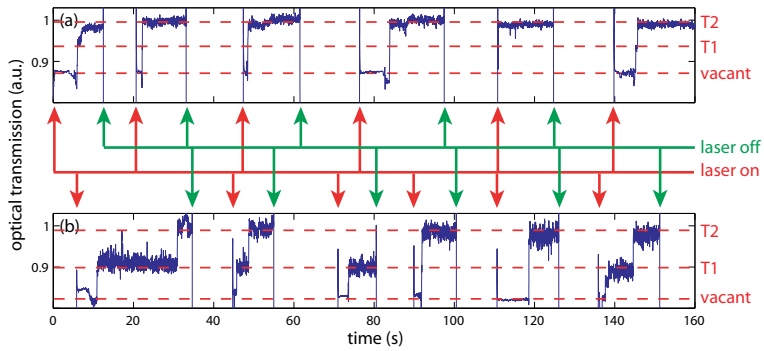

Figure F.3: Time traces of the optical power transmitted through the double-nanohole, showing the reversibility of the trapping by turning the laser on and off, using an incident optical power of (a) 13.4 mW and (b) 5.3 mW.

experiment using a low laser power of 3.5 mW. If a BSA molecule was immobilized between the tips of the double-nanohole, we would observe a jump in the signal with an SNR of $\tilde{8}$; however, this was not observed for more than 30 min. Therefore, the critical role of optical force in the trapping is confirmed.

In our past experiments, we were able to trap 12 nm diameter silica spheres24 that do not have a tendency to adsorb to gold. It is expected that the BSA has a similar polarizability as those silica spheres because it is almost the same volume, and it is also slightly elongated, which increases the polarizability with respect to a sphere of the same volume.

An interesting feature of the BSA trapping experiment is the ubiquitous appearance of two discrete levels of the trapping state. We consider two hypotheses to explain this "doublestep". First, a single BSA molecule and a two-molecule dimer might be trapped in the lower (T1) and the higher (T2) trapped states, giving a different dielectric loading area and therefore a different transmission change. However, that hypothesis is deficient in explaining that the double-step appeared in every instance of trapping, and furthermore, it was never observed in our polystyrene and silica nanospheres studies [6].

As a more likely hypothesis, we suggest that the BSA molecule is actually unfolded after being trapped. Unfolding between the N and F forms of BSA has been observed by changes in pH [128]. The optical polarizability increases with the elongated F form of the BSA, hence a stronger trapping potential is formed and more light is transmitted. In other words, the trap is strong enough to actually unfold the protein, which is not surprising since the trap already overcomes the Brownian motion of the protein for time scales of the order of minutes. Figure I.2b,c shows that for lower powers the particle spends less time in the unfolded state. This supports the hypothesis that the trap actually unfolds the protein because the optical force is weaker for lower powers. Figure I.3 also shows similar dependence of the unfolding tendency on the trapping power at the instance when the trapping beam is turned on.

In addition to the dependence on the incident power, the step between the two trapped states corresponds to an optical force in aperture trapping through Newtons third law, as described above. Since the step to trap folded BSA is comparable to the step to unfold, it stands to reason that the energies associated with each of these events are comparable and therefore of the order of the energy associated with thermal motion itself. It is expected that this is more than sufficient to unfold BSA because

it has a denaturing temperature of only 50 °C [208].

There is also expected to be a smaller contribution to the ability to unfold the protein that arises due to increased local temperatures at high powers. The percentage power changes are much larger than the absolute temperature changes, and so this effect is expected to be negligible. If the temperature change was noticeable, we would see a comparable reduction in the trapping time and increased fluctuations due to Brownian motion for increased laser power; however, trapping time reduction was not observed and an opposite dependence of fluctuation on laser power was observed. The working temperature at the trapping point is clearly below 50 °C since this is the denaturing temperature of the BSA [208]. If the temperature was higher than 50 °C, the BSA would be irreversibly unfolded, and we would not observe reversible unfolding as Figure I.2 shows. Under this small temperature change, we believe that thermal effects have negligible contribution to the trapping and unfolding of BSA.

To further test the protein unfolding hypothesis, we have repeated the trapping experiment in a solution with a lower pH of 3.57. Under such a pH, the BSA molecule is already in the F form [128]. Figure I.4 compares the time traces of transmitted optical powers under pH = 3.57 and pH = 7.4 environments, using the same incident laser power of 8.4 mW. As expected, the doublestep only appears in the higher-pH environment; it does not appear in the lower-pH but otherwise identical environment, neither at the transition when the trapping initially starts nor in the trapped state. This result confirms that the double-step in the transmission power comes from transitions between two forms of the BSA molecule.

The fluctuations in the optical transmission once the particle is trapped are predominantly the result of Brownian motion, not noise from the detection system. The noise from the detection system can be observed before the trapping event and it is significantly lower (by a factor of 5). We have performed a spectral analysis of the intensity fluctuations and found a lower frequency 3-dB shoulder for the unfolded protein than the folded protein (see Supporting Information), which may be attributed to the increased drag associated with the unfolded state for motion along the z-axis, with BSA's long axis along the x-direction. Since the trapping minimum is at the surface, this is clearly not a harmonic potential. Furthermore, there are hydrodynamic interactions with the surfaces of the aperture. Therefore, we are reluctant to perform spectral analysis to extract stiffness parameters, as has been done in the past [24, 136].

The SNR of this system (i.e., the system noise, not the fluctuations from Brown-

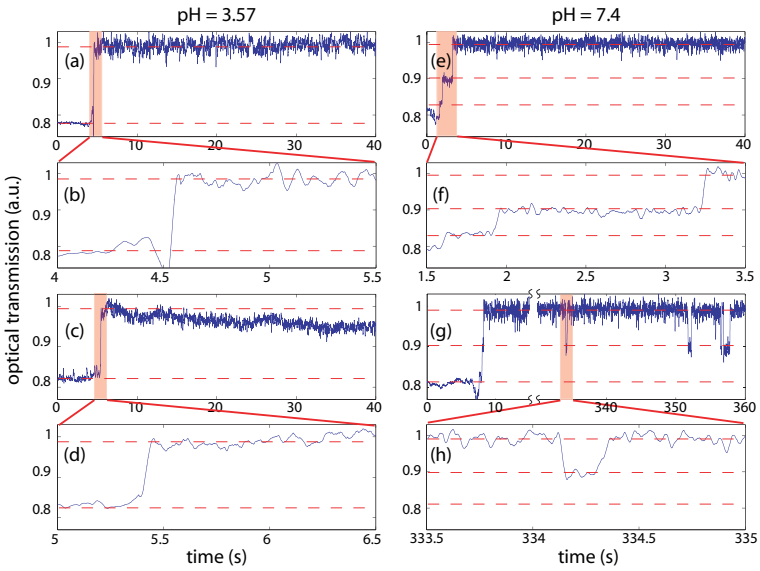

Figure F.4: The time traces of the optical power transmitted through the double-nanohole, using an incident optical power of 8.4 mW in a BSA solution in PBS buffer with (a-d) pH = 3.57, and (e-h) pH = 7.4.

ian motion) is 33. Therefore, this double-nanohole is very sensitive with potential to be developed into a biosensor for single protein detection. Sensing and trapping are often the dual-functionality of one optical system. For example, whispering gallery mode optical microresonators are common setups for both sensing [123–125] and trapping [40, 41]. Compared to an optical microresonator, the double-nanohole does not rely on a high-quality resonance and the sensing can be performed by simply measuring the transmitted power. On the basis of the single molecule studies of this work, we hope to extend this sensitivity to monitor protein binding at the single molecule level [209], which has many potential applications in, for example, drug discovery [129] as well as disease and infection detection [130]. Of course, to have a sensor requires both sensitivity and specificity. Therefore, we will have to modify our existing setup to allow for specific identification of molecules for which we have experience with Raman spectroscopy [14] and antigen.antibody binding [81, 84]. There is also the potential to do fluorescence-based identification, provided quenching at the Au surface can be avoided.

In conclusion, we have demonstrated optical trapping of a single BSA protein using a double-nanohole in an Au film. Interestingly, a double-step in the monitored optical transmission always showed up in the time traces due to unfolding of the BSA molecule from the strong optical force in the trap. This was confirmed by experiments of changing the incident laser power and of changing the solution pH. The high SNR in the optical transmission through the double-nanohole at trapping events makes the optical trap also a very sensitive sensor, albeit without specificity at present. We plan to extend the system to sense protein binding at a single molecule level in the future.

Supporting Information

Releasing the Trapped BSA

Figure F.5 reproduces Figure I.3a in the paper, with a zoom-in at an instant when the laser is turned on, clearly showing the vacant state before the trapped state. The transmission signal always starts with a vacant state when the trapping laser beam is turned on shows that the BSA is released when the trapping beam is turned off.

Thermal Fluctuation Spectrum of the Trapped BSA

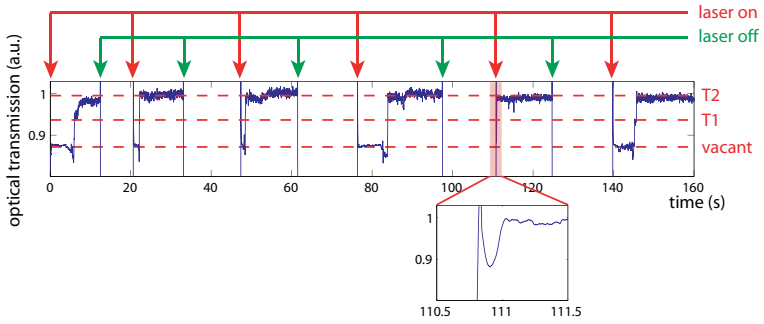

Figure F.5: Time traces of the optical power transmitted through the double-nanohole, showing the reversibility of the trapping by turning the laser on and off, using an incident optical power of 13.4 mW. The inset is a zoom-in to the signal.

Figure F.6 shows the thermal fluctuation spectrum of the trapped BSA. This spectrum was obtained by performing a fast Fourier transform to a time signal taken with 5 kHz sampling frequency. A nonlinear least square method was used to fit the spectrum, and the 3 dB turn-over frequencies were found to be 98 Hz for the folded BSA and 54 Hz for the unfolded BSA.

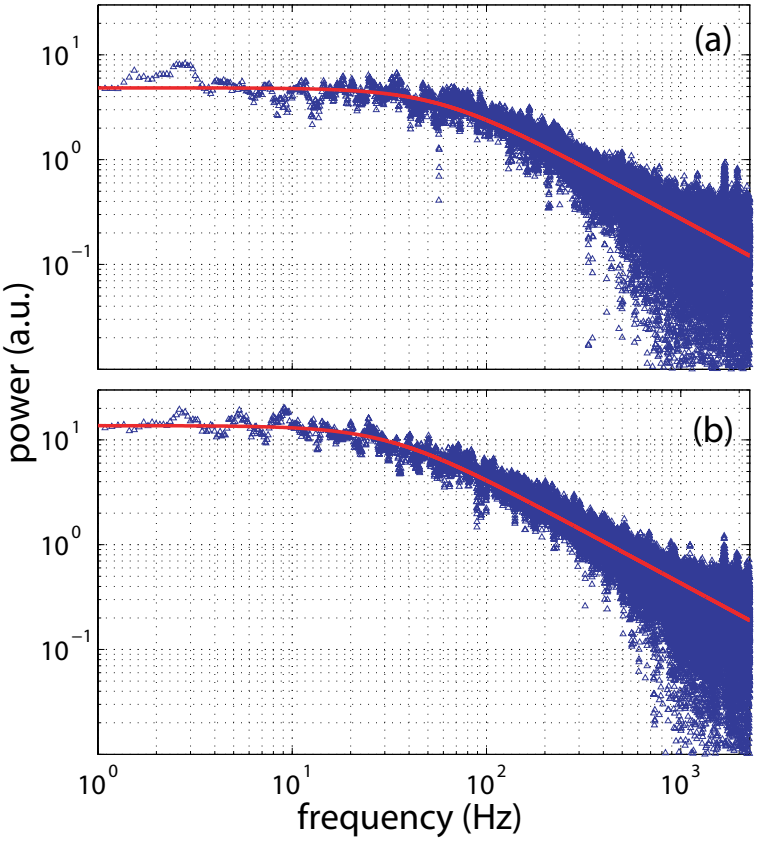

Figure F.6: The experimental thermal fluctuation spectra (blue triangles) and fits (red curves) of (a) folded BSA and (b) unfolded BSA.

Appendix G

Metal Nano-Grid Reflective Wave Plate

Originally published:
Y. Pang and R. Gordon. Metal nano-grid reflective wave plate. Optics Express, 17(4):2871–2879, 2009.

ABSTRACT

We design an optical wave plate using metallic nano-grids that operates in reflection mode. A single-mode matching technique is presented as a general method to design nano-grids with the desired phase difference between the reflected TM and TE polarizations. Our theoretical approach also allows for angled incidence calculations, and the approach was validated by comprehensive finite-difference time-domain electromagnetic simulations, for incident angles ranging from 0° to 45°. The zero-order wave plate is thinner than a single optical wavelength and therefore it is expected to have improved broad-band functionality when compared with existing birefringent crystal wave plates, for which an example is provided. The proposed wave plate is simple and compact, and can be built with existing nanofabrication techniques. Furthermore, it has significant potential for several applications including liquid-crystal displays devices and laser feedback setups.

G.1 Introduction

Polarization sensitive optical devices are essential optical elements for many optical experiments and devices. A wave plate is an optical device through which different polarizations receive different phase shifts. For example, a quarter-wave plate (QWP) introduces an extra $\pi/2$ phase difference between the two perpendicular polarizations. Most wave plates are made of birefringent materials [138–142] or artificial birefringence materials consisting of dielectric grids [210, 211], which provides different refractive indices for different polarizations along perpendicular axes as they transmit through the crystal. On the other hand, a polarizer is an optical device that permits one polarization of light to penetrate through and blocks the other perpendicular polarization. Wire-grid polarizers have long been used for long-wavelength applications [212, 213]. Recently, advances in nanofabrication have allowed for wire-grid polarizers that operate in the region from UV to near-IR [210, 211, 214–221]. To the best of the authors' knowledge, no wave plates, either on available markets or in research, are built using metallic nano-grid structures.

In this paper, a metallic nano-grid structure is analyzed to build a wave plate that operates in reflection mode. We demonstrate, both by theory and by comprehensive numerical simulations, that as light reflects from our structure, the TM polarization will receive an extra phase over the TE polarization. This phase difference can be tuned by changing the incident angle and the depth of the grid. The operation of the wave plate structure is based on the surface plasmon mode within the grids. In our theoretical analysis, a single-mode mode-matching technique is applied. This metallic nano-grid structure is simple and compact, and as it retards the reflected light instead of the transmitted light, we believe that it will introduce an extra degree of freedom when used in an optical experiment. For example, our reflective wave plate can be used in reflection geometry liquid-crystal displays [144], or for feedback experiments on lasers [145]. The proposed wave plate is amenable to existing nanofabrication techniques [222–224].

G.2 Theoretical Calculations

Figure G.1 shows the nano-grid structure analyzed in the paper. It is a metallic grid structure surrounded by dielectric background. The widths of a groove and grid are d_d and d_m, and are both smaller than a wavelength of the incident light. We choose

gold (Au) as the material of the structure because gold has a smaller material loss for the chosen near-IR wavelength of interest; however, the approach may be extended to other wavelengths and materials. The working principle of this nano-grid wave plate is as follows: the TE polarization is reflected at the top of the grids since it is cutoff within the grid region, whereas the TM polarization can penetrate into the grids and it is reflected at the bottom metal interface. In this way, the TM polarization gains an extra phase-shift due to the extra length of propagation into the grooves.

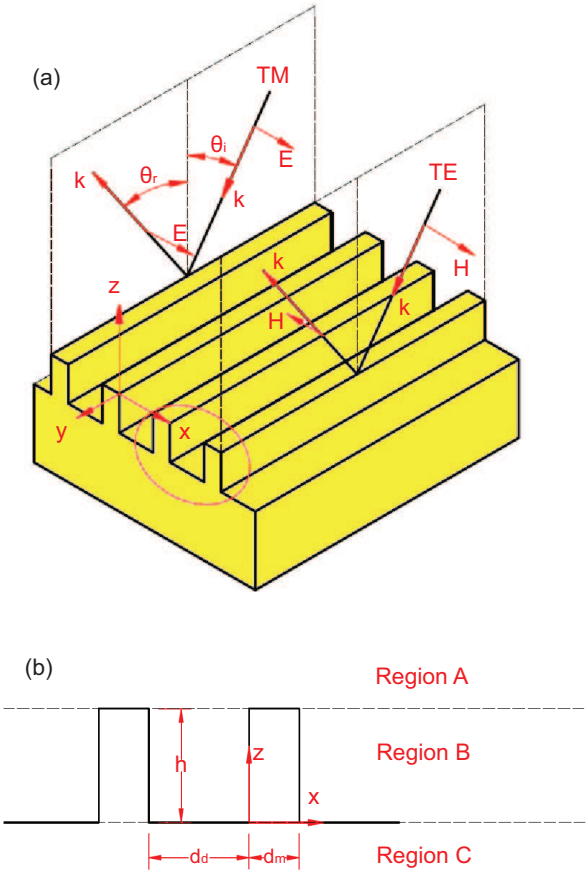

Figure G.1: Schematic showing the metallic nano-grids on a metallic substrate. (a) The conventions of the TM and the TE polarizations are shown: the electric field of the TM polarization and the magnetic field of the TE polarization are parallel to the $x-$direction. (b) Enlargement of the cross-section of the grid structure (the circled part in (a)). The dielectric region above the grid, the grid region and the metal substrate are referred to as Regions A, B and C.

In order to design a wave plate to give a desired phase shift between the TE and the TM polarizations, we need to know the propagation constants β of each polariza-

tion within the grid, and the phases of reflection. The TM polarization propagates in the grid in the form of a coupled surface plasmon polariton (SPP) mode; these are a periodic version of the single gap-mode for which there have been several investigations since 1969 [143]. To calculate the propagation constant β of the SPPs in an array of metallic grids, we match the boundary conditions between a metal layer and an air layer in the grids, which provides the following relations:

$$\frac{\tanh\left(\sqrt{\beta_{TM}^2 - k_0^2\epsilon_m}(x - \frac{d_m}{2})\right)}{\tanh\left(\sqrt{\beta_{TM}^2 - k_0^2\epsilon_d}(x + \frac{d_d}{2})\right)} = -\frac{\epsilon_m}{\epsilon_d}\frac{\sqrt{\beta_{TM}^2 - k_0^2\epsilon_d}}{\sqrt{\beta_{TM}^2 - k_0^2\epsilon_m}} \tag{G.1}$$

for the TM polarization and

$$\frac{\tanh\left(\sqrt{\beta_{TE}^2 - k_0^2\epsilon_m}(x - \frac{d_m}{2})\right)}{\tan\left(\sqrt{k_0^2\epsilon_d - \beta_{TE}^2}(x + \frac{d_d}{2})\right)} = \frac{\sqrt{\beta_{TE}^2 - k_0^2\epsilon_d}}{\sqrt{k_0^2\epsilon_m - \beta_{TE}^2}} \tag{G.2}$$

for the TE polarization, where ϵ_m and ϵ_d are the relative permittivities of metal and dielectric background, and $k_0 = \frac{2\pi}{\lambda_0}$ is the wave number in free space. From these relations, the desired propagation constants in the grid-array can be calculated for the TM SPP mode and the TE cutoff mode.

With the propagation constants, $\beta_{TE,TM}$, we can determine the phase of propagation inside the grid for the TM polarization. Now we need to calculate the reflection coefficients of both polarizations. This is done by single-mode mode-matching technique. We consider a single-mode truncation in every region due to the subwavelength scale of the grid structure. Furthermore, for the TM case, it is a good approximation to neglect multiple reflections within the grid region. The validity of these approximations will be discussed in an example.

We now use the mode-matching procedure to calculate the reflection of the TM polarization at the top of the grid structure, but it should be noted that the same calculation process is used on both polarization at different positions. As a general case, linearly polarized light is incident in the plane of the grid's grooves at an angle of θ_i. The sum of the incident and reflected fields in the free-space region (Region A in Figure G.1(b)) above the grid are given by:

$$H_A(x, y = 0, z = 0^+) = -\cos\theta_i(1 - r_{TM}^t)\hat{y} + \sin\theta_i(1 + r_{TM}^t)\hat{z}, \tag{G.3}$$

$$E_A(x, y = 0, z = 0^+) = \frac{k_0(1 + r_{TM}^t)}{j\omega\mu_0}\hat{x}, \tag{G.4}$$

where $k_0 = \frac{2\pi}{\lambda_0}$ is the propagation constant of the light in free space, r^t_{TM} is the reflection coefficient of the TM mode, the superscript t stands for "top". Notice that the reflection coefficients in this work are for the lowest order mode, as we are considering a single-mode truncation in the mode-matching. The magnetic fields within the grid (Region B in Figure G.1(b)) are:

$$H_B(x, y = 0, z = 0^-) = t^t_{TM} H_d \cosh\left[\sqrt{\beta^2_{TM} - k_0^2 \epsilon_d}(x + \frac{d_d}{2})\right](-\cos\theta_t \hat{y} + \sin\theta_t \hat{z}) \tag{G.5}$$

for $-\frac{d_d}{2} < x < 0$ (dielectric region) and

$$H_B(x, y = 0, z = 0^-) = t^t_{TM} H_m \cosh\left[\sqrt{\beta^2_{TM} - k_0^2 \epsilon_m}(x - \frac{d_m}{2})\right](-\cos\theta_t \hat{y} + \sin\theta_t \hat{z}) \tag{G.6}$$

for $0 < x < \frac{d_m}{2}$ (metallic region), where t^t_{TM} is the transmission coefficient of the TM SPP mode into the grid, ϵ_d and ϵ_m are the permittivities of dielectric and metal, θ_t is the transmission angle into the grid region, and β_{TM} is the propagation constant of the TM polarization. The cosh dependence of the field along the x-axis comes from the coupled SPP modes. Applying the boundary condition at the metal-dielectric interface of the grids, with $H_m = 1$, we obtain:

$$H_d = \frac{\cosh\left[\sqrt{\beta^2_{TM} - k_0^2 \epsilon_m}\frac{d_m}{2}\right]}{\cosh\left[\sqrt{\beta^2_{TM} - k_0^2}\frac{d_d}{2}\right]}. \tag{G.7}$$

It is also noted that the y component of the propagation constant k_y remains unchanged in regions A and B since the structure is uniform in the y direction, therefore the transmission angle θ_t can be found:

$$\theta_t = \arcsin\left(\frac{k_0 \sin\theta_i}{\beta_{TM}}\right). \tag{G.8}$$

The electric field E_B within the grid (Region B) can now be found by applying Ampere's law to the magnetic field, and is not shown here.

Now we apply the mode matching criteria at the interface between uniform dielectric (Region A) and the grid (Region B) by equating the transverse field components:

$$E_{A,\perp}(z = 0^+) = E_{B,\perp}(z = 0^-); \tag{G.9}$$

$$H_{A,\perp}(z=0^+) = H_{B,\perp}(z=0^-). \tag{G.10}$$

The subscript $\perp$ denotes the transverse components, i.e. only the $x-$ and the $y-$components of the fields. To use the orthogonality of the fields, we take the cross product of both sides of Eqs. G.9 with the complex conjugate of the magnetic field in region A, $H^*_{A,\perp}$, and integrate over the region $-\frac{d_d}{2} < x < \frac{d_m}{2}$ (i.e. the region between the mid-points of a groove and an adjacent metal wire):

$$\int_{-d_d/2}^{d_m/2} E_{A,\perp} \times H^*_{A,\perp} dx = \int_{-d_d/2}^{d_m/2} E_{B,\perp} \times H^*_{A,\perp} dx. \tag{G.11}$$

Similarly, take the complex conjugate on both sides of Eqs. G.10, cross product both sides with the electric field in region B, $E_{B,\perp}$, and integrate over the region $-\frac{d_d}{2} < x < \frac{d_m}{2}$:

$$\int_{-d_d/2}^{d_m/2} E_{B,\perp} \times H^*_{A,\perp} dx = \int_{-d_d/2}^{d_m/2} E_{B,\perp} \times H^*_{B,\perp} dx. \tag{G.12}$$

Eqs. G.11 and G.12 can now be solved using the expressions of the fields derived in G.4, G.3, G.5 and G.6 to get the complex reflection coefficient r^t_{TM}. The same approach can be used to find the reflection coefficients r^t_{TE} of the TE polarization at the top of the grid and r^b_{TM} of the TM polarization at the bottom of the grid (the superscript b stands for "bottom"). At the bottom of the grid, the TM mode in the grids is matched to the decaying plane wave in bulk metal instead of to the propagating plane wave in dielectric.

With β_{TM}, r^t_{TE} and r^b_{TM} available, the phase difference between the TE and TM modes reflected from the reflective grid wave plate can be determined:

$$\Delta\phi = Arg(r^b_{TM}) - Arg(r^t_{TE}) + \frac{2h\beta_{TM}}{\cos\left[\arcsin\left(\frac{k_0 \sin\theta_i}{\beta_{TM}}\right)\right]} - 2hk_0 \tan\left[\arcsin\left(\frac{k_0 \sin\theta_i}{\beta_{TM}}\right)\right] sin\theta_i, \tag{G.13}$$

where Eq. G.8 was used for the transmission angle θ_t.

G.3 Designing a QWP and a HWP

As an example, we designed a QWP for a wavelength of $\lambda_0 = 826.4$ nm at perpendicular incidence. The widths of the nano-grids and the grooves were chosen to

be $d_m = 50$ nm and $d_d = 100$ nm. The reason for this choice is that this groove width is below cutoff for the TE polarization at the chosen wavelength, and nano-metallic wiregrids at this scale can be readily fabricated [222]. We chose to use gold (Au) as the material, which had a relative permittivity $\epsilon_m = -28.74 + 2.010i$ at $\lambda_0 = 826.4nm$. The surrounding material was assumed to be air with relative permittivity being $\epsilon_d = 1$. We went through the steps described above and found that the reflection coefficient were $r^t_{TE} = 0.984\angle 223.5°$ for the TE polarization at the top of the grids, $r^b_{TM} = 0.985\angle 202.8°$ for the TM polarization at the bottom of the grids and $r^t_{TM} = 0.0409\angle 182.5°$ for the TM polarization at the bottom of the grids. As expected, both r^t_{TE} and r^b_{TM} were close to 1 in amplitude, and r^t_{TM} was close to zero in amplitude. Therefore, the approximation to neglect multiple reflections within the grid region was valid. For the resulting phase difference between the reflected TE and TM polarizations to be $\Delta\phi = 90°$ at an incident angle of $\theta_i = 0°$ (perpendicular incidence), the depth of the grids was calculated to be $h = 107.4nm$ by using Eq. G.13.

Figure I.2(a) showed the simulation result of the TE and TM waveforms perpendicularly reflected from the QWP designed above, simulated using a commercially available finite-difference time-domain (FDTD) electromagnetic simulating software package. Clearly, the reflected TM wave lagged the TE wave by a quarter of the wavelength. Again, this is because the TM polarization travels an extra distance into the grid. Clearly in the animation, the TM polarization traveled into the grid whereas the TE polarization was cutoff within the grid and was reflected at the top of the grid. This design of a QWP could be easily modified to build a half-wave plate (HWP); the only parameter needed to be changed was the height of the grid structure. To design a HWP, we plug $\Delta\phi = 180°$ into Eq. G.13 and found the corresponding height to be $h = 174.7nm$. The simulation result of this HWP was shown in Figure I.2(b), and the reflected TM wave lagged the TE wave by half a wavelength.

Figure I.3 showed the results of our investigation in angled incident cases. While keeping the height of the grids constant at $h = 107.4$ nm (same as the QWP designed above) we had chosen 3 cases: $\theta_i = 15°, 30°, 45°$ and compared again the FDTD simulation results with the theoretical results in each cases, together with the perpendicular incident case where $\theta_i = 0°$. It was clear that the simulation and theoretical results followed the same trend: the phase difference between the reflected TE and TM wave increases as the incident angle increases. This was a good indication that the one mode truncation assumption of the theoretical analysis was a valid

simplification.

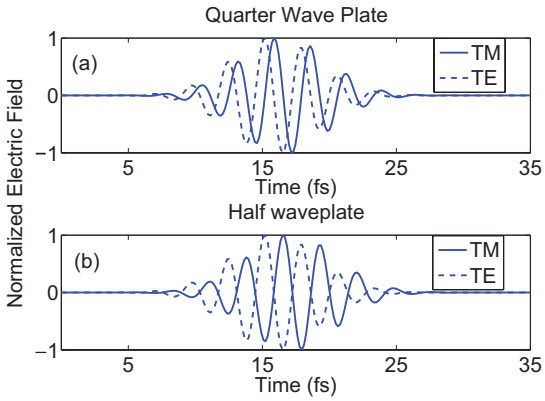

Figure G.2: Comprehensive numerical simulation results showing the waveforms of the reflected TE and TM polarizations for (a) a quarter-wave plate ($h = 107.4nm$) and (b) a half-wave plate ($h = 174.7nm$).

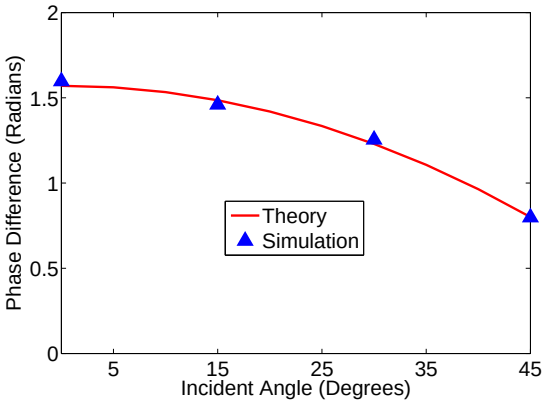

Figure G.3: Theoretical calculation and comprehensive numerical simulation results showing the phase differences between the reflected TE and TM modes, under different incident angles.

G.4 Discussions

The metallic nano-grids reflective wave plate designed in this paper has a number of potential applications and advantages. The feature that this wave plate works on reflection scheme can be utilized to build more compact devices. For example, in a design of an LCD device where a QWP and a reflector are needed [144], our

reflective wave plate can be used instead of the two components. This can be an advantage in miniaturizing portable devices. As another example, two QWPs and a Partial Reflector (PR) are used in an experiment of polarization self-modulation in VCSEL [145]. Our wave plate can be made half reflective by making the substrate thin enough, and used instead of the QWPs and PR originally used. The reflective wave plate does not only make the experiment more compact, but also does it bring the possibility of reaching higher modulation speed.

Another advantage of the reflective nano-grid wave plate is that it is inherently a zero-order wave plate. In fact, we expect the response of this wave plate under different wavelengths to be even better than the zero-order wave plates made of birefringent materials. This is due to the shorter beam path within the wave plate. For example, a polyimide transmissive HWP has a thickness of 14.5 μm operating at 1.55 μm [140], which corresponds to 15 wavelengths in the polyimide, whereas the height of our HWP corresponds to only about half of a wavelength within the structure. Under a 5% operating wavelength change, there will be a 0.75λ change to the beam path of a polyimide HWP, comparing to only a 0.025λ change to the beam path of our reflective wave plate. Therefore, we expect our wave plate to have a wider operating band than a birefringent wave plate, although the detailed analysis on this is beyond the scope of this paper.

G.5 Conclusions

In this paper, we designed an optical wave plate that operates at reflection using metallic nano-grids, or equivalently, nano grooves on metallic surface. By using effective index method and mode-matching theory, we had calculated the height of the grids for a QWP, and showed that the design can be easily changed to a HWP simply by changing the height of the grids. We also investigated the cases where light incidents into the wave plate at an angle, and had found that the resulting phase difference between the reflected TE and TM modes decreases as the incident angle changes from 0 deg to 45 deg. The theoretical result was confirmed by a comprehensive finite-difference time-domain electromagnetic simulator. We believe the designed wave plate is simple and compact, and is easy to build with the latest nano-fabrication technique.

Appendix H

Substrate-Based Platform for Boosting the Surface-Enhanced Raman of Plasmonic Nanoparticles

Originally published:
Q. Min, Y. Pang, D.J. Collins, N. A. Kuklev, K. Gottselig, D. W. Steuerman, and R. Gordon. Substrate-based platform for boosting the surface-enhanced raman of plasmonic nanoparticles. Optics Express, 19(2):1648–1655, 2011.

ABSTRACT

Metal nanoparticles allow for surface-enhanced Raman scattering (SERS), with applications including spectroscopy and highly-multiplexed biolabels. Despite advances in nanoparticles design nanoparticles, the SERS from these systems is still weak when compared with randomly roughened substrates, and this limits their efficacy for many applications. Here, we coherently boost the SERS signal of colloidally-synthesized silver nano-prisms over 50× by using multilayer substrates. Theoretical calculations verify the enhancement, and uncover the near-field response. This points the way toward a versatile platform for greater SERS enhancement from nanoparticles.

H.1 Introduction

Metal nanoparticles (MNPs) can have surface plasmon resonances that enhance the local electric field leading to surface enhanced Raman spectroscopy (SERS) [146–153]. MNPs offer added functionality in many applications, for example, with Raman bio-labels. These labels can be functionalized and bound to a target, such as cell surface markers, to provide a high-degree of multiplexed detection [152, 153]. MNPs can be defined lithographically [11, 225, 226] or grown in sollution [227]. The wet chemical approach allows for substantial shape control, and even single-crystal structures with lower scattering losses. Compared with randomly generated SERS substrates, the SERS response from MNPs is reliable and reproducible [148].

Despite the many advantages of MNPs, the SERS enhancements reported so far have been typically orders of magnitude less than randomly roughened substrates or aggregates [228, 229]. Even reports of 10^9 enhancement factors in core-shell structures are still three orders of magnitude smaller than generally accepted for single-molecule Raman demonstrations on random structures [148]. Therefore, a general means to increase MNP SERS by orders of magnitude would be a transformative step for the field.

Previous works show that a dielectric spaced metal layer could enhance the SERS signal for evaporated silver islands about 10-fold by tuning their plasmon resonance frequency [230–234] and changing the local density of states [20, 235–238]. However, further improvements are required to boost the SERS to the level of the randomly roughened surface case and ultimately to detect the single molecule Raman signal [146, 147, 239].

In this paper, we use the colloidally synthesized silver nano-prisms on top of a gold ground plane spaced by a TiO_2 dielectric layer to coherently enhance the SERS signal of rhodamine 6G (R6G). Over 50× SERS enhancement is achieved. Theoretical calculations and finite difference time domain (FDTD) simulations verify the experimental results and indicate more room for further SERS amplification with this configuration.

H.2 SERS Measurement with Multilayer Substrates

H.2.1 SERS Experimental Setup

Figure I.1(a) shows the schematic of the multilayer SERS substrate. An optically thick 100 nm Au layer was used as a ground plane (EMF Corp.). This was coated with a TiO_2 spacing layer evaporated by 7.5 kV electron beam source in an Angstrom Engineering physical vapor deposition system. The TiO2 layer refractive index, d_n, was measured to be 2.19 via white light reflection measurements. The purpose of the spacer layer was to tune the phase of the reflected light from the gold mirror as a function of thickness, t. For each thickness, we fabricated three different samples to ensure reproducibility.

Silver nano-prisms were synthesized in water by white-light assisted conversion of spherical nanoparticles [227]. This yielded an ensemble of prisms with average length on a side, d, of 80 nm, shown as the inset in Fig. I.1(b). A solution containing silver nano-prisms and dye were drop-cast (0.02 mL) on the substrates, where the concentration of the R6G dye was 1 μM. The sample was then allowed to dry for 5 hours. Ultra-pure water with a resistivity of 18.2 MΩ-cm (from Barnstead NANOpure Diamond water purification system) was used throughout the experiments.

The Raman spectra of the dye were taken using a Renishaw inVia Raman microscope with a 785 nm diode laser of 0.5 mW power illumination and an estimated density of 30 nano-prisms within the laser focus, as determined by scanning electron micrograph (SEM) studies of the surface – shown in Fig. I.1(b). The backward Raman scattered light was collected by a 20$\times$ objective (NA = 0.4) with a total integration time of 30 s. All the measurements were repeated at least 4 times in each experiment and all the experiments were repeated on several different days in order to ensure the consistency and the stability of the results.

H.2.2 Extinction Spectrum of Silver Nano-Prisms

The spectral dependence of the plasmon resonances were examined in solution, because of their relevance to SERS [240, 241]. Figure I.2 shows the extinction spectrum (Cary 5 UV-VIS-NIR Spectrophotometer) of the nano-prisms used in the experiment. Three extinction peaks were observed at 337 nm, 413 nm, and 673 nm, of which the 673 nm peak has the strongest extinction.

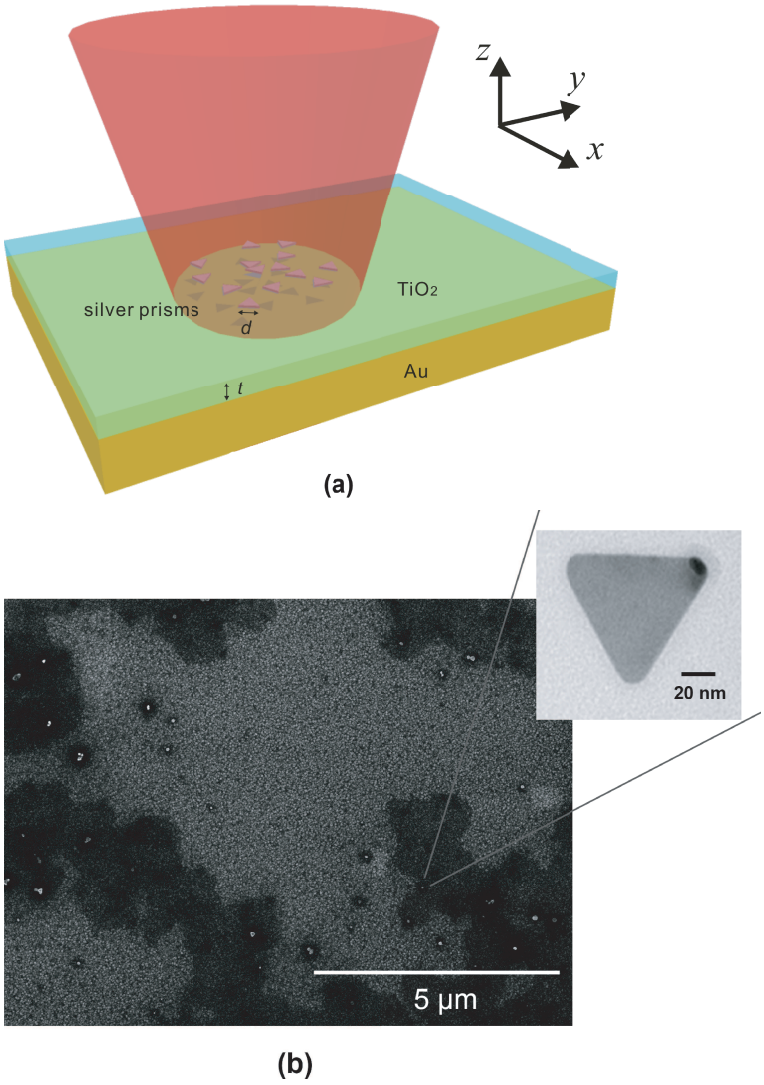

Figure H.1: Silver nano-prisms over the multilayer SERS substrate. (a) Schematic of silver nano-prisms on TiO_2 spacer layer over optically thick Au layer, where t is the thickness of TiO_2 and d is the side length of a nano-prism. The illumination pattern is not to scale and the actual experiment has about 30 MNPs within the focus. (b) The SEM of the multilayer SERS substrate surface. The inset shows a TEM image of a single silver nano-prism.

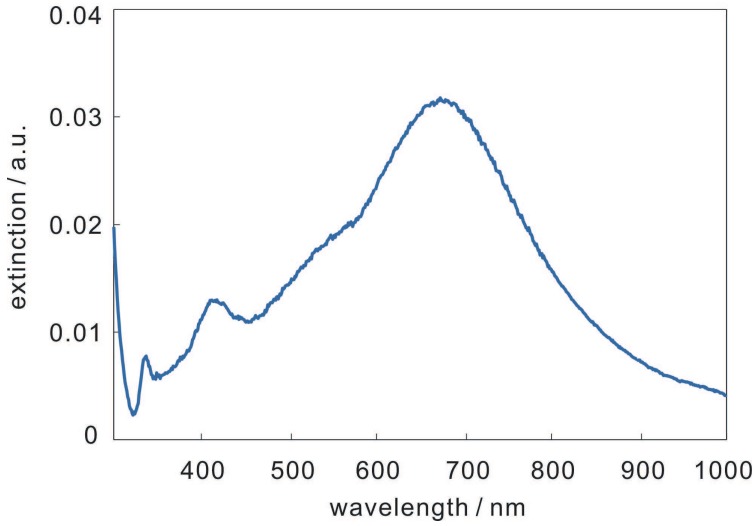

Figure H.2: Extinction spectrum of the silver nano-prisms used in the experiment in an aqueous environment, where the 673 nm extinction peak is clearly visible.

H.2.3 Theoretical Calculation on Phase Reflection

The primary objective of this experiment was to find the optimized dielectric spacer layer thickness for SERS enhancement. To coherently enhance the SERS, the reflected light from the ground plane should constructively interfere with the incident light beam. Upon reflection at the interface of a perfect electric conductor (PEC) and a dielectric, there is a 180° phase shift of the electric component. The optimal thickness is corresponding to the in-phase reflection configuration which is expected to be [242]:

$$(2 \times d)n_d = (m + \frac{1}{2})\lambda. \tag{H.1}$$

Here, n_d is the TiO_2 refractive index which is measured to be 2.19, λ is the excitation wavelength equal to 785 nm, and m is a whole number. The first and the second orders of optimized thicknesses dare determined to be 90 nm and 270 nm. Note here the PEC assumption will lead to discrepancies between the theory and experiment, and this will be captured with the FDTD simulation results below.

H.2.4 SERS Measurement Results

Figure I.3(a) shows a sample SERS spectrum from the multilayer SERS substrate. Three Raman shift peaks were observed, which are 1312 cm^{-1}, 1364 cm^{-1}, and 1509 cm^{-1}, respectively. The full analysis was performed on the 1509 cm^{-1} peak because no deconvolution was necessary (although the other peaks showed the same general enhancement behavior).

Figure I.3(b) shows the enhancement of SERS using silver nano-prisms as a function of dielectric layer thickness. The enhancement is with respect to a bare glass substrate with the same drop-casting of silver nano-prisms and dye. The uncertainty for each thickness was calculated from the standard deviation from at least four SERS measurements at different locations on the sample. Furthermore, the measurements were repeated on two additional samples, each with the same thickness, showing the same results. It can be seen that the enhancement factor changes with thickness variation, and the peak enhancements (45.4±1.6 and 51.6±4.7) were achieved when the TiO_2 equaled 40 nm and 200 nm, respectively. The uncertainty in these values comes from standard deviation over multiple measurements over randomly distributed nano-prisms. The difference in the thickness between the two peaks is 160 nm, which is close to the theoretical prediction of 179 nm. Also, the values are offset from the

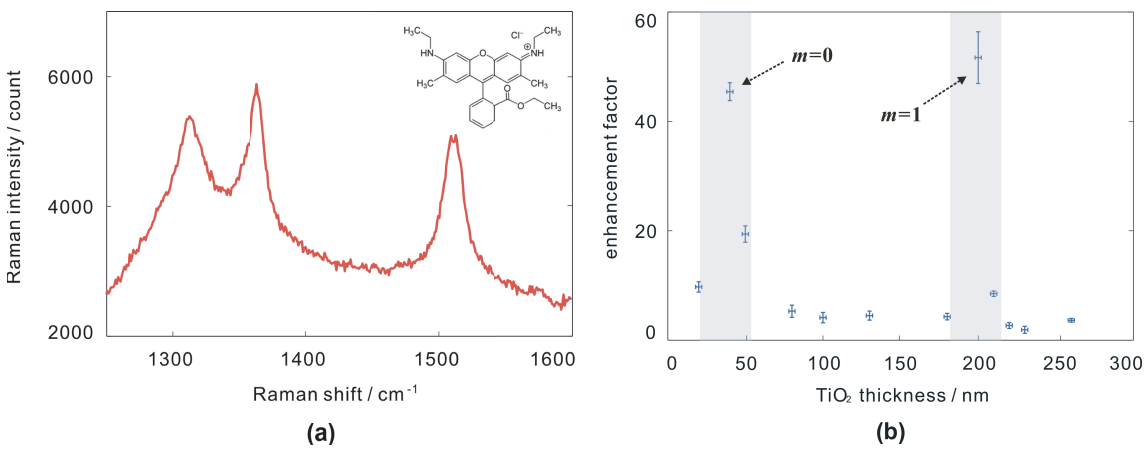

Figure H.3: Experimental SERS spectra. (a) An example Raman spectra for the R6G dye using the silver nano-prisms. (b) Enhancement of SERS using silver nano-prisms for the 1509 cm^{-1} Stokes shift peak as a function of dielectric layer thickness, normalized by the SERS signal from a bare glass substrate. The blue bands indicate the first order and the second order SERS enhancement peaks.

prediction of Eq. I.1, which will be discussed further below.

To ensure the generality of the enhancement for different MNPs, we repeated the experiments using Au nano-rods [243] instead of Ag nano-prisms, and similar enhancement factors and dielectric thickness dependencies were observed (not shown).

H.3 FDTD Simulation Results

In the experiment, the situation is complicated from the simple picture presented above by other factors such as the absorption of the metal ground-plane, coupling into the modes of the finite dielectric layer underneath the MNPs, multiple reflections by the dielectric layer and ground-plane and a finite collection aperture. In addition, the finite wavelength difference between the excitation and Stokes wavelengths should be considered. For a more comprehensive understanding, we used FDTD numerical analysis for comparison with experiments.

The Au permittivity values were taken from a previous work [47], and the Ag permittivity values were taken from a different work [48], and these are two commonly used references for those materials, respectively. A 2 nm mesh was also used around the silver nano-prism to ensure that plasmonic effects were accurately captured, as verified by convergence studies. The simulation region was enclosed with perfectly-matched layer boundaries in the direction perpendicular to the gold ground plane, and with 200 nm periodic boundaries in the directions parallel to the ground plane. The theoretical results were invariant to changes in periodicity. A plane wave was injected from the top of the structure.

Figure I.4 shows the resulting simulation of the SERS signal and its TiO_2 thickness dependence. To obtain the theoretical enhancement factor, we compare the near-field intensity of the nano-prism above the Au ground using different TiO_2 layer thicknesses to the control where the nano-prism was placed directly on a glass substrate without the Au ground. The SERS intensity I_{sers} is proportional to the localized electric field intensity both at the excitation wavelength E_{ex}^2 and the Raman wavelength E_{raman}^2 [244, 245]:

$$I_{sers} \propto= E_{ex}^2 \times E_{raman}^2. \tag{H.2}$$

To consider the size distribution of the Ag nano-prisms, we sample 60 nano-prisms from a TEM image of the sample in a location where we performed the SERS. We

perform FDTD simulations using nano-prisms of different sizes, and obtain the near field enhancement by summing the SERS intensity weighted by the nano-prism size distribution, and comparing the cases with and without the Au ground. The first order and the second order SERS enhancement peaks occur at 80 nm and 260 nm TiO2 thicknesses, which are slightly less than the PEC theoretical results because we used Au in the FDTD model instead of PEC for the ground plane in our theoretical computation. Since the finite skin depth of Au for 785 nm wavelength light leads to penetration into the metal, there is an additional phase shift at the metal-dielectric interface. The enhancement factors of these two in-phase thicknesses are approximately 40.36 and 32.85, which are smaller than the experiment.

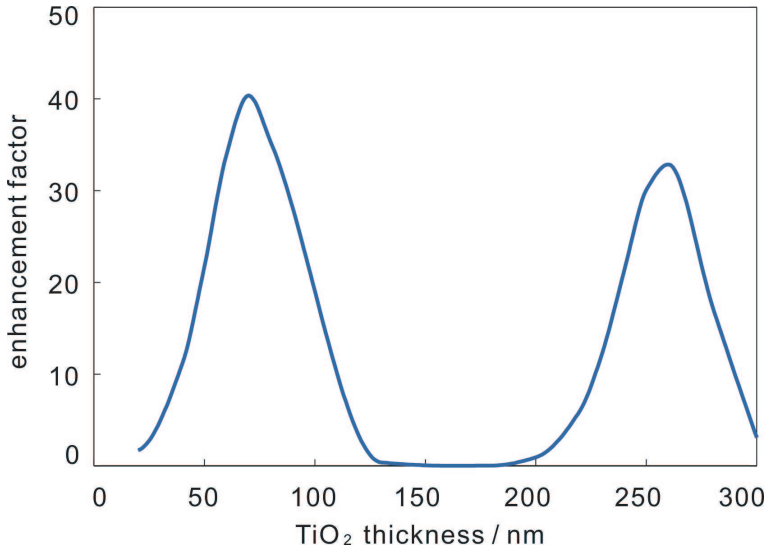

Figure H.4: Finite difference time domain simulations of enhancement factor, for 80 nm side nano-prism in the same configuration as in Fig. I.3(b).

Figure I.5 shows the electric field intensity around a 80nm prism (the average size), the dielectric layer and the reflector (outlined with dashed white lines) in the xz-plane. The local field intensity in the resonant cases of 80 nm and 260 nm thicknesses are one order of magnitude larger than the off-resonant case (160 nm). This results from the constructive and destructive interference of the image excitation created by the Au ground plane reflector.

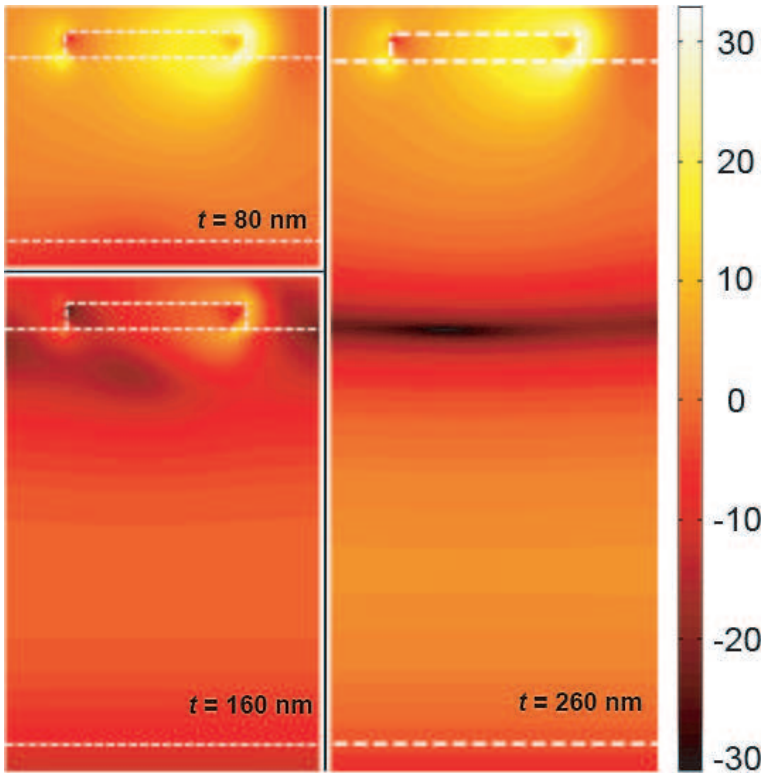

Figure H.5: Simulated local electric field intensity distributions close to a nano-prism for varying dielectric thicknesses (t = 80 nm, 160 nm, 260 nm) shown on a logarithmic scale. The dashed lines show the interfaces of the silver nano-prism, the dielectric layer and the gold ground plane.

H.4 Discussion

The experiment and calculations give comparable enhancement factors and spacer layer thickness dependencies. Aside from the finite penetration of light into the metal, the additional offset with respect to the theoretically expected optimal spacer layer thickness values remains an uncertainty in the experiment, but can be attributed to (at least in part) dye accumulation beneath the MNPs, off-axis excitation by the focusing objective and uncertainty in the dielectric thickness. The SERS signal peak values of experiment results are close to those given by the FDTD simulation. In the measurements, we measured locations of the sample where there was no obvious aggregation, as observed under the optical microscope. Even so, some aggregation may be present, and we cannot accurately capture that effect within our simple simulation.

Moreover, it is possible to envisage more advanced multilayer SERS schemes [13, 246, 247], such as a right corner reflector, which in the optimal geometry leads to an enhancement factor of 4 in terms of the localized field around the nano-prisms. As compared to the present system, the flat ground plane only has an enhancement factor of 2 [22]. Considering the SERS signal intensity is approximately proportional to the fourth power of the localized field [244, 245], then 16 times greater SERS signal enhancement is expected for the corner reflector substrate. Even more advanced schemes, such as the Yagi-Uda shaped MNPs, may be implemented to increase the enhancement still further. Based on these considerations, it is expected that at least 3 orders of magnitude enhancements in the MNP Raman should be possible through configuration optimization. Such boosts in the electric field could make single-molecule Raman demonstrations viable with MNPs [146, 147, 239].

H.5 Conclusion

We have demonstrated that the combination of simple substrate engineering and silver nano-prisms can enhance SERS by a factor of 50. Both the experiment and the theoretical calculations give comparable enhancement factor dependence on the dielectric spacer layer thickness. Similar results were also observed for Au nano-rods which indicate this multilayer substrate is a generic approach to boost the SERS signal for different MNPs grown in solution. FDTD simulations also verified this SERS enhancement quantitatively. With more advanced schemes utilizing corner reflectors

or Yagi-Uda antennas, it is expected that MNP SERS can be enhanced by 3 orders of magnitude to the regime of signal molecule detection. Obvious benefits will arise from this sensitivity boost for many applications including the use of MNPs as Raman biolabel markers, the development of more reliable Raman-enhanced templates, and the improvement of Raman-based pathogen sensors.

Appendix I

Antenna Design for Directivity Enhanced Raman Spectroscopy

Originally published:
A. Ahmed, Y. Pang, G. Hajisalem, and R. Gordon. Antenna design for directivity enhanced raman spectroscopy. International Journal of Optics, in press.

ABSTRACT

Antenna performance can be described by two fundamental parameters: directivity and radiation efficiency (RE). Here we demonstrate nanoantenna designs in terms of improved directivity. Performance of the antennas is demonstrated in Raman scattering experiments. The radiated beam is directed out of the plane by using a ground plane reflector for easy integration with commercial microscopes. Parasitic elements, parabolic and waveguide nanoantennas with a ground plane are explored. The nanoantennas were fabricated by a series of electron beam evaporation steps and focused ion beam milling. As we have shown previously, the circular waveguide nanoantenna boosts the measured Raman signal by 5.5× with respect to a dipole antenna over a ground plane; here we present the design process that led to the development of that circular waveguide nanoantenna. This work also shows that the parabolic nanoantenna produces a further four-fold improvement in the measured

Raman signal with respect to a circular waveguide nanoantenna. The present designs are nearly optimal in the sense that almost all the beam power is coupled into the numerical aperture of the microscope. These designs can find applications in microscopy, spectroscopy, light emitting devices, photovoltaics, single photon sources and sensing.

I.1 Introduction

Antennas have been widely used in radio communications for more than a century for efficient transmission of information over long distances. Since its discovery in 1895, enormous progress has been made with better control of antenna parameters (for a brief history see [248] and references therein). For example, directional emission was demonstrated by Yagi-Uda in the microwave regime [249] where the radiation from the feed element is directed with the assistance of reflector and director parasitic elements. The directivity of antennas has played a vital role in microwave communication systems, specifically in satellite communication for the realization of high gain antennas.

Radio antennas provide solutions to communication problems, whereas recent developments for realization of optical antennas were mainly dictated by microscopy and spectroscopy applications [250, 251]. Typically antennas have dimensions of the order of the operating wavelength, requiring antenna dimensions in nanometers for operation in the visible regime. In the visible-IR regime, the metal cannot be taken as a perfect conductor and the nanoantenna design must be modified due to plasmonic properties [252–255]. Recent developments in the nanotechnology have made the fabrication of such small structures possible, leading to the development of optical single element and Yagi-Uda equivalent nanoantennas [11–13, 15, 247, 256–262]. Directing the emission from optical emitters is highly desired for efficient detection, and by reciprocity, efficient excitation as well. Typical applications include light emitting devices [263, 264], photovoltaics [265–269], sensing [270, 271], spectroscopy [146, 272, 273], single photon sources [274, 275] and microscopy [250, 276, 277].

In a recent work, our group has shown that the scattered radiation from nanoparticles can be directed out of the plane of substrate and into the collection microscope using a ground plane reflector [9]. Enhancement of over 50× was observed in the measured Raman signal as compared to nanoprisms over a glass substrate. We also

demonstrated recently an experimental work on waveguide nanoantenna to boost the Raman signal by beam forming in the lateral plane [14]. A further 5.5× enhancement was observed with a circular waveguide nanoantenna as compared to a dipole nanoantenna over a gound plane.

The main objective of this work is to present the design of planner nanoantennas for optimal performance in directivity-enhanced Raman scattering (DERS). Here we present the details of the design process that led to the development of circular waveguide nanoantenna, the different designs considered for beam forming in the lateral plane and the possibility of higher local fields for further Raman enhancement. We also show experimentally that the parabolic reflector can enhance the Raman signal by 4× as compared to the circular waveguide nanoantenna owing to its improved directivity and enhanced local fields, however, it is challenging to fabricate.

I.2 Antenna Design Parameters

The total power radiated by an antenna can be given as

$$P_{rad} = \int_0^{2\pi} \int_0^{pi} p(\theta, \phi) \sin\theta d\theta d\phi \tag{I.1}$$

where $p(\theta, \phi)$ is the normalized angular power density also know as radiation pattern of an antenna. Directivity is defined as the antennas ability to radiate in a specific direction more efficiently as compared to a hypothetical isotropic radiator [22]:

$$D = \frac{4\pi}{P_{rad}} p(\theta, \phi). \tag{I.2}$$

Considering the numerical aperture (NA) of the microscope objective, a more suitable parameter for describing the beam forming ability of an antenna is the beam efficiency (BE)

$$BE = \frac{\int_0^{2\pi} \int_0^{pi} p(\theta, \phi) \sin\theta d\theta d\phi}{P_{rad}} \tag{I.3}$$

where θ_0 is the cone half angle. Cone angle of 30 degrees was calculated from the measured spot size d of approximately 1.5 μm, using: $\theta_0 = sin^{-1}(\lambda/2d)$. This corresponds to a NA of 0.28.

Radiation patterns of single element nanoantennas are typically dipolar in nature resulting in poor directivity $D_{max} = 1.5$. Directive emission at optical wavelengths has

been achieved using multielement nanoantennas [13, 258, 278]. Radiation patterns of those antennas reveal that the main beam is directed in the plane of the substrate thus cannot be readily used in an ordinary microscope setup. Further, vertical Yagi-Uda nanoantenna has been realized using top-down approach [15]. Improved directivity at optical wavelengths can have tremendous impact in areas such as optical microscopy, spectroscopy, sensing and applications involving single photon sources, where efficient collection and emission is critical.

Another important factor in the context of Raman measurements is the local field strength. It has been recently shown that maximum field enhancement results when power radiated by the antenna is equal to the power loss in the antenna [279–281]. This is commonly referred to as impedance matching in microwave antenna theory [22]. Even higher local field can be achieved by reducing the mode volume of the antenna by reducing the feedgap between the two elements of the dipole antenna [281].

I.3 Design and Fabrication

In this paper we investigate different nanoantenna designs for DERS with the desired features of out of plane radiation and enhanced local fields. The introduction of ground plane prevents loss of scattered radiation into the substrate and proper adjustment of antenna distance from the ground plane can result in radiation enhancement out of the plane. Further improvement of directivity is demonstrated by beam shaping in the lateral plane using different designs including parasitic elements, waveguide antennas and parabolic reflectors. The multilayer substrate is fabricated by electron beam evaporation and the different designs are milled using focused ion beam (FIB).

Figure I.1 illustrates the multilayer substrate used for the fabrication of nanoantennas studied in this work. The antennas were designed to be tested under Raman microscope. The dimensions of different layers and the dipole antenna were calculated to achieve best performance at wavelength of 840 nm (mean of excitation and Raman scattered wavelengths). The antenna consists of a 130 nm long and 50 nm wide dipole. Traditionally, dipole antenna characteristic lengths were of the order of wavelength of operation $\lambda/2$, but the real metal response requires that shorter effective wavelengths are introduced for the determination of dipole length in infrared and optical regions [254]. A 150 nm thick gold layer was used as ground plane to ensure

that it was optically thick.

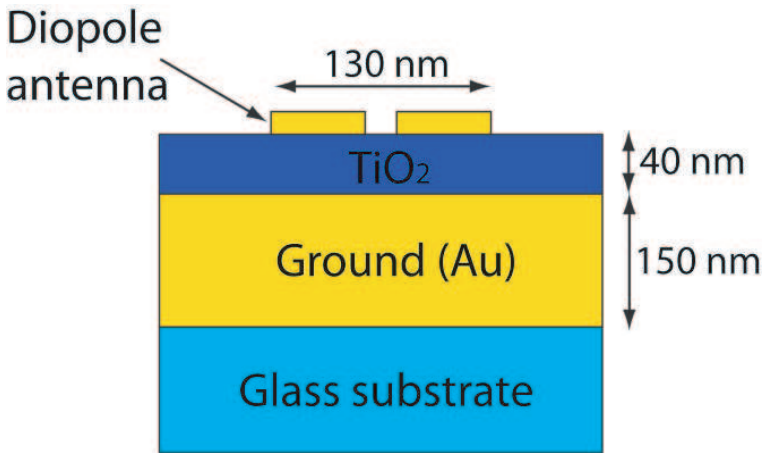

Figure I.1: Multilayer substrate to control the radiation pattern of a dipole antenna. Thicknesses of ground plane, dielectric (TiO_2) spacer and top gold layer are 150 nm, 40 nm and 50 nm respectively. Dipole antenna length of 130 nm with a 20 nm feedgap was used to operate at wavelength of 840 nm.

The optimal thickness of dielectric spacer (TiO_2) was calculated numerically to be 40 nm using finite-difference time-domain (FDTD) simulations. It should be noted that this is smaller than the typical quarter wavelength value due to penetration into the metal, as well as impedance matching effects [281].

The multilayer substrate was fabricated by evaporation of gold and TiO_2 onto glass substrate by means of electron beam evaporation under a pressure of 2×10^{-6} Torr. The proposed nanoantenna structures were milled on the top 50 nm thick gold layer using FIB. Figure I.2 shows the different nanoantennas investigated in this work for normal emission. Relative efficiencies of these structures are discussed in the simulation section below, where it is shown that the circular waveguide nanoantenna shown in Figure I.2c, results in best performance in terms of directivity.

Another promising design translated from the microwave antenna theory is that of the parabolic reflector antenna. We demonstrate DERS from the beam forming abilities of a parabolic reflector nanoantenna. Figure I.3 shows the schematic of the parabolic nanoantenna. A paraboloid shaped trench was milled into a silicon wafer using FIB. As shown in the figure, the focal length of this paraboloid was designed to be 500 nm, and the diameter of the top circle is 2 μm. A layer of 100 nm thick gold (optically thick) was evaporated onto the silicon wafer by means of electron beam evaporation under a pressure of 2×10^{-6} Torr.

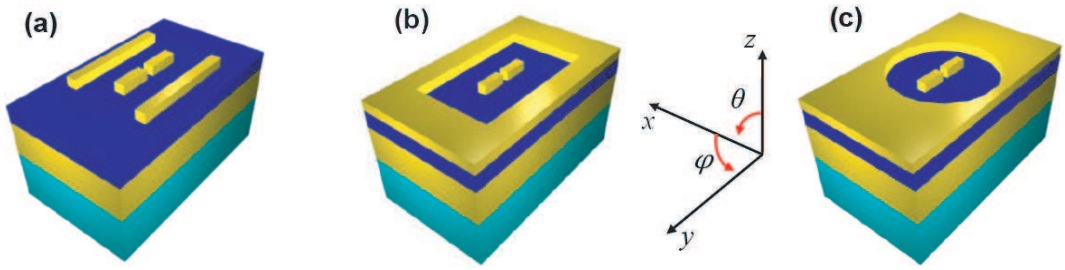

Figure I.2: (a) Dipole antenna over ground with two parasitic reflectors 150 nm long and 100 nm from the feed element. (b) Dipole antenna over ground plane with a square reflector of length 500 nm (square waveguide antenna). (c) Dipole antenna over ground plane with a circular reflector of radius 250 nm (circular waveguide antenna).

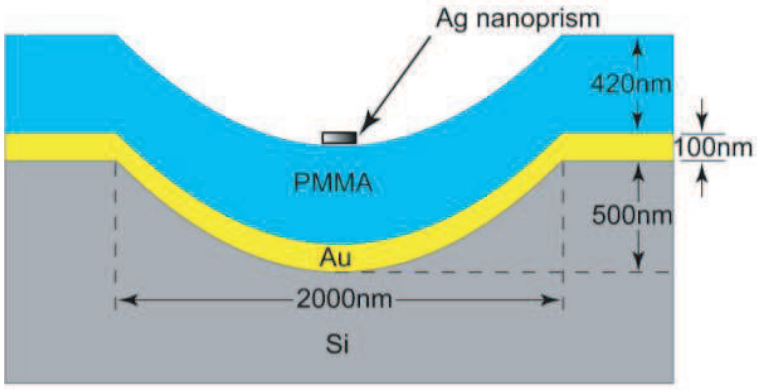

Figure I.3: The schematic drawing of the proposed parabolic reflector nanoantenna.

The conformity of the evaporated layer to the hole on silicon creates a parabolic reflector antenna on Au layer. PMMA was then spin-coated on top of the Au layer as a spacing dielectric layer. We chose PMMA and the spin-coating technique to make the spacer layer for reasons of simplicity and repeatable thickness control. Finally, Ag nanoprisms, synthesized in water by white-light assisted conversion of spherical nanoparticles [227], were mixed with 3 μMol rhodamine 6G dye and drop-coated onto the PMMA surface. The nanoprisms serve as the feed of the parabolic reflector nanoantenna.

The experiments of [9] are first repeated using PMMA for the determination of optimal thickness of the PMMA layer. As a result (not shown), the first and second order coherent SERS enhancement peaks are found at 120 nm and 420 nm PMMA thickness. We choose to spin-coat 420 nm PMMA (corresponding to the second order SERS enhancement) onto our parabolic reflector, since this thickness is more compatible with the focal length of our parabolic reflector, bringing the feed Ag nanoprism near the paraboloid focal point.

I.4 Simulation Results

The proposed structures were simulated using FDTD method. The simulation domain was terminated by perfectly matched layers (PMLs) for minimal reflections. The antenna structure was enclosed by a set of 2D field monitors forming a box to perform far-field projections and for the determination of field patterns. For the antenna structures shown in Figure I.2, an electric dipole source located at the feed-gap of the dipole antenna was used to excite the nanoantenna.

FDTD simulations indicate the following parameters for best performance for each type of antenna. Two 150 nm long parasitic reflectors, 100 nm away from the feed element resulted in a half power beam width (HPBW) of 110 degrees in the xz-plane. Radiation patterns of this structure show a very broad HPBW in the yz-plane. To further improve the directivity in both planes we introduced reflectors parallel to the x-axis as well. It was demonstrated numerically that a square reflector with length of 500 nm resulted in best performance. The corresponding HPBWs are 85 degrees and 90 degrees in the xz and yz-planes respectively. Even better performance is observed by using a circular waveguide antenna as shown in Figure I.2(c), producing a symmetrical beam out of the plane of substrate with HPBW of 85 degrees in both planes. Figure I.4(a, b) shows the radiation pattern in the xz and yz-planes respectively at

the wavelength of 840 nm. It can be seen that in the absence of ground reflector, most of the scattered power is directed into the substrate and away from the microscope objective.

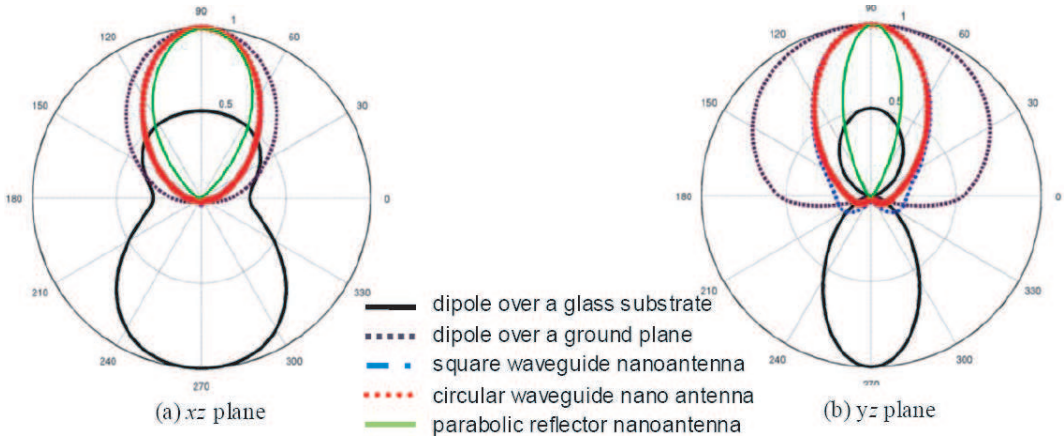

Figure I.4: Radiation patterns of a dipole antenna on a glass substrate, dipole over ground plane, square waveguide nanoantenna (side length = 500 nm), circular waveguide nanoantenna (radius = 250 nm) and parabolic reflector nanoantenna. Calculated using far field projections of 3D FDTD simulations (a) xz plane (b) yz plane.

The circular waveguide nanoantenna gives a nearly optimal radiation pattern resulting in the collection of almost all of the scattered light by a numerical aperture of 0.75. The radiation patterns of the parabolic reflector is also plotted in Figure I.4 for comparison. It can be seen that the parabolic reflector nanoantenna results in an even better directivity as compared to the circular waveguide nanoantenna.

The ring-reflector acts to create a lateral standing wave that reflects light back towards the central dipole antenna structure. This is most similar to the waveguide antenna, which has a lateral resonance when the wavelength is 3.4× the radius of the circular waveguide (i.e., at the lowest order mode cut-off) [22, 88]. Larger and smaller radii do not provide this resonance at the desired wavelength of 840 nm and thus give in smaller directivities. The radiation patterns of circular waveguide nanoantenna with slightly smaller and larger radii (not shown) show splitting of the main beam into two lobes, thus lowering the directivity in the normal direction.

Since the present design is optimized to work at around 840 nm, this corresponds to a radius of 250 nm, which is precisely the radius value that was found to give the greatest DERS in the experiment. The beam forming for this antenna design allows for directive emission into a numerical aperture of approximately 0.75; therefore, it is well suited for microscope setups.

Another parameter dictating the intensity of Raman signal is the local field enhancement that arises from plasmonic resonances, tapers, gaps and high-curvature in the antenna design [46, 47]. Impedance matching and reduction of mode volume of the antenna provides maximum local field enhancement [281]. Figure I.5(a, b) shows the local field intensity in the antenna gap for gap sizes of 20 and 5 nm respectively at the design wavelength of 840 nm (log scale).

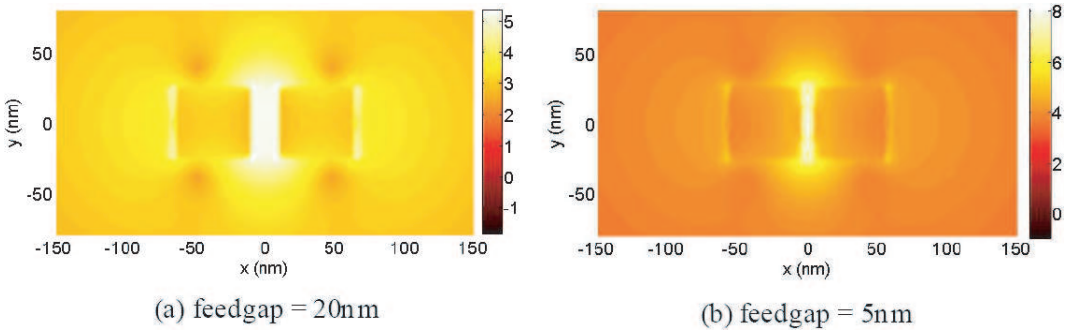

Figure I.5: E field intensity $|E/E_0|^2$ the design wavelength of 840 nm for (a) gap size of 20 nm (b) gap size of 5 nm (log scale).

By reducing the gap size from 20 nm to 5 nm, the normalized E field intensity $|E/E_0|^2$ increases by approximately 1000×. Intensity of Raman signal is proportional to the square of E field intensity thus we expect an enhancement of 106. The feedgap of the fabricated circular waveguide nanoantenna was 20 nm. Thus it is clear that the Raman signal can be considerably enhanced by reducing the feedgap, which is a challenging task.

Now we present the simulation results of the parabolic reflector nanoantenna. Figures I.6 shows the electric field intensity profile at a vertical segment of the structures at the design wavelength of 840 nm. It can be seen that the local field intensity at the Ag prism over a parabolic reflector is much larger than that over a planar reflector. From the field intensity profiles in the PMMA layer, it can be seen that the Ag nanoprism is placed at the second anti-node of the parabolic reflector at 840 nm wavelength, the same as in the planar reflector case; it is also at the focal point of the paraboloid. Therefore, the two effects, constructive interference and focusing, combine to give the enhanced Raman signal. Our parabolic reflector is able to collect more power from the incoming Gaussian wave to the Ag nanoprism feed element, indicating a better coupling between the far- and the near-field, or in an conventional antenna concept, a higher directivity.

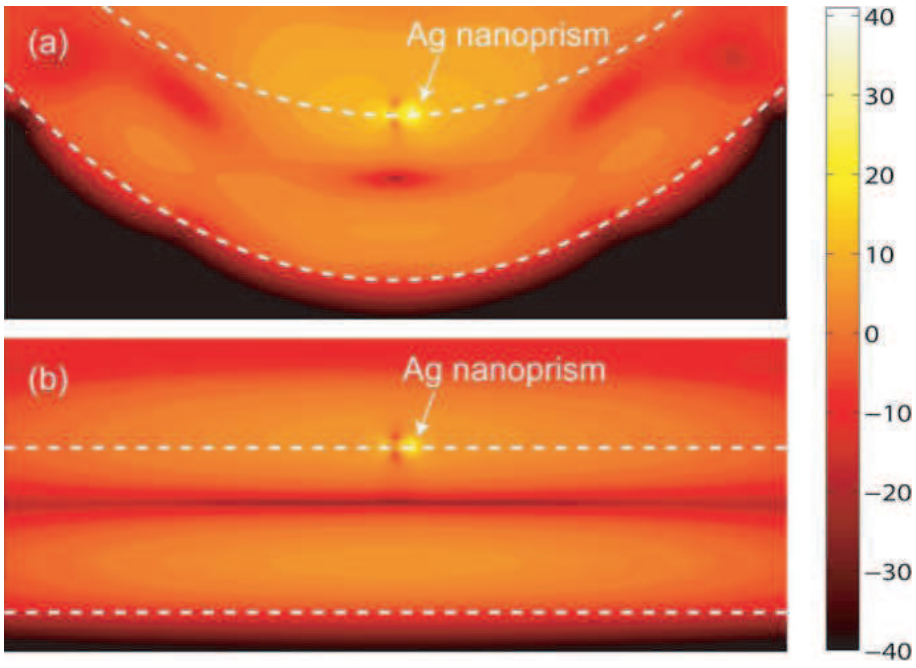

Figure I.6: FDTD simulation results comparing the vertical segment electric field intensity profiles of an Ag nanoprism above (a) a parabolic reflector and (b) a planar reflector. The white dotted lines show the Au ground plane and the PMMA layer surfaces. The color map is in dB scale.

In terms of Raman enhancement at the Ag nanoprism feed element, the relative Raman signal enhancement is proportional to the product of the excitation field intensity $|E_{exc}|^2$ the emitted Raman field intensity $|E_{raman}|^2$. The Raman enhancement factor was computed at the near-field of the Ag prism (within a rectangular box 10 nm away from the Ag prism). It was found from the local field enhancement that the Raman enhancement near an Ag prism in a parabolic reflector arrangement is 40× larger than in a planar reflector arrangement. It is due to this high local field effect that the parabolic reflector nanoantenna results in a stronger Raman signal as compared to the circular waveguide nanoantenna (of Fig. I.2c) which produces only 1.2× enhancement of the local field by the introduction of the circular ring around the dipole over a ground plane.

I.5 Raman Scattering Experiments

Raman scattering experiments were carried out for the fabricated circular waveguide and parabolic antennas using Rhodamine 6G as the Raman dye excited by a 785 nm laser. For this CW excitation, there is negligible two-photon fluorescence, which would show up as background in the Raman spectrum. The emitted wavelength at $1509cm^{-1}$ Stokes line (λ = 890 nm) was measured using a Renishaw inVia Raman microscope with a 100× objective and a spot size d of approximately 1.5 μm (as determined by mapping experiments). Raman dye, Rhodamine 6G (400 μM in ethanol) was drop coated and the sample was allowed to dry for 6 hours.

Figure I.7(a) shows the measured Raman signal intensity as a function of Raman shift using the circular waveguide nanoantenna. The circular reflector with radius of 250 nm resulted in the strongest DERS signal as is predicted by the numerical results of Figure I.4.

For comparison, detected intensities from dipole over ground and from the unmilled regions of the top gold surface (without any dipole antenna) are also shown. A dipole antenna of same dimensions and on the same substrate was fabricated by removing a ring of diameter 10 μm, to approximate the absence of the ring structure. This dipole over ground is used as the reference for the calculation of EF. The measured spot size of 1.5 μm results in illumination of an area of 1.76 μm^2, which is much larger than the area of the antenna gap. From the results of Figure I.7(a), it can be seen that the contribution from the gold surface alone (i.e., without the antenna) is small when compared to that from the antenna. It should be noted that the Raman

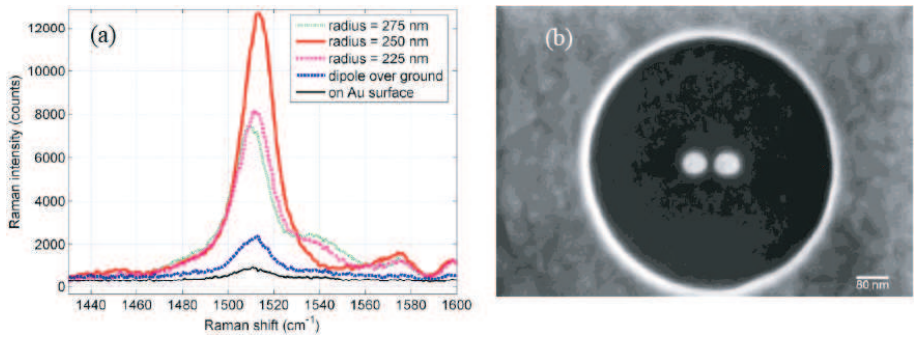

Figure I.7: (a) Raman spectra from the nanoantenna structure for various radii of circular reflector, dipole over a ground plane and the top unmilled Au surface. (b) Scanning electron microscopy image of the fabricated circular waveguide nanoantenna.

scattering intensity is boosted about 5.5× as compared to dipole over ground and about 13× with respect to the top Au surface. Note that this 5.5× increase is in addition to the 50× signal increase by use of the ground plane [9], and this additional enhancement is attributed to the improved directivity of the ring structure. Thus the total enhancement from the circular waveguide nanoantenna can be estimated to be 275× as compared to nanoparticles on a glass substrate. Figure I.7(b) shows an SEM image of the fabricated circular waveguide nanoantenna.

To demonstrate that the observed increase in Raman intensity is mainly from antenna directivity and with only a small contribution from local field enhancement, we calculated the enhancement factor arising from local electric field (EF_{loc}) in the antenna feedgap. $EF_{loc} = |E_{exc}|^2|E_{scat}|^2$, where $|E_{exc}|^2$ and $|E_{scat}|^2$ are the electric field intensities at the excitation wavelength of 785 nm and Stokes shifted scattered radiation at wavelength of 890 nm, respectively. We observe maximum $EF_{loc} = 1.2$. The measured 5.5× increase in Raman intensity is thus predominantly from improved directivity of the antenna. Numerically calculated EF using beam efficiency and radiation patterns of Figure I.4 with cone angle of 30 degrees is in excellent agreement with the experimental results.

Figure I.8 shows an SEM of an Ag nanoprism (a), the scanning ion microscopy image of the fabricated structure (b) and a 6×6 μm^2 map of the Raman signal using the 1509 cm^{-1} Stokes line around a parabolic reflector nanoantenna (c). A clear enhancement to the Raman signal is obtained from the parabolic reflector nanoantenna as compared to the surrounding area, where it is equivalent to a planar reflector nanoantenna. By comparing the maximum Raman signal from a parabolic reflector nanoantenna to the average surrounding signal, a 22× enhancement is obtained.

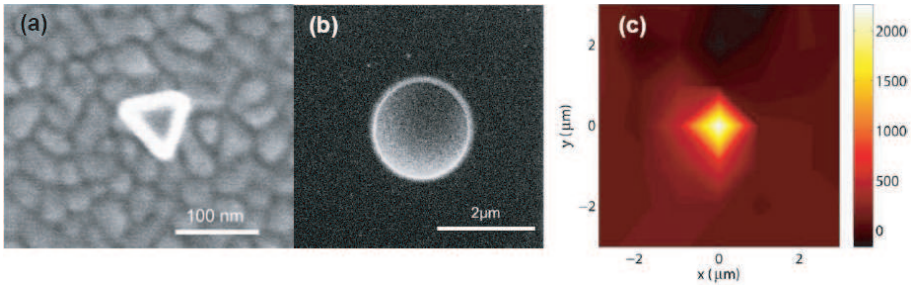

Figure I.8: (a) Scanning electron microscopy image of Ag nanoprism. (b) A scanning ion microscope image of the paraboloid drilled on silicon taken directly from the FIB. (c) A 6×6 μm^2 map of the Raman signal around a parabolic reflector nanoantenna.

Our previous experiments on Ag nanoprism over planar reflector experiments have

already shown a 50× Raman enhancement as compared to Ag nanoprisms on glass (without any reflector) [9]. Combining the result of this work and Ref. [9], we estimate that our designed parabolic reflector structure can enhance the SERS signal from metallic nanoprisms by 1100×. In other words, by directivity engineering, we have boosted the SERS signal from isolated metallic nanoprisms by 3 orders of magnitude.

We confirm that this high signal is not from an aggregation of nanoprisms by taking an SEM image of the antenna. We explain the Raman enhancement with respect to only nanoprisms on glass substrate by the high directivity from the parabolic antenna and enhanced local fields. In a SERS experiment where the nanoprisms are deposited directly onto glass, the light emission is in favor of the direction into the glass substrate due to higher refractive index of the glass. In comparison, the parabolic antenna gives an emission pattern with a tightly focused lobe into the air, with nearly all emitted light directed into the collecting microscope objective. In other words, we have improved the near- and far-field coupling from a poor efficiency to a nearly perfect efficiency by the parabolic antenna. Therefore, the 1100× enhancement between the two cases is not surprising.

The 22× SERS enhancement over the planar reflector from our experiment is very encouraging, but is still an underestimate of the parabolic reflector nanoantenna's DERS enhancement potential C still lower than our theoretical prediction of 40× enhancement. This may be due to the misalignment between the Ag nanoprism feed element and the Au parabolic reflector in the nanoantenna. The drop-coating technique is convenient to deposit the Ag nanoprisms; however, exactly controlling the nanoprism position is difficult. In future steps, we plan to build the metal feed element using lithographical methods such as FIB lithography. In that way, the position of the feed element can be precisely controlled, and an even higher SERS enhancement is hypothesized.

I.6 Conclusions

We have demonstrated directivity-enhanced Raman scattering (DERS) using directive nanoantennas including parasitic elements, parabolic and waveguide designs. The circular waveguide nanoantenna with a feedgap of 20 nm produces an enhancement factor of 275× as compared to nanopartilces over a glass substrate. This enhancement factor can be further increased by reducing the feedgap. Parabolic reflector results in an overall enhancement factor of 1100× as compared to nanoprisms over a glass sub-

strate; however, as demonstrated in this work, the fabrication of the parabolic structure is more challenging. The enhancement in these waveguide designs is specifically attributed to directivity effects; i.e., beam-shaping the antenna cone to fall within the numerical aperture of the imaging optics. Therefore, DERS is separate from other near-field enhancements that arise, for example, from plasmonic effects. Considering the numerical aperture of our microscope Raman system, the nanoantenna presented has near-perfect excitation and collection of the electromagnetic energy. This work is also exciting for related applications, for example, photovoltaics, light emitting applications, microscopy, sensing and single molecule detection [146, 271, 277].